Optical diagnostics for carbonaceous solid fuels and flame retarded polymers in laminar and turbulent flows
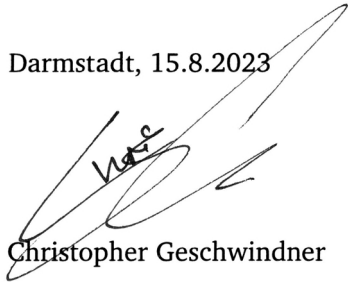
Erklärung

Hiermit erkläre ich, dass ich die vorliegende Arbeit, abgesehen von den in ihr ausdrücklich genannten Hilfen, selbständig verfasst habe.

Darmstadt, 15.8.2023

Christopher Geschwindner

Danksagung

Die vorliegende Dissertation ist das Ergebnis meiner Tätigkeit als wissenschaftlicher Mitarbeiter am Fachgebiet Reaktive Strömungen und Messtechnik (RSM) der Technischen Universität Darmstadt. Dabei kann ich einschließlich meiner Bachelor- und Masterarbeit auf mehr als acht Jahre zurückblicken, in denen mich das RSM in meiner wissenschaftlichen und persönlichen Entwicklung maßgeblich begleitet und geprägt hat.

An erster Stelle möchte ich mich bei Prof. Andreas Dreizler bedanken, der mir als Doktorvater die Möglichkeit gegeben hat, meine Promotion auf dem Gebiet der Lasermesstechnik reaktiver Strömungen durchzuführen. Er war stets ein aufmerksamer Gesprächspartner und hat mich in den wichtigen Momenten in die richtige Richtung gelenkt. Sein Vertrauen in meine Einschätzungen (insbesondere bei der Anschaffung von kostspieligem Labor-Equipment) war für meine erfolgreiche Arbeit am RSM enorm wichtig und ich bin dankbar für die zur Verfügung gestellte Infrastruktur, die eine solch aufwendige Forschung erst möglich gemacht hat.

Mein Dank gilt auch Herrn Prof. Dr.-Ing. Reinhold Kneer von der RWTH Aachen, der freundlicherweise das Korreferat dieser Dissertation übernommen hat. Für sein Interesse an meiner Arbeit und die Organisation zahlreicher Workshops und Klausurtagungen innerhalb des SFB/TRR 129, die viele wissenschaftliche Kooperationen auf dem Gebiet der Oxyfuel-Verbrennung begleitet haben, bin ich ihm sehr dankbar.

Ein weiterer wichtiger Bestandteil meiner Promotion war auch die Zugehörigkeit zur Gruppe von Dr. Benjamin Böhm, der die Konstante meiner Zeit am RSM war. Konferenzbesuche, Equipmentverteilung, Probleme im Labor oder sonstige Angelegenheiten konnten immer mit seiner Ruhe, Besonnenheit und fachlichen Kompetenz angegangen werden. Sein stets offenes Ohr hat nicht nur maßgeblich dazu beigetragen, mich nach meiner Bachelorarbeit im Fachgebiet zu halten, sondern auch knifflige Situationen einfach und schnell zu lösen. Des Weiteren möchte ich mich bei Dr. Brian Peterson und Alexander Nicolas für die Einladung zu einem Forschungsaufenthalt an der University of Edinburgh bedanken, der zu einer spannenden Zusammenarbeit geführt hat.

Die Arbeit beim RSM war für mich immer von einem freundlichen und kollegialen Miteinander geprägt, zu dem sowohl ehemalige als auch aktuelle Kolleg:innen beigetragen haben. Besonders hervorheben möchte ich Dr. Carl-Philipp Ding und Dr. Marius Schmidt, die meine Bachelor- und Masterarbeit betreut und damit die Grundlage für meine Promotion gelegt haben. Ich danke Cooper Welch für unsere nachfolgende Zusammenarbeit auf dem Gebiet der motorischen Direkteinspritzung und die daraus entstandene Freundschaft. Außerdem bin ich Dr. Jan Köser, Dr. Jhon Pareja und Dr. Ayane Johchi dankbar für die Einführung in die Feststoffverbrennung und den Betrieb des Mikrowellenplasmabrenners. Darüber hinaus danke ich Dr. Max Greifenstein, Dr. Florian Zentgraf und Dr. Andreas Preusche dafür, dass sie ihre wertvollen Erfahrungen im Labor mit mir geteilt haben, was mir bei meiner Arbeit sehr geholfen hat. Ich bin Dr. Christian Fach dankbar, dass er mich auf den Faserlaser aufmerksam gemacht hat, der einen Großteil meiner Experimente erst möglich gemacht hat.

Mein besonderer Dank gilt Dr. Tao Li, der mich seit Beginn meiner Promotion im Labor in vielerlei Hinsicht betreut hat und dessen unermüdliche Motivation zu einer Vielzahl gemeinsamer wissenschaftlicher Veröffentlichungen bis hin zu einem Topical Review geführt hat. Dr. Daniela Goedderz vom Fraunhofer LBF ist maßgeblich dafür verantwortlich, dass flammgeschützte Polymere einen zentralen Platz in dieser Dissertation einnehmen. Durch ihren unermüdlichen Einsatz für die Zusammenarbeit zwischen Polymerchemie und Verbrennungsdiagnostik sind die in dieser Dissertation besprochenen Arbeiten, insbesondere im Hinblick auf die Koordination der chemischen Analytik, erst möglich geworden.

Die Datenauswertung meiner Untersuchungen wäre ohne eine funktionierende IT-Infrastruktur und deren Administration nicht möglich gewesen. Hier sind insbesondere Hardy Hamel, Janik Hebel und

Robin Schultheis zu nennen, die mir stets zur Seite standen. Ebenso danke ich der Werkstatt um Roland Berntheisel, Dirk Feldmann, Sebastian Feuerbach und Mathias Felter, die für meine konstruktiven Ideen immer hilfreiche Verbesserungen parat hatten.

Mit meinen Kollegen Dr. Hendrik Nicolai, Dr. Johannes Emmert und Henrik Schneider, mit denen ich im SFB/TRR 129 gearbeitet habe, kann ich auf eine schöne gemeinsame Zeit zurückblicken. Weiterhin danke ich Dr. Martin Schiemann und David Tarlinski von der Ruhr-Universität Bochum sowie Dr. Konstantin Fröhlich, Laurent André und Pooria Farmand von der RWTH Aachen für die Diskussionen und die fruchtbare Zusammenarbeit im TRR.

Einen großen Anteil am Gelingen meiner Arbeit hatten meine zahlreichen Student:innen Daniel Mirschinka, Jonathan Holfelder, Katharina Westrup, Sabrina Jegust und Robin Stengl, denen ich für ihre zukünftige Laufbahn (evtl. auch im Rahmen einer Promotion) viel Erfolg wünsche. Andreas Ludwig, Gabriele Goet, Marion Müller, Angela Berger und Patricia John danke ich für die technische und administrative Unterstützung im Hintergrund, die mir während meiner gesamten Zeit am Fachgebiet den Rücken frei gehalten hat. Ebenso halte ich die gemeinsame Zeit mit allen weiteren Kolleg:innen am RSM und unserem digitalen Zwilling STFS (und vormals EKT) in guter Erinnerung.

Zum Abschluss möchte ich mich bei meinen Freund:innen und meiner Familie bedanken, die mich auf meinem Weg stets begleitet haben. Ich danke meiner Mutter Ute von ganzem Herzen dafür, dass sie mir immer die Möglichkeit gegeben hat, meinen Interessen nachzugehen und mich dabei bedingungslos unterstützt hat. Ich danke Esther für die wertvolle und schöne Zeit, die wir in den letzten Jahren miteinander verbracht haben und für die Freundschaft, die uns verbindet. Dasselbe gilt für Eva und Thomas, bei denen ich mich in all den Jahren immer gut aufgehoben gefühlt habe. Schließlich möchte ich mich bei meiner Freundin Hannah bedanken, die mich in den letzten Zügen meiner Promotion kennengelernt hat und mich in all der stressigen Zeit liebevoll unterstützt hat. Es ist schön, dich an meiner Seite zu haben.

Darmstadt, den 15.08.2023

Christopher Geschwindner

Abstract

The combustion of solid matter is a ubiquitous phenomenon governed by multiple factors, including the properties of the solid phase, the surrounding flow field, and the reactions involved in thermochemical conversion. This thesis addresses various aspects of this complex solid-flow-chemistry interaction, driven by two primary motivations: First, the mitigation of anthropogenic climate change necessitates solid fuel combustion technologies capable of carbon capture and storage. The application of oxy-fuel combustion and the subsequent substitution of coal for biomass offers pathways to achieve negative carbon dioxide emissions. Second, fire safety for polymers can be enhanced by the development and utilization of effective flame retardants. Rigorous and reliable testing procedures are indispensable for assessing the efficacy of such additives. The core focus of this thesis revolves around the comprehensive exploration of these interconnected phenomena, facilitated by the application of minimally intrusive optical diagnostics. Through these advanced measurement techniques, the underlying physicochemical phenomena governing solid-flow-chemistry interactions are scrutinized across a spectrum of experimental scenarios. By systematically varying specific elements of the solid-flow-chemistry interaction, the impacts of individual parameters and processes are investigated, accompanied by methodological advancements needed to experimentally address these intricate phenomena.

The initial segment of this work discusses aspherically shaped biomass particles dispersed within a turbulent round jet. Employing an ultra-high repetition rate fiber laser system, which operates at frequencies exceeding several 100 kHz, facilitates the measurement of key parameters characterizing turbulent fluid flows. The laser enables time-resolved flow velocimetry while achieving unparalleled temporal dynamic ranges. Furthermore, an extension of the laser system is showcased, featuring adaptable pulse-picking devices. This addition allows for remarkable flexibility in terms of repetition rates and pulsing strategies, which can be used to perform both statistical and time-resolved fluid flow measurements. In the context of a biomass-laden jet, the system is applied to perform two-phase velocimetry and simultaneous diffuse back-illumination measurements. This multi-parameter measurement setup allows for the continuous tracking of the slip velocity field and particle size evolution over time, consequently enabling the computation of the particle Reynolds number at a repetition rate of 200 kHz.

The second part of this dissertation focuses on the impact of oxidizer content and diluent composition on the transition from single particle to particle group combustion under laminar conditions. Bituminous coal is studied using a multi-parameter optical diagnostics setup to determine particle number density, three-dimensional volatile flame topology, and soot formation characteristics simultaneously. An imaging simulation tool is developed and applied to the specific camera settings to assess the measurement errors associated with particle number density determination arising from the line-of-sight nature of extinction imaging methods. Decreased formation of soot and heightened reactivity of the volatile flame is observed for increasing oxygen contents, while the substitution of nitrogen with carbon dioxide in oxy-fuel conditions shows a negligible effect on combustion behavior.

Finally, optical diagnostics including laser-induced fluorescence of the OH radical (OH-LIF) are utilized to explore flame retarded polypropylene. Various flame retardants, each with distinct mechanisms, are studied in micrometer-sized polymer particles and stick-shaped specimens akin to solid fuel particle investigations. Complementary thermal decomposition analyses provide insights into pyrolysis products that influence flame retardation. Remarkably, these investigations unveil a noticeable OH-LIF signal decrease for gas-phase active flame retardants that release radical scavengers. Furthermore, altered flame topology and extinction behavior during and after stick-shaped specimen interaction with a premixed methane flame are observed, showcasing the potential of the methodological approach.

The presented results provide both methodological advancements in the use of optical diagnostics for reactive multi-phase flows and new insights into the phenomena that occur during the combustion of solid fuels and flame retarded polymers.

Kurzfassung

Die Verbrennung von Feststoffen ist ein weitverbreitetes Phänomen, das von Faktoren wie den Eigenschaften der festen Phase, dem umgebenden Strömungsfeld und der thermochemischen Umwandlung beeinflusst wird. Diese Arbeit befasst sich mit verschiedenen Aspekten der komplexen Wechselwirkungen zwischen Feststoff, Strömung und Chemie, wobei zwei Hauptmotivationen im Fokus stehen: Erstens erfordert die Eindämmung des anthropogenen Klimawandels Technologien, die zur Abscheidung und Speicherung von Kohlenstoffdioxid (CO_2) geeignet sind. Die Anwendung der Oxy-Fuel-Verbrennung für Festbrennstoffe und der Austausch von Kohle durch Biomasse bieten Möglichkeiten, negative CO_2-Emissionen zu erzielen. Zweitens kann die Brandsicherheit von Polymeren durch den Einsatz wirksamer Flammschutzmittel verbessert werden. Für die Bewertung der Wirksamkeit solcher Additive sind verlässliche Prüfverfahren unerlässlich. Das Hauptaugenmerk dieser Arbeit liegt auf der umfassenden Erforschung dieser zusammenhängenden Phänomene, was durch die Anwendung minimal-invasiver optischer Diagnostik ermöglicht wird. Mithilfe fortschrittlicher Messtechnik werden relevante physikalisch-chemische Phänomene in unterschiedlichen experimentellen Umgebungen untersucht. Durch die systematische Variation spezifischer Aspekte der Feststoff-Strömung-Chemie-Interaktion werden die Auswirkungen einzelner Parameter untersucht. Hierdurch werden zudem wesentliche methodische Fortschritte erreicht.

Der erste Teil dieser Arbeit untersucht das Bewegungsverhalten asphärischer Biomassepartikel, die in einem turbulenten Freistrahl dispergiert sind. Ein Faserlaser mit Pulswiederholraten von mehreren 100 kHz wird für die Messung charakteristischer Größen turbulenter Strömungen eingesetzt. Der Laser ermöglicht zeitlich aufgelöste Geschwindigkeitsmessungen in einem bisher unerreichten zeitlichen Dynamikbereich. Darüber hinaus wird eine Erweiterung des Lasersystems mit geeigneten Puls-Picker-Systemen demonstriert. Dieser Ansatz ermöglicht flexibel einstellbare Wiederholungsraten und Pulsschemata, die sowohl für statistische als auch für zeitlich aufgelöste Strömungsmessungen verwendet werden können. Im Kontext eines biomassebeladenen Freistrahls wird das System zur Durchführung von Zweiphasen-Geschwindigkeitsmessungen und simultaner diffuser Rückbeleuchtung verwendet. Dieser Aufbau ermöglicht eine zeitlich aufgelöste Messung des Schlupfgeschwindigkeitsfelds, der Partikelgröße und somit der Partikel-Reynoldszahl bei 200 kHz.

Der zweite Abschnitt dieser Arbeit konzentriert sich auf den Einfluss des Sauerstoffgehalts und der Gaszusammensetzung auf den Übergang von Einzelpartikel- zu Partikelgruppenverbrennung von Steinkohle. Mittels optischer Diagnostik werden gleichzeitig Partikelanzahldichten, dreidimensionale volatile Flammenstrukturen und Rußbildung erfasst. Ein Imaging-Tool wird auf die spezifischen Kameraeinstellungen angepasst, um Messfehler bei der Bestimmung der Partikelanzahldichte abzuschätzen. Es wird eine verringerte Rußbildung und eine erhöhte Reaktivität der Volatilenflamme für steigende Sauerstoffgehalte beobachtet, während die Substitution von Stickstoff durch CO_2 in Oxy-Fuel-Bedingungen keine nennenswerten Auswirkungen auf das Verbrennungsverhalten zeigt.

Schließlich werden optische Diagnoseverfahren, darunter die laserinduzierte Fluoreszenz des OH-Radikals, eingesetzt, um das Verhalten von flammgeschütztem Polypropylen zu untersuchen. Verschiedene Flammschutzmittel mit unterschiedlichen Wirkungsmechanismen werden in Form von mikrometergroßen Polymer-Partikeln und stäbchenförmigen Proben untersucht. Thermische Zersetzungsanalysen liefern Erkenntnisse über Pyrolyseprodukte, die die Flammhemmung beeinflussen. Gasphasenaktive Flammschutzmittel zeigen hierbei eine deutliche Abnahme des Fluoreszenz-Signals in der Reaktionszone. Darüber hinaus werden Veränderungen in der Flammenstruktur und im Verlöschungsverhalten während und nach der Wechselwirkung der stäbchenförmigen Proben mit einer vorgemischten Methanflamme beobachtet, was das Potential des methodischen Ansatzes herausstellt.

Die vorgestellten Ergebnisse bieten sowohl methodische Fortschritte bei der Verwendung optischer Diagnoseverfahren für reaktive Mehrphasenströmungen als auch neue Erkenntnisse über die bei der Verbrennung von Festbrennstoffen und flammgeschützten Polymeren auftretenden Phänomene.

Contents

List of Figures

List of Tables

Nomenclature

Lowercase Latin letters		Unit
a	Minor axis radius of a prolate ellipsoid	m
b	Major axis radius of a prolate ellipsoid	m
c	Duty cycle factor for pulse picking	-
c_p	Specific heat capacity at constant pressure	JK/kg
d	Diameter	m
f	Frequency	Hz
f_s	Frequency of sound	Hz
k	Turbulent kinetic energy	m^2/s^2
l	Inter-particle distance	m
p	Pressure	$kg\,m/s^2$
r	Radius	m
s	Particle displacement	px
t	Time	s
t_l	Inter-pulse time	s
u	Velocity	m/s
u_k	Kolmogorov velocity scale	m/s
u_s	Slip velocity	m/s
v	Vibrational quantum number	-
w	Interrogation window length/size	px
x, y, z	Spatial coordinates	m

Uppercase Latin letters		Unit
C	Constant	-
D	Pipe diameter	m
$D_{Y,X}$	Mass diffusivity of species X in Y	m^2/s
$E(\kappa)$	Energy spectrum function	m^3/s^2
E_0	Output pulse energy of laser	J
$E_{ij}(\kappa_i)$	One-dimensional energy spectrum function	m^3/s^2
I_{OH}	Normalized OH-LIF intensity	-
IF	Interaction factor	-
J	Angular momentum quantum number	-
L	Length scale of large eddies	m
$\mathscr{L}$	Characteristic length scale	m
L_{Int}, L_{ii}	Integral length scale	m
M^2	Beam quality factor	-
N_e	Number of statistically independent samples	-
N_p	Number of particles	m^3
PND	Particle number density	-
R	Pixel resolution	m/px
$\mathscr{R}_{ij}$	Eulerian correlation coefficient	-

Nomenclature

R_{nf}	Non-flammability ratio	-
Re	Reynolds number	-
Re_L	Macroscopic Reynolds number	-
Re_p	Particle Reynolds number	-
St	Stokes number	-
T	Temperature	K
T_{Int}, T_{ii}	Integral time scale	s
T_t	Total recording time	s
TDR	Temporal dynamic range	-
$\mathscr{U}$	Characteristic velocity	m/s
U, V, W	Convection velocity of turbulent structures	m/s
U_u	Uncertainty of instantaneous velocity u	m/s
V_d	Domain volume	m^3
V_f	Reaction zone volume	m^3
V_p	Particle volume	m^3
V_s	Acoustic velocity	m/s
V_{nf}	Volume of non-flammable core	m^3

Lowercase Greek letters   **Unit**

α_p	Particle volume fraction	-
β	Aspect ratio	-
δ	Diffuser opening angle	deg
ε	Turbulent dissipation rate	m^2/s^3
ζ	Beam steering angle	deg
η_k	Kolmogorov length scale	m
θ	Deflection angle	deg
κ	Wavenumber	1/m
λ_{Taylor}	Taylor length scale	m
λ_l	Laser wavelength	m
μ	Dynamic viscosity	kg/(m s)
ν	Kinematic viscosity	m^2/s
ν_l	Laser frequency	1/s
ξ	Spatial variation	m
ρ	Density	kg/m^3
τ	Temporal lag	s
τ_f	Fluid time scale	s
τ_k	Kolmogorov time scale	s
τ_p	Particle response time	s
ϕ	Particle orientation	deg
χ	Steepest ray angle for diffuse back-illumination	deg
ω	Viewing angle	deg

X

Uppercase Greek letters		**Unit**
Λ	Acoustic wavelength	m

Indices and superscripts

′	Fluctuation
0	Initial
3D	Three-dimensional
a	Access
amb	Ambient
B	Bragg
b	Beam
bin	Binned
bu	Bulk
c	Camera
d	Domain
DBI	Diffuse back-illumination
def	Deflection
e	Statistically independent
EA	elliptic approximation
err	Error
ex	Extinction
f	Fluid
g	Transverse
glob	Global
I,II,III,...	Selected instant
i,j,k	Integer index
ig	Ignition
Int	Integral scale
jet	Jet
k	Kolmogorov scale
l	Laser
LIF	Laser-induced fluorescence
local	Local
m	Measured
max	Maximum
min	Minimum
nf	Non-flammable
OH	OH-LIF
p	Particle
pp	Particle-particle
proj	Projected
PRR	Peak reactivity rate
px	Pixel

s	Slip
sw	Switching
t	Total
Taylor	Taylor scale
turb	Turbulent
u	Streamwise velocity component
v	Overlap
x, y, z	Vector components

Operators and mathematical symbols

$\Delta\square$	Difference
$\dot{\square}$	Temporal derivative
$\langle\square\rangle$	Time average
$\sigma_\square$	Standard deviation
$\vec{\square}$	Vector

Physical & mathematical constants		Value
h	Planck's constant	$6.626\cdot10^{-34}\,\mathrm{J\,s}$

Abbreviations

AIR	Air
Al$_2$O$_3$	Aluminum oxide
AO	Acousto-optic
AOD	Acousto-optic deflector
AOM	Acousto-optic modulator
APP	Ammonium polyphosphate
ATH	Aluminum trihydroxide
BECCS	Biomass energy with carbon capture and storage
BBO	Beta barium borate
C$_2$H$_6$	Ethane
CCS	Carbon capture and storage
CH$_4$	Methane
CMOS	Complementary metal-oxide-semiconductor
CO$_2$	Carbon dioxide
CS	Correlation statistics
DBI	Diffuse back-illumination
DEHS	Di-ethylhexyl sebacate
DEPZn	Zinc diethylphosphinate
DPSS	Diode-pumped solid state
DP-PIV	Dual-pulse particle image velocimetry
DSLR	Digital single-lens reflex

DTF	Drop-tube furnace
EO	Electro-optic
EOM	Electro-optic modulator
FOV	Field of view
FTIR	Fourier-transform infrared spectroscopy
H_2O	Water
H_3PO_2	Phosphinic acid
HIT	Homogeneous isotropic turbulence
IF	Interaction factor
ISIS-CCD	In situ storage CCD
IW	Interrogation window
LDV	Laser Doppler velocimetry
LED	Light-emitting diode
LFR	Laminar flow reactor
LIF	Laser-induced fluorescence
LII	Laser-induced incandescence
MBMS	Molecular beam mass spectrometry
MOPA	Master oscillator power amplifier
N_2	Nitrogen
NH_3	Ammonia
O_2	Oxygen
OH	Hydroxyl
OH-LIF	Laser-induced fluorescence of the OH radical
OH-PLIF	Planar laser-induced fluorescence of the OH radical
OXY	Oxy-fuel
PAH	Polycyclic aromatic hydrocarbon
PDA	Phase Doppler anemometry
PDF	Probability density function
PE	Polyethylene
PET	Polyethylene terephthalate
PGC	Particle group combustion
PIV	Particle image velocimetry
PH_3	Phosphine
PND	Particle number density
PO	Phosphorus monoxide
PP	Polypropylene
PSD	Power spectral density
PSMP	Pentaerythritol spirobis(methylphosphonate)
PTV	Particle tracking velocimetry
Py-GCMS	Pyrolysis gas chromatography with mass spectrometry coupling
SPC	Single particle combustion
TDMS	Thermodesorption mass spectrometry
TDR	Temporal dynamic range
TeO_2	Tellurium dioxide
TGA	Thermogravimetric analysis

TG-FTIR	Thermogravimetric analysis coupled with Fourier transform infrared spectrometry
TG-MS	Thermogravimetric analysis coupled with mass spectrometry
TR-PIV	Time-resolved particle image velocimetry
UV	Ultraviolet
VUV	Vacuum ultraviolet photoionization

List of Publications

Peer-reviewed journal papers included in this thesis

[I] **Geschwindner, C.**; Westrup, K.; Dreizler, A. and Böhm, B.: "Ultra-high-speed time-resolved PIV of turbulent flows using a continuously pulsing fiber laser." In: *Experiments in Fluids* 63.4 (2022). DOI: 10.1007/s00348-022-03424-7.

[II] **Geschwindner, C.**; Westrup, K.; Dreizler, A. and Böhm, B.: "Pulse picking of a fiber laser enables velocimetry of biomass-laden jets at low and ultra-high repetition rates." In: *Proceedings of the Combustion Institute* 39.1 (2023), pp. 1325–1335. DOI: 10.1016/j.proci.2022.07.138.

[III] Li, T.; **Geschwindner, C.**; Dreizler, A. and Böhm, B.: "An experimental study of coal particle group combustion in conventional and oxy-fuel atmospheres using multi-parameter optical diagnostics." In: *Proceedings of the Combustion Institute* 39.3 (2023), pp. 3259–3269. DOI: 10.1016/j.proci.2022.07.081.

[IV] **Geschwindner, C.**; Goedderz, D.; Li, T.; Köser, J.; Fasel, C.; Riedel, R.; Altstädt, V.; Bethke, C.; Puchtler, F.; Breu, J.; Döring, M.; Dreizler, A. and Böhm, B.: "Investigation of flame retarded polypropylene by high-speed planar laser-induced fluorescence of OH radicals combined with a thermal decomposition analysis." In: *Experiments in Fluids* 61.2 (2020). DOI: 10.1007/s00348-019-2864-5.

[V] **Geschwindner, C.**, Goedderz, D., Li, T., Bender, J., Böhm, B. and Dreizler, A.: "The effects of various flame retardants on the combustion of polypropylene: Combining optical diagnostics and pyrolysis fragment analysis." In: *Polymer Degradation and Stability* 211 (2023), p. 110321. DOI: 10.1016/j.polymdegradstab.2023.110321.

Other peer-reviewed journal papers

[VI] Li, T.; **Geschwindner, C.**; Böhm, B. and Dreizler, A.: "Particle-resolved optical diagnostics of solid fuel combustion for clean power generation: a review." In: *Measurement Science and Technology*, DOI: 10.1088/1361-6501/acef49.

[VII] Tarlinski, D.; **Geschwindner, C.**; Li, T.; Böhm, B. and Schiemann, M.: "Particle temperature and composition measurements in the ignition phase of single coal particles and particle groups under conventional and oxy-fuel atmospheres." In: *Fuel* 332.1 (2023), DOI: 10.1016/j.fuel.2022.125894.

[VIII] Welch, C.; Schmidt, M.; **Geschwindner, C.**; Wu, S.; Wooldridge, M.S. and Böhm, B.: "The influence of in-cylinder flows and bulk gas density on early Spray G injection in an optical research engine." In: *International Journal of Engine Research* 24.1 (2023), pp. 82-98. DOI: 10.1177/14680874211042320

[IX] Farmand, P.; Nicolai, H.; Schumann, C.; Attili, A.; Berger, L. and Li, T.; **Geschwindner, C.**; Di Mare, F.; Hasse, C.; Böhm, B.; Janicka, J.; Pitsch, H.: "Numerical investigation and assessment of flamelet-based models for the prediction of pulverized solid fuel homogeneous ignition and combustion." In: *Combustion and Flame* 235 (2022), p. 111693. DOI: 10.1016/j.combustflame.2021.111693.

[X] Pati, A.; Paredi, D.; Welch, C.; Schmidt, M.; **Geschwindner, C.**; Böhm, B.; Lucchini, T.; D'Errico, G. and Hasse, C.: "Numerical and experimental investigations of the early injection process of Spray G in a constant volume chamber and an optically accessible DISI engine." In: *International Journal of Engine Research* 23.12 (2022). pp. 2073-2093. DOI: 10.1177/14680874211039422.

[XI] Attili, A.; Farmand, P.; Schumann, C.; Farazi, S.; Böhm, B.; Li, T.; **Geschwindner, C.**; Köser, J.; Dreizler, A. and Pitsch, H.: "Numerical Simulations and Experiments of Ignition of Solid Particles in a Laminar Burner: Effects of Slip Velocity and Particle Swelling." In: *Flow, Turbulence and Combustion* 106.2 (2021), pp. 515-531. DOI: 10.1007/s10494-020-00222-12.

[XII] Li, T.; Farmand, P.; **Geschwindner, C.**; Greifenstein, M.; Köser, J.; Schumann, C.; Attili, A.; Pitsch, H.; Dreizler, A. and Böhm, B.: "Homogeneous ignition and volatile combustion of single solid fuel particles in air and oxy-fuel conditions." In: *Fuel* 291 (2021), p. 120101, DOI: 10.1016/j.fuel.2020.120101.

[XIII] Li, T.; **Geschwindner, C.**; Köser, J.; Schiemann, M.; Dreizler, A. and Böhm, B.: "Investigation of the transition from single to group coal particle combustion using high-speed scanning OH-LIF and diffuse backlight-illumination." In: *Proceedings of the Combustion Institute* 38.3 (2021), pp. 4101-4109. DOI: 10.1016/j.proci.2020.06.314.

[XIV] Nicolai, H.; Li, T.; **Geschwindner, C.**; Di Mare, F.; Hasse, C.; Böhm, B. and Janicka, J.: "Numerical investigation of pulverized coal particle group combustion using tabulated chemistry." In: *Proceedings of the Combustion Institute* 38.3 (2021), pp. 4033-4041. DOI: 10.1016/j.proci.2020.06.081.

[XV] **Geschwindner, C.**; Kranz, P.; Welch, C.; Schmidt, M.; Böhm, B.; Kaiser, S.A. and de la Morena, J.: "Analysis of the interaction of Spray G and in-cylinder flow in two optical engines for late gasoline direct injection." In: *International Journal of Engine Research* 21.1 (2020), pp. 169-184. DOI: 10.1177/1468087419881535

Conference papers

[XVI] **Geschwindner, C.**, Westrup, K., Dreizler, A. and Böhm, B.: "Pulse Picking PIV: A Single-Cavity Fiber Laser System For Highly Flexible Repetition Rates And Pulsing Schemes." In: *20th International Symposium on Applications of Laser and Imaging Techniques to Fluid Mechanics.* 2022. DOI: 10.55037/lxlaser.20th.105

[XVII] Welch, C.; Schmidt, M.; **Geschwindner, C.**; Dreizler, A. and Böhm, B.: "Experimentelle Untersuchung der Spray-G Direkteinspritzung in einem optisch zugänglichen Motor." In: *30. Deutscher Flammentag für nachhaltige Verbrennung.* 2021.

[XVIII] **Geschwindner, C.**; Li, T.; Goedderz, D.; Dreizler, A. and Böhm, B.: "Untersuchung der Gasphasenaktivität von Flammschutzmitteln mittels simultaner OH-PLIF und DBI von PP-Partikeln." In: *30. Deutscher Flammentag für nachhaltige Verbrennung.* 2021.

[XIX] **Geschwindner, C.**; Westrup, K.; Li, T.; Dreizler, A. and Böhm, B.: "Experimentelle Untersuchung der Interaktion von Biomasse mit einem turbulenten plasmabeheizten Oxidatorgasstrom." In: *30. Deutscher Flammentag für nachhaltige Verbrennung.* 2021.

1 Introduction

1.1 Motivation

The scientific phenomena and methodological advancements investigated in this work are motivated by two paramount and extensively discussed concerns that necessitate comprehensive fundamental research: the mitigation of anthropogenic climate change through carbon capture and storage technologies, and the enhancement of fire safety in polymers facilitated by the use of effective flame retardants. This motivational chapter provides a concise overview of these key issues, shedding light on the underlying scientific questions that serve as the foundation for the research conducted in this thesis. The subsequent sections explore each issue in detail, emphasizing the existing gaps in our understanding and providing the necessary context for the research investigations conducted.

Biomass energy with carbon capture and storage The mitigation of anthropogenic climate change represents a great challenge, which demands a wide range of technological solutions for the decarbonization of emission-intensive industries. Even though the installed capacity of power stations based on renewable energies has risen worldwide in the last years, 64 % of greenhouse gas emissions stem from the utilization of fossil fuels in power generation and industry. This underlines the need for clean and reliably available energy from combustion as wind and solar power are subject to strong temporal fluctuations [6]. At the same time, a reduction of the carbon dioxide (CO_2) already present in the atmosphere is desirable to lower the greenhouse effect and further mitigate global warming. One attractive carbon capture and storage (CCS) technology is oxy-fuel combustion, in which fuels are burned in a mixture of pure oxygen and CO_2-enriched recirculated flue gas, enabling a sequestration of the carbon dioxide after condensation of the water vapor within the flue gas [7, 8]. This technology effectively enables a climate-neutral combustion of solid fossil fuels like bituminous coal and therefore represents a promising bridge technology. The introduction and utilization of biomass, which captures CO_2 from the atmosphere during its growth, and the simultaneous usage of oxy-fuel technology leads to negative CO_2 emissions. This approach is known as biomass energy with carbon capture and storage (BECCS) [9]. A detailed knowledge of the physicochemical interactions present in the combustion of pulverized coal and biomass in air and oxy-fuel environments is of great importance to employ this technology for the retrofit of existing and construction of future power stations.

Phosphorus-containing flame retardants for polymers The second issue addressed in this thesis is the widespread usage of polymer materials. Polymers have replaced other materials – particularly metals and alloys – in the construction of components in many engineering applications. Especially applicable to automotive and aerospace engineering, key features of polymers are their relatively low density, leading to lower part weights combined with an unparalleled design flexibility. The versatility of polymers enables the manufacturing of parts with complex geometries as they are required in the construction of fuselages and airfoils of modern fuel-efficient airplanes, where carbon fiber reinforced polymers are used. However, a crucial disadvantage of polymers is their high flammability, which requires the usage of tailor-made flame retardant additives. Especially in safety-critical applications, flame retardants are indispensable to guarantee mitigation of the fire hazard and the protection of human lives. Therefore, a reliable experimental characterization of the effectiveness of such additives is highly desirable [10].

These motivational aspects, the reduction of carbon emissions in power generation by BECCS and the introduction of sustainable flame retardants for polymers, share multiple phenomenological similarities on the meso- and microscale, which were studied in the works included in this dissertation using similar experimental methodologies. Essentially, both the combustion of flame retarded polymers and the thermochemical conversion of pulverized solid fuels like coal or biomass can be classified as *reactive solid (particle) matter interacting with gaseous flows*. As was shown in the publications forming the core of this doctoral thesis, both phenomena are connected through the interaction of a solid phase, the surrounding flow characteristics and combustion. Hence, in the case of a complex technical system like the boiler of a power station or a fire within a building, knowledge of the individual aspects of this *solid-flow-chemistry interaction* is crucial to accurately predict and control the desired or undesired thermochemical conversion of solid matter and/or particles.

1.2 Scientific questions addressed in this work

The complexity of individual aspects of the combustion of solid matter involves multiple parameters and their interactions, which are shown in Fig. 1.1. The combustion behavior of a solid material is dependent on its surrounding flow field, which can be laminar or turbulent, as well as the particle number density, ranging from single particles to dense particle clouds. If a flame retardant is added to the solid phase composition, inhibition of the combustion adds another level of complexity to this interaction triangle. In order to characterize the impact of specific phenomena on the overall combustion behavior, parametric experimental studies varying only one parameter should be carried out. As is apparent, many different combinations of parameter studies are possible. In addition, many further aspects play a crucial role for the physicochemical behavior of the reactive multi-phase flow, such as the particle and specimen shape or the composition of the surrounding atmosphere.
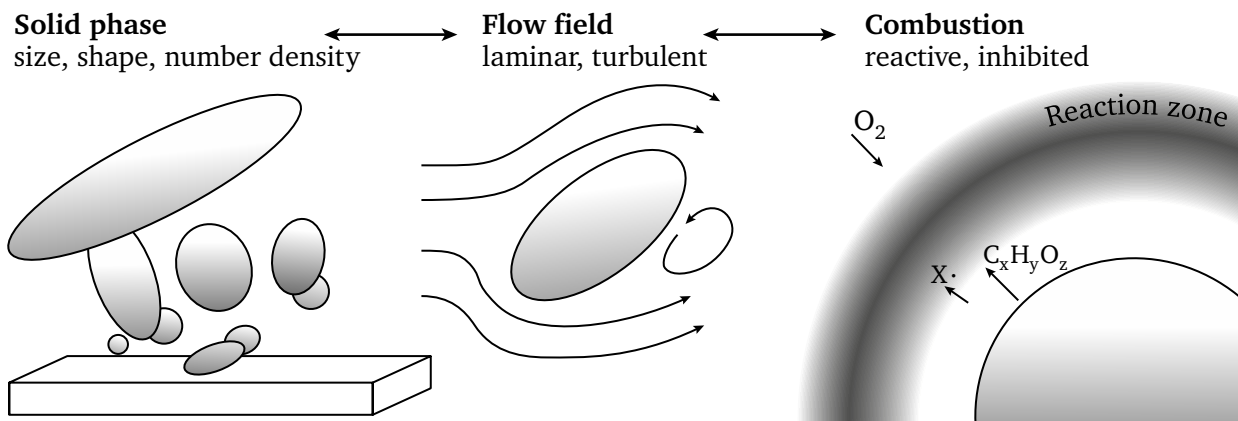
Figure 1.1: Typical interactions between solid phase, flow field, and combustion. Radical scavengers are denoted by $X\cdot$.

With regard to particle-resolved experimental investigations using laser-based in situ diagnostics, the combustion behavior of single bituminous coal particles and particle groups in laminar flows has been studied in previous works [11, 12]. For flame retarded polymers, in situ combustion studies have not yet been performed with optical diagnostics. However, many scientific questions are still open (as will be explained in the respective chapters) and need to be experimentally investigated using minimally-invasive optical diagnostics to not disturb the processes themselves while performing measurements. In this thesis, three groups of subject areas based on specific aspects of solid-flow-chemistry interactions were identified and investigated. The research in each of the three subject areas presented in this thesis advances the scientific understanding of the respective subject area with respect to both

methodological and phenomenological aspects. The publications included within this thesis are integral components of a broader body of work, encompassing additional investigations and collaborations as detailed in the list of publications (see pp. XV).

Subject area 1: Ultra-high repetition rate diagnostics of biomass-laden turbulent jets

This subject area deals with the interaction of solid biomass fuels with their surrounding turbulent flow field. Here, the surrounding carrier phase was isothermal and hence non-reactive while biomass particles of different shapes were dispersed in a high-velocity turbulent jet. The introduction of aspherical biomasses causes complex particle-turbulence interactions, which need to be investigated to understand the coupling between the movement of aspherical particle shapes and the surrounding turbulent carrier phase. These phenomena were studied at ultra-high repetition rates using a novel fiber laser system, which was first demonstrated for velocimetry in single-phase turbulent flows in **Paper I** [1]. The laser system was enhanced to enable a flexible repetition rate illumination of turbulent flows for optimized statistical and time-resolved velocimetry measurements using an acousto-optic pulse picking approach. This system was then applied for two-phase velocimetry of a biomass-laden jet, where particle Reynolds numbers could be measured at repetition rates of several 100 kHz as presented in **Paper II** [2]. Remaining drawbacks of this laser system were eliminated by using electro-optic modulation for pulse picking. This improved methodology was published in a conference paper and is hence not part of the official list of peer-reviewed publications included in this thesis, while being still discussed in this thesis [13]. To summarize, subject area 1 contains the following publications:

- **Paper I** [1]:
  Geschwindner, C.; Westrup, K.; Dreizler, A. and Böhm, B.: "Ultra-high-speed time-resolved PIV of turbulent flows using a continuously pulsing fiber laser." In: *Experiments in Fluids* 63.4 (2022). DOI: 10.1007/s00348-022-03424-7.

- **Paper II** [2]:
  Geschwindner, C.; Westrup, K.; Dreizler, A. and Böhm, B.: "Pulse picking of a fiber laser enables velocimetry of biomass-laden jets at low and ultra-high repetition rates." In: *Proceedings of the Combustion Institute* 39.1 (2023), pp. 1325–1335. DOI: 10.1016/j.proci.2022.07.138.

Subject area 2: Group combustion of solid fuels in laminar oxy-fuel environments

This part of the thesis focuses on the effect of particle number density on the combustion behavior of coal particles. The surrounding atmosphere of the laminar flow field of a flat flame burner was varied to study the combustion of changing particle number densities within air and oxy-fuel atmospheres, as documented in **Paper III** [3]. The comparison of these two atmospheres is especially relevant because a retrofit of existing power stations working with air to CO_2-rich oxy-fuel environments will also potentially change the combustion behavior of the pulverized fuel flames due to the higher heat capacity of CO_2 together with a lower diffusivity of oxygen (O_2) in CO_2. Multi-parameter three-dimensional optical diagnostics were used to derive conditioned statistical data. The measurement error of the particle number density measurements was evaluated using an imaging simulation, which was conceptualized and programmed from the ground up. Consequently, the use of laser-based measurements and the characterization of the associated measurement errors resulted in an improved understanding of the combustion behavior of particle groups in air and oxy-fuel atmospheres. To summarize, subject area 2 contains the following publication:

- **Paper III** [3]:
  Li, T.; **Geschwindner, C.**; Dreizler, A. and Böhm, B.: "An experimental study of coal particle group combustion in conventional and oxy-fuel atmospheres using multi-parameter optical diagnostics." In: *Proceedings of the Combustion Institute* 39.3 (2023), pp. 3259–3269. DOI: 10.1016/j.proci.2022.07.081.

Subject area 3: Optical diagnostics of flame retarded polymers

This field comprises the experimental investigation of flame retarded polymers using optical diagnostics. The combustion of single flame retarded polypropylene (PP) particles in laminar environments was studied by means of planar laser-induced fluorescence of the OH radical (OH-PLIF), which is a widespread method for the characterization of the combustion of gaseous fuels and which was successfully transferred to study the inhibition behavior of a well-known gas-phase active flame retardant in **Paper IV** [4]. In a next step, OH-PLIF was combined with diffuse back-illumination (DBI) to simultaneously measure the combustion and particle size of individual flame retarded polymer particles in a more extensive study containing four flame retardants with different modes of action in PP. This approach enabled a comparison of the material formulations by means of a dimensionless flame stand-off distance. The study, published in **Paper V** [5], revealed that the combustion characteristics of single polymer particles and coal particles are fairly similar in terms of the flame topology, since the dimensionless flame radius decreases with increasing particle size. To bridge the gap to a more realistic fire scenario, the optical diagnostics methods were also used to study standardized stick-shaped specimens as they are commonly used in standard material testing procedures for flame retarded polymers. This revealed that minimally-invasive optical combustion diagnostics can provide a comprehensive understanding of the inhibition behavior when combined with pyrolysis fragment analysis methods during thermal decomposition, which are commonly used in the polymer chemistry community. To summarize, subject area 3 contains the following publications:

- **Paper IV** [4]:
  Geschwindner, C.; Goedderz, D.; Li, T.; Köser, J.; Fasel, C.; Riedel, R.; Altstädt, V.; Bethke, C.; Puchtler, F.; Breu, J.; Döring, M.; Dreizler, A. and Böhm, B.: "Investigation of flame retarded polypropylene by high-speed planar laser-induced fluorescence of OH radicals combined with a thermal decomposition analysis." In: *Experiments in Fluids* 61.2 (2020). DOI: 10.1007/s00348-019-2864-5.

- **Paper V** [5]:
  Geschwindner, C., Goedderz, D., Li, T., Bender, J., Böhm, B. and Dreizler, A.: "The effects of various flame retardants on the combustion of polypropylene: Combining optical diagnostics and pyrolysis fragment analysis." In: *Polymer Degradation and Stability* 211 (2023), p. 110321. DOI: 10.1016/j.polymdegradstab.2023.110321.

2 Theoretical background

This chapter provides a concise overview of the fundamental principles necessary to comprehend the phenomena and methodological approaches investigated and described in this thesis. Section 2.1 delves into the fundamental aspects of systems characterized by particle-turbulence-chemistry interactions. It encompasses single-phase and multi-phase turbulent flows, elucidating the complex behavior of reactive streams of solid fuel particles, as well as the mechanisms governing the inhibition of polymer combustion by suitable flame retardants. Section 2.2 explores the fundamental principles of optical diagnostics, which play a pivotal role in this research. This discussion includes a brief analysis of relevant laser-optical devices and the underlying principles of optical measurement methods that have been extensively utilized throughout this thesis.

2.1 Phenomenological aspects

2.1.1 Laminar and turbulent flows

Fluid flows can be categorized into two fundamentally different regimes: laminar and turbulent flows. Laminar flows are characterized by smooth motion in parallel ordered layers with low levels of mixing. They have been extensively studied and well-described by classical theories [14, 15]. However, under certain conditions, laminar flows can undergo a transition to turbulent flows, marked by a significant alteration in their characteristics. This transition occurs due to the presence of perturbations in the flow, which disrupt orderly motion and introduce chaotic behavior. The transition from laminar to turbulent flows is influenced by the fluid's kinematic viscosity ν, with lower viscosity promoting the onset of turbulence. Turbulent flows, in contrast to laminar flows, exhibit complex, three-dimensional motion, high velocity fluctuations, and enhanced mixing. They are characterized by the presence of vortices and fluctuations in pressure and velocity. This section introduces the most important concepts within the field of turbulent flows relevant to this thesis. An extensive introduction to turbulent flows can be found in [16–18].

The transition from laminar to turbulent flows can be described using the Reynolds number Re, which quantifies the ratio of inertial forces to viscous forces in the flow and is computed as

$$\mathrm{Re} = \frac{\mathscr{U}\,\mathscr{L}}{\nu}, \tag{2.1}$$

where $\mathscr{U}$ denotes a characteristic velocity and $\mathscr{L}$ is a characteristic length scale. Turbulent flows are often studied in a statistical manner by decomposing the instantaneous velocity u_i (as well as the instantaneous pressure p) into a mean component $\langle u_i \rangle$ and a fluctuating component u_i' as $u_i = \langle u_i \rangle + u_i'$. Based on this approach, the Reynolds-averaged Navier-Stokes (RANS) equations can be derived, which differ from the standard Navier-Stokes equations by the appearance of the Reynolds stress $\langle u_i' u_j' \rangle$. This additional unknown term introduces a closure problem, as the number of equations is smaller than the number of unknowns, motivating the need for a determination of the Reynolds stresses through modeling approaches [16].

A distinct feature of turbulent flows is the wide range of scales they encompass, from large-scale structures to small-scale fluctuations. To derive the most important set of scales, the Eulerian correlation coefficient of velocity components in stationary turbulent fields $\mathscr{R}_{ij}$ is introduced by Eq. (2.2).

$$\mathscr{R}_{ij}(\vec{x},\vec{\xi},\tau) = \frac{\left\langle u_i'(\vec{x},t_0)\, u_j'(\vec{x}+\vec{\xi},t_0+\tau)\right\rangle}{\sqrt{\left\langle u_i'^2(\vec{x},t_0)\right\rangle \left\langle u_j'^2(\vec{x}+\vec{\xi},t_0+\tau)\right\rangle}} \tag{2.2}$$

The correlation coefficient $\mathscr{R}_{ij}$ can be computed for different dimensions $(i,j=1,2,3)$ and at different locations $\vec{x} = (x_1,x_2,x_3) = (x,y,z)$ with spatial variations $\vec{x}+\vec{\xi} = (x+\Delta x, y+\Delta y, z+\Delta z)$ (where $\Delta x = \xi$). The temporal lag τ is the time increment between the two times t_0 and $t_0+\tau$. Using the autocorrelation functions $\mathscr{R}_{ii}$, one can compute the integral length scales L_{ii} (or L_{Int}) and time scales T_{ii} at a position $\vec{x}$ within the flow field as

$$L_{ii}(\vec{x}) = \int_0^\infty \mathscr{R}_{ii}(\vec{x},\xi_i,\tau=0)\,\mathrm{d}\xi_i, \tag{2.3}$$

$$T_{ii}(\vec{x}) = \int_0^\infty \mathscr{R}_{ii}(\vec{x},\vec{\xi}=\vec{0},\tau)\,\mathrm{d}\tau. \tag{2.4}$$

The integral scales represent the characteristic size of energy-containing flow features such as large eddies and vortices. These structures facilitate the transfer of energy from larger scales to smaller scales through an energy cascade, which drives the continuous breakdown of turbulent energy until it is dissipated into heat.

According to Kolmogorov's first similarity hypothesis, the statistics of small-scale motions attain a universal form, which is solely determined by ν and the turbulent dissipation rate ε. Dimensional analysis using these two parameters leads to a derivation of the smallest scales within a turbulent flow given by Eq. (2.5) (also called Kolmogorov scales denoted by the index $\square_k$), which characterize the size of dissipative eddies. The Reynolds number based on the Kolmogorov scales is unity (as $\mathrm{Re}_k = \eta_k u_k/\nu = 1$), which underlines the notion that the scales or turbulent motion decrease through the cascade process until the viscous forces have a significant impact.

$$\eta_k = \left(\frac{\nu^3}{\varepsilon}\right)^{1/4} \tag{2.5a}$$

$$\tau_k = (\varepsilon\nu)^{1/4} \tag{2.5b}$$

$$u_k = \left(\frac{\nu}{\varepsilon}\right)^{1/2} \tag{2.5c}$$

An important set of intermediate scales between the scale of large eddies L and the Kolmogorov scales η_k are the Taylor microscales $\lambda_{\mathrm{Taylor}}$, which are often used in the study of isotropic turbulence. The transverse Taylor microscale λ_g can be computed from the transverse correlation coefficient $\mathscr{R}_{22}$ as $\lambda_g = [-\frac{1}{2}\,\partial^2\mathscr{R}_{22}/\partial\xi^2|_{\xi=0}]^{-1/2}$. This definition is easier to grasp through its geometric construction using $\mathscr{R}_{22}$: λ_g is determined by finding the intersection of the osculating parabola $1-\xi^2/\lambda_g^2$ with the abscissa (see Fig. 2.2(c)).

Having introduced some of the most important characteristic scales in turbulent flows, their relationship and scale separation plays an important role as it directly influences the measurement systems trying to capture turbulent flows in their entirety, both from the aspect of resolution as well as dynamic range. Defining the size of energy-containing large eddies as $L \equiv k^{3/2}/\varepsilon$, where $k = \frac{1}{2}\langle u_i'u_i'\rangle$ is the turbulent kinetic energy, the relations shown in Eq. (2.6) between the turbulent scales can be derived using the macroscopic Reynolds number $\mathrm{Re}_L = k^{1/2}L/\nu$ [16]. As can be seen from Eq. (2.6),

increasing Reynolds numbers lead to a larger separation of scales of the turbulent flow. Consequently, the dynamic range of flow velocity measurement techniques has to be increased capturing the entirety of the existing scales.

$$\eta_k/L = \mathrm{Re}_L^{-3/4} \tag{2.6a}$$

$$\lambda_g/L = \sqrt{10}\,\mathrm{Re}_L^{-1/2} \tag{2.6b}$$

To understand the contribution of different scales of the flow to the turbulent kinetic energy k, the energy spectrum function $E(\kappa)$ is considered as a function of the wavenumber κ (where $\int_0^\infty E(\kappa)\mathrm{d}\kappa = k$). Kolmogorov's second similarity hypothesis states that the statistics of motion in the intermediate range between large eddies and small-scale fluctuations are only determined by ε and are independent of ν for sufficiently large Reynolds numbers. In this inertial subrange where kinetic energy is transferred from the energy-containing range to the dissipation range, the spectrum attains the power-law form $E(\kappa) = C\varepsilon^{2/3}\kappa^{-5/3}$, which is also known as the Kolmogorov $-\frac{5}{3}$ spectrum including a constant C.

In practice, the experimental determination of energy spectra is often performed for one-dimensional spectra $E_{ij}(\kappa_1)$ as for example the longitudinal spectrum $E_{11}(\kappa_1)$, for which the power-law form $E_{11}(\kappa_1) = C_1\,\varepsilon^{2/3}\kappa_1^{-5/3}$ is equally applicable and has been confirmed in numerous experimental studies [16]. Figure 2.1 shows the relationship between the energy spectrum $E(\kappa)$ and the one-dimensional spectra $E_{11}(\kappa_1)$ and $E_{22}(\kappa_1)$ including a depiction of the scales L, λ_g and η_k for a model spectrum introduced in [16, p. 232]. The biggest share of turbulent kinetic energy is contained in the large scale vortices. As kinetic energy is transferred from large to small scales in the inertial subrange through the cascade process, the characteristic decay of all spectra scaling as $\propto \kappa^{-5/3}$ is apparent. As the Kolmogorov scale is approached at high wavenumber, the spectra decay more rapidly than any power of κ. In contrast to $E(\kappa)$, the one-dimensional spectrum $E_{11}(\kappa_1)$ is maximum at zero wavenumber and monotonically decreases as a function of κ_1.

The majority of spectra were obtained experimentally by a time-resolved measurement at a fixed position. Using this approach, temporal spectra were converted into spatial coordinates using Taylor's
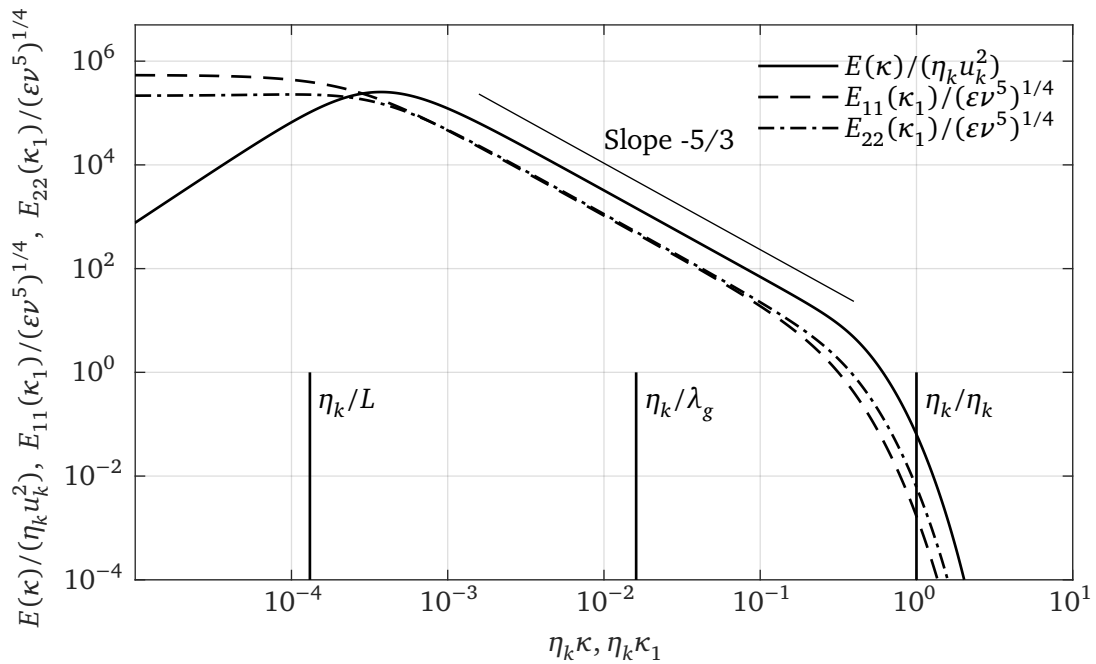
Figure 2.1: Comparison of spectra (based on the model spectrum in [16, p. 232]) in isotropic turbulence at $\mathrm{Re}_\lambda = 1000$ normalized by the Kolmogorov scales.

frozen flow hypothesis [19]. This model assumes that spatial patterns are carried past a fixed point with a convective velocity $\vec{U} = (U, 0, 0)$, which is classically assumed to be the local mean stream-wise velocity $\langle u \rangle$. Essentially, this means that the velocity $u(\vec{x} + \vec{\xi}, t + \tau)$ at a downstream location $\vec{x} + \vec{\xi} = (x_1 + \xi, x_2, x_3)$ and time $t + \tau$ can be approximated as $u(\vec{x} + \vec{\xi}, t + \tau) = u(\vec{x} + \vec{\xi} - \vec{U}\tau, t)$. Consequently, the space-time correlation can be expressed as $\mathscr{R}(\xi, \tau) = \mathscr{R}(\xi - U\tau, 0)$, which means that $\mathscr{R}(\xi, \tau)$ stays constant for any separation ξ or τ on the characteristic lines $\xi - U\tau = \text{const.}$ as is shown in Fig. 2.2(a). This property of $\mathscr{R}$ however violates the physical nature of correlation functions, which inherently decay in turbulence [20] (as e.g. shown in Fig. 2.2(c) for a typical spatial correlation function $\mathscr{R}(\xi)$). Still, Taylor's hypothesis represents an accurate model for low turbulence intensities but is known to fail for free shear flows and at high turbulence levels [16].

An alternative model for the determination of space-time correlations in turbulent flows was developed by He and Zhang [21] using an elliptic approximation (EA) of the iso-correlation contours of $\mathscr{R}(\xi, \tau)$, which approximates the shape of space-time correlations experimentally and numerically determined in shear flows [20–23]. The EA model expresses the correlations in terms of the characteristic velocities U and V as $\mathscr{R}(\xi, \tau) = \mathscr{R}(\sqrt{(\xi - U\tau)^2 + V^2\tau^2}, 0)$ resulting in elliptical iso-contours of the correlation function (Fig. 2.2(b)). For $V = 0$, the EA model is identical with Taylor's frozen flow model while for $U = 0$, the EA model expresses Kraichnan's random sweeping model [21]. Further model development for the approximation of $\mathscr{R}(\xi, \tau)$ requires the simultaneous measurement of space and time, which is especially challenging for high Reynolds numbers and small turbulent scales as these boundary conditions require a high dynamic range of the velocity measurement as well as a high spatio-temporal resolution.
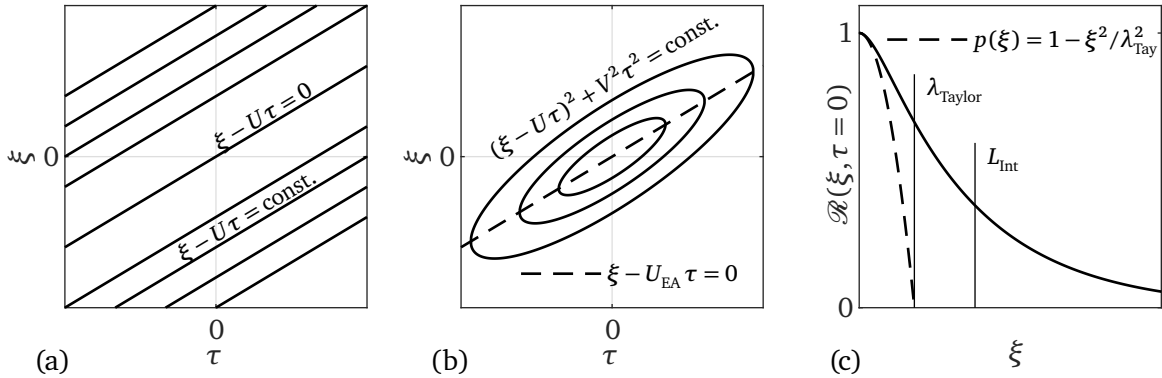
Figure 2.2: Iso-correlation contours of (a) frozen (Taylor's hypothesis) and (b) nonfrozen (EA model) turbulence. (Adapted from [20]) (c) Representative spatial autocorrelation function $\mathscr{R}(\xi)$ including a depiction of the determination of λ_{Taylor} and L_{Int}.

2.1.2 Dispersed particle-laden flows and particle-turbulence interaction

Dispersed particle-laden flows are ubiquitous in many disciplines of engineering and environmental sciences. From the combustion of biomass in furnaces, the transport of sediment in rivers to the formation of clouds in the atmosphere, multi-phase flows consisting of liquid or solid particles dispersed in an often turbulent carrier flow represent an important field of study requiring extensive experimental and numerical investigation. Compared to single-phase fluid flows discussed in Section 2.1.1, the description and modeling of multi-phase flows is much more complicated as multiple interacting phases are involved, whose behavior has to be captured and described accordingly. An extensive introduction into dispersed particle-laden flows is found in several books [24, 25] and review papers [26, 27].

The properties of particle-laden flows can be characterized by several important quantities. Considering a domain of volume V_d including a total number of particles N_p, the particle number density (PND) is defined as

$$\text{PND} = \frac{N_p}{V_d}. \tag{2.7}$$

Similarly, the volume fraction of particles α_p within this domain can be computed as

$$\alpha_p = \frac{\sum_{i=1}^{N_p} V_{p,i}}{V_d}, \tag{2.8}$$

where the volume of individual particles is denoted as $V_{p,i}$. For monodisperse particles of uniform volume V_p, the volume fraction of particles can be computed as $\alpha_p = \text{PND} \, V_p$.

The interaction of the surrounding flow field with the dispersed phase is captured by a set of additional parameters linking the properties of particles and the carrier phase. Based on the general definition in Eq. 2.1, a relative Reynolds number (also termed particle Reynolds number Re_p) is defined as

$$\text{Re}_p = \frac{d_p \, |\vec{u}_f - \vec{u}_p|}{\nu} = \frac{d_p \, |\vec{u}_s|}{\nu}. \tag{2.9}$$

In this definition, the characteristic length is the representative particle diameter d_p and the characteristic velocity is chosen to be the magnitude of the relative or slip velocity $|\vec{u}_s|$, which is calculated as $\vec{u}_s = \vec{u}_f - \vec{u}_p$, where the indices $\square_f$ and $\square_p$ denote the fluid and particle properties, respectively. In the fixed frame of a resting particle, Re_p can be used to determine the characteristics of the local flow field around the particle similar to the famous case of the flow past a sphere (or other rigid objects).

Further, the momentum response time of a particle τ_p in a carrier flow is important to describe the interaction of both phases as it displays the particle's ability to respond to changes in the surrounding fluid velocity. Based on the motion equation of a spherical particle in a fluid flow [25, p. 24], the response time of a particle for low Reynolds numbers can be computed as Eq. (2.10). Based on this, the Stokes number, defined as the ratio between particle and fluid timescales (Eq. (2.11)), represents a dimensionless number describing the ability of particles to follow the motions of the surrounding flow. If $\text{St} \ll 1$, particles perfectly respond to all changes of the flow field and can be termed tracers, which is important for the experimental characterization of fluid flows as outlined in Section 2.2.2.

$$\tau_p = \frac{\rho_p \, d_p^2}{18 \, \mu_f} \tag{2.10}$$

$$\text{St} = \frac{\tau_p}{\tau_f} \tag{2.11}$$

As discussed in Section 2.1.1, turbulent fluid flows exhibit a wide range of spatial and temporal scales with the Kolmogorov time scale τ_k representing the smallest scale at which the dissipation of kinetic energy into heat occurs. Consequently, different Stokes numbers based on the chosen fluid timescale can be found for different fluid mechanical configurations (e.g. in particle-laden turbulent round jets, the definition $\tau_f = D/u_{bu}$ is often found [28, 29] for the exit diameter D and the bulk flow velocity u_{bu}). Still, the most widely used Stokes number for the description of particle-turbulence interaction is based on the Kolmogorov timescale as $\text{St}_k = \tau_p/\tau_k$. Using this definition, different regimes of particle-turbulence interaction can be found [30] as outlined in Fig. 2.3, where the Stokes number St_k is displayed as a function of the particle volume fraction α_p.

For the smallest particle concentrations ($\alpha_p < 1 \cdot 10^{-6}$), only the motion of the particles is affected by the fluid phase with the turbulence structure of the carrier phase remaining almost unchanged. Therefore,
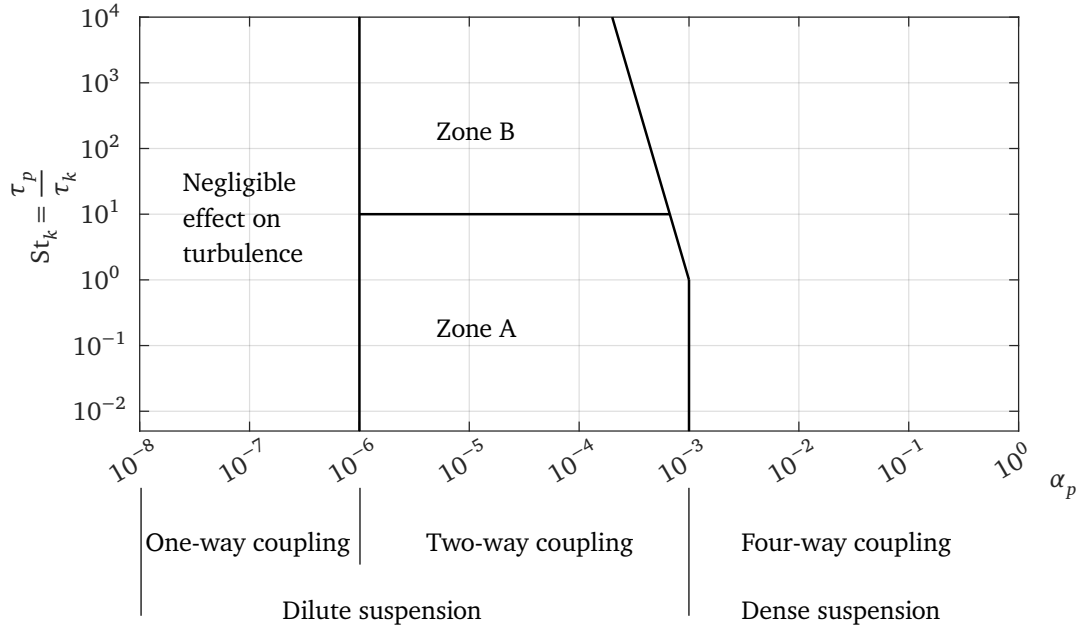
Figure 2.3: Classification map of particle-laden turbulent flows showing the interplay of volume fraction α_p and the Kolmogorov-based Stokes number St_k. (Adapted from [30])

one-way coupling occurs in this regime as the behavior of the fluid phase can be treated separately from the particle phase. Increasing the particle volume fraction beyond $\alpha_p > 1 \cdot 10^{-6}$, one enters the region in which *two-way coupling* occurs, as the fluid flow is now affected by the presence of particles with the particles themselves being affected by the fluid motion. Within this regime, zone A includes particles with $St_k \leq 10$ and particle Reynolds numbers $Re_p \leq 1$, which results in a large variety of different effects of the presence of particles on the turbulent flow. As τ_p increases (the particle size increases at a given particle concentration α_p), zone B is reached, in which vortex shedding occurs for particle Reynolds numbers beyond values of 400 for spheres [30]. It should be noted that the exact value of Re_p for the onset of vortex shedding also depends on the shape and orientation of the particle towards the local flow. For $\alpha_p > 1 \cdot 10^{-3}$, dense suspensions of particles result in an increasing importance of particle-particle collisions leading to *four-way coupling*. The upper separation line between zones A and B and the four-way coupling regime is slightly inclined as the probability of particle-particle collision rises as τ_p increases at a given value of τ_f.

The majority of investigations of particle-turbulence interaction have been performed using spherical particles, whose behavior however differs greatly from the modulation properties of aspherical particles, which have been fundamentally studied to a much lesser extent [27]. The most primitive shape representing an aspherical particle is an ellipsoid, whose properties have been recently studied in highly-resolved simulations to e.g. obtain the drag coefficients depending on their orientation and the particle Reynolds number [31–33]. The momentum response time of a prolate ellipsoid can be expressed as

$$\tau_p = \frac{2a^2 \rho_p}{9\mu_f} \frac{\beta \ln\left(\beta + (\beta^2 - 1)^{1/2}\right)}{(\beta^2 - 1)^{1/2}}, \tag{2.12}$$

where a is the minor axis radius and β is the aspect ratio of the ellipsoid (which is the ratio between major and minor axis radii) [27, 34].

2.1.3 Combustion of carbonaceous solid fuels

As discussed in Section 1.1, the combustion of coal and biomass represents a critical area of investigation due to its substantial impact on power generation and the urgent need to decarbonize the energy sector. Consequently, this subject has garnered significant attention and undergone extensive study. In line with this, the following section offers a concise overview of the composition and combustion characteristics of fossil and regenerative carbonaceous solid fuels.

Solid fuel types and composition

Solid fuels can be characterized based on their degree of carbonization or coalification. Coalification refers to the natural process by which buried plant matter evolves into a dense, dry, carbon-rich, and hard material. It is primarily influenced by heat and pressure over time, with heat playing a dominant role [35]. Depending on the degree of coalification, four major ranks of coal are defined: lignite (often known as brown coal), sub-bituminous coal, bituminous coal, and anthracite. Biomass, on the other hand, represents organic matter derived from living or recently living organisms and is not considered a fossil fuel. The different ranks of coal exhibit variations in color, hardness, and elemental composition.

The transition in composition from biomass through peat to different coal stages can be observed in the Van Krevelen diagram (Fig. 2.4), which provides a graphical representation of the elemental composition of fuels, depicting the hydrogen-to-carbon ratio (H/C) on the vertical axis and the oxygen-to-carbon ratio (O/C) on the horizontal axis [36]. In this diagram, solid fuel types with a lower degree of carbonization, such as biomass and peat, demonstrate higher atomic H/C and O/C ratios. Conversely, as the coal rank increases, both ratios notably decrease. As is apparent, the majority of carbonaceous solid fuels are found in a narrow band. Fuels with higher H/C and lower O/C ratios tend to exhibit higher energy content such as bituminous coals. Conversely, fuels with lower H/C and higher O/C ratios, such as biomass, often have lower energy content and may require different processing techniques such as torrefaction to improve their storage, transport and combustion properties.
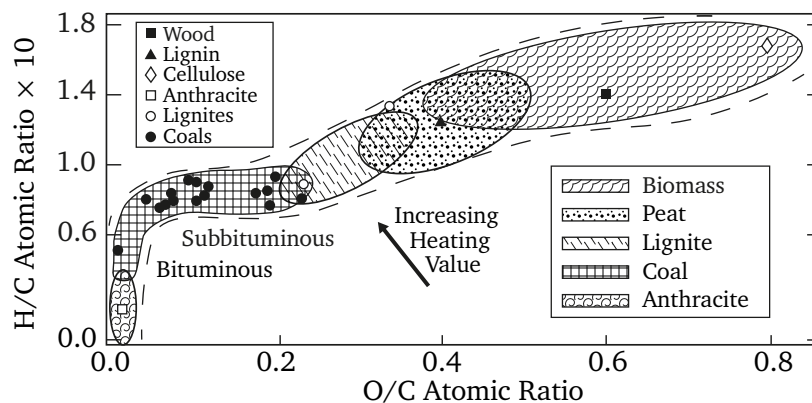
Figure 2.4: Van Krevelen diagram highlighting different carbonaceous solid fuels. (Adapted from [36, 37])

Solid fuels exhibit varied chemical compositions, consisting predominantly of carbon, hydrogen, oxygen, and a range of other elements that necessitate thorough characterization. Proximate analysis emphasizes the determination of relative quantities pertaining to essential components such as fixed carbon, volatile matter, ash, and moisture content. Conversely, ultimate analysis ascertains the precise elemental composition of the fuel, enabling a more intricate comprehension of its chemical properties

and energy content. The combination of proximate and ultimate analyses is indispensable for comprehensive characterization of solid fuels, facilitating the evaluation of their suitability for thermal conversion. Especially for biomass, the chemical composition of a chosen solid fuel can vary significantly depending on factors like the plant species, growth conditions, fertilizers or harvesting time, which requires tedious characterization and the generation of extensive data sets for kinetic modeling. In comparison to coal, biomass contains a larger fraction of volatile matter mostly exceeding 60%, which affects the interaction with the surrounding fluid phase altering the mixing, ignition and combustion properties [38]. In this work, the combustion of bituminous coal and the particle-fluid interaction of miscanthus is experimentally investigated.

Single particle and particle group combustion

The thermochemical conversion of solid fuel particles in furnaces consists of multiple phenomenological phases, which are depicted for a representative particle in Fig. 2.5. As particles enter the combustion chamber, they are heated resulting in the release of water and subsequently flammable volatile matter. After devolatilization, the fuel diffuses away from the particle mixing with the available oxidizer resulting in the ignition and homogeneous combustion of volatiles in a spherical flame surrounding the particle. This leads to an increase of the local gas temperature $T_{f,\text{local}}$ until all volatile matter is consumed. As the oxidizer further diffuses towards the particle, heterogeneous combustion (or char combustion) occurs, during which reactions take place on the particle surface until only mineral non-flammable residues are left, which make up the ash.
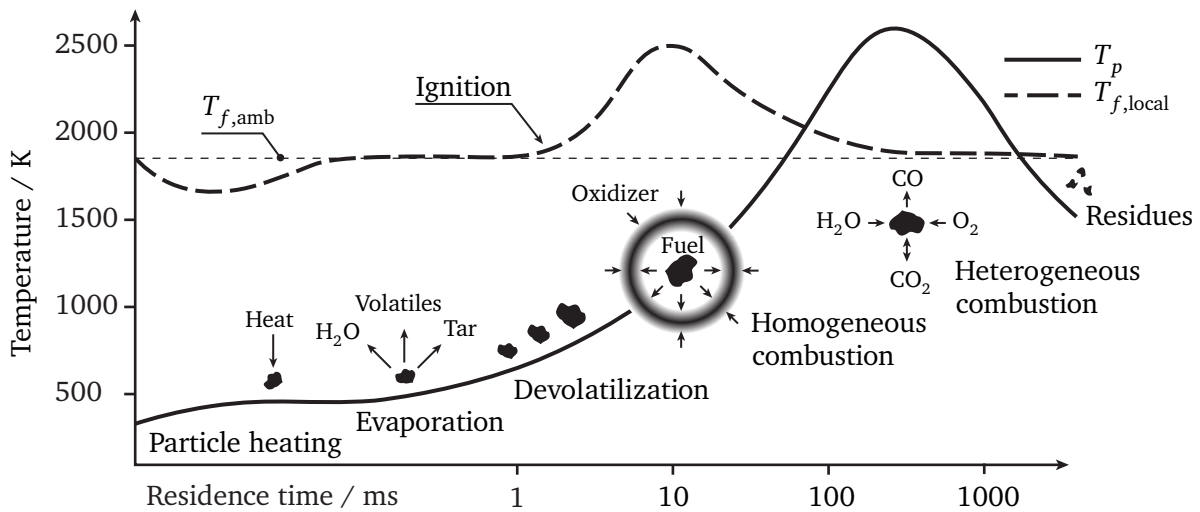
Figure 2.5: Temporal evolution of the combustion of a single solid fuel particle including relevant sub-processes. (Adapted from [11, 39])

While studies of single particle combustion (SPC) have been extensively reported in the literature, the experimental investigation of the combustion of streams or a group of particles is much more challenging, leading to fewer studies in this area [39]. The key difference between SPC and particle group combustion (PGC) lies in the importance of particle-particle interaction, which significantly influences the local transport processes and chemical reactions. The intensity of this interaction mainly depends on the local volume fraction α_p or PND of solid fuel particles, which can alternatively be expressed in terms of the inter-particle distance $l_{pp,1}$. Despite the challenges in conducting experiments on PGC, understanding these particle-particle interactions and their impact on combustion processes is crucial for characterizing the transition from single particle combustion to the complex interaction occurring in a group combustion scenario. Based on this, the definition of the interaction factor (IF)

can be used to determine the local interaction of two neighboring particles of size d_p and $d_{p,1}$ to $\text{IF} = \frac{1}{2}(d_p + d_{p,1})/l_{pp,1}$ [40].

Oxy-fuel combustion

Traditionally, the combustion of coal in power stations takes place within air atmospheres. However, as discussed in Section 1.1, the combination of biomass with oxy-fuel combustion in a CO_2-enriched atmosphere offers a pathway to achieve BECCS, a method that can effectively achieve negative CO_2 emissions [9]. The basic idea of oxy-fuel combustion starts with the separation of air into its primary components: nitrogen (N_2) and O_2. In this process, only O_2 is utilized for the combustion of the solid fuel. However, hydrocarbon combustion in pure O_2 can result in extremely high flame temperatures, which may cause irreversible damage to the boiler. To mitigate this issue, coal-fired power plants often introduce recycled flue gases into the boiler inlet flow to reduce the flame temperature. As there is no N_2 present in the combustion chamber, the flue gas mainly consists of CO_2 and water (H_2O). This composition allows for the recirculation, as well as the energetically efficient sequestration and storage, of CO_2. Thus, oxy-fuel combustion offers a promising approach to address the challenge of carbon capture and storage in the pursuit of sustainable energy solutions and was extensively reviewed in previous works [7, 8].

The presence of CO_2 (and H_2O) in oxy-fuel combustion introduces significant alterations in combustion behavior due to changed thermochemical properties compared to N_2. Consequently, oxy-fuel combustion exhibits different characteristics when compared to traditional air-firing combustion whose impact on combustor performance is not entirely understood, motivating the need for detailed experimental studies. Amongst several quantities of interest, three key properties of the combustion atmosphere change: the heat capacity (and heat sink), the mass diffusivity of O_2 in the respective diluent species and the radiative behavior. Table 2.1 lists some of these properties calculated for a temperature of 1123 °C.

Table 2.1: Properties of N_2 and CO_2 at a temperature of 1123 °C [7].

	N_2	CO_2	Ratio CO_2/N_2
Density (ρ) / kg/m³	0.244	0.383	1.6
Specific heat capacity (c_p) / kJ/(kg K)	1.22	1.31	1.1
Heat sink (ρc_p) / kJ/(m³ K)	0.298	0.502	1.7
Mass diffusivity of O_2 in other species ($D_{O_2,X}$) / m²/s	$1.7 \cdot 10^{-4}$	$1.3 \cdot 10^{-4}$	0.8

The replacement of N_2 with CO_2 in the oxy-fuel combustion environment introduces several notable changes. Firstly, the higher heat sink of CO_2 enables it to store 1.7 times more heat per unit volume compared to N_2. Consequently, the flame temperature decreases proportionally when the ratio of oxygen to inert gases is maintained, potentially causing challenges with flame stabilization in combustors. This issue is further exacerbated by the lower mass diffusivity of O_2 in CO_2, which leads to reduced transport rates of the oxidizer into the diffusion flames surrounding solid fuel particles. Moreover, the presence of CO_2 and H_2O in oxy-fuel combustion significantly impacts radiative heat transfer. Both CO_2 and H_2O are radiative species in contrast to N_2. As a result, the radiative heat flux increases even if the temperature remains unchanged. Additionally, the thermal radiation from soot and char particles becomes influential in the radiative heat transfer process. The formation of soot, intricately tied to the local interaction between fuel and oxidizer in coal flames, displays alterations as gas composition and flow dynamics shift during oxy-fuel combustion.

Considering the combined effects and interactions between these factors, extensive research on oxy-fuel combustion remains imperative, particularly when characterizing the transition from SPC to PGC.

The comprehensive understanding of these phenomena is crucial for advancing the knowledge in this field and optimizing oxy-fuel combustion systems.
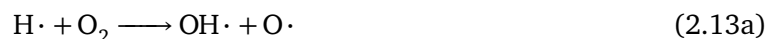
2.1.4 Flame retarded polymers

Polymers are widely utilized in diverse industries, such as construction, electronics, automotive, and consumer goods, due to their key advantages. These include lightweight properties, durability, design flexibility, and excellent electrical insulation. These characteristics make polymers highly desirable for various applications, e.g., enhancing overall performance of cars and airplanes.

While polymers have proven invaluable in many applications, their pronounced flammability poses a significant drawback that demands attention in sensitive applications. This especially concerns halogen-free polymers such as polyethylene (PE), PP or polyethylene terephthalate (PET), which are not inherently flame retarded compared to their halogen-containing counterparts. The potential hazards of fires, including the loss of human lives and substantial economic ramifications, underscore the urgent requirement for effective fire protection strategies. Consequently, the significance of flame retardation in polymers has garnered increasing recognition as industries strive to develop materials that are both safer and more sustainable [41–43]. Unlike the previous section that focused on enhancing the combustion of solid fuels, this section emphasizes the crucial objective of effectively inhibiting flames emerging from a solid material, i.e., a polymer.

To provide a foundation for understanding different inhibition mechanisms, the combustion of polymers is examined, emphasizing the thermal decomposition and combustion chemistry. The left part of Fig. 2.6 illustrates the processes involved in the combustion of polymers. Upon exposure to heat, polymers undergo decomposition through melting, pyrolysis, and vaporization. Polymer pyrolysis is generally an endothermic process, requiring a sufficient energy input to break bonds with bond dissociation energies typically ranging from 200 to 400 kJ/mol [44, 45]. The pyrolysis zone encompasses solid, liquid, and volatile products, often referred to as the mesophase [45]. While certain polymers naturally develop a char layer during decomposition, the polymer PP, studied within this thesis, exhibits a negligible char yield, resulting in a high fire hazard as the entire polymer material can potentially fuel a fire [45].

The volatile products generated in these processes consist of flammable hydrocarbon molecules that, when combined with oxygen, form a flammable mixture. During the combustion of hydrocarbon fuels, exothermic chain branching reactions (Eq. (2.13)) release heat and are primarily characterized by the presence of highly reactive hydrogen and hydroxyl (OH) radicals, with Eq. (2.13c) generating the highest heat of reaction [41, 46]. The reradiation of heat onto the polymer surface completes the flame stabilization cycle, which flame retardant substances aim to disrupt.

$$H\cdot + O_2 \longrightarrow OH\cdot + O\cdot \tag{2.13a}$$
$$O\cdot + H_2 \longrightarrow OH\cdot + H\cdot \tag{2.13b}$$
$$OH\cdot + CO \longrightarrow CO_2 + H\cdot \tag{2.13c}$$

Flame retardants exhibit a range of distinct modes of action to impede or suppress combustion processes in polymers as shown on the right side of Fig. 2.6. Gas-phase action involves scavenging radicals, disrupting heat and mass transport, and restricting the availability of combustible gases and oxygen. Condensed-phase action encompasses the promotion of charring, intumescence, and the formation of a protective barrier that limits the transport of fuel by inhibiting pyrolysis. Inorganic flame retardants, such as aluminum trihydroxide (ATH), decompose endothermically while releasing water, effectively dissipating heat from the reaction zone. The specific mode of action employed by a flame retardant is dependent on its composition and the particular polymer matrix under consideration. Understanding
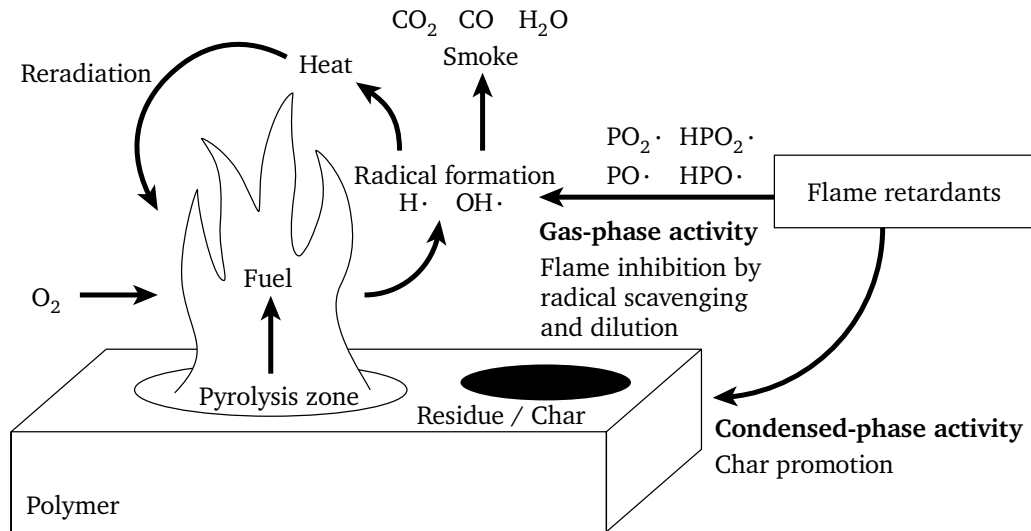
Figure 2.6: Combustion inhibition mechanisms of phosphorus-containing flame retardants added to polymer materials. (Adapted from [10])

these diverse mechanisms is vital for designing and selecting appropriate flame retardants to enhance the fire safety of polymer materials.

Traditionally, halogenated flame retardants based on e.g. bromine or chlorine have been widely used due to their efficacy in suppressing flames. However, increasing environmental concerns and potential health hazards associated with these halogenated compounds have led to their banning in many countries as first stated in the Montreal Protocol of 1987 [47]. Their persistence in the environment, potential for bioaccumulation, and toxicity have raised significant alarms, prompting the exploration of alternative flame retardants.

In recent years, phosphorus-based flame retardants have gained renewed attention as they offer reduced toxicity and a lower environmental impact compared to halogenated counterparts [10, 48]. Phosphorus-based substances have demonstrated promising flame inhibition properties while exhibiting improved environmental profiles. Previous investigations have revealed relevant reactions involving gas-phase active flame retardants containing phosphorus in a hydrocarbon flame, as summarized in Eq. 2.14 [10, 43, 48, 49]. These reactions involve the substitution or neutralization of highly reactive radicals through radical recombination within the gas phase. As a result, the progression of chain branching reactions involved in hydrocarbon oxidation is impeded or halted, leading to flame inhibition and reduced heat generation. The involvement of the phosphorus monoxide (PO) radical is widely acknowledged as pivotal in the flame inhibition mechanism [48].

$$PO\cdot + H\cdot \longrightarrow HPO \tag{2.14a}$$
$$PO\cdot + OH\cdot \longrightarrow HPO_2 \tag{2.14b}$$
$$HPO + H\cdot \longrightarrow H_2 + PO\cdot \tag{2.14c}$$
$$OH\cdot + H_2 + PO\cdot \longrightarrow H_2O + HPO \tag{2.14d}$$
$$HPO + OH\cdot \longrightarrow PO\cdot + H_2O \tag{2.14e}$$
$$HPO_2 + H\cdot \longrightarrow PO\cdot + H_2O \tag{2.14f}$$
$$HPO_2 + H\cdot \longrightarrow H_2 + PO_2\cdot \tag{2.14g}$$
$$HPO_2 + OH\cdot \longrightarrow PO_2\cdot + H_2O \tag{2.14h}$$

Several methods have been employed to assess the effectiveness of flame retardants in the gas phase, but most of these methods are intrusive and can disrupt the combustion processes [50]. Optical techniques, such as laser-induced fluorescence (LIF), offer a minimally invasive approach and have primarily been utilized in hydrocarbon gas flames with added inhibition agents. However, there is a significant gap in the literature regarding the characterization of gas-phase active flame retardants in burning polymer systems. This gap will be addressed in Section 5, where the methodology for evaluating the efficacy of flame retardants in burning polymers will be explained.

2.2 Methodological aspects

2.2.1 Lasers and optical devices

This section serves as an introduction to fundamental concepts and devices in laser optics that are pertinent to the research and advancements presented in this thesis. It starts by exploring pulsed solid-state lasers and provides a brief overview of the acousto-optic and electro-optic effects. Furthermore, it discusses measurement techniques employed in studying reactive multi-phase flows within the context of this thesis.

Pulsed solid state lasers

In turbulent flow systems, obtaining high temporal and spatial resolutions is crucial to capture the multitude of scales present in these phenomena. Minimally invasive laser diagnostics have proven invaluable for such measurements, especially in combustion systems [51]. Pulsed diode-pumped solid state (DPSS) lasers, schematically shown in Fig. 2.7(a), are often employed for laser diagnostics at kilohertz repetition rates [52, 53]. These lasers mostly employ a Q-switch to generate nanosecond pulses. The Q-switch blocks lasing action until the laser medium's population inversion reaches its peak, after which it rapidly releases the stored energy, resulting in short and intense laser pulses [54].
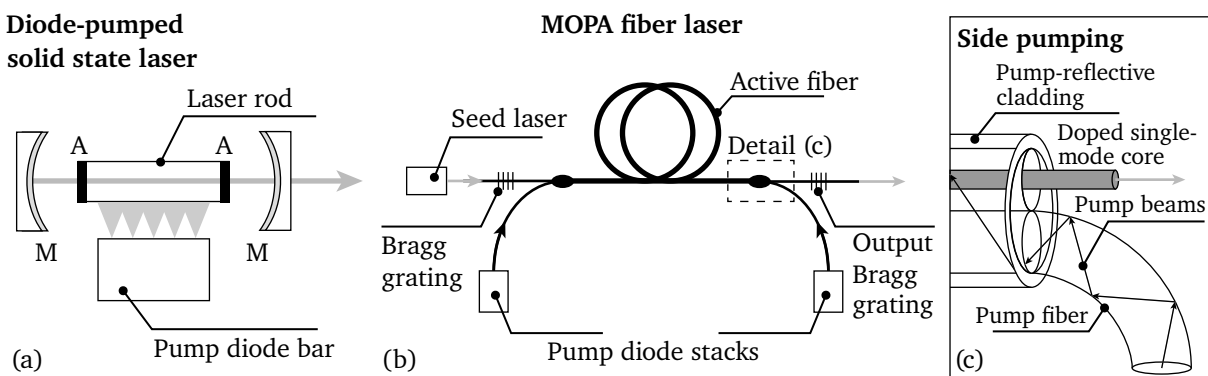
Figure 2.7: Schematic working principle of (a) the resonator of a DPSS laser (M = Mirror, A = pump-reflective layer) and (b) a master oscillator power amplifier (MOPA) fiber laser including (c) the side pumping mechanism of the active fiber. (Adapted from [4, 55])

Approaching repetition rates beyond 100 kHz, the continuous pulsing of Q-switched DPSS lasers faces significant limitations, primarily due to thermal stress within the laser cavity, restricting output power and repetition rates. To overcome these challenges, burst-mode lasers have been introduced, pulsing for a limited duration but with higher energies and repetition rates [53, 56]. State-of-the-art systems implement the master oscillator power amplifier (MOPA) approach, utilizing a low-power pulsed seed

laser amplified in subsequent stages to achieve high pulse energy. This approach provides flexibility in controlling pulse duration and energy, allowing the generation of pulses ranging from nanoseconds to femtoseconds with high average power and megahertz repetition rates.

Recently, pulsed MOPA fiber lasers have become available employing a side pumping strategy depicted in Fig. 2.7(b). Fiber lasers and amplifiers feature a distinctive design with a core fiber doped with rare earth ions surrounded by an undoped fiber for diode-laser pump beam guidance. The optimized core design ensures efficient excitation of the laser crystal as the pump radiation passes through the doped core. Unlike DPSS resonators, the large surface-to-volume ratio in optical fibers allows for efficient heat transfer. However, specific nonlinear loss mechanisms such as stimulated Brillouin and Raman scattering need to be considered leading to power limitations [57, 58].

Acousto-optic and electro-optic devices

The interactions between light and various external fields, such as acoustic waves and electric fields, give rise to phenomena known as the acousto-optic (AO) and electro-optic (EO) effects. These effects provide essential tools and devices used in a wide range of applications, from telecommunications and signal processing to laser technology and imaging [54, 59, 60].

The acousto-optic effect arises from periodic mechanical strain induced by an acoustic wave, creating a refractive index grating in the medium. When a light beam interacts with this grating, it undergoes diffraction in either multiple orders (Raman-Nath diffraction) at low acoustic frequencies or a single order (Bragg diffraction) at high acoustic frequencies, similar to X-ray diffraction in crystals [54, 60]. In the Bragg regime, the deflection angle θ can be calculated using the formula for Bragg diffraction $\sin\theta = (\lambda_l f_s)/(2V_s) = \lambda_l/(2\Lambda)$, with V_s being the velocity of sound, f_s the frequency of sound, λ_l the laser beam wavelength, and Λ the acoustic wavelength. The acousto-optic effect is harnessed in devices like acousto-optic modulators (AOMs) and acousto-optic deflectors (AODs), enabling applications such as laser scanning [54].

The electro-optic effect is a phenomenon observed in crystals, where an externally applied electric field alters the crystal's refractive indices. This effect can induce birefringence in otherwise isotropic crystals or modify existing birefringence. Two main types of the electro-optic effect are the Pockels effect (linear electrooptic effect) and the Kerr effect (quadratic electrooptic effect). In the Pockels effect, changes in refractive indices are directly proportional to the applied electric field. This effect finds practical applications in various optical devices to control and manipulate light propagation by modulating its phase, amplitude, or frequency [54, 60].

2.2.2 Optical diagnostics of reactive multi-phase flows

This thesis employs minimally invasive laser diagnostics to gather precise and comprehensive data about combustion processes, without disrupting the flow or chemical reactions [61]. These laser techniques offer high spatial and temporal resolutions, making them versatile in various combustion environments, particularly in solid fuel combustion experiments [39]. The laser diagnostic techniques utilized in this study are well-established and will be briefly explained in the following sections, with more comprehensive information available in the literature [61–63].

Particle image velocimetry (PIV)

Particle image velocimetry (PIV) is widely acknowledged as the standard experimental method for flow velocimetry [62, 64]. In PIV, fluid tracer particles are introduced into the flow and illuminated

by two short light pulses (usually a nanosecond-pulsed laser to avoid motion blur) with a precisely known time delay t_l. To ensure accurate tracking of the flow, it is important for the tracer particles to exhibit a Stokes number St $\ll$ 1, as discussed earlier in Eq. (2.10). A camera captures the Mie scattering of particles in two separate frames. By employing a cross-correlation algorithm within a defined interrogation window (IW), the fluid velocity can be computed by dividing the particle displacement signified by the peak of the cross-correlation function and t_l. Modern PIV algorithms operate in the frequency domain to speed up the correlation calculations, which requires a Fourier transform of the raw images. A common method to increase vector accuracy and density is a multi-pass approach with window overlaps in which a series of IWs with decreasing size are used to improve and refine vector calculations [62]. It is important to note, however, that the IW size still determines the spatial resolution of the velocity measurement in PIV, independent of the window overlap [65]. Alternatively, the tracking of single particles is possible leading to an unstructured grid of velocity data with higher local spatial resolution termed particle tracking velocimetry (PTV).

Typically, PIV is used in a planar arrangement to measure two velocity components (2D-2C) as it was the case in this thesis, but it can be extended to multiple dimensions and resolved in time (termed time-resolved particle image velocimetry (TR-PIV)). Current trends go towards 3D Lagrangian particle tracking methods, which provide a full picture of position, velocity, and acceleration of fluid elements in space and time [66].

Laser-induced fluorescence (LIF)

Laser-induced fluorescence (LIF) is a fundamental optical measurement technique wherein atoms or molecules absorb laser radiation to reach specific rotational-vibrational states and subsequently undergo transitions to lower energy levels, emitting radiation in the process. LIF finds extensive application in combustion diagnostics and has been discussed in numerous works in the literature [67, 68]. In this chapter, the focus lies on laser-induced fluorescence of the OH radical (OH-LIF) as it is applied for the hydroxyl (OH) radical, an important intermediate species in combustion systems.
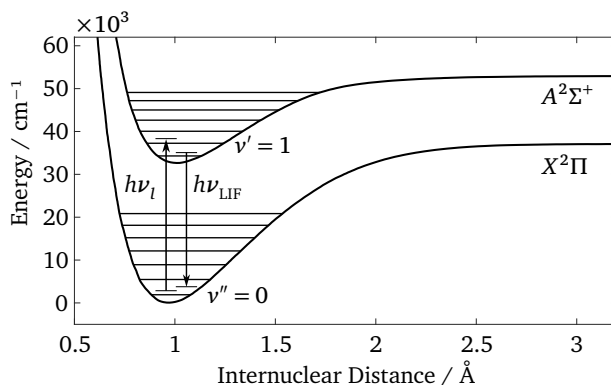
Figure 2.8: Rydberg-Klein-Rees potential energy curves of the ground state $X^2\Pi$ and first excited state $A^2\Sigma^+$ the OH molecule highlighting the excitation $v' = 1 \leftarrow v'' = 0$ at an incident photon energy of $h\nu_l$. (Adapted from [69])

Most commonly, excitation of the diatomic OH molecule is performed between $A^2\Sigma^+$ $(v' = 0) \leftarrow X^2\Pi$ $(v'' = 0)$ or $A^2\Sigma^+$ $(v' = 1) \leftarrow X^2\Pi$ $(v'' = 0)$ bands, where the latter was chosen in this thesis at laser wavelengths of around 283 nm as shown in Fig. 2.8. Here, $A^2\Sigma^+$ denotes the first excited electronic state and $X^2\Pi$ the electronic ground state. Compared to the excitation of the $v' = 0 \leftarrow v'' = 0$ band, the transition strength of the $v' = 1 \leftarrow v'' = 0$ is much lower [69]. However, after excitation, collisions will lead to vibrational and rotational energy transfer, lowering the energy of OH molecules and

therefore subsequent fluorescence will be Stokes shifted, enabling straightforward distinction between excitation and emission using spectral filters in the detection units.

The fluorescence emitted originates from various rotational levels in both $A^2\Sigma^+$ ($v' = 0$) and $A^2\Sigma^+$ ($v' = 1$), resulting in different wavelengths. Predissociation, caused by interaction with the $^4\Sigma^-$ state at higher vibrational levels, and collisional quenching, leading to de-excitation without radiation emission, are competing processes [70, 71]. The specific rotational excitation transition chosen in this thesis is the $Q_1(6)$ line from the state $X^2\Pi$ ($v'' = 0$) at the angular momentum quantum number $J = 13/2$. This transition was selected due to its uniform population over a wide temperature range and its successful application to OH-PLIF in solid fuel combustion [69, 71, 72].

Diffuse back-illumination (DBI)

Diffuse back-illumination (DBI) serves as an extinction imaging technique extensively employed in the analysis of multi-phase flows, including sprays and pulverized solid fuel combustion [39, 73]. The setup entails positioning a diffused light source, ideally a Lambertian emitter, in front of a camera that captures the light attenuated by objects within its path. Differing from shadowgraphy and schlieren imaging methods [63], the focus of DBI is not to visualize density gradients but rather to counteract beam steering by employing diffuse light instead of collimated light. Beam steering can lead to either a reduction or amplification in the recorded radiant flux. This phenomenon occurs when rays originating from the source experience refraction, causing them to fall beyond the defined angular aperture of the collection system, or when rays that initially exist beyond the collection cone are redirected inward. Nonetheless, when the illumination source adheres to criteria of sufficient extension, spatial uniformity, and Lambertian behavior, any light ray diverging from its original path due to refraction will be compensated by another ray possessing equivalent radiance originating from the same source. This quality makes DBI particularly suitable for capturing liquid-gas or solid-gas interfaces, as well as the projected sizes and shapes of particles [39].
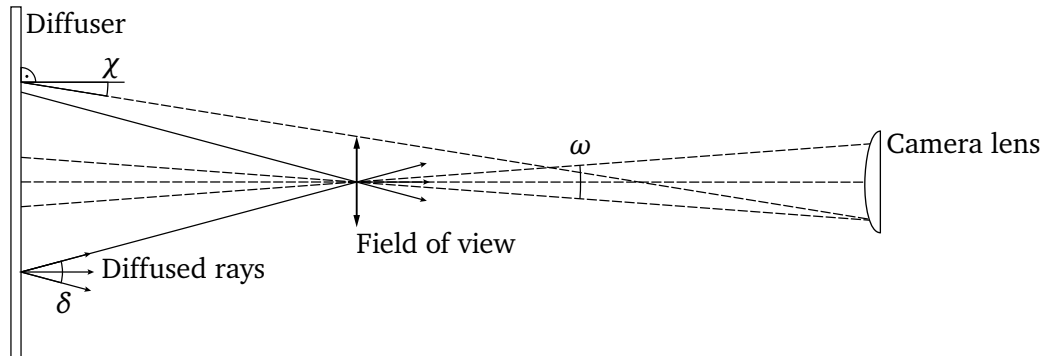
Figure 2.9: Optimized diffuse back-illumination (DBI) setup for the mitigation of beam steering. (Adapted from [73])

To address beam steering in a DBI setup, the calculations conducted by Westlye et al. [73] have unveiled a pivotal principle, visually illustrated in Fig. 2.9. This principle dictates that the Lambertian illumination's opening angle (δ) must surpass twice the combined value of the beam steering angle (ζ), which is often unknown, and the angle formed between the lens-captured steepest ray and a vector perpendicular to the light source's emission plane (χ): $\delta \geq 2\chi + 2\zeta$. This fundamental concept underscores the imperative of aligning the selected diffuser with the imaging system, particularly when using high-repetition-rate imaging necessitating short exposure durations. Opting for a wider opening angle involves a trade-off: it diminishes the signal collected by the imaging system's lens

while concurrently enhancing the effectiveness of beam steering mitigation. In scenarios encompassing substantial focal lengths and optical magnifications, which are typical in investigations focused on micrometer-sized solid fuel particles, a more restricted opening angle is requisite for a specific beam steering angle. As a result, utilizing narrower diffuser opening angles are sufficient for achieving high-resolution particle imaging while maintaining robust signal-to-noise ratios, effectively addressing the challenges stemming from beam steering.

3 Ultra-high-speed diagnostics of turbulent non-reactive biomass-laden jets

3.1 Outline and state of research

Understanding particle-flow interactions in solid fuel systems is crucial for the efficient combustion of carbonaceous fuels. Previous studies investigated solid fuel particles dispersed in a reactive laminar gaseous carrier flow using optical multi-parameter diagnostics [11, 39]. These experiments achieved high optical magnifications resulting in pixel resolutions of approx. 5 µm/px and were performed at recording rates of 10 kHz. Such resolutions were sufficient to track individual particle positions over time. However, extending comparable spatial resolutions to high-speed turbulent flows while simultaneously capturing particle movement demands significantly higher repetition rates for cameras and synchronized laser systems, depending on the specific diagnostic setup used. The primary objective of this chapter is to tackle this challenge by developing and implementing advanced diagnostic techniques that can capture particle dynamics in turbulent flows with enhanced temporal and spatial resolutions.

The need for ultra-high repetition rates becomes evident when considering the scenario of tracking a typical biomass particle over time with a diameter of $d_p = 200$ µm within a turbulent flow field while simultaneously capturing the fluid phase using PIV. To achieve a sufficient spatial resolution for the particle, a pixel resolution R of approximately 10 µm/px is required, ensuring an adequate number of data points. At the same time, capturing the PIV vector field with satisfactory spatial resolution demands a typical pixel displacement s_{px} of around 5 px, which, in turn, requires an IW size that is at least twice the size of s_{px}, determining the spatial resolution of the vector field. Considering a particle velocity of $u_p = 20$ m/s, the inter-pulse time t_l between two frames can be calculated using $t_l = (s_{px}R)/u_p$. The resulting value is $t_l = 2.5$ µs, implying that both the camera and laser systems need a repetition rate of at least $f_l = 1/t_l = 400$ kHz to continuously track the particle motion while resolving its size and shape using TR-PIV.

This straightforward analysis highlights the connection between the desired flow parameters and the necessary repetition rates. Specifically, higher flow velocities, smaller pixel displacements (leading to higher spatial resolutions of the PIV-derived flow field), and smaller R values all demand an increase in the repetition rate of the time-resolved diagnostics system. This realization underscores the critical importance of ultra-high repetition rates in effectively capturing the desired particle and flow dynamics within turbulent flows, demanding advancements in laser system specifications for velocimetry beyond the current state of the art. Hence, the primary objective of the works presented in this chapter is to develop and apply ultra-high repetition rate diagnostics for characterizing both the particle and fluid phases in a biomass-laden jet.

In the past, different laser types have commonly been used for high-speed PIV measurements, with notable examples being high-speed Q-switched DPSS lasers operating at single-cavity repetition rates of up to 150 kHz [52, 74], and burst-mode lasers that overcome thermal limitations by operating at a limited duty cycle, making them suitable for operation in the megahertz range [53, 56]. Due to the resolution of both space and time in TR-PIV, it is suited to both the determination of statistical quantities as well as temporal spectra and space-time correlations [75], as was first demonstrated by Wernet [76] for a turbulent jet using a DPSS laser at 25 kHz. Recent advancements in burst-laser technology

has enabled TR-PIV in a high-speed wind-tunnel at 50 kHz [77] and subsequently at 400 kHz [78] to measure temporal spectra. However, the high repetition rate restricted the active sensor area of the used complementary metal-oxide-semiconductor (CMOS) camera to a small field of view (FOV). In turbulent single-phase jets, dual-pulse ultra-high repetition rate PIV was performed at 100 kHz using a burst laser with operating durations of 100 ms, currently representing the highest possible temporal dynamic range (TDR) [79]. The data were subsequently analyzed to show deviations from Taylor's hypothesis in the intermediate region of the turbulent jet based on the convection velocity of turbulence structures extracted from space-time correlations [80]. However, both DPSS and burst-mode laser systems have technological and practical limitations, including thermal stress, limited burst durations, and high costs. To address these challenges, this work introduces a MOPA fiber laser capable of achieving ultra-high repetition rates of up to 400 kHz in Section 3.2 (**Paper I** [1]), enabling the utilization of TR-PIV in a single-phase turbulent round jet.

Investigating the interaction of particles with carrier-phase turbulence in multi-phase flows poses significant challenges. Computational studies often adopt the Lagrangian point-particle approach, utilizing empirical correlations for unresolved fluid-particle interactions [26]. This approach becomes particularly relevant when dealing with aspherical particle shapes, frequently encountered in biomass [27, 31, 33, 81]. Complementing experimental investigations of both phases are desired, but introduce increased complexity compared to single-phase velocimetry.

In the past, simultaneous measurement of particle and fluid phases was achieved through the introduction of phase Doppler anemometry (PDA) and laser Doppler velocimetry (LDV), as demonstrated in swirling flows [82, 83]. More recently, two-phase PIV has emerged as a widely used experimental technique for multi-phase flows. Two-phase PIV can be performed in different ways. In this thesis, a single-camera method was employed, utilizing the scattering intensity and size differences between the dispersed phase and fluid phase, separated using discrimination algorithms [84–86]. This approach was applied to investigate particle-turbulence interaction, resolving the Kolmogorov scales in a test stand replicating homogeneous isotropic turbulence (HIT) without mean velocity [87]. Alternatively, two-color methods based on fluorescence [88], phosphorescence [89], and incandescence [90] are available, but they require the introduction of a second camera and spectral filtering for two-phase velocimetry.

However, the majority of velocimetry measurements in multi-phase flows were conducted separately for each phase, which hinders the accurate determination of turbulence modulation caused by the presence of particles. Recent advancements in PIV measurements for turbulent jets have explored the influence of the Stokes number on particle velocity and concentration distributions, including 3D measurements revealing the phenomenon of preferential concentration [28, 29, 91]. Velocimetry in turbulent solid fuel flames has been conducted using LDV and PIV [92]; however, measurements of coal particles and tracers following the flow were carried out separately. TR-PIV investigations of multi-phase flows are even scarcer in the literature, mainly due to the need for high repetition rate lasers and cameras. For instance, Sabban et al. have utilized TR-PIV at a repetition rate of 3 kHz to study the behavior of fibers in forced homogeneous isotropic turbulence, addressing particle orientation through holographic imaging [93]. However, as previously mentioned, TR-PIV systems with similar projected pixel sizes often require laser and camera repetition rates beyond 10 kHz to effectively study technically relevant dispersed shear flows at high velocities, especially when capturing transient effects like particle rotation.

Based on these requirements, the fiber laser system introduced in **Paper I** was applied to perform multi-phase velocimetry of biomass-laden jets together with a simultaneously running DBI system, including a time-resolved measurement of the apparent particle Reynolds number (Section 3.3, **Paper II** [2] and conference paper [13]). Due to the small FOV of the camera resulting from cropping the sensor at high repetition rates, low-speed dual-pulse particle image velocimetry (DP-PIV) was employed to statistically characterize the single- and multi-phase flow fields. Given the laser's high repetition

rates, it effectively functions as a single-cavity dual-pulse laser, requiring a suitable pulse picking device to eliminate unwanted pulses. Consequently, pulse picking systems based on the acousto-optic and electro-optic effects were developed and characterized. The comprehensive approach adopted in this chapter enables a detailed examination of the particle and fluid phases in a biomass-laden jet, providing valuable insights for the advancement of high-speed diagnostics in particle-laden turbulent flows.

3.2 Ultra-high-speed time-resolved PIV of turbulent flows

3.2.1 Aim

In **Paper I** [1], the utilization of a compact fiber laser for ultra-high-speed TR-PIV measurements in a turbulent round jet is investigated. Operating at repetition rates of up to 1 MHz, this laser system offers promising potential for the characterization of turbulent flows. The primary focus of this study is to evaluate the feasibility and performance of the compact pulsed fiber laser for TR-PIV measurements, providing insights into its capabilities and limitations in capturing complex flow dynamics. As outlined in the previous section, the thorough characterization of this novel laser system is an important prerequisite for the application within turbulent multi-phase flows, which is presented in Section 3.3. By addressing the scientific aims listed below, this research aims to contribute to the advancement of high-speed PIV techniques for the experimental characterization of turbulent flows.

- The compatibility of the compact pulsed fiber laser with high-speed camera systems, such as a high-speed CMOS camera operating at different frequencies (e.g., 200 kHz, 400 kHz) and an in situ storage CCD camera for burst-mode PIV measurements at 500 kHz, is investigated.

- The measurement capabilities of the CMOS camera system are shown, including the quantification of measurement uncertainties for capturing turbulence statistics within a round jet.

- The measurement of turbulent scales, spectra, and space-time correlations is demonstrated at an unprecedented TDR while investigating the limitations of the novel TR-PIV system.

3.2.2 Methods

Fiber laser

In this study, a nanosecond-pulsed Yb-doped fiber laser (GLPN-500-1-50-M, IPG Photonics) was utilized. The laser's output properties are detailed in Table 3.1. As explained in Section 2.2.1, the MOPA laser architecture is based on amplifying a low-power seed laser in a diode-pumped gain medium. The fiber resonator design ensures efficient thermal management, eliminating the need for water cooling. The laser pulse travels through a polarization-maintaining single-mode delivery fiber and exits the laser head after second-harmonic generation at an output wavelength of 515 nm. The beam profile remains consistent across all power set points, exhibiting an excellent beam quality factor of $M^2 = 1.43$, allowing for the creation of thin laser sheets without the use of additional optics.

While this laser architecture facilitates ultra-high repetition rates for continuous outputs in the visible spectrum, the pulse energy diminishes as the inter-pulse time decreases beyond a repetition rate of 100 kHz at a fixed output power of 50 W. Consequently, the pulse energy is lower than that of conventional DPSS and pulse-burst systems, which typically operate in the millijoule range. To compensate for this drawback, a limited lateral expansion of the laser sheet while maintaining a simultaneous thin beam waist has to be realized, thereby ensuring a sufficiently high laser fluence in the measurement volume.

Table 3.1: Properties of the continuously pulsing ultra-high-speed fiber laser.

Property	Value
Output wavelength (λ_l)	515 nm
Polarization	s-polarized
Pulse widths	1.3 ns, 4.4 ns, and 11.8 ns
Repetition rates (f_l)	10–1000 kHz
Pulse energy	500 µJ (up to $f_l = 100$ kHz at 50 W)
Beam quality factor (M^2)	1.43
Beam diameter (d_b)	2.68 mm (at $1/e^2$)

Experimental setup

Velocimetry was conducted within the potential core of an axisymmetric turbulent jet, which exited as a fully developed pipe flow from a stainless steel pipe of diameter $D = 2.8$ mm (Fig. 3.1). Particle seeding was achieved using an aerosol generator creating di-ethylhexyl sebacate (DEHS) droplets with a mean size of 0.5 µm. The jet flow was operated isothermally at ambient conditions, and the operating points were chosen at bulk flow Reynolds numbers Re of 10,000 and 18,200 (details are listed in Table 2 of the original publication in A.1). The fiber laser system, along with high-speed cameras, was mounted on a traversable beam delivery system to create a laser sheet with a thickness of 290 µm to optimize both laser fluence and spatial resolution of the PIV measurements.
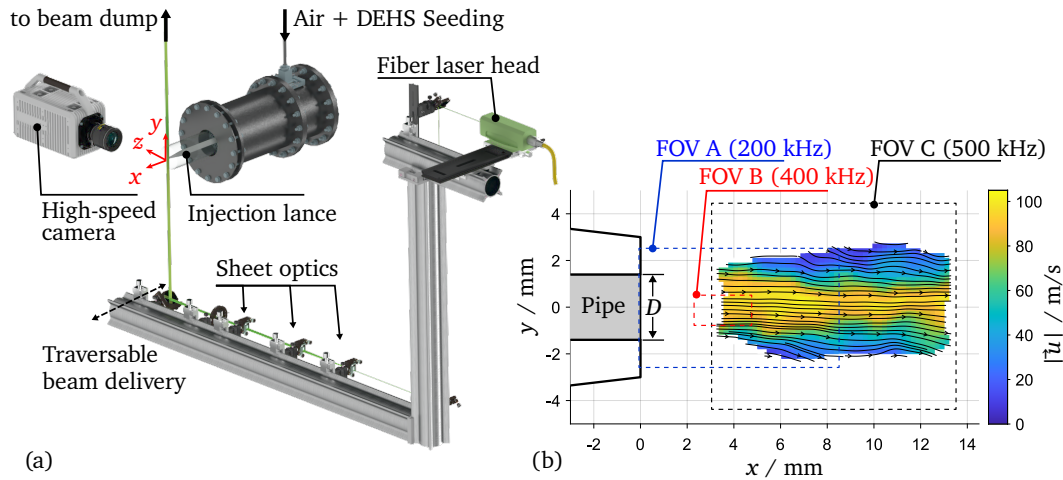
Figure 3.1: (a) Experimental setup for ultra-high-speed TR-PIV measurements. (b) Detail view of the near-nozzle region and measurement positions. The captured fields of view of the individual measurement configurations are displayed by dashed rectangles. (Adapted from [1])

Two high-speed camera systems, a continuous readout CMOS camera (further denoted by the camera model name SA-X2) and an in situ storage CCD (ISIS-CCD) camera (FOV C), were employed. The main focus of the flow field analysis lies on the SA-X2 recordings, which were performed at the jet exit at 200 kHz (FOV A) and higher-resolved measurements in the centerline region at 400 kHz (FOV B) shown in Fig. 3.1(b). The potential core of the round jet, with its small temporal and spatial turbulent scales, served as an ideal target for highlighting the capabilities and limitations of the ultra-high-speed repetition rate system. The images were captured and processed in the software Davis 10 (LaVision) using a correlation-based multi-pass algorithm with a window overlap of 75%. The final four passes at the smallest interrogation window size w were performed with a Gaussian weighting and vectors were subsequently validated using a universal outlier detection [94].

Given the continuous pulsing of the fiber laser, the duration of each recording was constrained solely by the storage capacity of the cameras. Consequently, the SA-X2 recordings resulted in over 1.2 million consecutive vector fields at 400 kHz. In theory, this setup could offer a remarkable temporal dynamic range (TDR) up to 600,000, denoting the ratio of the highest to the lowest resolvable frequency (TDR = $f_{\max}/f_{\min}$). However, practical limitations, such as noise, spatial resolution, and variance in power spectral density estimation, were assessed based on the experimental findings, potentially influencing the actual achieved TDR.

3.2.3 Results and discussion

Initiated partly by the challenges posed by increased noise levels at ultra-high repetition rates, the analysis began with a thorough assessment of the raw images captured by both camera systems. For the SA-X2 camera, spherical particle shapes were clearly distinguishable, allowing for accurate PIV measurements. However, with the ISIS-CCD camera, defocusing was necessary due to its large pixel size optimized for storage gates, resulting in undesired particle flashing during motion across the field of view. Despite being capable of capturing images with sufficient signal-to-noise ratio at 1 MHz, the PIV system's poor dynamic range of the velocity measurement was constrained by the large pixel size of the ISIS-CCD chip (66.3 μm/px) and limited flow rates dictated by the particle seeder resulting in pixel displacements below 2 px.

Furthermore, the analysis verified the absence of peak locking by examining the velocity histograms at selected positions (Fig. 5 in **Paper I** shown in A.1). Peak locking, a systematic error in PIV measurements, arises when particle images are smaller than one pixel, resulting in preferential particle displacements of integer multiples that can impact the accuracy of the velocity field [95]. This finding is crucial as it serves as a prerequisite for employing measurement uncertainty algorithms, which are sensitive to data affected by peak locking [96].

Measurement uncertainty evaluation is essential to ensure accurate and reliable estimation of local turbulence statistics in PIV measurements. Apart from systematic errors like peak locking, PIV systems introduce additional errors to instantaneously measured velocities, which are superimposed on the true velocity fluctuations caused by turbulent motion and therefore motivate the correction of these measured values. This is expressed by Eq. (3.1), where the apparent variance of the measured velocity distribution $\sigma_{u,m}^2$ is a superposition of the true velocity fluctuations $\sigma_{u,\text{turb}}^2$ and the error variance $\sigma_{u,\text{err}}^2$, which is similar to the mean-square of the uncertainty of instantaneous velocities $\sigma_{U_u}^2$ [96, 97].

$$\sigma_{u,m}^2 = \sigma_{u,\text{turb}}^2 + \sigma_{u,\text{err}}^2 \approx \sigma_{u,\text{turb}}^2 + \sigma_{U_u}^2 \tag{3.1}$$

Various methods have been proposed in the literature to directly determine the measurement uncertainty from PIV recordings [96]. In this study, a robust method for quantifying random uncertainty, known as the correlation statistics (CS) method proposed by Wieneke [98], was chosen. The selection of the CS method was motivated by its favorable performance compared to other methods [96] and its ready availability in the software Davis, which was utilized for PIV processing.

Figure 3.2 presents the probability density functions (PDFs) of the uncertainty for the instantaneously measured streamwise velocity measured at 400 kHz using the CS method for various interrogation window sizes w. The uncertainty distributions reveal that increasing the IW size leads to lower uncertainty, indicating a trade-off between spatial resolution and velocity measurement accuracy. As the CS method considers the individual contributions of each pixel within the IW to the correlation calculation, larger IWs, which include more particles, result in lower uncertainties. Conversely, smaller IWs tend to overemphasize the contribution of noise to the correlation calculation, leading to higher uncertainties.
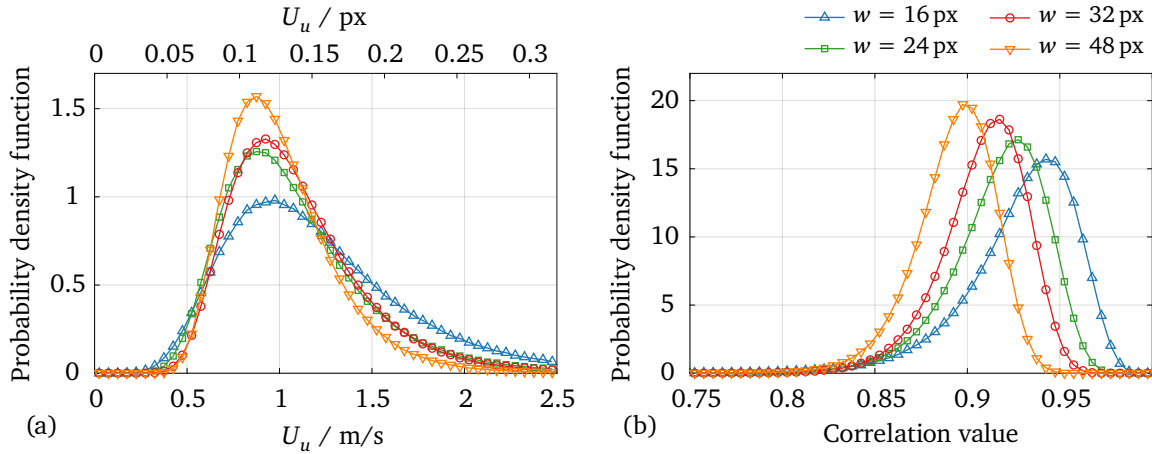
Figure 3.2: (a) PDFs of the uncertainty of the streamwise velocity component u and (b) corresponding PDFs of the correlation value on the centerline at a position of $x = 1.2D$ for the 400 kHz measurements. (Adapted from [1])

However, the uncertainty levels show similar levels for IW sizes of 24 px and 32 px, deviating from the aforementioned trend. The presented uncertainties are therefore further analyzed in conjunction with the correlation values in Fig. 3.2(b). As the IW size increases, the correlation values for the PIV vector calculation decrease, contrary to the trend observed in the uncertainty distributions. This behavior could be attributed to the inhomogeneous flow field, where differently positioned particles within a shear flow cause a gradient of particle movement within the IW, lowering the correlation value for larger values of w. Effectively, this means that an increase of the IW size from 24 px to 32 px decreases the correlation level outweighing the decreased amount of noise in the correlation calculation for the final uncertainty estimation. The findings highlight the importance of selecting an appropriate IW size to balance spatial resolution and accuracy. Based on the computed uncertainty values, the correction of the turbulence level based on the CS method and the influence of interrogation window size on higher-order statistics are further discussed in the full publication (Tables 3 and 4 in **Paper I** shown in A.1).

In addition to the evaluation of statistical properties of the turbulent flow, the high imaging rate and sample size of the TR-PIV data sets allowed for a high-resolution analysis of velocity time series. By increasing the repetition rate to 400 kHz, the constrained active sensor area provides temporally re-solved data but lacks spatial information over larger displacements. Extracting longitudinal integral turbulent scales T_{11} based on $\mathscr{R}_{11}$, it is observed that decreasing the IW size leads to earlier decor-relation of turbulent fluctuations as is shown in Fig. 3.3(a). This can be attributed to the combined effects of increased spatial low-pass filtering of small turbulent structures in larger IW and higher noise levels for the vector computation in smaller IW. The computed integral scales between $T_{11} = 11.3\,\mu s$ ($w = 16\,px$) and $T_{11} = 15.3\,\mu s$ ($w = 48\,px$) demonstrate the need for ultra-high repetition rates to accurately measure the integral time scale, which had previously only been achieved by pulse-burst lasers with significantly lower amounts of consecutively recorded samples [79]. The temporal (and spatial) autocorrelation results further support these findings, revealing the influence of IW size on the decorrelation behavior of turbulent fluctuations along the axial coordinate.

The effective number of statistically independent samples $N_e = T_t/(2T_{11})$ revealed a value of 137,831 for $w = 16\,px$, ensuring robust computation of statistical moments. The standard measurement un-certainty of the mean axial velocity is $U_{\langle u \rangle} = \sigma_u/\sqrt{N_e} = 0.01\,m/s$, which is remarkably small due to the high value of N_e, showing the benefit of this TR-PIV system compared to low-speed PIV systems offering superior spatial resolution and lower measurement noise resulting in lower uncertainties of individually measured velocities at the cost of lower amounts of samples per recording. Based on the
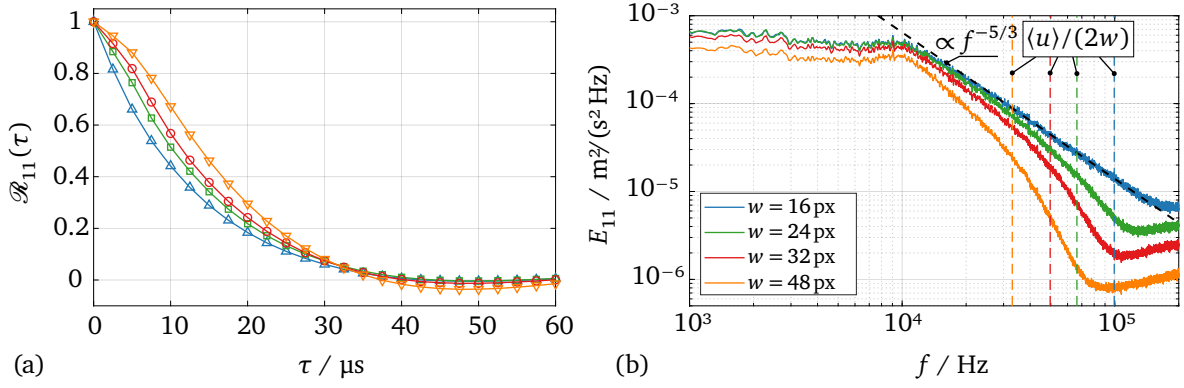
Figure 3.3: (a) Longitudinal temporal autocorrelation coefficient and (b) temporal power spectral density estimation at an axial distance of $x = 1.2D$ measured at 400 kHz. (Adapted from [1])

integral scales, the Taylor microscale was estimated to a value of 199 µm and the Kolmogorov length scale was estimated to a value of 15 µm.

Furthermore, this study examined longitudinal temporal turbulence spectra shown in Fig. 3.3(b) to investigate the filtering characteristics for varying values of w. Welch's method, including Hann window functions, was chosen for the computation of the power spectral density (PSD) estimates, which segments the time series and averages individual periodograms, lowering the variance of the PSD at the cost of spectral resolution. The spectra start to decay around 10 kHz, marking the onset of the inertial subrange with the characteristic decay curve of $E_{11} \propto f^{-5/3}$. The maximum resolvable frequency beyond the sampling theorem depends on several factors, including the spatial filtering due to the finite size of IWs, the particle frequency response, and noise levels. Smaller IW sizes yield higher noise levels, and a trade-off between noise and spatial resolution must be considered when analyzing turbulence using PIV data. As shown in Fig. 3.3(b), almost all spectra exhibit a steeper slope of decay beyond a value of $\langle u \rangle / (2w)$, which represents the highest resolvable frequency based on the finite size of the IW employing Taylor's frozen flow hypothesis. For $w = 16$ px, this limit is reached at around $f = 100$ kHz, resulting in an effective TDR of approx. 1500. This indicates that, for this study, the finite spatial resolution of the vector field is the main limiting factor of the frequency resolution of turbulence spectra.

The computation of spatial spectra for these data would usually rely on transforming temporal to spatial quantities due to the decreased amount of active pixels of the CMOS camera at ultra-high repetition rates. Taylor's hypothesis of frozen turbulence is typically used for this transformation, assuming turbulent structures are convected by the mean velocity $\langle u \rangle$. However, it is known to fail in free shear flows and high turbulence levels as outlined in Section 2.1.1. Despite the limited spatial dynamic range of the presented TR-PIV measurements, the applicability of Taylor's hypothesis could be tested using the space-time correlation $\mathscr{R}_{11}(\xi, \tau)$ which is displayed in Fig. 3.4.

The isocorrelations in the shape of elongated ellipses are in line with previous investigations of turbulent shear flows [99] and the elliptical space-time correlation model of He and Zhang [21]. Deviations from Taylor's hypothesis are observed, as the isocorrelation contours should be straight lines representing the convection velocity of turbulent structures through the flow field (compare Fig. 2.2(a)). In the limited FOV of the 400 kHz measurements, minor deviations from this assumption are encountered, which is probably due to the low turbulence level of about 5 % at the measurement position. At 200 kHz, it is apparent that the space-time correlations become more asymmetric with increasing spatial and temporal lags indicating a deviation from the elliptical model, which employs one constant convection speed of turbulence structures demanding a uniform angular orientation of the ellipses. Comparing the convection of fluid elements by mean axial velocity with the correlation peak's location over several time lags reveals significant deviations at large lags. The decreased axial turbulent
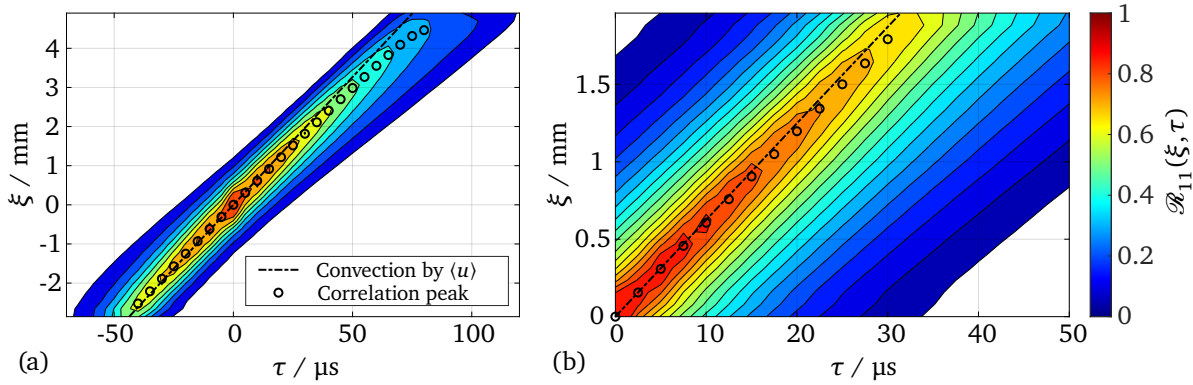
27

Figure 3.4: Space-time correlations of the streamwise velocity fluctuations for (a) 200 kHz and (b) 400 kHz at at an axial position of $x = 1.2D$. (Adapted from [1])

convection speed on the centerline is influenced by the magnitude and direction of turbulent fluctuations, leading to slower convection in the axial direction for fluid elements transported radially away from the centerline. Further investigations are needed to quantify the different contributions to this phenomenon, particularly considering Eulerian and Lagrangian space-time correlations [20, 100].

To conclude, the application of a Yb-doped fiber laser for ultra-high-speed TR-PIV was successfully demonstrated in the near-nozzle region of a turbulent round jet using two high-speed cameras, a CMOS and an ISIS-CCD camera. The system provided sufficient pulse energy and excellent beam profile characteristics at up to 1 MHz. The continuously pulsing laser allowed recording large time series, enabling the derivation of statistical quantities, space-time correlations, and turbulence spectra. A detailed analysis of said quantities including measurement uncertainties was performed while varying the IW size. Space-time correlations revealed deviations from Taylor's hypothesis. Pulsed fiber laser technology offers valuable insights into turbulent flows with high flexibility, benefiting future ultra-high-speed PIV investigations with unprecedented temporal dynamic ranges in a compact format.

3.3 Pulse picking PIV and multi-phase velocimetry of biomass-laden jets

3.3.1 Aim

The objective of this section is to expand the diagnostic system based on the introduction of the fiber laser for velocimetry of turbulent flows, with the overarching goal of experimentally characterizing biomass-laden jets. As demonstrated in the previous section, one limitation of ultra-high repetition rates required for temporal particle tracking is the need to crop the high-speed camera sensors, which limits the field of view (FOV). Complimentary conventional low-speed PIV is therefore desirable, which is useful to capture a wide range of spatial scales in the flow field surrounding the biomass particles. However, low-speed PIV cameras usually demand a separate dual-pulse low-speed laser system. Therefore, the development of a single cavity laser system with highly flexible repetition rates and pulsing schemes based on pulse picking of the fiber laser was a primary focus of this research, as thoroughly discussed in **Paper II** [2] and an additional conference paper [13]. This laser system can effectively be used for ultra-high-speed and low-speed PIV measurements independent of the used camera systems. As both laser pulses emerge from the same cavity, beam overlap is not necessary, which simplifies the experimental setup and improves the traceability of single particles potentially leading to improved PIV correlation values. Additionally, the application of the fiber laser within a multi-parameter measurement system for the characterization of biomass-laden jets is exemplified in **Paper II**, demonstrating

its capabilities for multi-phase velocimetry measurements. In summary, the works presented in this section address the following scientific issues:

- Two realized pulse picking system based on the acousto-optic and electro-optic effect are presented, exploring their limitations in terms of factors such as the smallest possible inter-pulse time, pulse energy losses, and beam profile alterations.

- The application of a multi-parameter diagnostics system to characterize multi-phase flows incorporating pulse picking is discussed, including the measurement of particle Reynolds numbers at high temporal and spatial resolutions in biomass-laden jets.

These studies contribute to the advancement of experimental techniques for turbulent flow measurements and provide valuable insights into the behavior of biomass-laden jets, enhancing the understanding of complex multi-phase flows.

3.3.2 Development and characterization of pulse-picking PIV systems

For the characterization of turbulent flows, PIV systems typically incorporate two coupled nanosecond-pulsed solid-state laser cavities, enabling microsecond inter-pulse times necessary for optimized particle displacement and high spatial resolution of the resulting flow field. These PIV illumination sources require short illumination pulse widths (nanosecond pulses), thin laser sheet focus, and high fluence in the probe volume to achieve sufficient scattering intensity from tracer particles [62]. However, current technological advances in laser and camera systems motivate further improvements in PIV lasers, as outlined in the following aspects driving the need for enhancements:

- **Repetition rate flexibility**: To capture statistical flow properties, low-speed dual-frame cameras with large sensors and small pixel pitches are ideal, while time-resolved measurements require ultra-high repetition rate cameras. Therefore, a single laser system offering a wide range of repetition rates is desirable.

- **Pulse scheme flexibility**: TR-PIV requires a steadily pulsing laser, while low-speed cameras require pulse pairs for PIV measurements. The laser system should provide pulses only when needed, avoiding unnecessary light emission during recording.

- **Single cavity dual-pulse output**: Current DPSS PIV lasers with two cavities complicate beam alignment and suffer from pulse-to-pulse beam inhomogeneity. A single-cavity dual-pulse output simplifies these aspects and improves performance as particle images appear similar in subsequent imaging frames.

The motivation behind the work presented in this section is to design a PIV laser system that fulfills all necessary requirements for PIV while incorporating the proposed improvements. This is achieved by coupling the previously introduced ultra-high repetition rate fiber laser with a pulse picking device to selectively block unwanted pulses from a continuous pulse train.

In pulse picking PIV, pulse pairs are selectively picked from a continuously running high-speed laser. This enables dual-pulse (or multi-pulse) measurements with low-speed dual-frame cameras, as the laser repetition rate can be adjusted accordingly. As the laser is running at a fixed repetition rate f_l, it has to be an integer multiple of the camera recording rate f_c: $f_l = c f_c (c \in \mathbb{N})$. For a given camera recording rate, a variation of the duty cycle factor c yields all possible inter-pulse times $t_l = 1/f_l$. The fiber laser is especially suited to this as repetition rates up to $1\,\text{MHz}$ are necessary to achieve inter-pulse times of only a few microseconds required for high-speed turbulent flows. Additionally, the continuously pulsing laser output is essential for enabling pulse picking PIV as the recording time of low-speed cameras is not constrained. The only remaining drawback is that the pulse energy of the

fiber laser decreases with repetition rate beyond $f_l = 100\,\text{kHz}$ such that an output power of $50\,\text{W}$ is maintained. In the following, two pulse picking laser systems shown in Fig. 3.5 are presented.
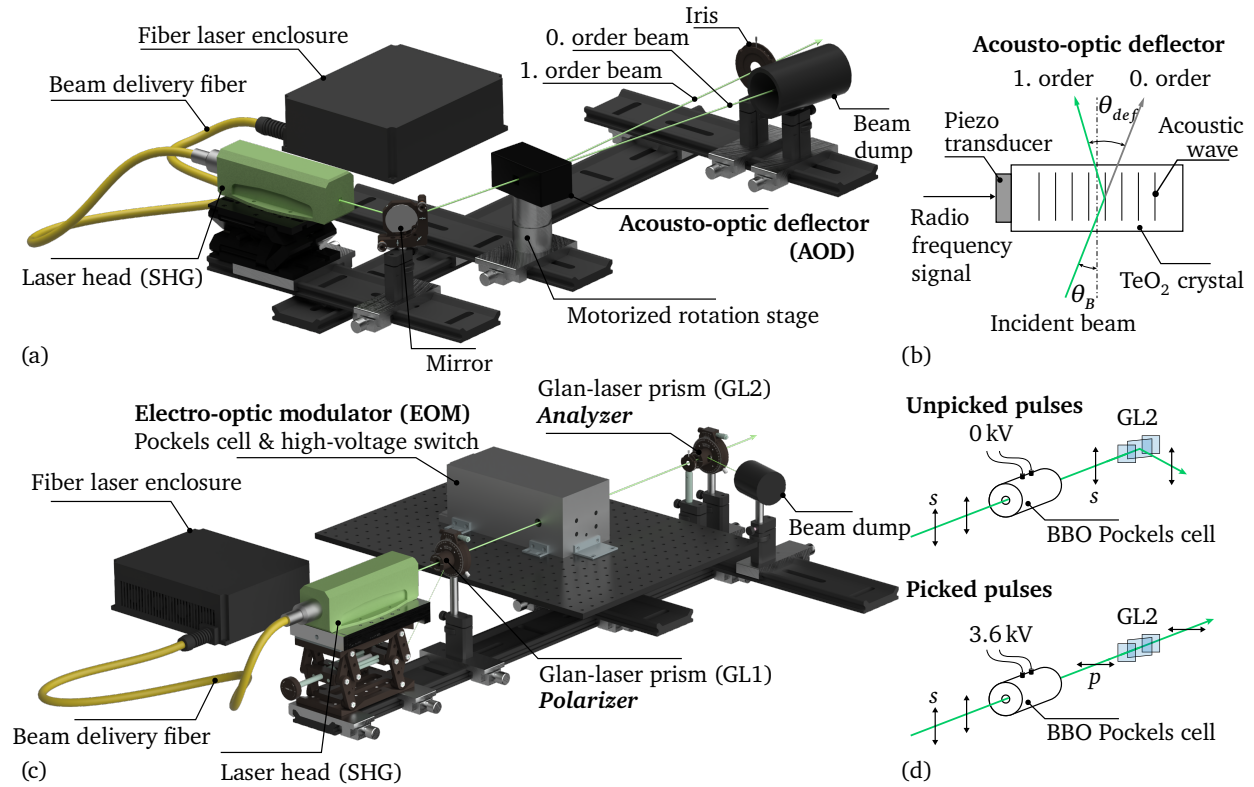

Figure 3.5: Experimental setups and working principles of both realized pulse picking systems based on the acousto-optic (a,b) and electro-optic (c,d) effect. (Adapted from [13])

AOD picking system   The first experimental setup shown in Fig. 3.5(a,b) utilizes an AOD for pulse selection. This AOD operates by diffracting an incident laser beam through a tellurium dioxide (TeO_2) crystal, driven by a voltage-controlled radio frequency driver in sync with the camera frame rate. A piezo transducer generates the sound wave necessary for pulse picking. The TeO_2 crystal exhibits an acoustic velocity of $V_s = 650\,\text{m/s}$, resulting in a transit time (or access time t_a) of $4.12\,\mu s$ for the sound wave to travel across the full beam diameter ($2.68\,\text{mm}$). When the sound wave is present, the deflected pulses (first-order beams) are directed into the measurement volume. In the absence of the sound wave, pulses are guided into a beam dump, effectively blocking unwanted pulses. The incident angle and output intensity of the deflected pulses can be optimized by rotating the AOD on a motorized rotation stage. This versatile principle can also be applied to laser scanning, where the sound wave frequency is modulated using a step function [101].

EOM picking system   The second pulse picking option, illustrated in Fig. 3.5(c,d), employs an electro-optic modulator (EOM) based on a voltage-controlled beta barium borate (BBO) Pockels cell featuring a $4\,\text{mm}$ clear aperture. The EOM is operated at its half-wave voltage of $3.6\,\text{kV}$, suitable for a laser wavelength of $515\,\text{nm}$. A voltage-controlled high-voltage switch enables a maximum switching repetition rate of $500\,\text{kHz}$. When the half-wave voltage is applied to the BBO crystal, it rotates the polarization of the incident pulses by $90°$, resulting in p-polarized light that can pass through a Glan-laser prism made from calcite (Analyzer, GL2) located behind the EOM. Conversely, unwanted s-polarized pulses pass through the BBO crystal and are reflected by the prism into a beam dump. To ensure and adjust the vertical orientation of the polarization plane at the laser output, another Glan-laser prism (GL1)

is positioned directly behind the laser head, serving as a polarizer. While other polarizing optics could be used, Glan-laser prisms offer superior extinction ratios for the polarized output beam (typically in the order of 100,000:1), making them a preferred choice for Q-switches in pulsed solid-state lasers.

Performance and limitations

After the introduction and setup both pulse picking options, a characterization of their performance and technical limitations was performed. Based on this analysis, the selection of a device suited to a specific application is enabled.

First, the smallest possible inter-pulse duration was evaluated. The EOM creates an electric field in the Pockels cell, causing birefringence in the BBO crystal to rotate the polarization of the laser beam. The EOM's switching time is only 4 ns while the subsequent propagation of the electric field change happens at the speed of light. Therefore, the switching time of the EOM itself does not constitute a limitation to the smallest possible inter-pulse time for a maximum laser repetition rate of 1 MHz, equal to an inter-pulse time of 1 μs. Consequently, the EOM pulse picking device is only limited by the picking rate of max. 500 kHz, which is much higher than the recording rates at which state-of-the-art high-speed cameras operate without a sensor crop.

The inter-pulse duration limitation of the AOD relies on the device's access time $t_a = d_b / V_s$, signifying the time taken for an acoustic wave to travel across the entire beam diameter d_b. In the current TeO_2 crystal, the access time is approximately 4 μs, corresponding to a laser repetition rate of 250 kHz, setting the lower limit of t_l for this system [59]. Although the rise and fall time of the radio frequency driver is about 50 ns, it is much smaller in magnitude compared to the access time. Still, as outlined in **Paper II** [2], an AOD pulse picking system can be operated at lower inter-pulse durations than the access time limit by adjusting the picking window to avoid diffraction of unwanted pulses before and after the selected pulse pair. However, as the following analysis shows, this leads to partially overlapping beam profiles of the picked laser pulses. Based on the relationship of t_a and t_l, three scenarios are possible:

- **Fully overlapping picked beams** $(t_l > t_a)$: In this regime, the inter-pulse time t_l is larger than the passage time of the sound wave over the beam width t_a. Each desired pulse can be picked while unwanted pulses are fully avoided.

- **Partially overlapping picked beams** $(t_a/2 < t_l < t_a)$: In this scenario, the inter-pulse time is smaller than the access time, resulting in partially overlapping pulses picked by the AOD. The timing chart in Fig. 3.6(a) illustrates this configuration for a symmetrically picked pulse pair P_1 and P_2 with negligibly small incident angles, while also showing the presence of the sound wave at the transducer-facing beam edge position E and the opposite edge O.

  The sound wave reaches position E optimally just after P_0 passed through the AOD. During the time between this point and the arrival time t_1 of P_1, the sound wave travels a distance of $d_b t_l / t_a$ across the beam, as depicted in Fig. 3.6(b). This results in only a fraction of t_l / t_a of the beam width of P_1 being deflected. Similarly, at $t = t_2$, an interaction length of $d_b t_l / t_a$ at the opposite beam edge is achieved for P_2, as the switching window t_{sw} is adjusted to avoid deflection of P_3, set as $t_{sw} = 3t_l - t_a$. In DP-PIV, quantifying the spatial overlap d_v / d_b between both picked pulses is crucial, as it determines the necessary beam expansion for a given axial extent of the FOV, where d_v denotes the absolute width of the spatial overlap. The calculation of the overlap is visually demonstrated in Fig. 3.6(c) as $d_v / d_b = 2t_l / t_a - 1$.

- **Non-overlapping picked beams** $(t_a/3 < t_l < t_a/2)$: The partially-overlapping picking approach for DP-PIV reaches its limit when the overlap of both deflected pulses disappears, which occurs at $t_l = t_a/2$. At higher laser repetition rates, the cross-sections of both picked pulses are completely
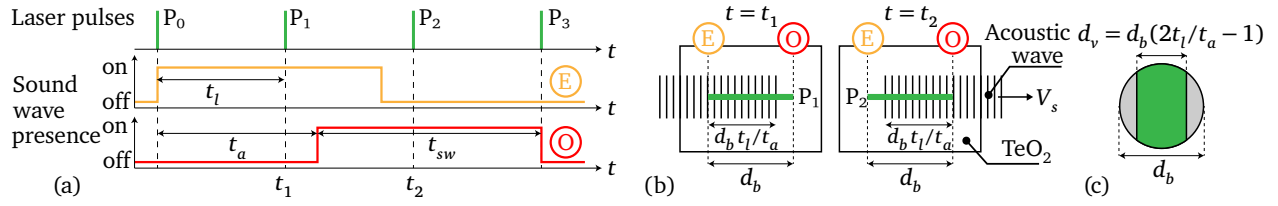
Figure 3.6: AOD-based selection of two pulses at $t_a > t_l$ including (a) a timing chart and (b) visualizations of the interaction between the acoustic wave and the laser pulse (green line). (c) Depiction of the calculation of the beam overlap. (Adapted from [2])

separated spatially. When $t_l = t_a/3$, t_{sw} becomes zero, indicating that deflection of unwanted neighboring pulses cannot be avoided beyond this point.

Figure 3.7 illustrates measured beam profiles for different configurations of the AOD and EOM pulse picking systems, along with the output beam profile of the fiber laser shown in Fig. 3.7(a). Minimal changes are aimed to maintain a homogeneous intensity distribution within the expanded laser sheet. In the EOM picking system, the beam passes through three optical elements: GL1, a Pockels cell, and a second analyzing Glan-laser prism. The beam profile of a single picked pulse shows slight intensity disturbances due to imperfections in the BBO crystal but retains similar focusing abilities as the original output. As discussed above, the AOD pulse picking system's smallest inter-pulse duration depends on the access time of about $4\,\mu s$, equivalent to a laser repetition rate of $250\,kHz$ for which both picked pulses are shown in Fig. 3.7(c,d). It can be observed that both pulses almost retain the full beam width with disturbances being visible in a wavy pattern stemming from the interaction with the sound wave in the AOD crystal. At a higher repetition rate of $312.5\,kHz$ (Fig. 3.7(e,f)), the picked pulses only partially overlap to avoid interference. However, this setup remains suitable for DP-PIV measurements by expanding the laser beams for sufficient overlap in the measurement volume as can be seen in Fig. 3(b) of **Paper II**, in which this configuration was used for DP-PIV.
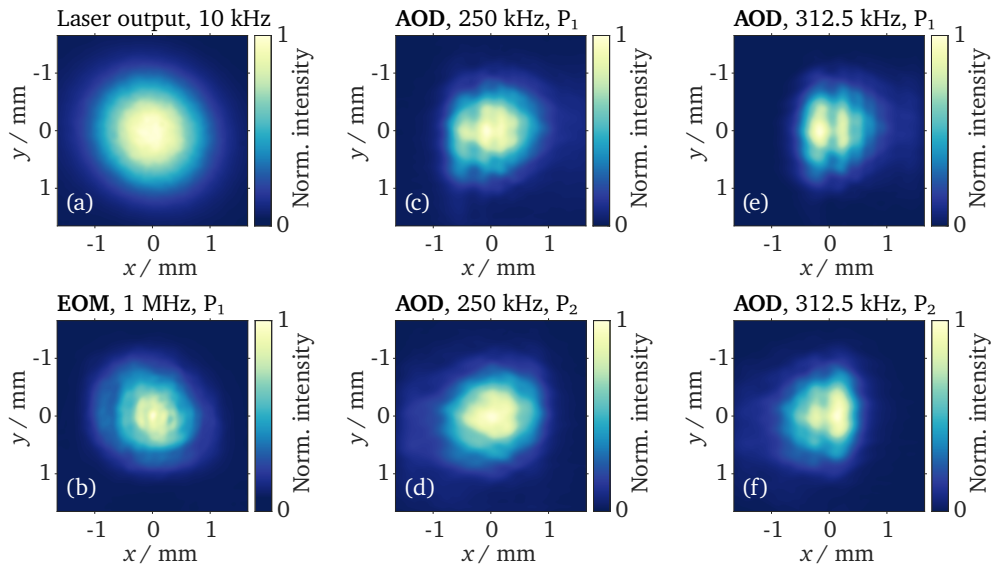
Figure 3.7: Measured laser beam profiles of the fiber laser head output (a), the EOM pulse picking system (b), and the AOD pulse picking device (c-f) running at different operating conditions. (Adapted from [13])

Finally, the pulse energy losses caused by laser beams interacting with critical optical elements in each pulse picking system were measured using a pyroelectric pulse energy meter. In the EOM setup, measurements were carried out behind each optical element, yielding a total remaining normalized

pulse energy of $0.875\,E_0$, where E_0 represents the output pulse energy of the fiber laser. Interestingly, the primary cause of pulse energy losses was found to be the suboptimal broadband anti-reflective coating on the Glan-laser prisms, rather than the Pockels cell. Implementing laser-line coatings could potentially boost the picking system's efficiency. On the other hand, the AOD demonstrated an optimized first-order diffraction efficiency of $0.883\,E_0$. Consequently, both systems exhibited reasonably acceptable pulse energy losses, each below 13%.

3.3.3 Multi-phase velocimetry of biomass-laden jets

After introducing the fiber laser as a tool for ultra-high repetition rate velocimetry of single-phase turbulent jets in Section 3.2, and expanding it to a universally applicable single-cavity laser suitable for both TR-PIV and DP-PIV measurements, this section delves into its integration into a multi-parameter measurement system for characterizing non-reactive biomass-laden turbulent jets. It is essential to mention that during the experiments presented in this section, only the AOD pulse picking device was available, which also prompted the subsequent development of the EOM pulse picking system shortly afterward.

Experimental setup

Investigations were conducted on a biomass-laden turbulent jet originating from the same ceramic-insulated round pipe as described in **Paper I** (Section 3.2). The experimental setup is illustrated in Fig. 3.8. The experiments were conducted under ambient conditions, and the air flow rate was controlled using mass-flow controllers. The air was divided to feed an aerosol generator with fluid tracers (particle size $0.2\,\mu m$) and a custom biomass particle seeder. The jet Reynolds number was 7500, corresponding to an axial bulk velocity of $u_{bu} = 41.75\,m/s$. The investigated pulverized raw miscanthus particles ranged in size from $90\,\mu m$ to $150\,\mu m$, and low particle concentrations were chosen to minimize inter-particle interactions. The Stokes number (estimated as $St \approx 210$ using Eq. (2.12)) indicates that particles are expected to trail behind the flow within the pipe but decelerate slower than the carrier phase as the jet expands axially resulting in a significant slip.
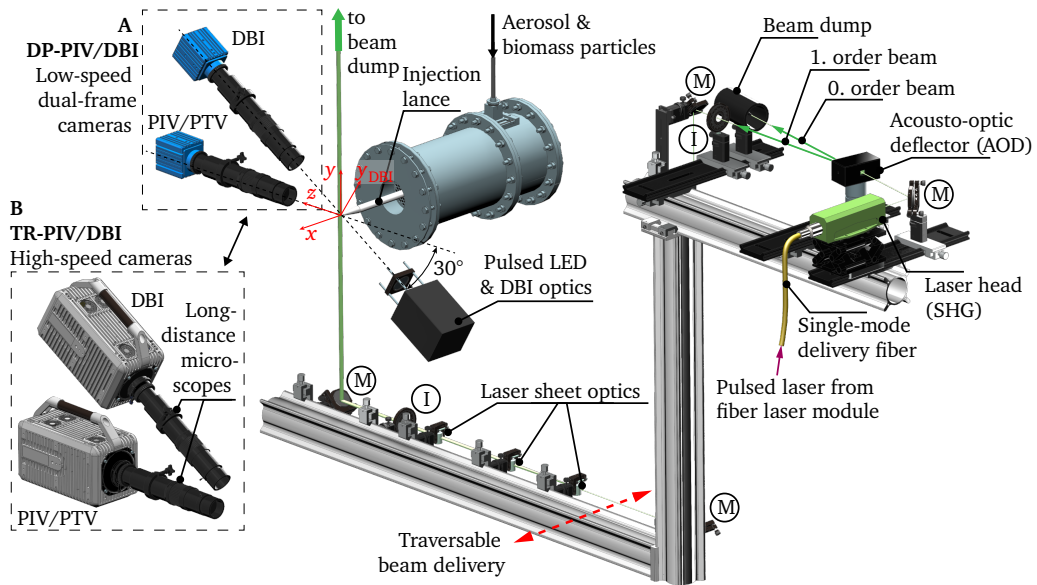

Figure 3.8: Experimental setup and optical beam path. Cameras include the low-speed dual-pulse system **A** and high-speed system **B** for TR-PIV measurements. Mirrors (M) and irises (I) are highlighted. (Adapted from [2])

Two camera systems, referred to as system **A** and system **B**, were utilized. System **A** consists of two low-speed dual-frame cameras operating at 25 Hz, providing a FOV of 12.84×10.83 mm². On the other hand, system **B** utilizes two high-speed cameras running at 200 kHz, with a cropped FOV of 3.8×1.1 mm² (equivalent to 384×112 px²). For the two-phase PIV measurements, one camera from each system was used, while the other camera faced a pulsed light-emitting diode (LED) for DBI imaging. To prevent spectral overlap, a temporal separation was implemented between LED and laser pulses. The DBI FOV was inclined at an angle of 30° to the PIV FOV, ensuring the axial coordinate alignment during calibration. For the high-speed TR-PIV measurements, laser, LED, and cameras were synchronized to run simultaneously, while the AOD pulse picking approach was adopted for low-speed DP-PIV measurements at a laser repetition rate of 312.5 kHz (equal to an inter-pulse time of 3.2 µs).

Results and discussion

The processing of PIV and DBI images involved several steps. Figure 4 in **Paper II** (A.2) [2] presents image recordings of miscanthus particles captured in both low-speed and high-speed systems. Two-phase PIV recordings were separated into tracer and biomass images using threshold-based binarization. While the fluid velocity field was determined using a standard multi-pass PIV algorithm, biomass particle velocities were derived based on their centroid movement. Biomass particles in DBI recordings were identified based on the attenuation of the background signal following a matching with large particles in PIV images. Subsequent parameter extraction from DBI images included the circle-equivalent diameter, ´as well as the orientation and aspect ratio of a fitted ellipse.

While the single-phase flow field could be determined using the AOD pulse picking approach (as shown in Fig. 5 of **Paper II** [2] in appendix A.2), the multi-parameter measurement of a miscanthus particle is further analyzed as shown in Fig. 3.9 for the ultra-high speed system **B**. Here, a TR-PIV FOV positioned at $x/D \approx 8$ in the intermediate region of the turbulent jet is chosen, as this region is characterized by merging shear layers, leading to increased turbulence levels along the centerline. Due to the high Stokes number of the investigated biomass particles, a significant slip velocity is expected.

The velocity fields (Fig. 3.9(a)) illustrate a miscanthus particle moving through a region of decreasing fluid velocity and high turbulence at two selected time points, along with corresponding slip velocity fields (Fig. 3.9(b)). Most slip velocity vectors point left, indicating that the axial particle velocity surpasses the axial fluid velocity, resulting in a wake on the lee side of the particle. As the jet develops spatially, the average axial velocity of the particle reduces less drastically than that of the carrier phase, as expected. The flow structure's temporal evolution around the particle is assessed using the particle Reynolds number Re_p (Fig. 3.9(e)). Re_p increases from 80 to nearly 300 with an increase in the slip velocity magnitude. A comparison with $\mathrm{Re}_{p,\langle u \rangle}$, calculated using pseudo slip $|\langle \vec{u} \rangle - \vec{u}_p|$ from single-phase pulse picking PIV measurements, reveals a significant discrepancy, emphasizing the necessity of multi-phase velocimetry for accurately determining particle-flow interaction. Furthermore, the particle orientation ϕ decreases over time (Fig. 3.9(c,d,f)), leading to reduced drag and possibly decreased turbulence enhancement through vortex shedding. As the particle rotation speed $\dot{\phi}$ remains relatively constant, the alignment of particles with the axial jet coordinate is potentially not maintained after leaving the FOV.

In conclusion, the utilization of the ultra-high repetition rate diagnostics system has offered a valuable means to observe the dynamics of micrometer-sized particles in turbulent flows with exceptional spatio-temporal resolutions. The successful integration of the ultra-high repetition rate pulsed fiber laser with an appropriate pulse picking system has resulted in a highly versatile dual-pulse and time-resolved PIV measurement system, applicable in both single- and multi-phase environments. By employing a simultaneously running DBI imaging system to determine slip velocity, particle diameter, and orientation, a detailed temporal analysis of the particle Reynolds number for aspherical miscanthus particles dispersed within a high-velocity turbulent jet was enabled. These findings underscore
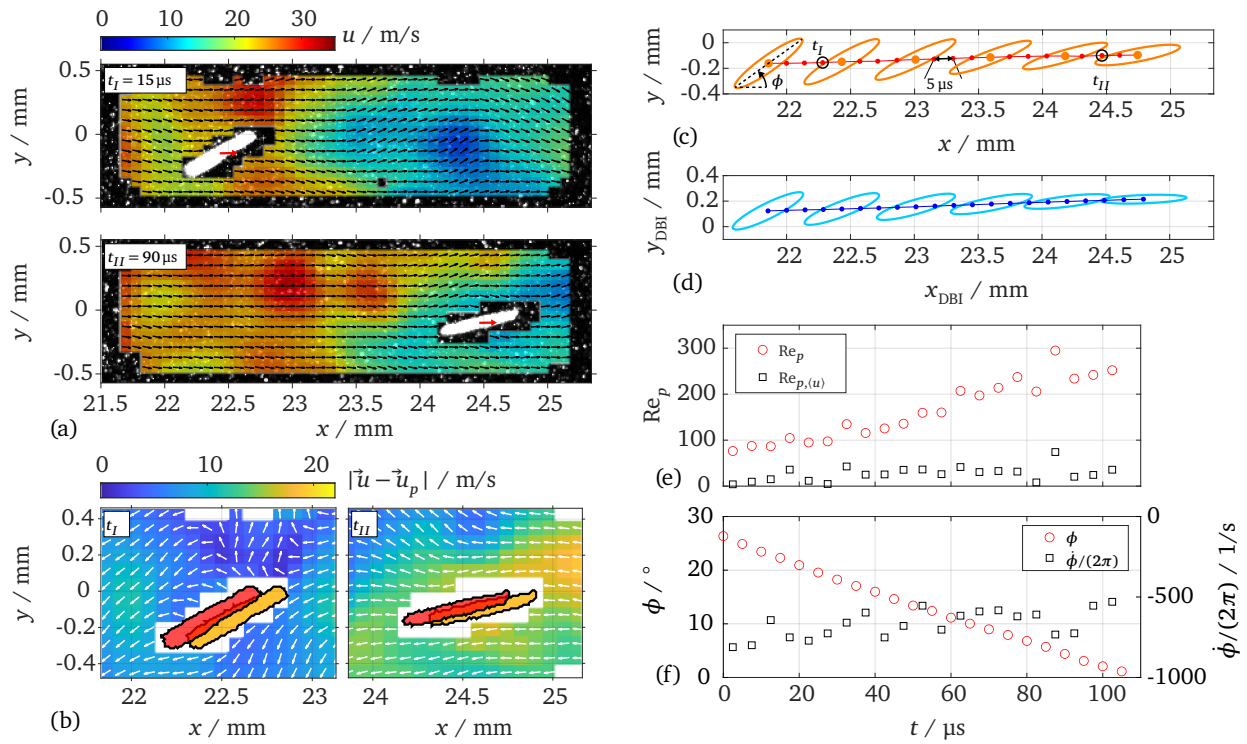
Figure 3.9: Multi-parameter measurement of a miscanthus particle passing through the intermediate region of the turbulent jet including depictions of (a) velocity fields, (b) slip velocity fields, (c,d) ellipse fits of the solid fuel particle for PIV and DBI images, and (e,f) a time-resolved evaluation of particle Reynolds numbers and rotation behavior. (Adapted from [2])

the significance of ultra-high repetition rates in enhancing the understanding of particle dynamics within turbulent flows and present new avenues for studying multi-phase systems in a wide range of engineering applications.

4 Group combustion of solid fuel particles in laminar environments

4.1 Aim and state of research

This chapter focuses on investigating particle group combustion (PGC) in a laminar flow reactor (LFR) using advanced optical diagnostics. A recent review paper [39], authored together with Dr.-Ing. Tao Li with whom this study was collaboratively conducted, covers various experimental setups and methodical approaches utilized by researchers when exploring PGC, comprehensively showcasing the current state of research. As previously introduced in Section 2.1.3, solid fuel combustion studies can be broadly categorized into two types: single particle combustion (SPC) and particle group combustion (PGC), which takes into account the impact of particle-particle interactions on flame characteristics. **Paper III** [3] specifically examines the dynamics of particle group combustion in a well-controlled LFR environment, leveraging state-of-the-art optical techniques to gain deeper insights into the underlying processes.

In the realm of test stand environments, literature features experiments conducted in both drop-tube furnaces (DTFs) and LFRs, with the latter offering improved accessibility for optical measurements [39]. Some studies have utilized cost-effective digital single-lens reflex (DSLR) cameras to record color images of PGC or perform pyrometric temperature measurements [102, 103]. However, these techniques posed challenges in obtaining precise temperature information, particularly for bituminous coal, and in distinguishing between particle surface temperature and soot particle temperature in groups of combusting particles. Recently, the transition from single to group combustion in the LFR was characterized using particle temperature measurements and probe sampling via a two-color pyrometry system with simultaneous shadow imaging [104]. Other approaches involve employing chemiluminescence imaging with spectral filters and broad-band thermal radiation detection to explore particle cloud flames [102, 105–109]. Additionally, digital in-line holography has been used for particle size and 3D position measurements of pulverized coal flames [110].

OH-PLIF has proven effective in accurately detecting the volatile flame surrounding solid fuel particles during homogeneous combustion, as demonstrated for single solid fuel particles [72] with high spatial resolutions. Balusamy and colleagues carried out flow field measurements [92] followed by OH-PLIF, Mie scattering, and laser-induced incandescence (LII) measurements to assess soot within a swirling coal flame [111]. Xu et al. recently employed OH-PLIF to investigate the effects of ambient temperature and oxygen content on the volatile combustion of coal particle streams in a Hencken-type burner. However, unlike the SPC scenario, the combustion of a group of particles requires multi-dimensional diagnostics, necessitating an extension beyond the planar approach.

Recent progress in high-speed volumetric LIF measurements of OH radicals has allowed for the 3D reconstruction of volatile flames and a detailed analysis of PGC flame topology [112]. Combining this technique with instantaneous PND measurements using DBI, ignition and flame extinction characteristics were investigated in an N_2/O_2 atmosphere with 10 vol% O_2 [40]. To achieve a deeper understanding of solid fuel combustion, multiple essential quantities need to be acquired in situ with high spatio-temporal resolutions. Building upon previous experiments [40, 112], **Paper III** extends the investigation to different environments, including air (AIR) and oxy-fuel (OXY) atmospheres with varying O_2 content. The focus lies in exploring PGC of solid fuels, employing simultaneous DBI, 3D

OH-LIF, and Mie scattering measurements. Additionally, addressing an open question from the previous study [40] regarding the transition from SPC to PGC, a DBI imaging simulation tool was developed and applied to the current data to assess measurement errors of PND. To summarize, the present chapter covers the following objectives explored in **Paper III** [3] (see Section A.3):

- Development of a novel diffuse back-illumination (DBI) imaging simulation tool to quantify PND measurement errors within an idealized environment. Subsequent application of the tool to experimental data obtained from the multi-parameter measurement system.

- Investigation of the impact of PND and surrounding gas atmosphere (specifically O_2 content and diluent composition) on volatile combustion and soot formation dynamics of a particle group composed of bituminous coal in a well characterized laminar flow reactor (LFR).

4.2 Experimental setup

Multiparameter experiments were conducted in the laminar flow reactor (LFR) depicted in Fig. 4.1. A ceramic honeycomb structure was used to stabilize a premixed flat flame, and particles were introduced through a central tube via carrier gases of different composition. To investigate PGC, a larger particle injection tube with a 2.9 mm inner diameter replaced the previous 0.8 mm jet in [40], enabling higher solid particle flow rates. The LFR allowed for operation in N_2/O_2 and CO_2/O_2 atmospheres with varying post-flame O_2 content ranging from 10–40 vol% O_2 (AIR10 to AIR40 and OXY20 to OXY40). Measurements were conducted with Colombian high-volatile bituminous coal particles of diameter 106–125 μm and different PNDs. Details of each atmosphere, including equivalence ratios and gas temperature profiles, are described in [113], while proximate and ultimate analyses of the fuel particles are reported in [114]. Three simultaneously running optical diagnostics systems were used, whose FOVs are shown in Fig. 4.1. Further information on technical details is available in **Paper III** in Section A.3.
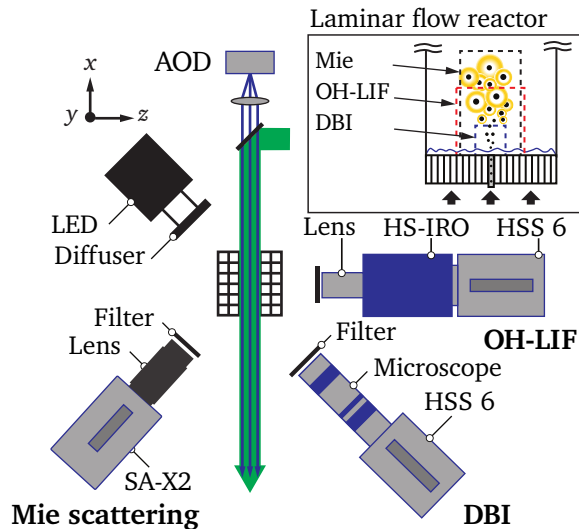

Figure 4.1: Experimental setup of multi-parameter diagnostics for PGC in a LFR. (Adapted from [3])

Scanning OH-LIF was conducted for volatile flame visualization using a 10 kHz dye laser, tuned to 283.01 nm to excite the $Q_1(6)$ transition of the $A^2\Sigma^+$ ($v' = 1$) $\leftarrow X^2\Pi$ ($v'' = 0$) system. The laser beam was scanned at 1 kHz frequency using an AOD, and then parallelized through laser sheet optics, resulting in 10 individual scan positions, similar to [40]. The laser sheets had a thickness of 130 μm, and the scan planes were at an average distance of 420 μm from each other. Fluorescence was detected

using a CMOS camera, combined with a high-speed intensifier and a band-pass filter, with a recorded projected pixel size of 32.4 μm/px in the imaged scanning planes.

For measuring PND, a high-speed **diffuse back-illumination (DBI)** system was utilized with a high-power LED operating at 1 kHz with a pulse duration of 1 μs. The LED pulses were triggered in the middle of each OH-LIF scan cycle for synchronization. A CMOS camera equipped with a long-distance microscope captured particle shadow images with a projected pixel size of 9.2 μm. To eliminate signals from flame luminosity, a band-pass filter was chosen to match the LED emission spectrum.

Mie scattering measurements of solid and soot particles were conducted using a DPSS Nd:YAG laser operating at 10 kHz, triggered with a time offset of 5 μs relative to the OH-LIF measurements. The laser was combined with the dye laser for OH-LIF using a dichroic mirror and aligned with the burner centerline. The forward Mie scattering was captured by a CMOS camera with an exposure time of 5 μs and a projected pixel size of 36.8 μm. To suppress interference signals from luminescent particle flames, a band-pass filter was applied to the camera.

4.3 Error estimation of DBI-based PND measurements

An accurate measurement of the particle number density (PND) is crucial for capturing the transition from SPC to PGC during volatile combustion. As explained in Section 2.1.2, PND can be determined by considering the number of particles N_p within a domain volume V_d (or V_{jet}) as was demonstrated in [40]. In this study, N_p was extracted from binarized DBI images and ranges from 1 to 250 particles per frame. The mean volume V_{jet} was computed from the projected particle jet boundary with the assumption of rotational symmetry. Both parameters are inherently associated with measurement errors, which have to be investigated.

First, a sensitivity study of the influence of N_p on V_{jet} was performed. Single and normalized mean images in split view are shown for selected N_p and corresponding particle ranges of $N_p = 51 - 100$ and $N_p = 151 - 200$ in Figure 4.2(a,b). The 2D particle residence boundaries (yellow dashed lines) are determined using a fixed threshold of 0.95 for each range of N_p. The overall mean boundary (red solid line) is obtained by including all N_p values. Comparing both boundaries, a slight expansion of the width of the particle residence area, driven by increasing volatile release and thermal expansion within the flame, is observed for rising values of N_p. As can be observed in Figure 4.2(c), PND is only minimally affected by the choice of a domain based on N_p (V_{bin}) compared to the global jet V_{glob}, which was subsequently chosen for PND determination. Comparing these curves to the one of Li et al. 2021 [40] with a jet diameter of 0.8 mm but similar particle sizes shows a steeper slope due to the smaller residence volume of the old jet, emphasizing that direct comparison of PND values is difficult for varying burner configurations to quantify particle interaction.

To determine the measurement error of N_p using the DBI system, a synthetic imaging tool was developed in MATLAB and applied to the current data. Figure 4.3(a) displays the 3D domain derived from the experimental boundary (dashed red lines) into which an exemplary number of 200 ellipsoids of random aspect ratios in a range of 1-2 and the given sieving size range were randomly positioned. The Gilbert-Johnson-Keerthi algorithm was used to detect particle-domain and particle-particle collisions [115], which is applicable to investigate convex bodies. Therefore, the concave 3D domain is separated into convex pieces, which are individually used for collision detection with convex particles. Subsequently, particle images were generated through projection and pixelation as shown in Figure 4.3(b,c) resulting in overlapping particle shapes caused by the line-of-sight nature of the DBI method. The synthetic images were post-processed using the identical particle recognition algorithm than the real images. Figure 4.2(d) displays the results of an extensive parameter variation of $N_{p,3D}$ resulting in an increasing underestimation of imaged particles $N_{p,proj}$. However, considering that $N_{p,proj}$ is mostly smaller than 200 in the experiment, the error in PND calculation remains below 15% due to particle
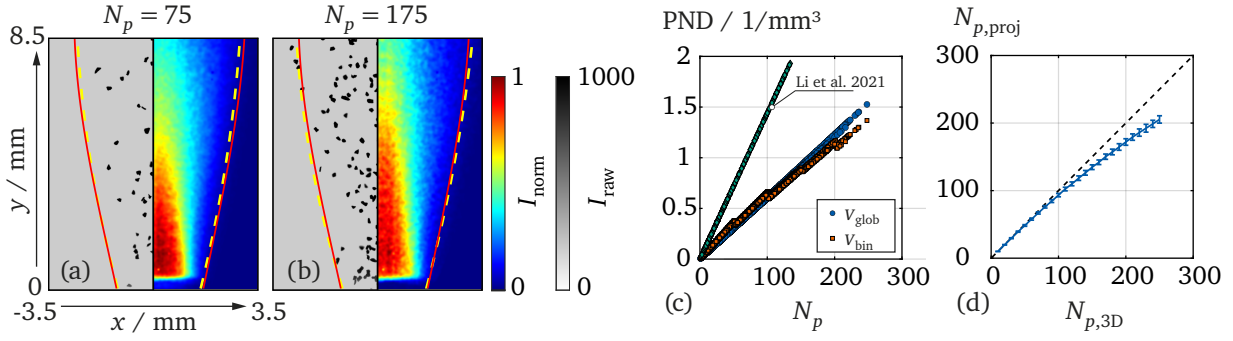
Figure 4.2: (a,b) DBI raw and normalized mean images for different N_p. (c) PND with respect to N_p for different V_{jet} and compared to [40]. (d) Relationship of real particle number $N_{p,3D}$ and $N_{p,proj}$ after considering projection and pixelation using synthetic images.

overlap. To improve accuracy in dense particle clouds, tomographic particle tracking velocimetry is highly desirable to resolve 3D particle locations in the future. Alternatively, a statistical correction of PND could be performed using correction factors derived from the presented imaging simulations.
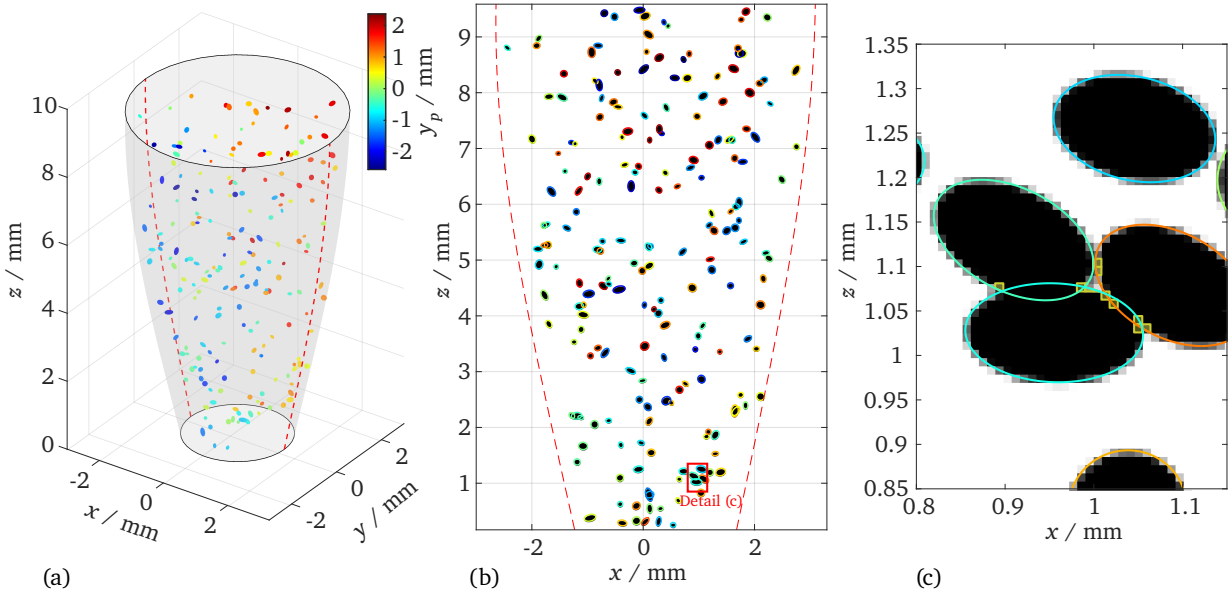

Figure 4.3: Synthetic DBI image creation by (a) placing ellipsoidal particles into a 3D domain and (b,c) subsequently projecting the outlines (colored curves) onto an artificial imaging sensor followed by pixel discretization. Yellow polygons in (c) signify particle boundary pixels affected by multiple particles demanding local refinement.

4.4 Results and discussion

Additionally to PND, mean particle velocities were derived from DBI images using a standard PIV algorithm and are displayed for different PNDs in Fig. 4 in **Paper III** (see Section A.3). The axial particle velocity decreases with increasing PNDs, which is consistent with previous investigations [40]. This causes a longer particle residence time in the LFR at increasing particle concentrations. Besides, the axial particle velocity is higher in AIR than in OXY atmospheres due to the higher fluid velocities for these atmospheres determined in previous works [113].

The scanning OH-LIF images were intensity-corrected and linearly interpolated to generate 3D volatile flame structures. Results of this procedure are exemplarily shown for different O_2 contents at a similar PND in Fig. 5 in **Paper III** (see Section A.3), where non-flammable regions in the fuel-rich central region of the particle flame disappear with increasing oxygen availability. Again, this result is consistent with previous experimental [40] and a corresponding numerical investigation [116], showing that local gas temperature and fuel-air ratio are responsible for non-flammability within the central region of PGC volatile flames of a particle jet. As PND is kept constant, the local gas temperature, mainly decreasing through particle heating, should be similar, emphasizing the effect of O_2 concentration on flame extinction.

The Mie scattering images show both coal and soot particles, which can be easily distinguished from another by the size and intensity differences as shown in Fig. 6 of **Paper III** (see Section A.3), where instantaneous images are compared at a constant PND for varying O_2 content. Lower O_2 concentrations exhibit intensive soot formation, which can be explained by the promotion of soot through emerging polycyclic aromatic hydrocarbons (PAHs) created from lighter hydrocarbon molecules or directly released as volatile matter [117]. Conversely, increasing the O_2 availability causes a dramatic reduction of soot formation. This observation is similarly confirmed in PND-conditioned mean isocontour images of Mie scattering and OH-PLIF for varying O_2 concentrations, displayed in Fig. 7 of **Paper III** (see Section A.3), where increasing soot formation is correlated with appearing flame extinction. The same trends are also applicable to OXY atmospheres shown in Fig. 9 of **Paper III** (see Section A.3).

Using the same split view, Fig. 4.4(a-d) shows results for atmosphere AIR20 with increasing PND (number under atmosphere). Similar to the previously discussed effects of O_2 content and in line with [40], a non-flammable region surrounded by a reaction zone grows in size with rising PND. However, as more particles are injected into the flue gases of the flat flame, increasing devolatilization rates push the reaction further outward and downward, actually causing a reduction of the lift-off height. This observation could be explained by both the decreasing particle velocities at higher PND and the Bunsen-like shape of the pilot flame caused by the increased jet diameter. Additionally, strong soot formation might cause radiative heat transfer to enhance preheating and earlier devolatilization of solid fuel particles at high number densities. As a frame of reference, Fig. 4.4(e,f) again shows the previously discussed influence of O_2 content at constant PND.
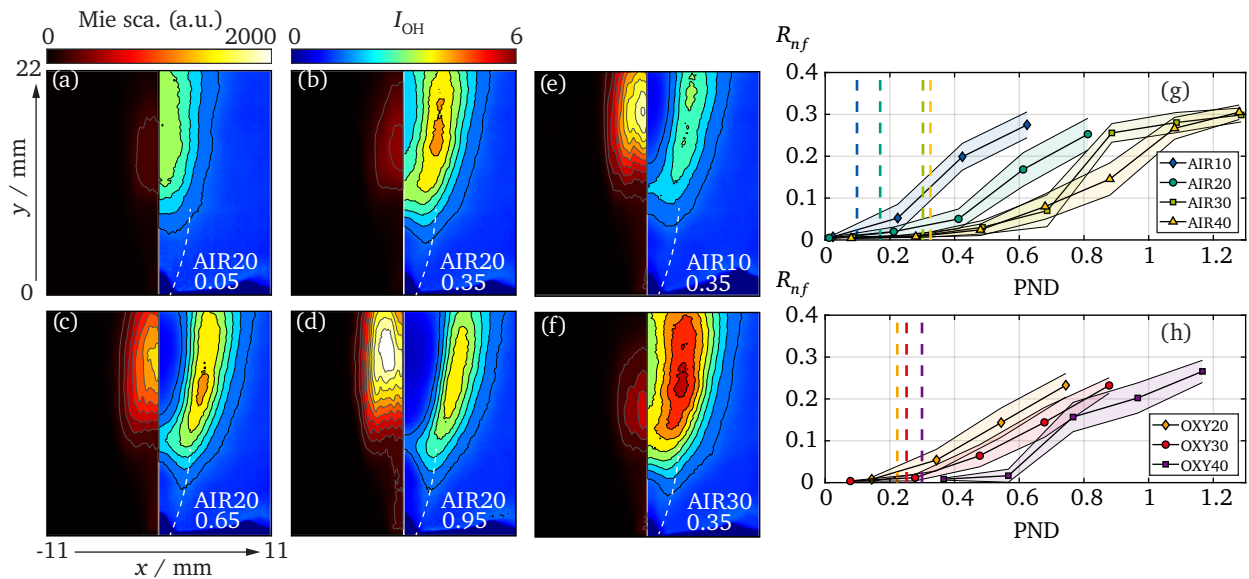

Figure 4.4: (a-f) Mean Mie scattering and OH-PLIF images for group combustion of goal particles in various atmospheres at multiple PNDs. (g,h) Non-flammability ratio R_{nf} as a function of PND.

To evaluate the combined effects of O_2 content, PND and diluent composition on volatile flame topology of PGC, Fig. 4.4(g,h) displays the non-flammability ratio $R_{nf} = V_{nf}/(V_f + V_{nf})$ determined from 3D volatile flame structures, where V_{nf} is the volume of the non-flammable core and V_f is the volume of the reaction zone, determined by areas exceeding a fixed threshold of 1.4 with respect to the background-normalized OH-LIF signal intensity (similar to [40]). Dashed lines highlight the mean PND of each gas composition, at which no flame extinction was detectable, representing a transition limit from weak to strong inter-particle interaction.

As can be observed, decreasing O_2 contents and increasing PNDs are correlated with increasing values of R_{nf}, promoting non-flammable region within the volatile flame. However, a comparison of AIR and OXY atmospheres yields similar results, signifying a negligible influence of diluent composition for PGC in this study. As outlined in Section 2.1.3, amongst several influences, two main effects have to be considered to explain this behavior. On the one hand, the lower diffusivity of O_2 in CO_2 compared to N_2 should cause an earlier onset of oxygen depletion causing flame extinction. On the other hand, the heat sink (ρc_p) of CO_2 is significantly higher than that of N_2, resulting in a higher amount of heat stored in the same volume. As the different atmospheres in the LFR exhibit similar gas temperatures [113], it is expected that the heating of a similar amount of particles results in lower temperatures for AIR atmospheres than OXY atmospheres, similar to the observations made for earlier ignition delay of single particles in OXY atmospheres in [113]. The competition of both of these effects in PGC seems to balance out as suggested by the similar correlation of PND and R_{nf} for AIR and OXY atmospheres.

In summary, this experimental multi-parameter study revealed new insights into the transition from SPC to PGC by utilizing conditioned statistics to address the influence of PND, O_2 content, and diluent composition on the volatile flame topology and soot formation. To estimate the measurement errors introduced through the line-of-sight nature of the DBI-based determination of PND, synthetic images were generated in a newly developed simulation tool, which made direct use of the experimental data generated in this study. Main results include the suppression of soot formation by rising O_2 concentrations, also promoting the reactivity of the volatile consumption. Similar to a previous study [40], rising PNDs lead to increasing flame extinction quantified by the non-flammability ratio R_{nf} computed from 3D volatile flame structures. Finally, the effect of CO_2 replacement was found to have a negligible influence on the flame topology and soot formation, which was explained by the competing effects of decreased oxygen diffusivity and higher heat sink of CO_2 compared to N_2.

5 Optical diagnostics of flame retarded polymers

5.1 Outline and state of research

This chapter highlights the advancements in optical diagnostics applied to flame retarded polymers. As mentioned in Section 2.1.4, the widespread use of polymers necessitates tailored flame retardant solutions, driving fundamental research on the impact of flame retardant additives on polymer combustion under various test conditions. Flame retardants are classified based on their mode of action into condensed-phase active, gas-phase active, and endothermically decomposing substances. The focus of the works presented in this thesis is primarily on gas-phase inhibition during combustion. Considering the previously discussed topics of carbonaceous solid fuel combustion, the combustion of flame retarded polymers adds another layer of complexity as it involves active flame inhibition within a reactive multi-phase system. As will be demonstrated, this research explores similar methodological approaches originating from solid fuel combustion research to investigate these phenomena.

Extensive research has been devoted to investigating the inhibitory effect of gas-phase active flame retardants in canonical hydrocarbon flames without a present polymer specimen. Experimental configurations, such as spherically expanding flames [118] or opposed-jet flames [119–123] have been employed to assess the impact of flame retardants, complemented by numerical studies [124]. The effectiveness of gas-phase active flame retardants strongly depends on the specific flame type utilized, underscoring the significance of exploring various canonical and complex burner setups [125]. Additionally, in situ studies of flame retarded polymer combustion are essential for gaining insight into the polymers' influence on pyrolysis and combustion processes [126–129].

A wide range of diagnostic methods are available to assess the gas-phase effectiveness of flame retardants, each with varying applicability to realistic fire conditions and precision of measured parameters [50]. Chemical analyses, including thermogravimetric analysis coupled with Fourier transform infrared spectrometry (TG-FTIR), thermodesorption mass spectrometry (TDMS), thermogravimetric analysis coupled with mass spectrometry (TG-MS), and pyrolysis gas chromatography with mass spectrometry coupling (Py-GCMS), are commonly used to provide detailed information on species relative to decomposition temperature [50, 130, 131]. However, these decomposition analyses are typically performed at lower heating rates than those experienced by samples in combustion systems. For studying physicochemical phenomena during polymer combustion and evaluating flame retardant inhibition, chemically active radical measurement methods such as molecular beam mass spectrometry (MBMS) [132], vacuum ultraviolet photoionization (VUV) [133], and OH-LIF (limited to inhibited gas flames) have been employed [119–121, 123]. While probe-based methods like MBMS provide detailed knowledge of the chemistry within a flame, their intrusive nature can be a drawback, which is not present in optical methods like LIF. The research presented in this thesis aims to extend the application of OH-LIF to study the combustion of flame retarded polymer specimens, an area that has not been explored before.

With the objective of studying flame retarded polymers in situ, **Paper IV** [4] focuses on OH-PLIF of polymer particles blended with a well-known gas-phase active flame retardant, utilizing the laminar flow reactor (LFR) introduced in Section 4. This method, previously demonstrated for the ignition and volatile combustion of coal particles [72], is adapted to analyze the gas-phase combustion of pyrolyzing polymer particles. The investigation centers on the thermoplastic polymer polypropylene (PP) due to

its simple chemical structure and widespread use in commodity plastics. Building on the successful application of OH-PLIF to flame retarded PP, **Paper V** [5] extends the experimental setup to a multi-parameter optical diagnostics system, exploring three additional flame retardants in both particle and stick-shaped PP specimens. Both papers include chemical decomposition analyses to comprehensively understand the flame inhibition effects on polypropylene combustion.

5.2 In situ OH-PLIF of flame retarded polypropylene particles

5.2.1 Aim

Paper IV [4] investigates the combustion behavior of micrometer-sized PP particles in the presence of the phosphorus-containing flame retardant pentaerythritol spirobis(methylphosphonate) (PSMP). By employing high-speed planar laser-induced fluorescence of the OH radical (OH-PLIF) and conducting thermal decomposition analysis, the study aims to gain comprehensive insights into the flame retardant's pyrolysis fragments and their impact on the combustion process. The analysis of pyrolysis fragments was performed by Dr. Daniela Goedderz, and her doctoral thesis [49] encompasses the findings of **Paper IV**. Individual contributions of each author are listed in Section B. The publication addresses the following scientific aims:

- The decomposition products released from the flame retardant during combustion are obtained and potential radical scavengers, influencing the combustion process through flame poisoning, are identified.

- The ignition and combustion of single particles is temporally tracked by OH-PLIF and relevant parameters of the spherical flame are extracted. Based on this, the changes induced by the flame retardant on the diffusion flame surrounding the particles is analyzed.

5.2.2 Materials and experimental setup

The particles used in this study were produced through compounding PP and PSMP with a co-rotating twin-screw extruder. Pelletization and grinding resulted in particle diameters ranging from 100–150 µm. The research focused on two specimens: neat PP and a flame retarded formulation containing 10 wt% of PSMP. PSMP is a well-known phosphorus-containing flame retardant for polypropylene applications, whose gas-phase activity has been the subject of some earlier studies [134, 135]. The chemical structures of polymer and flame retardant are shown in Fig. 5.3 in Section 5.3. The details of the thermal decomposition analysis conducted in **Paper IV** can be found in Section 2.2 of the original publication (see Section A.4). Additionally, cone calorimetry as a standard procedure in polymer combustion testing was performed.

Particle combustion studies using OH-PLIF were conducted within the laminar flow reactor (LFR) introduced in Section 4.2 to visualize reaction zones surrounding neat and flame retarded PP particles. The experimental setup shown in Fig. 4 of **Paper IV** (see Section A.4) utilized a fully premixed flat flame with an excess oxygen content in the flue gas of 10 vol% (atmosphere AIR10 described in [113]). The same dye laser system, line transition for OH-LIF, and high-speed intensified CMOS camera recording images at 10 kHz were utilized as in **Paper III** (see Section 4.2). Traversing the burner height position provided two FOVs for investigation. The obtained pixel resolution of OH-PLIF images was 24.6 µm/px, and the optical resolution measured with a Siemens star was 100 µm.

5.2.3 Results and discussion

Following shot-to-shot background correction and normalization of the OH-PLIF images to eliminate the effects of pulse energy fluctuations and the ultraviolet (UV) laser sheet's inhomogeneous beam profile, relevant parameters of the spherical diffusion flame were extracted during particle image post-processing. Fig. 5.1 displays the corrected OH-LIF images and corresponding radially averaged OH-LIF intensity profiles for selected PP particles. As particles ascend, released pyrolysis products ignite and combust in the diffusion flame, leading to an observable increase in the OH-LIF intensity surrounding the particle. To ensure accurate analysis, only particles centrally hit by the UV laser sheet were included, as indicated by the shadow cast on the left side of the particles. This approach guarantees proper assessment of the flame stand-off distance and prevents underestimation. From the radial intensity profile, two parameters were extracted for analysis: the radius of peak reactivity rate r_{PRR} (defined at the position of the highest positive gradient of the LIF signal) and the peak intensity value in the flame $I_{max,OH}$.
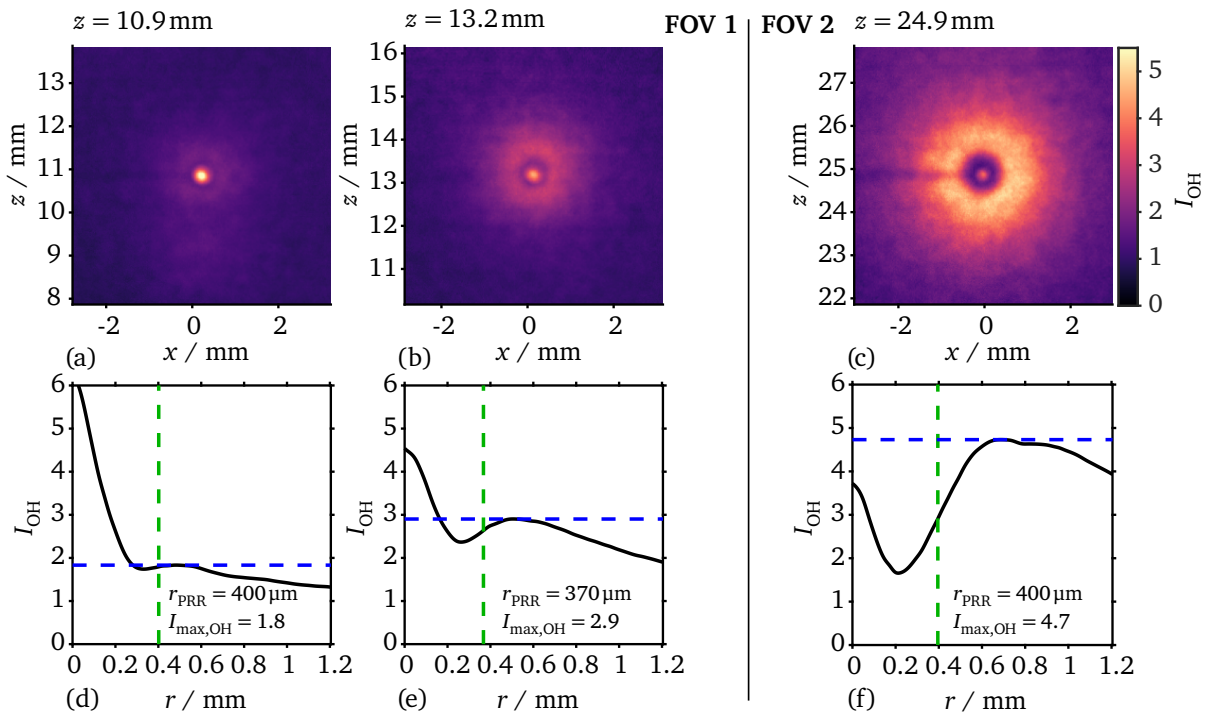

Figure 5.1: Evolution of the ignition and combustion of exemplary PP particles at increasing centroid positions z tracked by OH-PLIF including corresponding radial profiles of the normalized OH signal intensity $I_{OH,norm}$. (Adapted from [4])

Extending the analysis to multiple particles, 10 neat PP and 18 PP particles flame retarded with PSMP were studied. The evolution of r_{PRR} and $I_{max,OH}$ was analyzed for various heights above the burner head, as shown in Fig. 5.2. Each data point represents a value extracted from a single OH-PLIF image, and for clarity, individual points of a single particle are connected by lines in Fig. 5.2(b).

The results indicate that the flame retarded polymer had larger average values of r_{PRR} compared to neat PP. At $z = 28\,mm$, r_{PRR} was $373\,\mu m$ for PP and $427\,\mu m$ for PP + $10\,wt\%$ PSMP, respectively. This distinction remained consistent across most axial positions, indicating that the outgassing flame retardant influenced the radial position from the beginning of ignition. As the combustion process progressed, the outgassing decomposition products pushed the diffusion flame outward, until both curves coincided at $z = 30\,mm$. The TDMS experiments performed with the same samples revealed that the
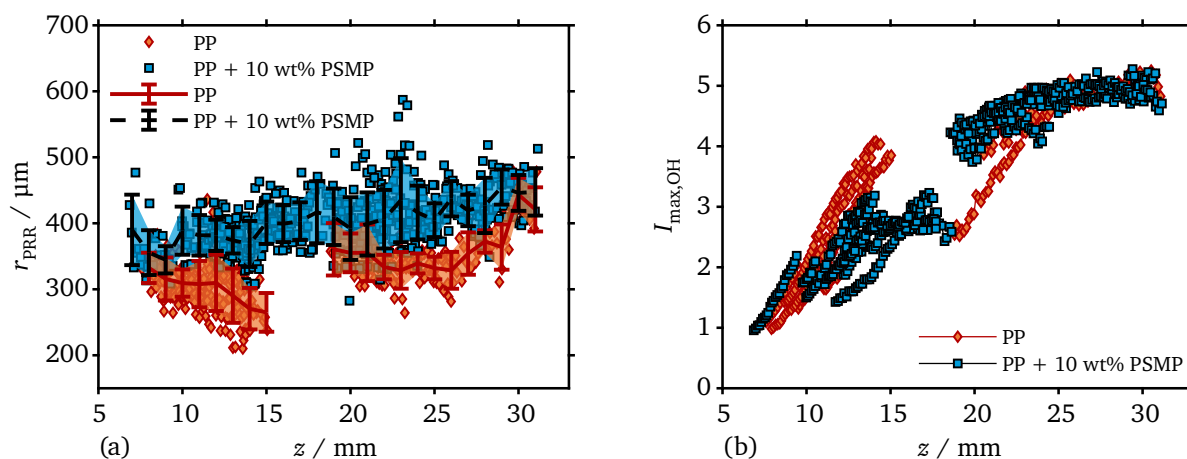
Figure 5.2: (a) Radius of peak reactivity rate and (b) normalized peak OH-LIF signal within the diffusion flame including neat PP and PP + 10 wt% PSMP for different positions above the burner head. (Adapted from [4])

major part of the flame retardant's decomposition fragments was released before the decomposition of PP, possibly explaining this observation.

The evolution of $I_{max,OH}$ shows an apparent retardation of the ignition process. Neat PP particles reached an $I_{max,OH}$ of around 4 at $z = 14\,mm$, whereas the flame retarded PP particles only achieved an $I_{max,OH}$ of 3 at the same height, indicating the gas-phase activity of the PSMP fragments. However, a large scattering of values is detectable, which could be potentially caused by agglomerations or particle size deviations. Beyond $z = 20\,mm$, both compounds showed a similar evolution of $I_{max,OH}$, approaching a value of 5 indicative of a fully developed diffusion flame where flame inhibition was not noticeable. Nevertheless, flame retardant fragments might still be present in the fuel-rich gap between the reaction zone and particle. TDMS experiments suggested that the flame retardant fragments were still evolving through a detectable pyrolysis process.

In conclusion, the study demonstrated the influence of the flame retardant PSMP on the combustion process of PP particles, with flame retardant particles showing larger radial positions and a delayed ignition process successfully detected by OH-PLIF. Corresponding thermal decomposition analyses showed that the thermal decomposition of PSMP produced radical scavenging fragments confirming its gas-phase activity. However, as the particle diameter was not measured simultaneously, it is not clear whether these trends change with particle size motivating the need for a simultaneous determination of flame and particle size in a subsequent study.

5.3 Optical multi-parameter diagnostics of flame retarded PP particles and specimens

5.3.1 Aim

Following the introduction of OH-PLIF for in situ combustion analysis of flame retarded polymer particles, **Paper V** [5] extends the previous study by incorporating OH-PLIF measurements of PP samples with three additional flame retardants. An adapted diagnostic setup served as a multi-parameter measurement system. To enhance statistical significance, an AOD laser scanner was employed to increase the number of particles centrally hit by the UV laser sheet. Simultaneous particle size measurements using DBI generated size-selective statistics, improving comparability among different samples. Four

flame retardants were mixed in PP at a fixed concentration of 10 wt%, ensuring an identical amount of combustible polymer. The selected flame retardants exhibit different fire behaviors and modes of action. In summary, this publication addresses the following scientific analyses:

- An OH-PLIF analysis of flame retardants with different modes of action added to PP particles was performed with a special focus on the detection gas-phase activity.

- The low statistics and lack of in-situ particle diameter measurement of **Paper IV** were addressed by improving and extending the optical diagnostics setup.

- The high heating rates in the laminar flow reactor may not represent real fire scenarios. Therefore, the interaction of a premixed flame with a larger polymer slab containing the same chemical formulations as the particles was also investigated using optical diagnostics.

5.3.2 Materials and methodology

Four different flame retardants, including PSMP, zinc diethylphosphinate (DEPZn), aluminum trihydroxide (ATH), and ammonium polyphosphate (APP), were mixed with PP at a fixed concentration of 10 wt%. These flame retardants were chosen for their diverse fire behavior and mode of action. PSMP and DEPZn are known for their gas-phase activity, releasing phosphorus-containing radicals in different polymers [4, 136]. In contrast, ATH and APP act as condensed-phase flame retardants, promoting char formation by reacting to aluminum oxide or polyphosphoric acid while releasing water vapor or ammonia in the gas phase [137, 138]. The endothermic decomposition of ATH into water additionally provides local cooling and dilution.

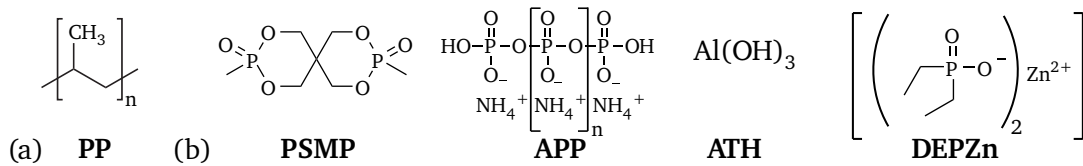(a) **PP**   (b) **PSMP**   **APP**   **ATH**   **DEPZn**

Figure 5.3: Chemical compounds of PP and investigated flame retardants. (Adapted from [5])

Following the procedures outlined in **Paper IV**, flame retarded PP composites were manufactured by extrusion with 10 wt% of the respective flame retardant, followed by pelletizing, grinding, and size separation using a vibratory sieve shaker. Standardized samples were subjected to thermogravimetric analysis (TGA) coupled with Fourier-transform infrared spectroscopy (FTIR) and cone calorimeter tests, each performed in triplicate under defined conditions.

Laser-optical combustion experiments were conducted using two setups, shown in Fig. 5.4. The first setup involves the LFR to study polymer particle combustion at high heating rates. The second setup investigates the interaction of a premixed methane flame with a horizontally aligned stick-shaped polymer specimen, measuring $70 \times 10 \times 4\,mm^3$.

The particle combustion experiments in the LFR extended the setup described in **Paper IV** with a larger jet diameter but were conducted at the same atmosphere AIR10. Similar to **Paper III**, the UV laser for OH-PLIF was guided through an AOD, resulting in 10 parallel laser sheets. However, instead of using the scanning approach for three-dimensional reconstructions, it was employed to increase the number of particles centrally hit, ensuring a higher amount of particles for statistical evaluation. To address the lack of particle diameter measurement in **Paper IV**, a DBI system operated at a repetition rate of 10 kHz and a high pixel resolution of 5.2 µm/px for accurate particle size determination. Both OH-PLIF and DBI systems recorded parameters simultaneously, enabling statistical evaluation and selective observation of flame retardation effects, linking properties of the volatile flame to particle
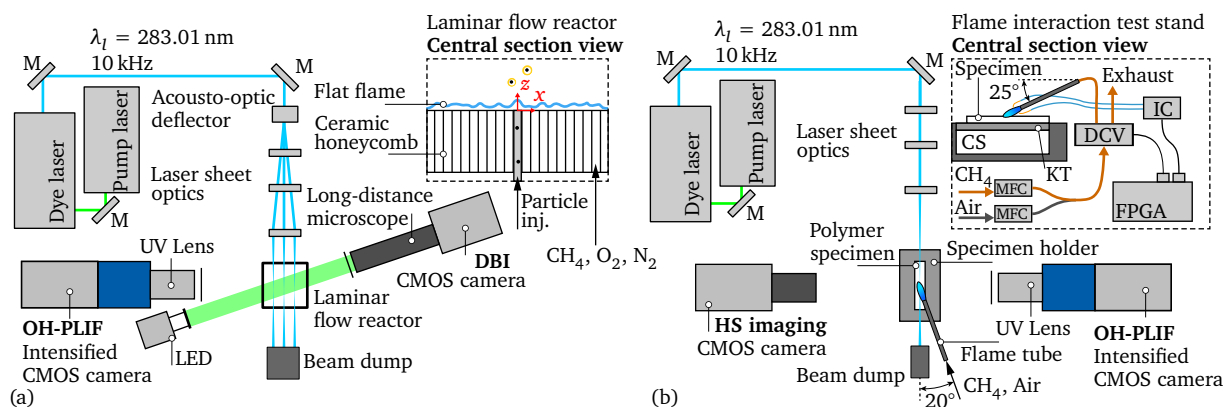
Figure 5.4: Experimental setups of (a) particle combustion experiments in the LFR and (b) the investigation of the interaction of a premixed flame with stick-shaped specimens. Detailed explanations of are found in **Paper V** (see Section A.5). (Adapted from [5])

size. An exemplary multi-parameter measurement of a single PP particle is shown in Fig. 3 of **Paper V** (see Section A.5).

The second experimental setup investigates the combustion of flame retarded polymer sticks in a newly designed flame interaction test stand, where polymer specimens are exposed to a stable premixed methane (CH_4) Bunsen flame. During the testing, high-speed OH-PLIF and luminosity images were captured to observe the combustion process. The test procedure involves precise ignition and extinguishing of the external flame after 60 s of interaction with the polymer specimen. While realistic fire scenarios for burning polymers often involve diffusion flames, using a stable laminar premixed flame with a fixed equivalence ratio provides a controlled and repeatable setup, facilitating comparisons between different polymer specimens. The effectiveness of flame retardants heavily relies on the burner and flame setup [125], especially when dealing with flame retarded polymers, which introduce added complexity due to polymer decomposition. In this context, premixed flames generate higher flue gas temperatures, influencing thermal decomposition and inhibitory processes in both the gas and condensed phases.

5.3.3 Results and discussion

Thermal decomposition analysis

The thermal decomposition analysis mostly confirmed the modes of action, which were previously observed in the literature. Looking at the TGA curves, the lowest residues for both neat flame retardants and flame retarded PP at elevated temperatures were found for PSMP clearly indicating high volatility, whereas the lowest value was detected for APP, which is known to provide flame retardancy through condensed-phase activity. The subsequent TG-FTIR analysis allowed the monitoring of released substances during thermal decomposition, where defined absorption bands indicate the chemical species. Generally, the temperatures at which the flame retardants' decomposition products are released reach higher levels when incorporated into the flame retarded PP composites due to the interplay between the polymer matrix and the flame retardants during pyrolysis.

The thermal decomposition of neat PP is characterized by the release of flammable alkenes starting at a temperature of 378 °C. The chemical decomposition behavior of PSMP was already observed in TG-MS measurements discussed in **Paper IV** [4], where a characteristic aldehyde compound is released and strong gas-phase activity including the formation of the PO radical was confirmed. For APP, the main decomposition product ammonia (NH_3) is tracked in the FTIR measurements. The remaining residue

of 8 wt% shows that the majority of the initial flame retardant forms a non-volatile residue indicating the formation of a char barrier, confirming APP's condensed-phase activity. As expected, ATH's main decomposition product is water with aluminum oxide (Al_2O_3) remaining as a condensed-phase barrier, which shifts the decomposition temperatures of PP + 10 wt% ATH to significantly higher temperatures than those of the neat polymer. DEPZn also provides a delayed pyrolysis of the flame retarded polymer compound with the main decomposition products being ethane (C_2H_6) and phosphinic acid (H_3PO_2). The latter further decomposes into phosphine (PH_3) and phosphoric acid, as was confirmed by MBMS measurements of Lau et al. [132, 139]. It should be noted that both C_2H_6 and PH_3 are flammable gases, which could impede the flame retardation effectivity of DEPZn. Due to its low residue of 35 %, DEPZn is expected to show a gas-phase activity and moderate char yield.

Multi-parameter diagnostics of particle combustion

Next, the particle combustion experiments in the LFR are analyzed under high heating rate conditions. Despite prior sieving of particles, a widely scattered size distribution was measured by DBI, with particles ranging from 80 μm to over 300 μm. These deviations, particularly the presence of agglomerates, are observed, where particles melt, adhere, and fuse during rapid heating in the flat flame. To ensure a meaningful statistical comparison, particles were categorized into three size intervals with cutoff points at $d_{p,1} = 154$ μm and $d_{p,2} = 188$ μm, enabling a reliable assessment of the flame retardant behavior for small, medium, and large particles.

Figure 5.5(a-c) displays the maximum normalized OH fluorescence signal $I_{max,OH}$ detected in the particle flame at various height positions. The curves for different particle sizes exhibit similar trends, with particle ignition starting around $z = 5$ mm, marked by a notable increase in the OH-LIF signal. Up to $z = 14$ mm, the flame retardant additives show minor variations among size distributions. However, beyond this point, PSMP and DEPZn exhibit a downward branch, indicating a reduction in the normalized OH-LIF signal and a pronounced radical scavenging activity. In contrast, APP displays no change from neat PP, confirming its lack of gas-phase activity as condensed-phase activity is suppressed at the high heating rates for micrometer-sized particles. ATH, as a water-generating flame retardant, shows higher OH-LIF signals compared to PP, potentially due to released water vapor dissociating into OH radicals in the exhaust atmosphere.

Further, the spatial extent of the spherical envelope flame for different particle sizes is investigated using the dimensionless flame radius $r_{max,OH}/r_p$ displayed in Fig. 5.5(d-f). This parameter is calculated based on the radius of the maximum OH-LIF signal and the circle-equivalent radius detected by DBI. Subtle differences can be observed in the curves for various compositions within each size interval. Surprisingly, even for gas-phase active flame retardants like PSMP and DEPZn, no significant increase in flame radius is observed compared to neat PP. As the height above the burner increases, all dimensionless flame distances show an upward trend, which might indicate a Stefan flow emerging from the particle during pyrolysis.

Comparing the three size intervals, it becomes evident that smaller particles exhibit a higher dimensionless flame distance at each height compared to larger particles. This behavior aligns with previous observations in single coal particles with high volatile content [112], where larger particles experienced slower heating and devolatilization rates, resulting in a closer flame proximity. Similarly, the maximum normalized OH-LIF signal intensity evolution indicates greater differences in the flame retardant's inhibition efficiency for large particles, substantiated by the reduced devolatilization rate of the flame retardant contained in the PP polymer matrix.
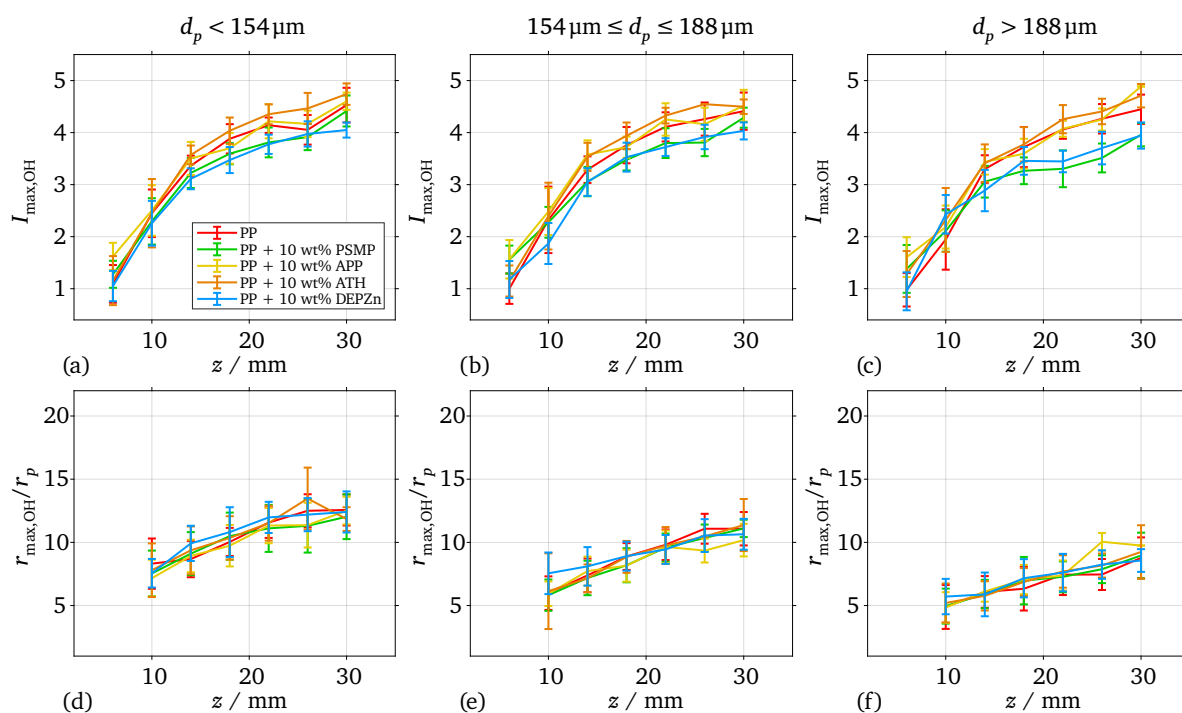
Figure 5.5: (a-c) Peak normalized OH-LIF intensity and (d-f) dimensionless flame radius for all investigated flame retarded polymer particles compared to neat PP. (Adapted from [5])

Combustion of polymer sticks

The thermal decomposition analysis employed low heating rates in an inert environment, whereas the particle combustion experiments were conducted at high heating rates, limiting the evaluation of flame retardants with condensed-phase action. To address this limitation, a custom test stand was designed, resembling the standardized horizontal burning test. This setup allows for the investigation of stick-shaped polymer specimens interacting with a methane (CH_4) flame using advanced optical diagnostics.

The photographs in Fig. 5.6 show different time points relative to the ignition of the external flame. PSMP and APP in PP exhibit rapid self-extinguishing behavior compared to other flame retardants. In contrast, neat PP and DEPZn in PP sustain a flame. The combustion of ATH-containing samples in PP also self-extinguishes before the moment when neat PP and DEPZn in PP are externally extinguished. DEPZn in PP exhibits a distinctive behavior, characterized by the emergence of multiple smaller flames within the main flame volume, likely due to the release of combustible gases detected in the TG-FTIR analysis. The flames of phosphorus-containing samples, including PSMP, APP, and DEPZn, display a purple to orange hue immediately after ignition, possibly attributed to the formation of luminous decomposition products from the flame retardants, as opposed to soot observed downstream in neat PP and ATH in PP after approximately 45 s of interaction with the external CH_4 flame. This hypothesis could be explained by the spatial separation of the blue-colored portion of the flame and the soot luminosity for non-phosphorus-containing compounds, in contrast to the uniform orange hue observed right after ignition for phosphorus-containing samples.

Figure 5.7 displays OH-PLIF images averaged over 200 ms just before the external flame's extinction, revealing the interaction between the CH_4 flame and the combusting polymer specimens after nearly 60 s of interaction. For reference, Fig.5.7(f) shows the external flame 200 ms after igniting, where almost no pyrolyzation of the polymer should have taken place yet. Samples containing PP, PP + ATH, and PP + APP show relatively large regions of increased OH fluorescence signal before the external
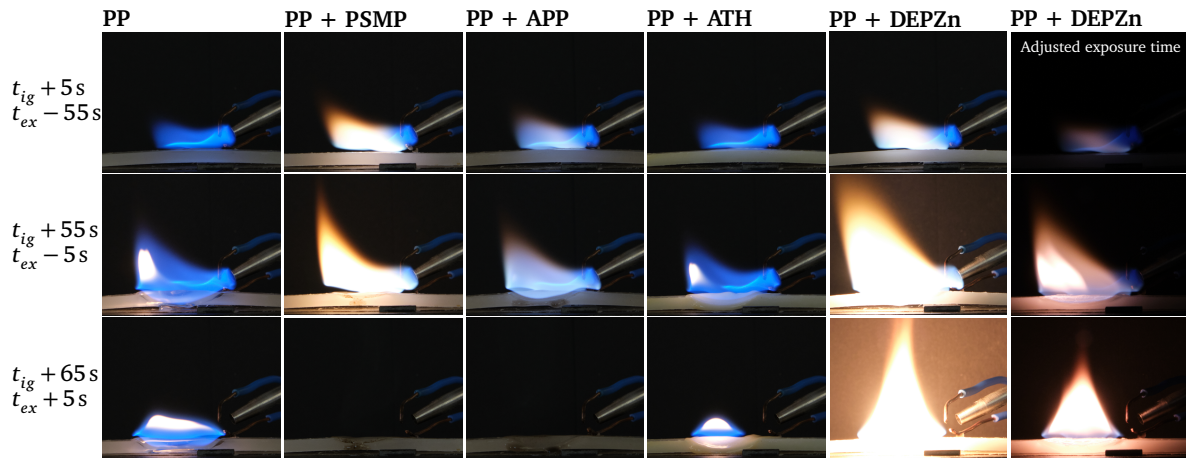
Figure 5.6: Photographs of the combustion of stick-shaped specimens at different instants relative to the time of ignition t_i and extinction t_e of the external flame. (Adpated from [5])

flame's extinction, while phosphorus-containing flame retardants with gas-phase activity exhibit reduced flame volumes. Notably, the reaction zone size is reduced for PP + PSMP due to its radical scavenging effect in the gas phase. For PP + DEPZn, the reaction zone is smaller compared to PP, but additional flames emerging directly from the specimen's surface influence the combustion due to the release of combustible substances, possibly C_2H_6 and PH_3. Similar to the particle experiments, the highest OH signal intensity is observed for PP + ATH, where water from ATH decomposition increases the OH signal intensity in the gas phase. This observation is likely due to the low concentration of ATH used in this sample, rendering the cooling effect undetectable.
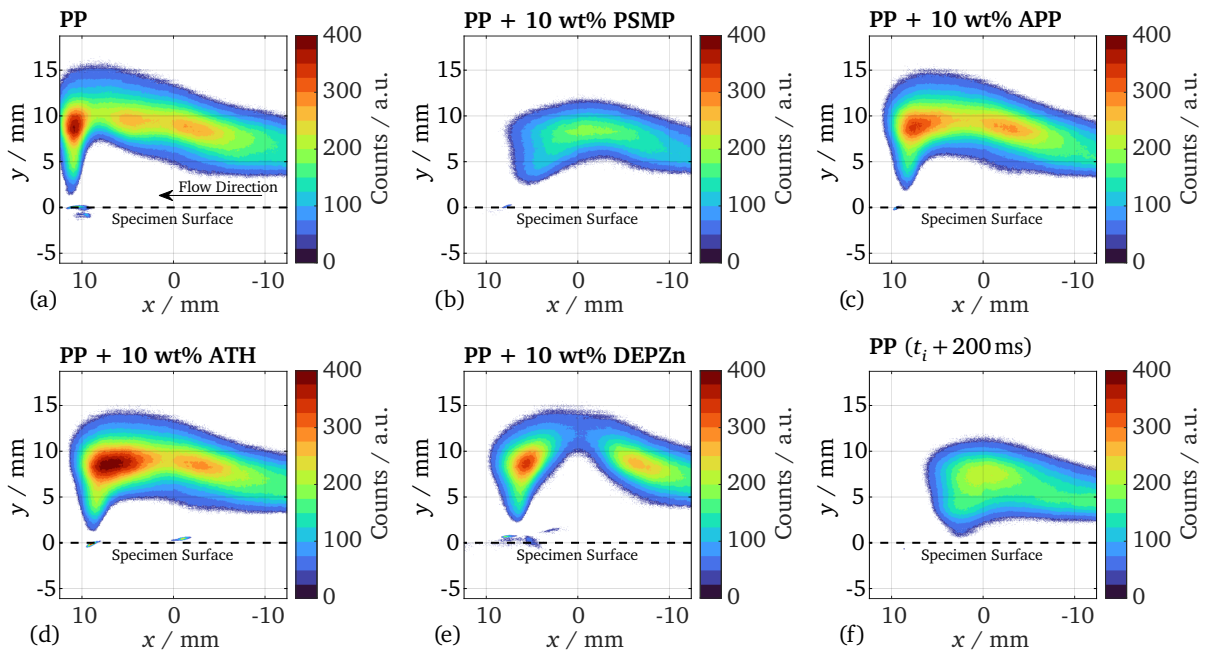

Figure 5.7: (a-e) OH-PLIF of stick-shaped specimens interacting with a CH_4 Bunsen flame just before extinction of the external flame. (f) Reference case of neat PP taken just after ignition of the external flame. (Adpated from [5])

The temporal evolution of the OH-LIF signal intensity is further examined after the CH_4 Bunsen flame extinction (refer to Fig. 12 of **Paper V** in Section A.5). Neat PP displays a gradually expanding self-sustaining flame, while PP + PSMP exhibits rapid self-extinguishing behavior accompanied by smoke

release. PP + APP and PP + ATH demonstrate conical flames with flickering motion, indicating local fuel deficiencies in the reaction zones. The flames of PP + APP extinguish after 550 ms, while those of PP + ATH continue flickering for several seconds before eventually ceasing. The reduced pyrolysis rate due to the condensed-phase modes of action of ATH and APP likely accounts for this behavior, making their gas-phase effects undetectable using OH-PLIF, akin to the particle combustion experiments. Samples containing PP + DEPZn exhibit self-sustaining conical reaction zones with a luminous signal above the surface, suggesting the release of gaseous decomposition products from the polymer sample. To investigate this behavior, high-speed imaging capturing both the polymer sample and the self-sustaining combustion in a similar FOV to OH-PLIF was performed. The formation of bubbles within the molten polymer sample can be observed, releasing combustible gases that contribute to the ongoing combustion of the polymer, competing with the flame inhibition effect.

Concluding remarks

This study investigated the gas-phase combustion of flame retarded PP containing 10 wt% of different flame retardants (PSMP, APP, ATH, DEPZn). Characteristic decomposition products were identified using TG-FTIR, while OH-PLIF (alongside complementing cone calorimetry) enabled the detection of gas-phase effects for flame inhibition. This work demonstrated the extension of OH-PLIF to flame retarded polymer particles based on **Paper IV** [4], facilitating the simultaneous determination of the dimensionless flame radius and the normalized peak OH-LIF intensity in the diffusion flame surrounding particles. Additionally, optical diagnostics of stick-shaped specimens in an adapted horizontal burning test stand provided insights into the combustion of larger samples, where condensed-phase activity was not suppressed, unlike the particle experiments in the LFR exhibiting high heating rates. The findings revealed that PSMP exhibited the most significant decrease in the OH-LIF signal, while ATH led to increased OH signal intensity due to water release during decomposition. DEPZn showed observable jet-like flames, but still had a detectable flame inhibition effect in the gas phase. The combination of various optical measurement techniques and chemical pyrolysis fragment analyses provided a comprehensive understanding of combustion processes and flame retardant interactions during ignition and combustion.

6 Summary and outlook

6.1 Summary

The research conducted in this thesis represents significant advances in the experimental study of various phenomena within the context of solid-flow-chemistry interactions. Specifically, two technically relevant examples were investigated in detail: the combustion of carbonaceous solid fuels, such as biomass and coal, and flame retardancy of polymers. Within the five peer-reviewed publications included in this thesis, three distinct subject areas were identified. These lead to substantial contributions to the phenomenological understanding of these processes. The key achievement lies in the development and adaptation of minimally intrusive optical measurements, allowing for the precise and non-invasive characterization of the studied phenomena. By addressing complex challenges and advancing experimental techniques, this research has provided valuable insights and opened new ways for future studies in this field.

In the first subject area, which was discussed in Section 3, the interaction between solid fuel particles and the surrounding carrier-phase turbulence was investigated in a non-reactive round jet. To achieve the necessary spatial and temporal resolutions, a pulsed fiber laser system was adapted and integrated into a TR-PIV system for flow velocimetry. The capabilities of this system were successfully demonstrated in a single-phase turbulent jet, achieving unprecedented temporal dynamic ranges. The investigation yielded valuable insights, including a detailed analysis of measurement errors and spatial resolution for determining turbulent scales, spectra, and space-time correlations. Notably, deviations from Taylor's frozen flow hypothesis were identified, revealing important aspects of turbulent shear flows. Expanding efforts, the ultra-high repetition rate of the fiber laser system facilitated the design of a single-cavity laser suitable for both dual-pulse and time-resolved PIV measurements. By combining it with pulse picking systems based on the acousto-optic and electro-optic effects, the setups' performance and limitations were thoroughly characterized. Finally, the improved diagnostics setup was applied to study the particle-turbulence interaction of single miscanthus particles. Utilizing a multi-parameter measurement system, particle-flow interactions were observed and analyzed with remarkable spatial and temporal resolutions.

In Section 4, the combustion of bituminous coal particles in a laminar flat flame burner was investigated using comprehensive multi-parameter optical diagnostics, comprising subject area 2. The primary objective was to understand the transition from SPC to PGC and analyze the combined effects of PND, gas-phase O_2 content, and diluent composition, including both air and oxy-fuel conditions. A DBI system was employed to determine particle concentration; however, its line-of-sight nature introduced measurement errors that necessitated ground truth data for accurate quantification. To address this, a new particle generation tool was developed, enabling the creation of virtual images based on measured line-of-sight particle residence volume and properties. A thorough parameter study allowed the evaluation of the magnitude of the error in determining PND. The investigation further utilized scanning OH-PLIF, DBI, and Mie scattering to observe volatile flame structures and soot formation under varying boundary conditions. The results showed that increasing the gas-phase O_2 content could effectively suppress soot formation, particularly prevalent at high PND. Three-dimensional volatile flame structures were observed, revealing that an increase in PND and a decrease in gas-phase O_2 concentration led to non-flammability in the fuel-rich core or the flame. Interestingly, these trends were consistent across both air and oxy-fuel environments. Additionally, it was hypothesized that the

effects of decreased oxygen diffusivity and higher heat sink of CO_2 could potentially balance out, though this would need confirmation in future studies. The multitude of results obtained from the experiments provided valuable insights into solid fuel combustion transitioning from single to dense streams of particles.

Subject area 3 (discussed in Section 5) focused on investigating the inhibition of combustion in solid materials, specifically examining the effect of flame retardants on polymers. Notably, the diagnostic methods established for solid fuel combustion were successfully adapted for in situ flame inhibition studies of polymers, highlighting the versatility of the experimental approach in gaining valuable insight into the gas-phase activity of flame retardants. The application of OH-PLIF to burning flame retarded polypropylene particles represented an important achievement, showcasing its potential in identifying gas-phase activity of flame retardants. Complementing this, thermal decomposition analyses provided essential information on the chemical decomposition products, aiding in determining the mode of action of flame retardants. Building upon this foundation, the optical diagnostics setup was expanded into a multi-parameter measurement system, enabling the determination of the normalized OH-LIF intensity and dimensionless stand-off distance of the diffusion flame surrounding particles treated with four different flame retardants, each with distinct modes of action. The results indicated a reduction in OH-LIF signal intensity within the flame for gas-phase active flame retardants, confirming the viability of using laser-induced fluorescence for studying flame inhibition. To extend this methodology to larger polymer samples, the interaction of stick-shaped specimens with a premixed CH_4 Bunsen flame was explored, demonstrating the applicability of optical diagnostics in studying polymer combustion and flame inhibition in real fire scenarios. The combination of optical diagnostics and pyrolysis fragment analysis methods proved to be a meaningful approach for gaining a comprehensive understanding of the chemistry and combustion dynamics of flame retarded polymers.

By identifying gaps in our understanding of solid-flow-chemistry interactions and advancing experimental techniques, the research presented in this thesis has provided valuable insights into the fundamental mechanisms governing solid fuel combustion and flame retardancy. The versatility of the developed experimental approach was evident in its successful application across different subject areas, highlighting its potential for gaining comprehensive understanding of complex combustion processes. Overall, the research conducted in this thesis opens new avenues for future studies and paves the way for practical applications in fields ranging from energy production to fire safety.

6.2 Outlook

This section offers an outlook on future research directions in the experimental study of solid-flow-chemistry interactions building upon the achievements of this thesis. This mainly concerns further analysis of the existing data and potential parameter studies beyond the current scope of this thesis.

Subject area 1 encompassed multi-phase TR-PIV measurements, generating an extensive dataset examining the interaction between biomass particles and surrounding carrier phase turbulence in a non-reactive environment. A thorough statistical evaluation for investigating the influence of particle size, shape, and rotation velocity on turbulence modulation and slip velocity field topology is possible, holding significant implications for future reactive cases involving volatile transport. One limitation was the spatial dynamic range of ultra-high-speed measurements, constrained by the small FOV due to cropping the active sensor area. To address this, the use of backside-illuminated CMOS cameras optimized for ultra-high repetition rate imaging, exemplified by the TMX 7510 (Phantom) operating at 76 kHz with a frame size of $1280 \times 800\,px^2$, could provide improvements. Additionally, TR-PIV measurements of single-phase turbulence highlighted the spatial resolution, determined by the IW size, as a limiting factor for resolving the smallest turbulence structures. Optical flow velocimetry methods [140–142], generating dense motion fields, offer a valuable enhancement for this issue. Moreover, a

complementary numerical study featuring fully resolved particles in the turbulent jet, similar to previous work [143], would facilitate comparison. Future fiber lasers with higher output powers at similar repetition rates could enable TR-PIV measurements of larger volumes, potentially enabling pulsed volumetric illumination for ultra-high-speed 3D Lagrangian particle tracking experiments, addressing gaps in our understanding of Eulerian and Lagrangian turbulence statistics coupling [66, 100].

In subject area 2, which focuses on group combustion experiments of solid fuels, potential future investigations could involve exploring additional parameters and employing complementary diagnostic methods. To gain insights into the detailed formation of soot and its precursors, a combination of LIF of PAHs and LII is desirable [144]. Shifting from coal combustion to biomass combustion, variations in solid fuel composition, size, and shape may influence devolatilization and volatile flame structure. To better understand the negligible differences observed between air and oxy-fuel atmospheres, accompanying numerical simulations (as demonstrated in [116]) could provide valuable insights into the underlying effects. Additionally, a study linking the global PND to a local interaction distance between particles could be evaluated for the given configuration, in conjunction with the developed imaging simulation tool. Beyond its use in this work, the DBI imaging simulation algorithm offers the opportunity to systematically analyze the limitations and uncertainties of line-of-sight imaging methods for determining parameters such as particle size, shape, number density, and volume fraction. A systematic study for different characteristic residence volume shapes, potentially investigating the role of the number of simultaneously running DBI systems with multiple cameras, could also be conducted. These explorations would provide further insights into the complex combustion processes of solid fuels and contribute to the continuous improvement of diagnostic methodologies in this field.

The experiments conducted in subject area 3 have revealed the immense research potential of optical diagnostics in the testing and evaluation of flame retarded polymers. The current focus of the research community in this domain centers on either detailed reaction kinetics for flame inhibition modeling or investigating polymers in application-relevant test procedures [10, 50]. However, the results presented in this thesis have illuminated an alternative research approach, where physicochemical effects on the micro- and mesoscale can be linked to the underlying chemical kinetics, ultimately enabling the prediction of burning polymer specimen behavior and the inhibition potential derived from flame retardant additives. A systematic study exploring the impact of further individual parameters of solid-flow-chemistry interactions, progressively increasing in complexity, is highly desirable. By decoupling the individual processes that prevail in the combustion of flame retarded polymers, a better understanding of their individual contributions can be achieved, facilitating the modeling of these effects. This holistic understanding of flame retardancy at different scales could pave the way for more efficient and targeted design of flame retarded polymers, enhancing their safety across various applications.

References

Peer-reviewed publications included in this cumulative thesis

[1] Geschwindner, C., Westrup, K., Dreizler, A. and Böhm, B.: "Ultra-high-speed time-resolved PIV of turbulent flows using a continuously pulsing fiber laser." In: *Experiments in Fluids* 63.4 (2022). DOI: 10.1007/s00348-022-03424-7.

[2] Geschwindner, C., Westrup, K., Dreizler, A. and Böhm, B.: "Pulse picking of a fiber laser enables velocimetry of biomass-laden jets at low and ultra-high repetition rates." In: *Proceedings of the Combustion Institute* 39.1 (2023), pp. 1325–1335. DOI: 10.1016/j.proci.2022.07.138.

[3] Li, T., Geschwindner, C., Dreizler, A. and Böhm, B.: "An experimental study of coal particle group combustion in conventional and oxy-fuel atmospheres using multi-parameter optical diagnostics." In: *Proceedings of the Combustion Institute* 39.3 (2023), pp. 3259–3269. DOI: 10.1016/j.proci.2022.07.081.

[4] Geschwindner, C., Goedderz, D., Li, T., Köser, J., Fasel, C., Riedel, R., Altstädt, V., Bethke, C., Puchtler, F., Breu, J., Döring, M., Dreizler, A. and Böhm, B.: "Investigation of flame retarded polypropylene by high-speed planar laser-induced fluorescence of OH radicals combined with a thermal decomposition analysis." In: *Experiments in Fluids* 61.2 (2020). DOI: 10.1007/s00348-019-2864-5.

[5] Geschwindner, C., Goedderz, D., Li, T., Bender, J., Böhm, B. and Dreizler, A.: "The effects of various flame retardants on the combustion of polypropylene: Combining optical diagnostics and pyrolysis fragment analysis." In: *Polymer Degradation and Stability* 211 (2023), p. 110321. DOI: 10.1016/j.polymdegradstab.2023.110321.

Other references

[6] Shukla, P. R., Skea, J. and Reisinger, A., eds.: *Climate change 2022: Mitigation of climate change*. Geneva: IPCC, 2022. URL: https://www.ipcc.ch/report/ar6/wg3/downloads/report/IPCC_AR6_WGIII_FullReport.pdf.

[7] Toftegaard, M. B., Brix, J., Jensen, P. A., Glarborg, P. and Jensen, A. D.: "Oxy-fuel combustion of solid fuels." In: *Progress in Energy and Combustion Science* 36.5 (2010), pp. 581–625. DOI: 10.1016/j.pecs.2010.02.001.

[8] Li, S., Xu, Y. and Gao, Q.: "Measurements and modelling of oxy-fuel coal combustion." In: *Proceedings of the Combustion Institute* 37.3 (2019), pp. 2643–2661. DOI: 10.1016/j.proci.2018.08.054.

[9] Kemper, J.: "Biomass and carbon dioxide capture and storage: A review." In: *International Journal of Greenhouse Gas Control* 40 (2015), pp. 401–430. DOI: 10.1016/j.ijggc.2015.06.012.

[10] Velencoso, M. M., Battig, A., Markwart, J. C., Schartel, B. and Wurm, F. R.: "Molecular Firefighting-How Modern Phosphorus Chemistry Can Help Solve the Challenge of Flame Retardancy." In: *Angewandte Chemie (International ed. in English)* 57.33 (2018), pp. 10450–10467. DOI: 10.1002/anie.201711735.

[11] Köser, J. C.: "Untersuchung der frühen Abbrandphase von Feststoffpartikeln mit optischer Diagnostik." Dissertation. Darmstadt: Technische Universität Darmstadt, 2020. DOI: 10.25534/tuprints-00013410.

[12] Li, T.: "Experimental Investigations of Solid Fuel Combustion with Multi-dimensional and Multi-parameter Laser Diagnostics." Dissertation. Darmstadt: Technische Universität Darmstadt, 2021. DOI: 10.26083/tuprints-00019412.

[13] Geschwindner, C., Westrup, K., Dreizler, A. and Böhm, B.: "Pulse Picking PIV: A Single-Cavity Fiber Laser System For Highly Flexible Repetition Rates And Pulsing Schemes." In: *20th International Symposium on Applications of Laser and Imaging Techniques to Fluid Mechanics*. 2022. DOI: 10.55037/lxlaser.20th.105.

[14] Durst, F.: *Fluid mechanics: An introduction to the theory of fluid flows*. Second extended edition. Graduate texts in physics. Berlin and Heidelberg: Springer, 2022.

[15] Spurk, J. H. and Aksel, N.: *Fluid Mechanics*. 3rd ed. Cham: Springer International Publishing, 2020. DOI: 10.1007/978-3-030-30259-7.

[16] Pope, S. B.: *Turbulent flows*. 10. print. Cambridge: Cambridge Univ. Press, 2013.

[17] Bailly, C. and Comte-Bellot, G.: *Turbulence*. Cham: Springer International Publishing, 2015. DOI: 10.1007/978-3-319-16160-0.

[18] Tennekes, H. and Lumley, J. L.: *A first course in turbulence*. 12. print. Cambridge: The MIT Press, 1989.

[19] Taylor, G. I.: "The Spectrum of Turbulence." In: *Proceedings of the Royal Society of London. Series A - Mathematical and Physical Sciences* 164.919 (1938), pp. 476–490. DOI: 10.1098/rspa.1938.0032.

[20] He, G., Jin, G. and Yang, Y.: "Space-Time Correlations and Dynamic Coupling in Turbulent Flows." In: *Annual Review of Fluid Mechanics* 49.1 (2017), pp. 51–70. DOI: 10.1146/annurev-fluid-010816-060309.

[21] He, G.-W. and Zhang, J.-B.: "Elliptic model for space-time correlations in turbulent shear flows." In: *Physical review. E, Statistical, nonlinear, and soft matter physics* 73.5 Pt 2 (2006), p. 055303. DOI: 10.1103/PhysRevE.73.055303.

[22] Wills, J. A. B.: "On convection velocities in turbulent shear flows." In: *Journal of Fluid Mechanics* 20.3 (1964), pp. 417–432. DOI: 10.1017/S002211206400132X.

[23] Zhao, X. and He, G.-W.: "Space-time correlations of fluctuating velocities in turbulent shear flows." In: *Physical review. E, Statistical, nonlinear, and soft matter physics* 79.4 Pt 2 (2009), p. 046316. DOI: 10.1103/PhysRevE.79.046316.

[24] Brennen, C. E.: *Fundamentals of Multiphase Flow*. Cambridge: Cambridge University Press, 2014. DOI: 10.1017/CBO9780511807169.

[25] Crowe, C. T., Schwarzkopf, J. D., Sommerfeld, M. and Tsuji, Y.: *Multiphase flows with droplets and particles*. 2. ed. Boca Raton: CRC Press, 2012.

[26] Balachandar, S. and Eaton, J. K.: "Turbulent Dispersed Multiphase Flow." In: *Annual Review of Fluid Mechanics* 42.1 (2010), pp. 111–133. DOI: 10.1146/annurev.fluid.010908.165243.

[27] Voth, G. A. and Soldati, A.: "Anisotropic Particles in Turbulence." In: *Annual Review of Fluid Mechanics* 49.1 (2017), pp. 249–276. DOI: 10.1146/annurev-fluid-010816-060135.

[28] Lau, T. C. W. and Nathan, G. J.: "Influence of Stokes number on the velocity and concentration distributions in particle-laden jets." In: *Journal of Fluid Mechanics* 757 (2014), pp. 432–457. DOI: 10.1017/jfm.2014.496.

[29] Lau, T. C. W. and Nathan, G. J.: "The effect of Stokes number on particle velocity and concentration distributions in a well-characterised, turbulent, co-flowing two-phase jet." In: *Journal of Fluid Mechanics* 809 (2016), pp. 72–110. DOI: 10.1017/jfm.2016.666.

[30] Elgobashi, S.: "An Updated Classification Map of Particle-Laden Turbulent Flows." In: *IUTAM Symposium on Computational Approaches to Multiphase Flow*. Ed. by S. Balachandar and A. Prosperetti. Vol. 81. Fluid Mechanics and Its Applications. Dordrecht: Springer Netherlands, 2006, pp. 3–10. DOI: 10.1007/1-4020-4977-3_1.

[31] Zastawny, M., Mallouppas, G., Zhao, F. and van Wachem, B.: "Derivation of drag and lift force and torque coefficients for non-spherical particles in flows." In: *International Journal of Multiphase Flow* 39 (2012), pp. 227–239. DOI: 10.1016/j.ijmultiphaseflow.2011.09.004.

[32] Sanjeevi, S. K., Kuipers, J. and Padding, J. T.: "Drag, lift and torque correlations for non-spherical particles from Stokes limit to high Reynolds numbers." In: *International Journal of Multiphase Flow* 106 (2018), pp. 325–337. DOI: 10.1016/j.ijmultiphaseflow.2018.05.011.

[33] Fröhlich, K., Meinke, M. and Schröder, W.: "Correlations for inclined prolates based on highly resolved simulations." In: *Journal of Fluid Mechanics* 901 (2020). DOI: 10.1017/jfm.2020.482.

[34] Shapiro, M. and Goldenberg, M.: "Deposition of glass fiber particles from turbulent air flow in a pipe." In: *Journal of Aerosol Science* 24.1 (1993), pp. 65–87. DOI: 10.1016/0021-8502(93)90085-N.

[35] Chaudhuri, S. N.: "Coal Rank Classification." In: *Encyclopedia of Mineral and Energy Policy*. Ed. by G. Tiess, T. Majumder and P. Cameron. Berlin, Heidelberg: Springer, 2016, pp. 1–3. DOI: 10.1007/978-3-642-40871-7_99-1.

[36] van Krevelen, D. W.: *Coal: Typology-physics-chemistry-constitution*. 3rd ed. Amsterdam: Elsevier, 1993.

[37] Prins, M. J., Ptasinski, K. J. and Janssen, F. J.: "From coal to biomass gasification: Comparison of thermodynamic efficiency." In: *Energy* 32.7 (2007), pp. 1248–1259. DOI: 10.1016/j.energy.2006.07.017.

[38] Vassilev, S. V., Baxter, D., Andersen, L. K., Vassileva, C. G. and Morgan, T. J.: "An overview of the organic and inorganic phase composition of biomass." In: *Fuel* 94 (2012), pp. 1–33. DOI: 10.1016/j.fuel.2011.09.030.

[39] Li, T., Geschwindner, C., Dreizler, A. and Böhm, B.: "Particle-resolved optical diagnostics of solid fuel combustion for clean power generation: a review." In: *Measurement Science and Technology* (2023). DOI: 10.1088/1361-6501/acef49.

[40] Li, T., Geschwindner, C., Köser, J., Schiemann, M., Dreizler, A. and Böhm, B.: "Investigation of the transition from single to group coal particle combustion using high-speed scanning OH-LIF and diffuse backlight-illumination." In: *Proceedings of the Combustion Institute* 38.3 (2021), pp. 4101–4109. DOI: 10.1016/j.proci.2020.06.314.

[41] Dasari, A., Yu, Z.-Z., Cai, G.-P. and Mai, Y.-W.: "Recent developments in the fire retardancy of polymeric materials." In: *Progress in Polymer Science* 38.9 (2013), pp. 1357–1387. DOI: 10.1016/j.progpolymsci.2013.06.006.

[42] Green, J.: "Mechanisms for Flame Retardancy and Smoke suppression -A Review." In: *Journal of Fire Sciences* 14.6 (1996), pp. 426–442. DOI: 10.1177/073490419601400602.

[43] Klinkowski, C., Burk, B., Bärmann, F. and Döring, M.: "Moderne Flammschutzmittelfür Kunststoffe." In: *Chemie in unserer Zeit* 49.2 (2015), pp. 96–105. DOI: 10.1002/ciuz.201500648.

[44] Wilkie, C. A. and Morgan, A. B., eds.: *Fire retardancy of polymeric materials*. 2. ed. Boca Raton: CRC Press/Taylor & Francis, 2010.

[45] Schartel, B.: "Burning of Plastics." In: *Plastics Flammability Handbook*. Ed. by J. Troitzsch and E. Antonatus. München: Hanser, 2021, pp. 23–52.

[46] Law, C. K.: *Combustion Physics*. Cambridge: Cambridge University Press, 2010. DOI: 10.1017/CBO9780511754517.

[47] *Montreal protocol on substances that deplete the ozone layer: Final act, 1987*. Nairobi: UNEP, 1987.

[48] Schartel, B.: "Phosphorus-based Flame Retardancy Mechanisms-Old Hat or a Starting Point for Future Development?" In: *Materials* 3.10 (2010), pp. 4710–4745. DOI: 10.3390/ma3104710.

[49] Goedderz, D.: "Neue Flammschutzmittel für PET und Aufklärung der Wirkmechanismen." Dissertation. Darmstadt: Technische Universität Darmstadt, 2021. DOI: 10.26083/tuprints-00018599.

[50] Salmeia, K., Fage, J., Liang, S. and Gaan, S.: "An Overview of Mode of Action and Analytical Methods for Evaluation of Gas Phase Activities of Flame Retardants." In: *Polymers* 7.3 (2015), pp. 504–526. DOI: 10.3390/polym7030504.

[51] Aldén, M.: "Spatially and temporally resolved laser/optical diagnostics of combustion processes: From fundamentals to practical applications." In: *Proceedings of the Combustion Institute* 39.1 (2023), pp. 1185–1228. DOI: 10.1016/j.proci.2022.06.020.

[52] Böhm, B., Heeger, C., Gordon, R. L. and Dreizler, A.: "New Perspectives on Turbulent Combustion: Multi-Parameter High-Speed Planar Laser Diagnostics." In: *Flow, Turbulence and Combustion* 86.3-4 (2011), pp. 313–341. DOI: 10.1007/s10494-010-9291-2.

[53] Slipchenko, M. N., Meyer, T. R. and Roy, S.: "Advances in burst-mode laser diagnostics for reacting and nonreacting flows." In: *Proceedings of the Combustion Institute* (2020). DOI: 10.1016/j.proci.2020.07.024.

[54] Träger, F.: *Springer Handbook of Lasers and Optics*. Berlin, Heidelberg: Springer, 2012. DOI: 10.1007/978-3-642-19409-2.

[55] Eichler, H. J. and Eichler, J.: *Laser*. Berlin, Heidelberg: Springer, 2015. DOI: 10.1007/978-3-642-4143 8-1.

[56] Thurow, B., Jiang, N. and Lempert, W.: "Review of ultra-high repetition rate laser diagnostics for fluid dynamic measurements." In: *Measurement Science and Technology* 24.1 (2013), p. 012002. DOI: 10.10 88/0957-0233/24/1/012002.

[57] Samson, B. and Dong, L.: "Fiber lasers." In: *Handbook of Solid-State Lasers*. Elsevier, 2013, pp. 403–462. DOI: 10.1533/9780857097507.2.403.

[58] Ter-Mikirtychev, V. V.: *Fundamentals of Fiber Lasers and Fiber Amplifiers*. Vol. 181. Cham: Springer International Publishing, 2019. DOI: 10.1007/978-3-030-33890-9.

[59] Bass, M.: *Handbook of Optics*. 2nd ed. New York: McGraw-Hill, 1995.

[60] Ghatak, A. K. and Thyagarajan, K.: *Optical Electronics*. Cambridge University Press, 2012. DOI: 10.101 7/CBO9781139167857.

[61] Wolfrum, J., Dreier, T., Ebert, V. and Schulz, C.: "Laser-Based Combustion Diagnostics." In: *Encyclopedia of Analytical Chemistry*. Ed. by R. A. Meyers. Chichester, UK: John Wiley & Sons, Ltd, 2006. DOI: 10.1 002/9780470027318.a0715.pub3.

[62] Raffel, M., Willert, C. E., Scarano, F., Kähler, C. J., Wereley, S. T. and Kompenhans, J.: *Particle Image Velocimetry*. Cham: Springer International Publishing, 2018. DOI: 10.1007/978-3-319-68852-7.

[63] Tropea, C., Yarin, A. L. and Foss, J. F.: *Springer handbook of experimental fluid mechanics*. Berlin: Springer, 2007.

[64] Scharnowski, S. and Kähler, C. J.: "Particle image velocimetry - Classical operating rules from today's perspective." In: *Optics and Lasers in Engineering* 135 (2020), p. 106185. DOI: 10.1016/j.optlaseng.2 020.106185.

[65] Kähler, C. J., Scharnowski, S. and Cierpka, C.: "On the resolution limit of digital particle image velocimetry." In: *Experiments in Fluids* 52.6 (2012), pp. 1629–1639. DOI: 10.1007/s00348-012-1280-x.

[66] Schröder, A. and Schanz, D.: "3D Lagrangian Particle Tracking in Fluid Mechanics." In: *Annual Review of Fluid Mechanics* 55.1 (2023), pp. 511–540. DOI: 10.1146/annurev-fluid-031822-041721.

[67] Kohse-Höinghaus, K.: "Laser techniques for the quantitative detection of reactive intermediates in combustion systems." In: *Progress in Energy and Combustion Science* 20.3 (1994), pp. 203–279. DOI: 10.10 16/0360-1285(94)90015-9.

[68] Daily, J. W.: "Laser induced fluorescence spectroscopy in flames." In: *Progress in Energy and Combustion Science* 23.2 (1997), pp. 133–199. DOI: 10.1016/S0360-1285(97)00008-7.

[69] Luque, J. and Crosley, D. R.: "Transition probabilities in the $A^2\Sigma^+ - X^2\Pi_i$ electronic system of OH." In: *The Journal of Chemical Physics* 109.2 (1998), pp. 439–448. DOI: 10.1063/1.476582.

[70] van der Loo, M. P. J. and Groenenboom, G. C.: "Ab initio calculation of $(2+1)$ resonance enhanced multiphoton ionization spectra and lifetimes of the $(D, 3)^2\Sigma^-$ states of OH and OD." In: *The Journal of Chemical Physics* 123.7 (2005), p. 074310. DOI: 10.1063/1.1997133.

[71] Johansson, O.: "Development and application of photofragmentation laser-induced fluorescence for visualization of hydrogen peroxides." Dissertation. Lund: Lund University, 2011. DOI: 10.1016/j.com bustflame.2011.02.021.

[72] Köser, J., Becker, L. G., Vorobiev, N., Schiemann, M., Scherer, V., Böhm, B. and Dreizler, A.: "Characterization of single coal particle combustion within oxygen-enriched environments using high-speed OH-PLIF." In: *Applied Physics B* 121.4 (2015), pp. 459–464. DOI: 10.1007/s00340-015-6253-3.

[73] Westlye, F. R., Penney, K., Ivarsson, A., Pickett, L. M., Manin, J. and Skeen, S. A.: "Diffuse back-illumination setup for high temporally resolved extinction imaging." In: *Applied optics* 56.17 (2017), pp. 5028–5038. DOI: 10.1364/AO.56.005028.

[74] Edgewave: *IS-Series - Short Pulse InnoSlab Lasers*. 2021. URL: https://www.edge-wave.de/web/wp-co ntent/uploads/ISweb.pdf (visited on 05/31/2021).

[75] Willert, C. E.: "High-speed particle image velocimetry for the efficient measurement of turbulence statistics." In: *Experiments in Fluids* 56.1 (2015). DOI: 10.1007/s00348-014-1892-4.

[76]   Wernet, M. P.: "Temporally resolved PIV for space–time correlations in both cold and hot jet flows." In: *Measurement Science and Technology* 18.5 (2007), pp. 1387–1403. DOI: 10.1088/0957-0233/18/5/027.

[77]   Beresh, S., Kearney, S., Wagner, J., Guildenbecher, D., Henfling, J., Spillers, R., Pruett, B., Jiang, N., Slipchenko, M., Mance, J. and Roy, S.: "Pulse-burst PIV in a high-speed wind tunnel." In: *Measurement Science and Technology* 26.9 (2015), p. 095305. DOI: 10.1088/0957-0233/26/9/095305.

[78]   Beresh, S. J., Henfling, J. F., Spillers, R. W. and Spitzer, S. M.: "'Postage-stamp PIV': small velocity fields at 400 kHz for turbulence spectra measurements." In: *Measurement Science and Technology* 29.3 (2018), p. 034011. DOI: 10.1088/1361-6501/aa9f79.

[79]   Miller, J. D., Jiang, N., Slipchenko, M. N., Mance, J. G., Meyer, T. R., Roy, S. and Gord, J. R.: "Spatiotemporal analysis of turbulent jets enabled by 100-kHz, 100-ms burst-mode particle image velocimetry." In: *Experiments in Fluids* 57.12 (2016). DOI: 10.1007/s00348-016-2279-5.

[80]   Roy, S., Miller, J. D. and Gunaratne, G. H.: "Deviations from Taylor's frozen hypothesis and scaling laws in inhomogeneous jet flows." In: *Communications Physics* 4.1 (2021). DOI: 10.1038/s42005-021-00528-0.

[81]   Panahi, A., Vorobiev, N., Schiemann, M., Tarakcioglu, M., Delichatsios, M. and Levendis, Y. A.: "Combustion details of raw and torrefied biomass fuel particles with individually-observed size, shape and mass." In: *Combustion and Flame* 207 (2019), pp. 327–341. DOI: 10.1016/j.combustflame.2019.06.009.

[82]   Borée, J., Ishima, T. and Flour, I.: "The effect of mass loading and inter-particle collisions on the development of the polydispersed two-phase flow downstream of a confined bluff body." In: *Journal of Fluid Mechanics* 443 (2001), pp. 129–165. DOI: 10.1017/S0022112001005134.

[83]   Sommerfeld, M. and Qiu, H.-H.: "Detailed measurements in a swirling particulate two-phase flow by a phase-Doppler anemometer." In: *International Journal of Heat and Fluid Flow* 12.1 (1991), pp. 20–28. DOI: 10.1016/0142-727X(91)90004-F.

[84]   Kiger, K. T. and Pan, C.: "PIV Technique for the Simultaneous Measurement of Dilute Two-Phase Flows." In: *Journal of Fluids Engineering* 122.4 (2000), pp. 811–818. DOI: 10.1115/1.1314864.

[85]   Schmidt, B. E. and Sutton, J. A.: "Evaluation of gas- and particle-phase separation methods for velocity measurements in turbulent multiphase flows." In: *Experiments in Fluids* 61.12 (2020). DOI: 10.1007/s00348-020-03082-7.

[86]   Khalitov, D. A. and Longmire, E. K.: "Simultaneous two-phase PIV by two-parameter phase discrimination." In: *Experiments in Fluids* 32.2 (2002), pp. 252–268. DOI: 10.1007/s003480100356.

[87]   Tanaka, T. and Eaton, J. K.: "Sub-Kolmogorov resolution partical image velocimetry measurements of particle-laden forced turbulence." In: *Journal of Fluid Mechanics* 643 (2010), pp. 177–206. DOI: 10.1017/S0022112009992023.

[88]   Towers, D. P., Towers, C. E., Buckberry, C. H. and Reeves, M.: "A colour PIV system employing fluorescent particles for two-phase flow measurements." In: *Measurement Science and Technology* 10.9 (1999), pp. 824–830. DOI: 10.1088/0957-0233/10/9/309.

[89]   Fond, B., Abram, C., Heyes, A. L., Kempf, A. M. and Beyrau, F.: "Simultaneous temperature, mixture fraction and velocity imaging in turbulent flows using thermographic phosphor tracer particles." In: *Optics Express* 20.20 (2012), pp. 22118–22133. DOI: 10.1364/OE.20.022118.

[90]   Fan, L., McGrath, D., Chong, C. T., Mohd Jaafar, M. N., Zhong, H. and Hochgreb, S.: "Laser-induced incandescence particle image velocimetry (LII-PIV) for two-phase flow velocity measurement." In: *Experiments in Fluids* 59.10 (2018). DOI: 10.1007/s00348-018-2610-4.

[91]   Lau, T. C. W., Frank, J. H. and Nathan, G. J.: "Resolving the three-dimensional structure of particles that are aerodynamically clustered by a turbulent flow." In: *Physics of Fluids* 31.7 (2019), p. 071702. DOI: 10.1063/1.5110323.

[92]   Balusamy, S., Schmidt, A. and Hochgreb, S.: "Flow field measurements of pulverized coal combustion using optical diagnostic techniques." In: *Experiments in Fluids* 54.5 (2013). DOI: 10.1007/s00348-013-1534-2.

[93]   Sabban, L., Cohen, A. and van Hout, R.: "Temporally resolved measurements of heavy, rigid fibre translation and rotation in nearly homogeneous isotropic turbulence." In: *Journal of Fluid Mechanics* 814 (2017), pp. 42–68. DOI: 10.1017/jfm.2017.12.

[94] Westerweel, J. and Scarano, F.: "Universal outlier detection for PIV data." In: *Experiments in Fluids* 39.6 (2005), pp. 1096–1100. DOI: 10.1007/s00348-005-0016-6.

[95] Michaelis, D., Neal, D. R. and Wieneke, B.: "Peak-locking reduction for particle image velocimetry." In: *Measurement Science and Technology* 27.10 (2016), p. 104005. DOI: 10.1088/0957-0233/27/10/104005.

[96] Sciacchitano, A., Neal, D. R., Smith, B. L., Warner, S. O., Vlachos, P. P., Wieneke, B. and Scarano, F.: "Collaborative framework for PIV uncertainty quantification: comparative assessment of methods." In: *Measurement Science and Technology* 26.7 (2015), p. 074004. DOI: 10.1088/0957-0233/26/7/074004.

[97] Sciacchitano, A. and Wieneke, B.: "PIV uncertainty propagation." In: *Measurement Science and Technology* 27.8 (2016), p. 084006. DOI: 10.1088/0957-0233/27/8/084006.

[98] Wieneke, B.: "PIV uncertainty quantification from correlation statistics." In: *Measurement Science and Technology* 26.7 (2015), p. 074002. DOI: 10.1088/0957-0233/26/7/074002.

[99] Del Álamo, J. C. and Jiménez, J.: "Estimation of turbulent convection velocities and corrections to Taylor's approximation." In: *Journal of Fluid Mechanics* 640 (2009), pp. 5–26. DOI: 10.1017/S0022112009991029.

[100] Viggiano, B., Basset, T., Solovitz, S., Barois, T., Gibert, M., Mordant, N., Chevillard, L., Volk, R., Bourgoin, M. and Cal, R. B.: "Lagrangian diffusion properties of a free shear turbulent jet." In: *Journal of Fluid Mechanics* 918 (2021). DOI: 10.1017/jfm.2021.325.

[101] Li, T., Pareja, J., Becker, L., Heddrich, W., Dreizler, A. and Böhm, B.: "Quasi-4D laser diagnostics using an acousto-optic deflector scanning system." In: *Applied Physics B* 123.3 (2017). DOI: 10.1007/s00340-017-6663-5.

[102] Zeng, Z., Zhang, T., Zheng, S., Wu, W. and Zhou, Y.: "Ignition and combustion characteristics of coal particles under high-temperature and low-oxygen environments mimicking MILD oxy-coal combustion conditions." In: *Fuel* 253 (2019), pp. 1104–1113. DOI: 10.1016/j.fuel.2019.05.101.

[103] Yuan, Y., Li, S., Zhao, F., Yao, Q. and Long, M. B.: "Characterization on hetero-homogeneous ignition of pulverized coal particle streams using CH* chemiluminescence and 3 color pyrometry." In: *Fuel* 184 (2016), pp. 1000–1006. DOI: 10.1016/j.fuel.2015.11.032.

[104] Tarlinski, D., Geschwindner, C., Li, T., Böhm, B. and Schiemann, M.: "Particle temperature and composition measurements in the ignition phase of single coal particles and particle groups under conventional and oxy-fuel atmospheres." In: *Fuel* 332 (2023), p. 125894. DOI: 10.1016/j.fuel.2022.125894.

[105] Adeosun, A., Xiao, Z., Yang, Z., Yao, Q. and Axelbaum, R. L.: "The effects of particle size and reducing-to-oxidizing environment on coal stream ignition." In: *Combustion and Flame* 195 (2018), pp. 282–291. DOI: 10.1016/j.combustflame.2018.05.003.

[106] Liu, Y., Geier, M., Molina, A. and Shaddix, C. R.: "Pulverized coal stream ignition delay under conventional and oxy-fuel combustion conditions." In: *International Journal of Greenhouse Gas Control* 5 (2011), S36–S46. DOI: 10.1016/j.ijggc.2011.05.028.

[107] Prationo, W. and Zhang, L.: "Influence of steam on ignition of Victorian brown coal particle stream in oxy-fuel combustion: In-situ diagnosis and transient ignition modelling." In: *Fuel* 181 (2016), pp. 1203–1213. DOI: 10.1016/j.fuel.2016.03.003.

[108] Sarroza, A. C., Bennet, T. D., Eastwick, C. and Liu, H.: "Characterising pulverised fuel ignition in a visual drop tube furnace by use of a high-speed imaging technique." In: *Fuel Processing Technology* 157 (2017), pp. 1–11. DOI: 10.1016/j.fuproc.2016.11.002.

[109] Yuan, Y., Li, S., Li, G., Wu, N. and Yao, Q.: "The transition of heterogeneous–homogeneous ignitions of dispersed coal particle streams." In: *Combustion and Flame* 161.9 (2014), pp. 2458–2468. DOI: 10.1016/j.combustflame.2014.03.008.

[110] Wu, Y., Wu, X., Yao, L., Xue, Z., Wu, C., Zhou, H. and Cen, K.: "Simultaneous particle size and 3D position measurements of pulverized coal flame with digital inline holography." In: *Fuel* 195 (2017), pp. 12–22. DOI: 10.1016/j.fuel.2017.01.024.

[111] Balusamy, S., Kamal, M. M., Lowe, S. M., Tian, B., Gao, Y. and Hochgreb, S.: "Laser diagnostics of pulverized coal combustion in O2/N2 and O2/CO2 conditions: velocity and scalar field measurements." In: *Experiments in Fluids* 56.5 (2015). DOI: 10.1007/s00348-015-1965-z.

[112] Li, T., Schiemann, M., Köser, J., Dreizler, A. and Böhm, B.: "Experimental investigations of single particle and particle group combustion in a laminar flow reactor using simultaneous volumetric OH-LIF imaging and diffuse backlight-illumination." In: *Renewable and Sustainable Energy Reviews* 136 (2021), p. 110377. DOI: 10.1016/j.rser.2020.110377.

[113] Li, T., Farmand, P., Geschwindner, C., Greifenstein, M., Köser, J., Schumann, C., Attili, A., Pitsch, H., Dreizler, A. and Böhm, B.: "Homogeneous ignition and volatile combustion of single solid fuel particles in air and oxy-fuel conditions." In: *Fuel* 291 (2021), p. 120101. DOI: 10.1016/j.fuel.2020.120101.

[114] Pielsticker, S., Heuer, S., Senneca, O., Cerciello, F., Salatino, P., Cortese, L., Gövert, B., Hatzfeld, O., Schiemann, M., Scherer, V. and Kneer, R.: "Comparison of pyrolysis test rigs for oxy-fuel conditions." In: *Fuel Processing Technology* 156 (2017), pp. 461–472. DOI: 10.1016/j.fuproc.2016.10.010.

[115] Gilbert, E. G., Johnson, D. W. and Keerthi, S. S.: "A fast procedure for computing the distance between complex objects in three-dimensional space." In: *IEEE Journal on Robotics and Automation* 4.2 (1988), pp. 193–203. DOI: 10.1109/56.2083.

[116] Nicolai, H., Li, T., Geschwindner, C., Di Mare, F., Hasse, C., Böhm, B. and Janicka, J.: "Numerical investigation of pulverized coal particle group combustion using tabulated chemistry." In: *Proceedings of the Combustion Institute* 38.3 (2021), pp. 4033–4041. DOI: 10.1016/j.proci.2020.06.081.

[117] Solomon, P. R., Serio, M. A. and Suuberg, E. M.: "Coal pyrolysis: Experiments, kinetic rates and mechanisms." In: *Progress in Energy and Combustion Science* 18.2 (1992), pp. 133–220. DOI: 10.1016/0360-1285(92)90021-R.

[118] Sikes, T., Mathieu, O., Kulatilaka, W. D., Mannan, M. S. and Petersen, E. L.: "Laminar flame speeds of DEMP, DMMP, and TEP added to H2- and CH4-air mixtures." In: *Proceedings of the Combustion Institute* 37.3 (2019), pp. 3775–3781. DOI: 10.1016/j.proci.2018.05.042.

[119] Vora, N. and Laurandeau, N. M.: "Analysis of CF 3 Br Flame Suppression Activity Using Quantitative Laser-Induced Fluorescence Measurements of the Hydroxyl Radical." In: *Combustion Science and Technology* 166.1 (2001), pp. 15–39. DOI: 10.1080/00102200108907818.

[120] Vora, N., Siow, J. E. and Laurandeau, N. M.: "Chemical scavenging activity of gaseous suppressants by using laser-induced fluorescence measurements of hydroxyl." In: *Combustion and Flame* 126.1-2 (2001), pp. 1393–1401. DOI: 10.1016/S0010-2180(01)00259-0.

[121] Siow, J. E. and Laurandeau, N. M.: "Flame inhibition activity of phosphorus-containing compounds using laser-induced fluorescence measurements of hydroxyl." In: *Combustion and Flame* 136.1-2 (2004), pp. 16–24. DOI: 10.1016/j.combustflame.2003.08.010.

[122] MacDonald, M. A., Jayaweera, T. M., Fisher, E. M. and Gouldin, F. C.: "Inhibition of nonpremixed flames by phosphorus-containing compounds." In: *Combustion and Flame* 116.1-2 (1999), pp. 166–176. DOI: 10.1016/S0010-2180(98)00034-0.

[123] MacDonald, M., Gouldin, F. and Fisher, E.: "Temperature dependence of phosphorus-based flame inhibition." In: *Combustion and Flame* 124.4 (2001), pp. 668–683. DOI: 10.1016/S0010-2180(00)00236-4.

[124] Steinhausen, M., Ferraro, F., Schneider, M., Zentgraf, F., Greifenstein, M., Dreizler, A., Hasse, C. and Scholtissek, A.: "Effect of flame retardants on side-wall quenching of partially premixed laminar flames." In: *Proceedings of the Combustion Institute* (2022). DOI: 10.1016/j.proci.2022.07.207.

[125] Bouvet, N., Linteris, G., Babushok, V., Takahashi, F., Katta, V. and Krämer, R.: "Experimental and numerical investigation of the gas–phase effectiveness of phosphorus compounds." In: *Fire and Materials* 40.5 (2016), pp. 683–696. DOI: 10.1002/fam.2319.

[126] Korobeinichev, O., Shmakov, A., Paletsky, A., Trubachev, S., Shaklein, A., Karpov, A., Sosnin, E., Kostritsa, S., Kumar, A. and Shvartsberg, V.: "Mechanisms of the Action of Fire-Retardants on Reducing the Flammability of Certain Classes of Polymers and Glass-Reinforced Plastics Based on the Study of Their Combustion." In: *Polymers* 14.21 (2022). DOI: 10.3390/polym14214523.

[127] Korobeinichev, O., Gonchikzhapov, M., Tereshchenko, A., Gerasimov, I., Shmakov, A., Paletsky, A. and Karpov, A.: "An experimental study of horizontal flame spread over PMMA surface in still air." In: *Combustion and Flame* 188 (2018), pp. 388–398. DOI: 10.1016/j.combustflame.2017.10.008.

[128] Korobeinichev, O. P., Paletsky, A. A., Kuibida, L. V., Gonchikzhapov, M. B. and Shundrina, I. K.: "Reduction of flammability of ultrahigh-molecular-weight polyethylene by using triphenyl phosphate additives." In: *Proceedings of the Combustion Institute* 34.2 (2013), pp. 2699–2706. DOI: 10.1016/j.proci.2012.06.045.

[129] Li, Y., Guibaud, A., Citerne, J.-M., Consalvi, J.-L., Coimbra, A., Sarazin, J., Bourbigot, S., Torero, J. L. and Legros, G.: "Effects of flame retardants on extinction limits, spread rate, and smoke release in opposed-flow flame spread over thin cylindrical polyethylene samples in microgravity." In: *Proceedings of the Combustion Institute* (2022). DOI: 10.1016/j.proci.2022.08.030.

[130] Battig, A., Müller, P., Bertin, A. and Schartel, B.: "Hyperbranched Rigid Aromatic Phosphorus-Containing Flame Retardants for Epoxy Resins." In: *Macromolecular Materials and Engineering* 306.4 (2021), p. 2000731. DOI: 10.1002/mame.202000731.

[131] Ciesielski, M., Diederichs, J., Döring, M. and Schäfer, A.: "Advanced Flame-Retardant Epoxy Resins for Composite Materials." In: *Fire and Polymers V*. Vol. 1013. ACS Symposium Series. American Chemical Society, 2009, pp. 174–190. DOI: 10.1021/bk-2009-1013.ch011.

[132] Lau, S. and Atakan, B.: "Isothermal pyrolysis investigation of aluminum diethylphosphinate mixed as a flame retardant additive into ultra-high molecular weight polyethylene." In: *Combustion and Flame* 222 (2020), pp. 272–284. DOI: 10.1016/j.combustflame.2020.08.048.

[133] Liang, S., Hemberger, P., Neisius, N. M., Bodi, A., Grützmacher, H., Levalois-Grützmacher, J. and Gaan, S.: "Elucidating the thermal decomposition of dimethyl methylphosphonate by vacuum ultraviolet (VUV) photoionization: pathways to the PO radical, a key species in flame-retardant mechanisms." In: *Chemistry (Weinheim an der Bergstrasse, Germany)* 21.3 (2015), pp. 1073–1080. DOI: 10.1002/chem.201404271.

[134] Pfaendner, R., Metzsch-Zilligen, E. and Stec, M.: "Use of organic oxy imides as flame retardants for plastics and flame-retardant plastics composition and mouldings produced therefrom." 2014. URL: https://patents.google.com/patent/WO2014154636A1/en.

[135] Salmeia, K. A., Gooneie, A., Simonetti, P., Nazir, R., Kaiser, J.-P., Rippl, A., Hirsch, C., Lehner, S., Rupper, P., Hufenus, R. and Gaan, S.: "Comprehensive study on flame retardant polyesters from phosphorus additives." In: *Polymer Degradation and Stability* 155 (2018), pp. 22–34. DOI: 10.1016/j.polymdegradstab.2018.07.006.

[136] Braun, U., Bahr, H., Sturm, H. and Schartel, B.: "Flame retardancy mechanisms of metal phosphinates and metal phosphinates in combination with melamine cyanurate in glass-fiber reinforced poly(1,4-butylene terephthalate): the influence of metal cation." In: *Polymers for Advanced Technologies* 19.6 (2008), pp. 680–692. DOI: 10.1002/pat.1147.

[137] El-Sabbagh, A., Steuernagel, L., Meiners, D., Ziegmann, G. and Toepfer, O.: "Optimization of flame retardant content with respect to mechanical properties of natural fiber polymer composites: Case study of polypropylene/flax/aluminum trihydroxide." In: *Polymer Composites* 37.11 (2016), pp. 3310–3325. DOI: 10.1002/pc.23530.

[138] Ristolainen, N., Hippi, U., Seppälä, J., Nykänen, A. and Ruokolainen, J.: "Properties of polypropylene/aluminum trihydroxide composites containing nanosized organoclay." In: *Polymer Engineering & Science* 45.12 (2005), pp. 1568–1575. DOI: 10.1002/pen.20367.

[139] Lau, S., Gonchikzhapov, M., Paletsky, A., Shmakov, A., Korobeinichev, O., Kasper, T. and Atakan, B.: "Aluminum Diethylphosphinate as a Flame Retardant for Polyethylene: Investigation of the Pyrolysis and Combustion Behavior of PE/AlPi-Mixtures." In: *Combustion and Flame* 240 (2022), p. 112006. DOI: 10.1016/j.combustflame.2022.112006.

[140] Dérian, P.: "Wavelets and Optical Flow Motion Estimation." In: *Numerical Mathematics: Theory, Methods and Applications* 6.1 (2013), pp. 116–137. DOI: 10.4208/nmtma.2013.mssvm07.

[141] Nicolas, A., Zentgraf, F., Linne, M., Dreizler, A. and Peterson, B.: "Assessment and application of wavelet-based optical flow velocimetry (wOFV) to wall-bounded turbulent flows." In: *Experiments in fluids* 64.3 (2023), p. 50. DOI: 10.1007/s00348-023-03594-y.

[142] Liu, T. and Shen, L.: "Fluid flow and optical flow." In: *Journal of Fluid Mechanics* 614 (2008), pp. 253–291. DOI: 10.1017/S0022112008003273.

[143] Schneiders, L., Meinke, M. and Schröder, W.: "Direct particle–fluid simulation of Kolmogorov-length-scale size particles in decaying isotropic turbulence." In: *Journal of Fluid Mechanics* 819 (2017), pp. 188–227. DOI: 10.1017/jfm.2017.171.

[144] Schulz, C., Kock, B. F., Hofmann, M., Michelsen, H., Will, S., Bougie, B., Suntz, R. and Smallwood, G.: "Laser-induced incandescence: recent trends and current questions." In: *Applied Physics B* 83.3 (2006), pp. 333–354. DOI: 10.1007/s00340-006-2260-8.

A Journal publications

This section includes copies of all peer-reviewed scientific publications topically included in this cumulative dissertation.

A.1 Paper I - Ultra-high-speed PIV of turbulent flows

This paper was published in the journal Experiments in Fluids (Springer Nature) as open access. Open access articles in Springer Nature journals are published under Creative Commons licences, and in the case of Experiments in Fluids, the articles are published under a CC BY licence (Creative Commons Attribution 4.0 International licence). The CC BY licence allows readers to freely copy, redistribute, alter, transform, or build upon the material, even for commercial use, as long as proper credit is given to the original authors. Therefore, the authors retain full copyright of their article.

RESEARCH ARTICLE

Ultra-high-speed time-resolved PIV of turbulent flows using a continuously pulsing fiber laser

Christopher Geschwindner[1] · Katharina Westrup[1] · Andreas Dreizler[1] · Benjamin Böhm[1]

© The Author(s) 2022

Abstract

The application of a compact pulsed fiber laser for high-speed time-resolved particle image velocimetry (TR-PIV) measurements in the potential core of a turbulent round jet is presented at repetition rates of up to 500 kHz. The master oscillator power amplifier laser architecture consists of a pulsable seed diode whose emission is amplified in a Yb-doped fiber. The pulsed laser is operated continuously at repetition rates ranging from 10 kHz to 1 MHz with adjustable pulse widths at an output power of 50 W. The maximum rated pulse energy of 486 μJ is reached at 100 kHz, making the laser suitable for measurements of turbulent flows and highly transient phenomena. To demonstrate the feasibility of the laser for flow velocimetry, TR-PIV is conducted in a turbulent round jet. Two different high-speed camera systems are employed: a high-speed CMOS camera running at 200 kHz and 400 kHz and an in situ storage CCD camera for burst-mode PIV measurements at 500 kHz. For the CMOS system, the capability of measuring several characteristic quantities of turbulent flows is discussed with regard to the effects of uncertainty and spatial resolution. The presented system extends the range of suitable laser systems for high-speed PIV measurements offering continuous pulsing at repetition rates of up to 1 MHz at a compact footprint. The amount of consecutive images is solely limited by the onboard storage of the camera, which enables unprecedented temporal dynamic ranges.

Graphical Abstract

✉ Christopher Geschwindner
geschwindner@rsm.tu-darmstadt.de

1 Department of Mechanical Engineering, Reactive Flows and Diagnostics, Technical University of Darmstadt, Otto-Berndt-Straße 3, D-64287 Darmstadt, Germany
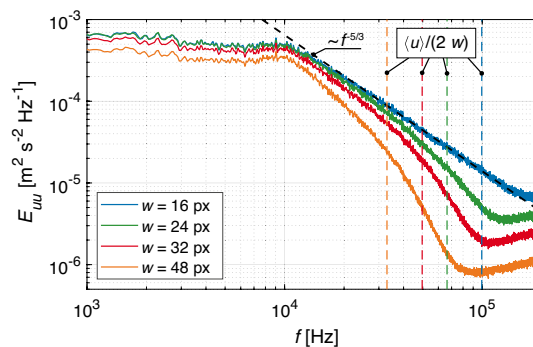
1 Introduction

Particle image velocimetry (PIV) has become a widely used experimental method to measure flow fields in various applications (Raffel et al. 2018; Westerweel et al. 2013). For the investigation of transient phenomena as they appear in turbulent flows, high-speed PIV (HS-PIV) systems with kilohertz repetition rates have become an established standard. Typically, nanosecond-pulsed high-power lasers are needed

🍃 Springer

to generate images with sufficient signal-to-noise ratio and low motion blur caused by particle movement during illumination. Within this work, we use the term *high-speed* for repetition rates beyond 1 kHz and *ultra-high-speed* for repetition rates beyond 100 kHz given that these terms have been defined loosely within the context of PIV or imaging methods.

Generally, two different approaches exist to generate time-resolved high-speed PIV (TR-PIV) recordings depending on the temporal recording scheme (Beresh 2021). The first option, employed within this work, is to operate both laser and camera systems continuously, creating a set of temporally equidistant images. The second approach, high-speed double-pulse PIV (DP-PIV), is commonly used when the maximum desirable particle shift between two consecutive images dictated by the interrogation window (IW) size requires an inter-frame time Δt smaller than the minimally possible duration between two laser pulses of one cavity or the minimally possible inter-frame recording duration of the camera at a given amount of utilized pixels. This recording scheme has been enabled by the introduction of high-speed dual-cavity lasers in combination with double-frame recording modes on modern high-speed camera sensors. As both laser cavities can be triggered individually, the particle shift of high-speed flows can be captured without the limitation of the repetition rate of a single laser cavity, which, however, still dictates the effective temporal resolution of the high-speed time series. TR-PIV data can be used to derive both statistical properties of turbulent flows and quantities only computable from time series of velocities such as integral time scales or spectra (Willert 2015; Beresh 2021). The latter makes TR-PIV suitable for replacing single-point hot-wire measurements with the additional benefit of local spatial information suitable for space–time correlation measurements (Wernet 2007). In the following, a brief summary of current high-speed camera and laser technologies for PIV applications is given including representative examples of investigations in the literature. Eventually, continuously pulsing fiber lasers are introduced in the context of flow velocimetry.

A multitude of digital high-speed imaging sensor technologies has emerged over the course of the last decades, which has enabled diagnostics of turbulent and highly transient flow phenomena. For high-speed PIV, three main technological approaches are worth noting: complementary metal-oxide-semiconductor (CMOS) sensors, burst image sensors including in situ storage image sensors (ISIS), and multi-sensor camera arrays. An overview on high-speed imaging technologies is found in Tsuji (2018) and Thurow et al. (2013). Continuous readout CMOS cameras are the most common category of imaging sensors found in high-speed PIV as they offer relatively small pixel sizes in the order of 20 μm/px enabling high spatial resolutions for

optimized particle imaging when coupled to high-quality lenses. Temporally, they offer frame rates of several 10 kHz at megapixel sensor sizes and can be run faster when the amount of active pixels is decreased. For instance, TR-PIV at 400 kHz for spectra measurements is possible when a small field of view (FOV) is chosen as exemplified by Beresh et al. (2018). The dual-frame exposure capabilities of such sensors can as well be utilized to perform DP-PIV given that a higher amount of active pixels is preferred over a desired temporal resolution. State-of-the-art ISIS sensors can be operated in burst-mode at full sensor size at repetition rates of up to 100 MHz (Suzuki et al. 2020). As the charge of each acquired image is stored on memory arrays on the sensor itself, the sensor size limits the number of acquired frames to a few hundred images. Due to the need of space for the in situ storage, however, the ratio of the photoactive area to the total sensor size for conventional CCD sensors is small, resulting in relatively large effective pixel sizes (e.g., 66.3 μm/px for the chip developed by Etoh et al. (2003) of the Shimadzu HPV-2 used within this study) and distortions of small imaged objects (Rossi et al. 2014), which imposes a challenge for the imaging of small tracer particles. Recently, CMOS burst image sensors, which make use of a spatial separation between the photosensitive pixels and their corresponding memory, have been developed to achieve an improved sensor array design for high-resolution imaging (Tochigi et al. 2013; Suzuki et al. 2020). When the amount of active pixels at a given frame rate is too small, multiple cameras can be optically combined in an array such that every sensor only images one or two frames (in dual-frame exposure mode) of the time series. Such systems have enabled full-frame megahertz PIV measurements (Wernet and Opalski 2004; Murphy and Adrian 2010; Brock et al. 2014) but obviously come at the cost of a very limited amount of consecutive recordings.

As of yet, three main laser architectures have been used for high-speed PIV measurements: clustered multi-channel (CMC) laser systems, diode-pumped solid state (DPSS) bulk lasers, and burst-mode lasers (Thurow et al. 2013; Slipchenko et al. 2020). CMC laser systems are used when high pulse energies at repetition rates much higher than individual laser cavities can provide are needed, such that each cavity corresponds to a single frame in the final PIV recording. Similar to multi-sensor camera arrays, the amount of consecutive pulses is limited by the amount of laser cavities, making CMC lasers only suitable for the observation of single events like flows close to propagating shock waves (Murphy and Adrian 2010). High-speed Q-switched DPSS lasers offer continuous pulsing operation at single-cavity repetition rates up to 150 kHz (Edgewave IS and GX series) and have been used extensively in fluid mechanics and combustion research applications (Böhm et al. 2011). In DP-PIV systems, dual-cavity DPSS lasers offer flexible transient adjustment of

the inter-frame pulse duration Δt, which, for instance, has enabled high-speed PIV in statistically unsteady turbulent flows in running combustion engines (Baum et al. 2014). Operation of DPSS laser systems is, however, challenging due to the limitations imposed by high thermal loads at high repetition rates and the optical beam overlap needed for flexible DP-PIV pulsing. In order to overcome the thermal limitations at higher repetition rates, burst-mode lasers operate at a limited duty cycle and are therefore able to reach sufficient energy output for operation in the megahertz range (Slipchenko et al. 2020). Modern systems rely on the *master oscillator power amplifier* (MOPA) architecture pioneered by Lempert et al. (1996) in which a low-power seed laser is guided through several amplification stages. Recent advancements have allowed for the development of compact doublet pulse systems incorporating fiber seed lasers utilized for DP-PIV at repetition rates of 100 kHz yielding pulse energies of 800 μJ at burst durations of 10 ms (Smyser et al. 2018). Longer burst durations of up to 100 ms have been enabled by dual-wavelength diode pumping (Slipchenko et al. 2014) utilized for spatio-temporal correlation measurements from DP-PIV at 100 kHz in the intermediate region of a turbulent jet (Miller et al. 2016). The data were subsequently analyzed to demonstrate deviations from Taylor's hypothesis of frozen turbulence by showing that the mean convective velocity is larger than the actual velocity of the time-delayed cross-correlation function (Roy et al. 2021). Other notable recent investigations using pulse-burst lasers include PIV measurements of supersonic jets emerging into a transonic wind tunnel (Beresh et al. 2015) and subsequent spectra measurements at 400 kHz (Beresh et al. 2018) and 1 MHz (Beresh et al. 2020) using a limited amount of active pixels on CMOS sensors. In reactive flows, pulse-burst lasers have been recently applied for 100 kHz PIV in a gas turbine swirl combustor simultaneously with OH* chemiluminescence imaging (Philo et al. 2021). While pulse-burst lasers have facilitated the majority of recent investigations with a focus on ultra-high-speed laser diagnostics, they suffer from limited burst durations due to overheating of the amplifier stages and a complicated optical architecture that demands high investment and maintenance costs and explains their almost exclusive usage within research applications.

As is apparent from the presented state-of-the-art laser systems for HS-PIV, several technological and practical limitations have to be dealt with when scaling laser systems up for ultra-high repetition rate PIV applications. First, thermal stress within the laser cavity limits the continuously available output power and repetition rate of DPSS systems, while the high pulse energy output of pulse-burst lasers is temporally limited by thermal constraints in the amplifiers. Thermal lensing changes the beam profile for increasing pump energies in both systems, too. Hence, neither laser architecture can currently provide a continuously pulsing

high-energy output at repetition rates beyond 150 kHz with unchanged beam profile characteristics over all power set points. Second, both DPSS and pulse burst lasers require the full laser system to be mounted rigidly onto a balanced surface for stable operation, which might be challenging for test environments with limited optical access and possible vibrations as they, e.g., appear in optically accessible engines. Third, the financial investment and maintenance costs of DPSS bulk lasers, and especially pulse-burst lasers, are high as they are often custom-built and not aimed toward a larger industrial market, limiting their usage to specific research applications in aerodynamics and combustion. This limitation might impede the wide-spread application of HS-PIV outside of these research communities.

Within this work, we introduce fiber lasers as an alternative laser architecture suitable for HS-PIV, which show an improved performance on all of the three discussed limitations. In the following, a brief introduction into the characteristics of fiber lasers is given. Fiber lasers have become a widespread variant among solid-state lasers within the last decades, frequently used in materials processing applications such as silicon scribing (Yang et al. 2016), milling (Williams et al. 2014), and marking (Gabzdyl 2008). Comprehensive information of fiber laser technology is provided by Samson and Dong (2013) and Ter-Mikirtychev (2019). The distinctive feature of fiber lasers and amplifiers is the fiber resonator design consisting of a core fiber doped with rare earth ions such as Nd^{3+}, Yb^{3+}, Er^{3+}, or Tm^{3+} covered in an undoped fiber through which the diode-laser pump beam is led. The center core design of such double-clad fibers is optimized such that the pump radiation always passes the doped center core, leading to an excitation of the laser crystal. In contrast with DPSS resonators or pulse-burst amplifiers, the ratio of the surface area to the volume of the crystal is large in optical fibers, leading to an efficient heat transfer to the outside of the fiber diminishing the need for active water cooling entirely. However, other loss mechanisms peculiar to fiber optics such as stimulated Brillouin scattering, stimulated Raman scattering, and Kerr nonlinearity have to be considered (Samson and Dong 2013).

Nanosecond-pulsed fiber lasers suitable for HS-PIV can either be realized by Q-switching or amplification of a diode laser seed pulse within a MOPA configuration. The latter approach allows for a flexible setting of the laser pulse width combined with a diffraction-limited beam quality at high fiber amplifier gains. As will be demonstrated with the fiber laser unit used within this work, pulsed MOPA configurations can be operated continuously at repetition rates of 1 MHz for average power outputs of 50 W with excellent beam quality factors. As the output laser beam is already led through a fiber, collimated output fibers can be directly mounted to fiber lasers enabling flexible output beam coupling in challenging environments. The fiber-based beam

path allows compact footprints and the use of standard components, enabling relatively low costs of ownership compared to DPSS and pulse-burst systems.

In this work, we systematically explore the feasibility of a state-of-the-art pulsed Yb:YAG fiber laser for ultra-high-speed TR-PIV measurements up to repetition rates of 500 kHz. Two camera systems, a high-speed CMOS camera and an in situ storage CCD camera, are used to capture the particle images taken in the potential core of a turbulent round jet.

The paper is structured as follows. Section 2 describes the basic properties of the utilized fiber laser system followed by a description of the experimental methodology in Sect. 3. Initial analysis of the investigations includes the assessment of the raw PIV images in Sect. 4.1 and the mitigation of peak locking in Sect. 4.2. Further, the computation of statistical turbulent moments based on an analysis of the measurement uncertainty is presented in Sect. 4.3, followed by a discussion of turbulent scales derived from correlation measurements in Sect. 4.4. The computation of temporal power spectral density measurements is discussed in Sect. 4.5, and the applicability of Taylor's hypothesis through an analysis of space–time correlations is presented in Sect. 4.6. The main findings are summarized in Sect. 5.

2 Fiber laser system

The laser system utilized for PIV within this study is a commercial nanosecond-pulsed Yb:YAG fiber laser (GLPN-500-1-50-M, IPG Photonics) depicted in Fig. 1a. The nanosecond-pulsed Yb:YAG fiber laser is based on the *master oscillator power amplifier* (MOPA) architecture in which a low-power seed laser is amplified by guiding the seed pulse through a pumped gain medium in which stimulated emission increases the final output power significantly. Here, a pulsed seed diode laser operated at 1030 nm is amplified within a Yb-doped double-clad fiber as depicted in Fig. 1b. The linear s-polarization of the seed laser beam is maintained within the single-mode fiber. Energy-efficient diode laser pumping of the fiber gain medium enables a compact

footprint of the laser module of $0.07 \, \text{m}^2$ ($0.27 \, \text{m} \times 0.26 \, \text{m}$), which is solely cooled through fans. The amplified laser pulse is guided into a water-cooled laser head by a 1.7-m-long delivery fiber, resulting in second-harmonic generation (SHG) to the final output wavelength of 515 nm. Table 1 summarizes the main technical properties of the fiber laser system.

Continuous operation of the laser is possible at pulse repetition rates (PRR) of 10 kHz to 1 MHz with a nominal average output power of 50 W. The MOPA architecture allows for a direct control of the seed laser pulse width. The maximum pulse energy of approx. 500 μJ is kept constant between 10 kHz and 100 kHz and further decreases with repetition rate such that the output power is kept constant at 50 W.

A measurement of the output laser beam profile at a PRR of 100 kHz using a beam-profiling CMOS camera (Win-CamD-LCM, Dataray) is shown in Fig. 2. As is apparent, the beam shows a symmetric Gaussian profile with only minor deviations, indicating the diffraction-limited beam quality obtained through the laser architecture. In fact, a fit of a 2D Gaussian profile described by $I(x, y) = \exp(-(x^2 + y^2)/\sigma^2)$ to the normalized profile yields a standard deviation

Table 1 Properties of the fiber laser. All values were obtained at the maximum setpoint of the diode laser drivers

Property	Value	Setting
Output wavelength	515 nm	
Polarization	s-polarized	
Pulse widths	1.3 ns (P_1), 4.4 ns (P_2), 11.8 ns (P_3)	
Repetition rates f	10 kHz–290 kHz	P_3
	10 kHz–600 kHz	P_2
	10 kHz–1 MHz	P_1
Pulse energies	486 μJ	$f = 100 \, \text{kHz}, P_3$
	162 μJ	$f = 300 \, \text{kHz}, P_2$
	48 μJ	$f = 1 \, \text{MHz}, P_1$
M^2	1.43	$f = 100 \, \text{kHz}, P_3$
Beam diameter ($1/e^2$)	2.68 mm	$f = 100 \, \text{kHz}, P_3$

Fig. 1 **a** Fiber laser system. **b** Internal fiber-based MOPA architecture
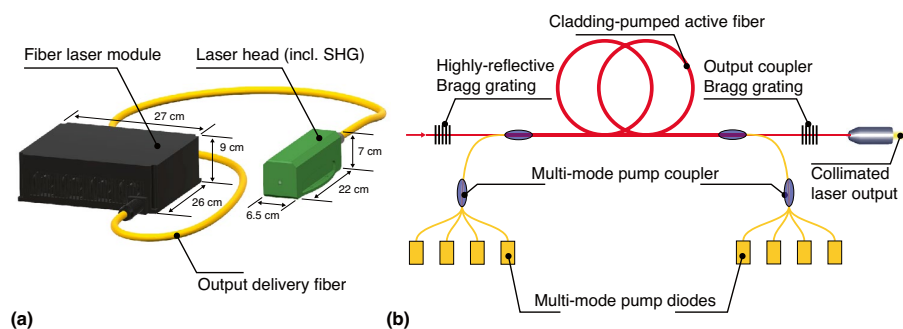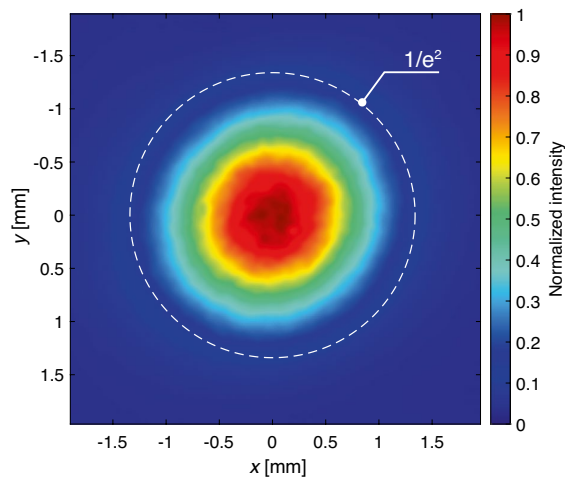
Fig. 2 Output beam intensity profile of the fiber laser. The dashed circle represents the radius of the fitted Gaussian bell curve at which the peak intensity has dropped to $1/e^2$

of $\sigma = 0.67\,\mathrm{mm}$ with a coefficient of determination of $R^2 = 0.987$. The beam diameter, calculated at a normalized intensity of $1/e^2$ is 2.68 mm. The measured beam quality factor of $M^2 = 1.43$ underlines the great potential of the laser to be focused to small beam waists, which is important for precise material processing applications. This is as well beneficial for PIV as thin laser sheets are needed to reach high spatial resolutions, although the bell-shaped laser profile has to be expanded wide enough in the perpendicular dimension to guarantee a homogeneous particle scattering intensity throughout the whole field of view. It has to be noted that the size and shape of the beam profile remain unchanged when the output intensity is varied which underlines the advantage of the laser architecture in contrast with thermal lensing occurring in bulk lasers and amplifiers of pulse-burst lasers.

3 Experimental methodology

To demonstrate the feasibility of the fiber laser system for the diagnostics of turbulent flows, TR-PIV was conducted within the potential core of an axisymmetric turbulent jet exiting as a fully developed pipe flow, which is a well-investigated generic configuration (Papadopoulos and Pitts 1998; Xu and Antonia 2002; Mi et al. 2001). The experimental setup is displayed in Fig. 3a.

A pipe of diameter $D = 2.8\,\mathrm{mm}$ was mounted horizontally within the burner head of the microwave plasma heater test stand at TU Darmstadt (Eitel et al. 2015). The stainless steel pipe can be used for fuel injection into hot co-flows and was therefore coated with a ceramic insulation, which
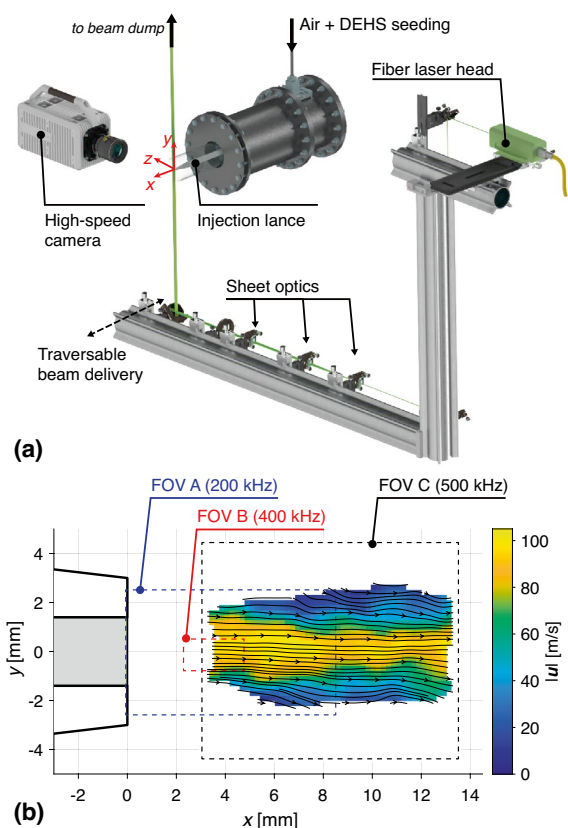
Fig. 3 a Experimental setup of the PIV measurements. **b** The fields of view investigated are displayed by dashed rectangles, whereby FOV A and FOV B were imaged using the SA-X2 and FOV C was imaged using the HPV-2

increased the size of the tip to an outer diameter of 6 mm as depicted in Fig. 3b. It was bent 90° upwards to facilitate injection of the jet flow from above. The straight part of the pipe from the bending to the jet exit had a length of 185D to ensure a fully developed turbulent pipe flow as boundary condition. Particle seeding was provided by an aerosol generator (AGF 10, Palas) generating di-ethylhexyl sebacate (DEHS) droplets with a mean size of 0.5 μm. The seeder was placed directly in front of the pipe connection to mitigate the influence of agglomeration on the particle size distribution. The air flow through the aerosol generator and pipe was regulated by mass flow controllers (EL-Flow Prestige, Bronkhorst) which were connected to a pressurized dried air supply system. The co-flow did not run during the experiments such that the ambient can be approximated as quiescent. As the near-field potential core region of the jet was analyzed within this study, the ambient air was not seeded with tracer particles. The jet flow was operated isothermally at ambient conditions of $T = 295\,\mathrm{K}$ and $p = 1\,\mathrm{bar}$. The operating points chosen for the experimental investigation at bulk

flow Reynolds numbers *Re* of 10,000 and 18,200 are displayed with the respective laser and camera configuration in Table 2.

The output head of the fiber laser was mounted directly on a traversable beam delivery system including all additional optics as shown in Fig. 3a. The high-speed cameras were rigidly connected to the traversing system as well (not shown) to fix the relative position of the laser beam and the field of view. The laser sheet was created by a set of cylindrical lenses (effective focal lengths of $f_1 = -50$ mm, $f_2 = 300$ mm, and $f_3 = 1000$ mm), which resulted in a beam thickness in the probe volume of 290 mm (FWHM) while being laterally expanded to a length of 35 mm. The laser sheet thickness was optimized as a compromise between high fluence resulting in sufficient Mie scattering signal from the DEHS particles and high spatial resolution on the one side, and the prevention of out-of-plane motion of the quickly moving particles in the turbulent flow on the other side.

Two high-speed camera systems were utilized in the TR-PIV analysis, a continuous readout CMOS camera (Photron FASTCAM SA-X2) and an in situ storage CCD camera (Shimadzu HPV-2), to evaluate their performance for UHS-TR-PIV measurements at different frame rates. The lens configurations and pixel calibration values are displayed in Table 2. Although the apertures of the camera lenses were fully open causing a limited depth of field, the small laser beam thickness resulted in a uniform size distribution of the particle images, which was verified by defocussing the lens and simultaneously observing changes in the imaged particle sizes throughout the frame. The fields of view of all three configurations are shown in Fig. 3b including an instantaneous vector field measured in configuration C. The SA-X2 recordings were used to capture the flow field directly at the jet exit at 200 kHz and for higher-resolved measurements in the centerline region starting at $x = 0.9D$ using a repetition rate of 400 kHz. The characteristic temporal and spatial turbulent scales of a round jet are smallest within its potential core, which

therefore serves as an ideal target to highlight the capabilities of an ultra high-speed repetition rate system at a finite spatial resolution, whose effect on measured turbulence properties will be discussed in Sect. 4. For the HPV-2 measurements, the flow velocity was increased and the measurement position was traversed slightly downstream to optimize the particle shift for the lower spatial resolution and higher repetition rate of the imaging system. The spatial resolution of correlation-based PIV algorithms was thoroughly investigated by Kähler et al. (2012) and is around the size of the interrogation window as long as particle images do not exceed more than 3 px.

The PIV images were captured and processed in the software Davis 10 (LaVision). The data acquisition system, laser, and camera were synchronized using an external timing unit (9520 Series, Quantum Composers). The length of each recording was solely limited by the on-board storage of the cameras, which resulted in over 1.2 million vector fields at 400 kHz for the SA-X2. Theoretically, this setting would allow for a temporal dynamic range (TDR), defined as the ratio of the highest to the lowest resolvable frequency, of over 600,000. However, as shown in Sect. 4.5 in the frequency domain, this value is limited by multiple other factors like noise, spatial resolution, and the variance of the power spectral density estimation (Beresh 2021) and will be evaluated based on the experimental results. For PIV processing, a correlation-based multi-pass algorithm with a window overlap of 75% was used. The final four passes at the smallest interrogation window size *w* were performed with a Gaussian weighting. This ensures better spatial resolution as the local information around the IW centroid is weighted higher and is commonly used in state-of-the-art PIV codes. The vectors were subsequently validated using the universal outlier detection method of Westerweel and Scarano (2005) using a 5×5 median filter kernel. No additional denoising (as proposed by Oxlade et al. (2012) for TR-PIV spectra measurement) was performed to sincerely assess the quality of the PIV data set for further analysis.

Table 2 Operating points and hardware used for the TR-PIV investigations of the near-nozzle region in the turbulent jet

Configuration	A	B	C
Bulk flow velocity u_b	55 m/s	55 m/s	100 m/s
Gas temperature T	295 K	295 K	295 K
Reynolds number Re	10,000	10,000	18,200
Camera system	SA-X2	SA-X2	HPV-2
Repetition rate f	200 kHz	400 kHz	500 kHz
Number of vector fields N	294,226	1,242,298	101
Lens configuration	Sigma 105 mm, *f*/2.8	Sigma 180 mm, *f*/3.5	Sigma 180 mm, *f*/3.5
Extension tube	–	–	80 mm
Pixel resolution	34.03 μm/px	19.60 μm/px	34.22 μm/px
Interrogation window length w	24 px	16 px, 24 px, 32 px, 48 px	24 px
Active sensor size	256 px × 152 px	128 px × 72 px	312 px × 260 px

4 Results and discussion

4.1 Assessment of raw particle images

As an initial step of analysis, the data quality of the raw images is assessed. Figure 4 shows representative single-shot particle images and their associated computed vector fields for every configuration. Recordings obtained with the SA-X2 CMOS camera show clearly distinguishable spherical particle shapes with sufficient signal-to-noise ratio to reliably compute a vector field. The single-shot raw images of the HPV-2 CCD in situ storage camera (Fig. 4e) were obtained at a similar pixel resolution than those at 200 kHz of the SA-X2 but could only be properly processed when defocussing the image slightly such that single particles have merged into a continuous structure. This was necessary as the large pixel size of the HPV-2 ($66.3 \, \mu m \times 66.3 \, \mu m$) is mainly needed for storage gates, which limits the ratio of the photoactive area to the entire pixel area (also referred to as fill factor) to only 0.6%. This poses a problem to accurate imaging of small-scale structures as it was reported by Rossi et al. (2014) for the same camera chip model. When small moving structures like particles are imaged in focus at the given magnification, the particle image does not span more than one pixel and even disappears completely when a particle position between two neighboring photoactive CCD areas is imaged. Subsequently, the particle image flashes and disappears as particles are moving from frame to frame which can only be avoided by defocusing the image slightly. Still, the mean correlation value of the PIV processing was 0.84 for the adjusted imaging system of the HPV-2, which

underlines the validity of the data for an ultra-high-speed flow analysis. It can be expected that the next generation of in situ storage cameras with smaller pixel pitch values based on CMOS technology can further improve the metrological performance of such a setup when high repetition rates are preferred over the amount of consecutively recorded frames (Suzuki et al. 2020).

It should be noted that at a repetition rate of 1 MHz, the PIV system was capable of capturing images with sufficient signal-to-noise ratio such that PIV processing would have been possible. However, due to the large pixel size and hence poor spatial resolution of the ISIS-CCD chip in combination with the limited flow rates dictated by the maximum throughput of the used seeder, all particle shifts were below 2 px such that the dynamic range of the computed vector field was poor.

4.2 Peak locking

A common systematic error introduced in PIV measurements is peak locking (Michaelis et al. 2016). This effect is relevant when the Mie scattering signal of a single particle is imaged smaller than one pixel, leading to a loss of sub-pixel accuracy resulting in preferential particle displacements to integer multiples of the imaged pixel resolution. Figure 5 displays the velocity histograms of the entire field of view of all vector fields of one measurement in units of pixel displacements together with the associated modulo plots for the two worst-resolved camera configurations. For the HPV-2, a total of 808 vector fields from eight camera bursts are included. Instead of comparing the velocity histograms at a fixed point, the display of velocities within the entire camera frame increases the amount of data points for the
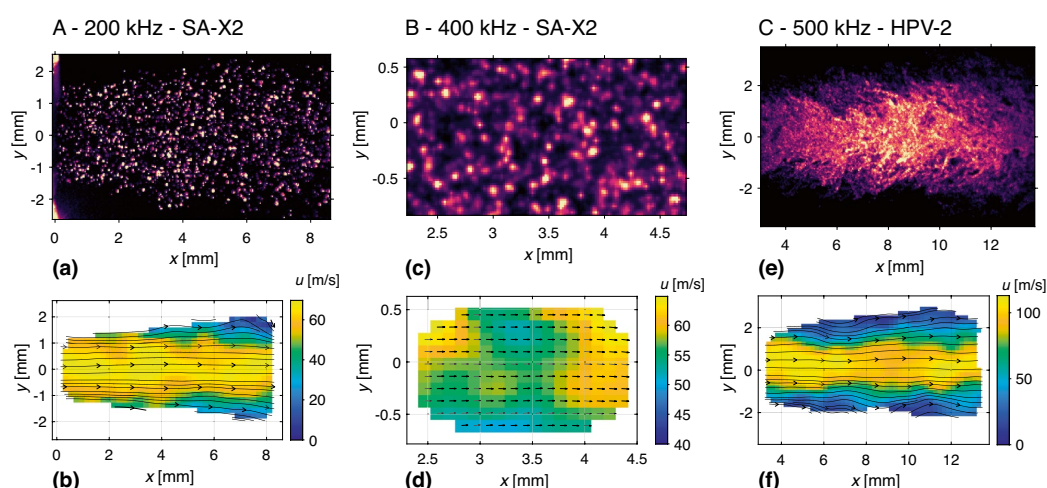
Fig. 4 Instantaneous snapshots of PIV raw images and their corresponding processed vector fields for all measurement configurations
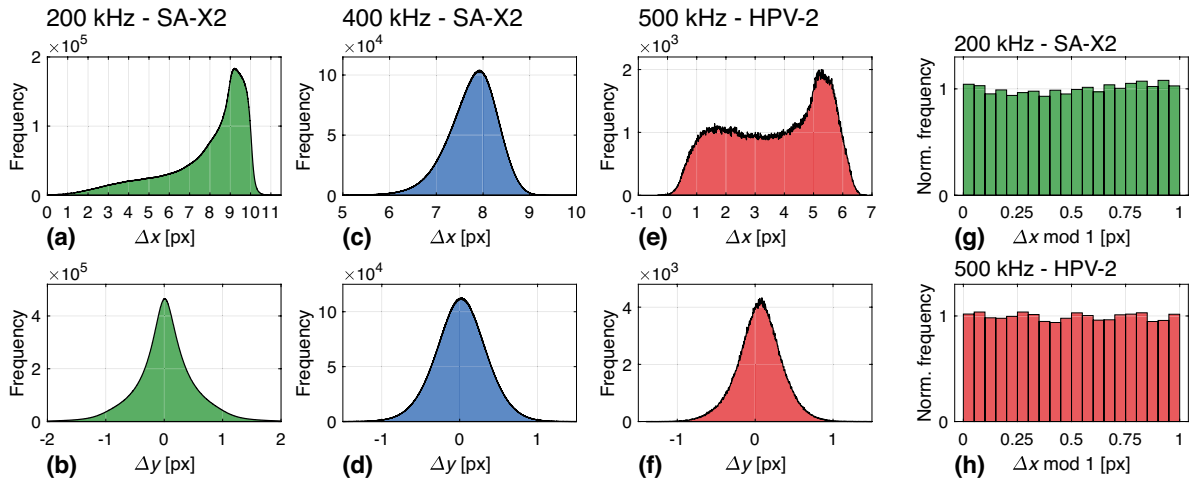
Fig. 5 a–f Velocity histograms within the entire FOV of the respective configurations displayed as pixel shifts Δx and Δy for all employed measurement setups. **g–h** Normalized histograms of the sub-pixel shift for the streamwise velocity component of measurements at 200 kHz using the SA-X2 and 500 kHz using the HPV-2 highlighting the suppression of peak locking of the presented PIV measurements

HPV-2 in comparison to the high amount of consecutively recorded vector fields of the SA-X2 CMOS camera. Hence, as the measurements encompass different fields of view, the histograms contain a wide range of velocities depending on their position within the jet (i.e., lower velocities in the shear layer and higher velocities in the centerline region of the potential core). As is apparent, the distributions show no clear sign of a preferential displacement toward integer multiples, demonstrating the negligible effect of peak locking for all presented measurements. Previously conducted high-speed TR-PIV measurements by Wernet (2007) (25 kHz) and Beresh et al. (2018) (400 kHz) both had to mitigate the effect of peak locking through the use of either special PIV processing algorithms or diffusion filters to spread out the particle image over several pixels. In this investigation, no additional filtering or post-processing was necessary as the pixel magnification was high enough to image particle scattering images larger than 1.5 pixels on average.

4.3 Measurement uncertainty and turbulence statistics measurement

Apart from the systematic errors introduced by peak locking, PIV measurements suffer from additional sources of uncertainty, whose quantification is important to reach accurate estimations of the local turbulence statistics. Generally, the measurement of statistical moments does not require time-resolved PIV but is usually performed using low-speed DP-PIV systems with statistically independent single shots of the flow field (as recently exemplified by Scharnowski et al. (2019) in a high-speed wind tunnel). However, as has been pointed out by Willert (2015) for the example of wall-bounded flows, TR-PIV offers the capability of efficiently extracting statistical measurements and quantities, which require a time series of the flow field like temporal correlations and spectra from the same measurement. For the CMOS camera, the large number of samples (in the case of 400 kHz over 1.2 mio. consecutively recorded vectors) is made possible by the continuously pulsing fiber laser and is solely limited by the on-board memory size of the camera. It should be noted, however, that the effective number of statistically independent samples N_e is lower and will be computed using the temporal autocorrelation of fluctuating velocities in Sect. 4.4.

As the camera noise level is increased substantially for measurements at repetition rates of several 100 kHz compared to the full frame operation at max. 12.5 kHz, the following section explores the PIV measurement uncertainty with respect to the size of the chosen interrogation window at a fixed position on the jet centerline and how the turbulence level and higher-order statistics are affected by the spatial filtering effect associated with an increase in the interrogation window size.

For the streamwise velocity component u, the turbulence level is computed by the ratio of the standard deviation σ_u, also referred to as the root-mean-square of the velocity fluctuations $\sqrt{\langle u'^2 \rangle}$, and the mean velocity $\langle u \rangle$ as is shown in Equation (1).

$$\mathrm{Tu}_u = \frac{\sigma_u}{\langle u \rangle} = \frac{\sqrt{\langle u'^2 \rangle}}{\langle u \rangle} \tag{1}$$

Generally, all measurement systems introduce errors to instantaneously measured velocities, whereby the apparent standard deviation of the measured velocity distribution $\sigma_{u,m}$

is a superposition of the true velocity fluctuations caused by turbulent motion of the flow $\sigma_{u,turb}$ and the measurement error $\sigma_{u,err}$ and can be expressed as Equation (2).

$$\sigma_{u,m}^2 = \sigma_{u,turb}^2 + \sigma_{u,err}^2 \approx \sigma_{u,turb}^2 + \sigma_{U_u}^2 \qquad (2)$$

This relationship implies that accurate turbulence level measurements should be conducted such that the error variance $\sigma_{u,err}^2$ is small compared to the actual fluctuations $\sigma_{u,turb}^2$. Otherwise, it is necessary to quantify the measurement error reliably such that the true velocity fluctuations $\sigma_{u,turb}^2$ can be extracted from the measured standard deviation of the velocity fluctuations. As the true error variance $\sigma_{u,err}^2$ is unknown, it will be approximated by the mean-square of the uncertainty of instantaneous velocities $\sigma_{U_u}^2$ which holds true for accurate uncertainty quantification methods as the number of independent observations approaches infinity (Sciacchitano et al. 2015; Sciacchitano and Wieneke 2016).

In the literature, several methods have been proposed to directly determine the measurement uncertainty from PIV recordings as was collaboratively explored by Sciacchitano et al. (2015). Alternatively, Scharnowski et al. (2019) have presented a method with which the measurement uncertainty and turbulence level can be extracted simultaneously through a variation in the particle shift Δx by altering the inter-frame time Δt of a DP-PIV system. Although this method is promising for accurate turbulence level measurements using DP-PIV systems, it has drawbacks with regard to the presented TR-PIV measurements in this study: a variation in the inter-frame time is not feasible for ultra-high repetition rates as a further decrease in Δt simultaneously increases the measurement uncertainty due to an increase in camera noise at higher recording speeds and a decreased signal-to-noise ratio due to a decrease in the laser pulse energy resulting in a lower Mie scattering intensity of individual tracer particles.

Therefore, the correlation statistics (CS) method of Wieneke (2015) was chosen to quantify the random uncertainty of the PIV measurements discussed within this study. As current uncertainty quantification methods including CS do not account for the error bias introduced through peak locking (Sciacchitano et al. 2015), the prevention of small particle images resulting in distorted velocity histograms as discussed in Sect. 4.2 is an important prerequisite for a reliable quantification of the random error.

To exemplify a turbulence level correction based on the uncertainty estimation, configurations A and B including measurements at 400 kHz and 200 kHz with varying interrogation window sizes are used in the following analysis at a fixed position of $x = 1.2D$ on the centerline. For configuration B, Fig. 6a shows the distribution of the instantaneous uncertainty of the streamwise velocity U_u both in units of meters per second and pixel shifts per image pair.

The uncertainty distributions reveal that an increase in the interrogation window size lowers the uncertainty (also expressed as the mean uncertainty $\langle U_u \rangle$ in Table 3). The uncertainty from the CS method takes the individual contribution of each pixel within the IW to the correlation calculation into account. Thus, as the IW size is increased, a larger number of particles is included in the correlation computation which mitigates the influence of noise that is overemphasized for smaller IW sizes and leads to an overall lower uncertainty value. Hence, a higher spatial resolution comes at the cost of higher individual velocity measurement uncertainties. This is especially evident when comparing the largest and smallest IW sizes in Fig. 6a. However, when observing the uncertainties for IW lengths of 24 px and 32 px, both distributions show similar uncertainties. This discontinuity from the previously identified trend might be explained when observing the distribution of the correlation values in Fig. 6b. As the IW size increases, the correlation
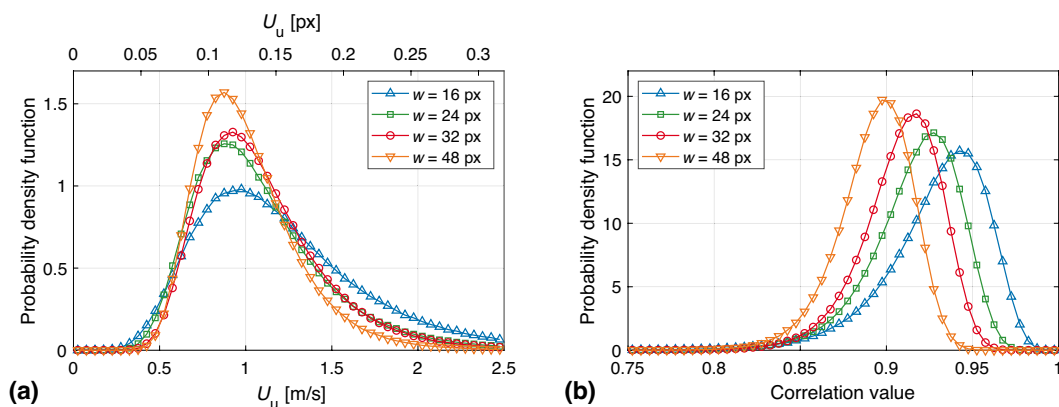
Fig. 6 **a** Uncertainty distribution of the streamwise velocity component. **b** Correlation value distribution for different interrogation window sizes at 400 kHz

Table 3 Uncertainty quantification based on the method of Wieneke ([2015](#)) and subsequent correction of the streamwise turbulence level for 400 kHz and 200 kHz at 1.2D (centerline). The last 2 data rows show results for elliptically weighted IW with weighting factors $w_x \times w_y$ for an IW length of $w = 32$ px

f	IW length w	$\langle U_u \rangle$	$\left\langle \dfrac{U_u}{u} \right\rangle$	$\dfrac{\sigma^2_{U_u}}{\sigma^2_{u,m}}$	$\mathrm{Tu}_{u,m}$	$\mathrm{Tu}_{u,corr}$
400 kHz	16 px / 313.5 µm	0.158 px / 1.236 m/s	2.00%	2.41%	5.86%	5.78%
400 kHz	24 px / 470.3 µm	0.1386 px / 1.087 m/s	1.75%	1.50%	5.45%	5.41%
400 kHz	32 px / 624.1 µm	0.1396 px / 1.094 m/s	1.76%	1.49%	4.95%	4.91%
400 kHz	48 px / 940.6 µm	0.129 px / 1.009 m/s	1.63%	1.42%	4.09%	4.06%
200 kHz	24 px / 816.6 µm	0.137 px / 1.070 m/s	1.64%	2.67%	3.42%	3.38%
	IW weights $w_x \times w_y$					
400 kHz	32 px × 16 px	0.1392 px / 1.091 m/s	1.76%	1.37%	5.11%	5.08%
400 kHz	16 px × 32 px	0.143 px / 1.124 m/s	1.82%	1.74%	4.83%	4.79%

values for the PIV vector calculation decrease, which is contrary to the trend of the uncertainty distributions. A reason for this could be the inhomogeneous nature of the turbulent shear flow in which these particles move: although the number of particles per IW increases with w, additionally included particles are differently positioned in the inhomogeneous flow field and therefore behave differently, lowering the correlation value. Besides, Westerweel ([2008](#)) has presented a theoretical analysis of how gradients within the correlation window correlation window lower the peak correlation values. Hence, for an increase in the IW size from 24 px and 32 px, the correlation values are decreased, which outweighs the decreased amount of noise in the correlation calculation for the uncertainty calculation.

As shown in Table 3, the mean absolute uncertainty ranges between 0.14 px and 0.16 px, which is equal to mean relative uncertainties between 1.63% and 2% of individually measured velocities. For the correction of the streamwise turbulence level, the ratio of the variance of the measurement uncertainty and the measured variance of the velocity fluctuations $\sigma^2_{U_u}/\sigma^2_{u,m}$ provides a measure of the amount of uncertainty contained in the measured velocity fluctuations. For the measurements taken at 400 kHz, this ratio increases as the IW size decreases, which results in a higher relative correction of the turbulence level from the measured value $\mathrm{Tu}_{u,m}$ to the corrected value $\mathrm{Tu}_{u,corr}$. At 200 kHz, an additional temporal filtering of the turbulent fluctuations results in a significantly smaller measured turbulence level, which translates into an increased ratio between measurement uncertainty and measured fluctuations. The results of the corrected turbulence levels finally show that as the repetition rate is increased and the IW size is decreased, the extent of temporal and spatial filtering of turbulent structures decreases leading to higher measured turbulence levels. The measured turbulence levels are similar to previously conducted measurements of the exit conditions of turbulent jets performed by Papadopoulos and Pitts ([1998](#)) ($\approx 4\%$ at $x/D = 0.16$), Xu and Antonia ([2002](#)) (4%), and Mi et al.

([2001](#)) ($\approx 3\%$ at $x/D = 0.05$) which used velocity measurements based on hot wire anemometry. Given that the measurements presented in Table 3 are located further downstream at $x/D = 1.2$, a slightly increased value to the literature references is reasonable.

Two additional rows in Table 3 show results for elliptically weighted interrogation windows with weighting factors $w_x \times w_y$ of 32 px × 16 px (axially aligned) and 16 px × 32 px (radially aligned). As both IWs have the same size, they should include a similar amount of noise. Still, the uncertainty of u of the radially aligned IW is on average higher than that of the axially aligned IW, further explaining the trends observed in Fig. 6 based on the inclusion of differently moving particles in the inhomogeneous flow as interrogation windows are increased in sized radially. It is interesting to note that $\sigma^2_{U_u}/\sigma^2_{u,m}$ for the axially aligned elliptically weighted IW is even lower than that of the square window of size $w = 48$ px, underlining the additional benefit of IWs with adapted shapes in shear flows.

The increasing measured turbulence level with decreasing IW size can be directly seen from the widths of the velocity histograms of configuration B in Fig. 7. Apart from the width of the distribution, which is associated with the standard deviation or magnitude of measured velocity fluctuations, it can be observed that the shape of the distribution functions are affected by a change of IW size, too. Namely, the smaller the size of the IW is set, the larger is the deviation of the skewness S and kurtosis K from the Gaussian reference values of $S = 0$ and $K = 3$ as is shown in Table 4. A similar trend is observed for elliptically weighted IWs with different orientations but equal size: the axially aligned IW displays a stronger departure from a Gaussian distribution than the radially aligned counterpart. Interestingly, former investigations in the exit region of a turbulent pipe jet have shown similar values to those measured with the smallest IW size of 16 px: Figure 1 of Papadopoulos and Pitts ([1998](#)) shows a measured skewness of –0.5 and a kurtosis of 3.4 at the jet exit (read from plot) and distributions of
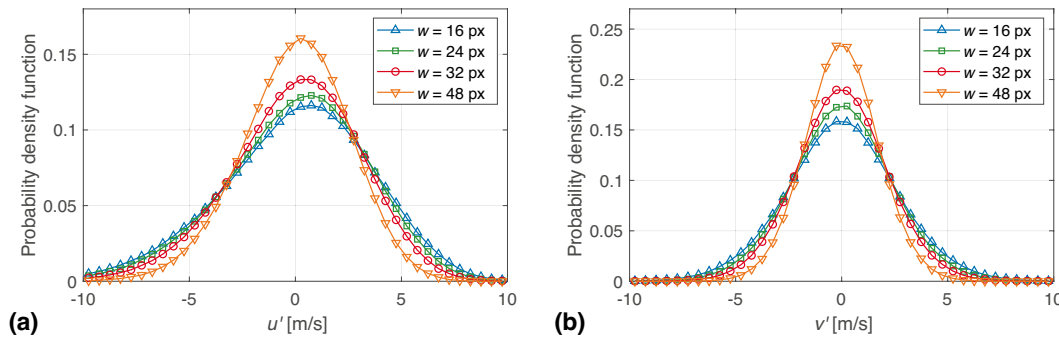
Fig. 7 Histograms of fluctuating velocities u' (**a**) and v' (**b**) for different interrogation window sizes at 400 kHz

Table 4 Skewness and kurtosis of the velocity fluctuations for 400 kHz at 1.2D (centerline)

f	IW length w	Skewness S_u	Kurtosis K_u	Skewness S_v	Kurtosis K_v
400 kHz	16 px / 313.5 µm	−0.43	3.38	−0.010	3.32
400 kHz	24 px / 470.3 µm	−0.40	3.30	−0.010	3.26
400 kHz	32 px / 624.1 µm	−0.35	3.25	−0.002	3.22
400 kHz	48 px / 940.6 µm	−0.25	3.14	−0.002	3.16
	IW weights $w_x \times w_y$				
400 kHz	32 px × 16 px	−0.38	3.25	−0.003	3.20
400 kHz	16 px × 32 px	−0.31	3.24	−0.002	3.23

the scalar fluctuations show similar values in Fig. 21 of Mi et al. (2001). Both experiments were conducted with wire probes, which were smaller than the majority of turbulent structures of the respective flows and only minimally filtered the measured quantities spatially. It can therefore be concluded that the larger the IW size is chosen, the higher will be the low-pass filtering effect resulting in a closer-to-Gaussian distribution shape quantified by higher-order statistics such as skewness and kurtosis.

To conclude, in an inhomogeneous flow as discussed herein, an increase in the IW size results in more particles being taken into account during vector calculations that are further away from the centerline and therefore exhibit different conditions in the shear flow of the turbulent jet. Filtering over a multitude of such differently moving particles results in a distribution closer to a normal distribution, suppressing the underlying probability distribution of turbulence structures. Similar to the measurement of turbulence intensities, the effect of spatial filtering of the IW needs to be considered when computing higher-order statistics in turbulent shear flows.

4.4 Measurement of turbulent scales using autocorrelations

Apart from the statistical analysis performed in Sect. 4.3, the high imaging rate and large sample size of the presented PIV

data sets enable a high-resolution analysis of velocity time series for correlations and power spectral density estimates. As the repetition rate is increased to 400 kHz for the highest temporal dynamic range, an IW length of 16 px only yields 32 vectors to be extracted along the axial coordinate (128 px window length with 75% IW overlap), limiting the spatial dynamic range. Therefore, this *postage-stamp* approach (Beresh et al. 2018) serves as a promising tool to extract temporally resolved data but lacks at providing simultaneous spatial information over larger spatial displacements.

First, the longitudinal integral turbulent scales are extracted at a planar spatial position $\mathbf{x} = (x, y)$ based on the Eulerian autocorrelation function

$$\rho_{uu}(\mathbf{x}, \xi, \tau) = \frac{\langle u'(\mathbf{x}, t)\, u'(\mathbf{x} + \xi, t + \tau)\rangle}{\sqrt{\langle u'^2(\mathbf{x}, t)\rangle\, \langle u'^2(\mathbf{x} + \xi, t + \tau)\rangle}} \quad (3)$$

where the spatial lag in two dimensions is denoted by $\xi = (\xi, \eta)$ and the temporal lag is expressed by τ. From this definition as the most general form of a space–time correlation in the Eulerian sense, the temporal autocorrelation can be calculated by setting $\xi = \mathbf{0}$, whereas the spatial autocorrelation is computed along the axial direction using $\xi = (\xi, 0)$ and $\tau = 0$. Figure 8a shows the results of the temporal autocorrelation at a position of $x = 1.2D$ on the centerline ($y = 0D$) and Fig. 8b displays the spatial autocorrelation at a position of $x = 0.9D$ on the centerline ($y = 0D$), such that

the full field of view of the 400 kHz measurements (until $x = 1.6D$) is encompassed by the spatial lag.

For both the spatial and temporal autocorrelations, a decrease in the IW size leads to an earlier decorrelation of the turbulent fluctuations. This observation can be explained by two superimposed effects. First, larger IW sizes lead to increased spatial filtering of small turbulent structures. These smaller structures will however decay quicker (according to the energy cascade) and are therefore not taken into account leading to an increased value of the correlation coefficient compared to smaller interrogation windows, which resolve smaller turbulent structures. Second, velocity vectors calculated within smaller interrogation windows are computed at higher noise levels, as less particles contribute to the overall correlation calculation. Consequently, a correlation of noisier velocity signals leads to a decreased value of the correlation coefficient as both the temporal and spatial lag increase (Nobach 2015).

Based on the correlation functions calculated, the integral scales (Eqs. (4) and (5)) are listed in Table 5. For the temporal autocorrelation, the computation of the integral time scale T_{uu} is realized by numerically integrating the correlation function until the first zero-crossing using the trapezoidal rule. Due to the limited spatial range, the integral length scale L_{uu} is only evaluated for the smallest IW of 16 px by integrating over all available data points. The correlation value at the highest spatial lag is 0.028 and therefore close to the zero-crossing such that the left out area under the correlation curve is small and the computed integral length scale is slightly underestimated. As the computed values show, an accurate measurement of the integral time scale requires high repetition rates (beyond 200 kHz to at least acquire 10 samples before the zero-crossing), which has been previously only achieved by pulse-burst lasers at significantly lower amounts of consecutively recorded samples (Miller et al. 2016).

Table 5 Longitudinal integral time scale at $x = 1.2D$ and length scale at $x = 0.9D$ (downstream) for 400 kHz TR-PIV measurements

f	IW length w	T_{uu}	L_{uu}
400 kHz	16 px / 313.5 μm	11.3 μs	623 μm
400 kHz	24 px / 470.3 μm	12.9 μs	
400 kHz	32 px / 624.1 μm	13.7 μs	
400 kHz	48 px / 940.6 μm	15.3 μs	

$$T_{uu} = \int_0^\infty \rho_{uu}(\tau)\, \mathrm{d}\tau \tag{4}$$

$$L_{uu} = \int_0^\infty \rho_{uu}(\xi)\, \mathrm{d}\xi \tag{5}$$

Additionally, the effective number of statistically independent samples N_e can be computed using Equation (6), where T_t is the total observation time of the time-resolved measurement (Sciacchitano and Wieneke 2016). For an IW size of 16 px, N_e is 137,831, showing that even though the temporal autocorrelation function is well-resolved, a large number of statistically independent samples for the robust computation of statistical moments remain.

$$N_e = \frac{(N-1)\, \Delta \tau}{2\, T_{uu}} = \frac{T_t}{2\, T_{uu}} \tag{6}$$

To put the measurements of statistical quantities into perspective, the standard measurement uncertainty of the mean axial velocity can be computed as $U_{\langle u \rangle} = \sigma_u / \sqrt{N_e} = 0.01$ m/s (Sciacchitano and Wieneke 2016). This small value truly shows the advantage of a TR-PIV measurement equipped with a continuously pulsing laser in combination with a large on-board memory of the camera to achieve a high value of N_e. In comparison to state-of-the-art low-speed PIV systems, it should be concluded that despite the lower amounts of N_e of these systems
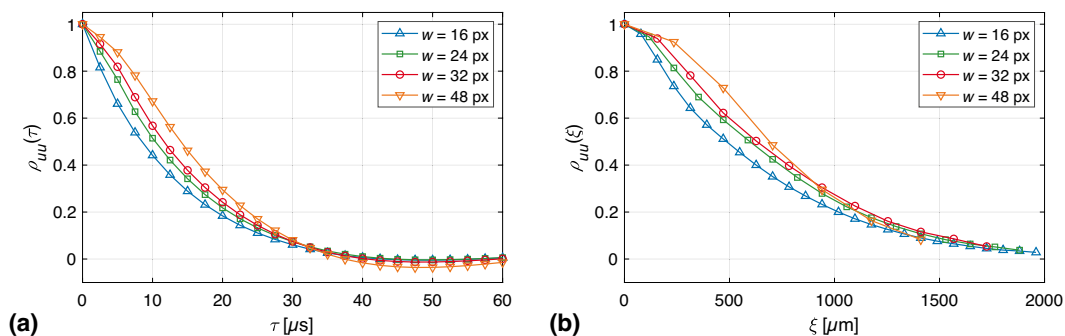
Fig. 8 Longitudinal autocorrelation functions of the streamwise velocity component ρ_{uu} from 400 kHz TR-PIV. **a** Temporal autocorrelation at a fixed position of $x = 1.2D$. **b** Spatial autocorrelation along the centerline at $x = 0.9D$

(typically around 1000), they still offer superior spatial resolution and lower measurement noise leading to lower uncertainties of individually measured vectors. For instance, Scharnowski et al. (2019) report a value of $\langle U_u \rangle = 0.05 \, \text{px}$ for an interrogation window length of 16 px compared to our measured value at the same IW size of $\langle U_u \rangle = 0.16 \, \text{px}$.

Based on the calculation of the integral scales, further characteristic turbulent scales can be determined. In isotropic turbulence, the Taylor microscale is defined as

$$\lambda = \sqrt{\frac{15\nu\sigma_u^2}{\varepsilon}} \tag{7}$$

where the dissipation rate of turbulent kinectic energy is given by ε and the kinematic viscosity is denoted by ν. A direct experimental determination of the Taylor microscale without the need of assuming isotropic turbulence requires a highly resolved measurement of the transverse autocorrelation R_{vv}, at which an osculating parabola is fitted, whose zero-crossing determines λ (Pope 2012). Due to the limited spatial resolution of the given measurements, this direct approach is unfortunately not feasible and equation (7) will be used instead. The smallest dissipative length scale is the Kolmogorov length scale η_k, which is given by equation (8).

$$\eta_k = \left(\frac{\nu^3}{\varepsilon}\right)^{\frac{1}{4}} \tag{8}$$

As is apparent from the definitions of λ and η_k, the dissipation rate of turbulent kinetic energy ε is required for the computation of both values. The determination of ε is, however, strongly affected by a limited spatial resolution, as ε is defined through the gradient tensor of fluctuating velocities, instead of the velocity fluctuations themselves (Pope 2012). A number of investigations have developed methods to improve the accuracy of dissipation rate measurements from PIV to extract ε from, e.g., curve fitting of energy spectra (Xu and Chen 2013) or using a large-eddy approach to correct for the filtering of the IW size (Bertens et al. 2015), but the results of these methods are dependent on the individual flow boundary conditions and further assumptions. Hence, we will employ a simple dimensional analysis to roughly estimate the turbulent dissipation rate using the integral length scale L_{uu} and the standard deviation of the axial velocity component σ_u (Batchelor 1953):

$$\varepsilon = \frac{C_\varepsilon \, \sigma_u^3}{L_{uu}} \approx \frac{\sigma_u^3}{L_{uu}} \tag{9}$$

Unfortunately, as discussed by Burattini et al. (2005), the constant C_ε is dependent on the boundary conditions of the flow and can not be assumed to be a universal constant. Available data in the literature ranges from values of

$C_\varepsilon = 0.5$–2.5 depending on flow type and turbulent Reynolds numbers (Burattini et al. 2005), which is why we estimate C_ε as unity in Equation (9). This approach at least guarantees an estimation of the order of magnitude of the derived turbulent scales. The results of the estimation of turbulent scales are 199 µm for the Taylor microscale and 15 µm for the Kolmogorov scale. The spatial resolutions of the PIV system estimated to be around 314 µm for the smallest IW size is in the order of the Taylor microscale and much larger than the Kolmogorov length.

4.5 Power spectral density estimation

Turbulence spectra provide detailed knowledge on the scales through which turbulent kinetic energy is transported in the energy cascade. Therefore, they offer the capability to compare differently resolved PIV measurements and their low-pass filtering characteristics on the small-scale portion of the turbulent structures. Their computation from time-resolved data is usually performed by a periodogram, which represents the Fourier transform of the biased estimate of the temporal autocorrelation. As 1242 298 consecutive time-resolved samples could be obtained at a repetition rate of 400 kHz, a periodogram spanning a frequency range of 0.32 Hz to 200 kHz (given by the sampling theorem) could theoretically be computed. However, the variance of the periodogram does not approach zero as the number of samples N is increased, making the periodogram an inconsistent estimate of the power spectrum (Hayes 1996). The widely used method of Welch solves this issue by intruducing a windowing scheme, such that the time series is separated into smaller overlapping portions for which a periodogram is computed. Subsequently, the individually computed periodograms are averaged, which results in a variance of zero as N approaches infinity, leading to a consistent estimate of the power spectrum (Welch 1967). Thus, a lower variance of the power spectral density is achieved by effectively lowering the spectral resolution, which is determined by the amount of samples in each window. This underlines the need for large amounts of continuously recorded velocity samples enabled by the fiber laser system to achieve low-variance high-resolution power spectrum estimates.

Figure 9 displays the temporal power spectral density estimations calculated using Welch's method on the centerline of the potential core at an axial distance of $x = 1.2D$. The signal was divided into portions of 6200 consecutive velocity samples and the overlap was chosen to be 50%. A Hann window function was applied to each periodogram calculation to minimize spectral leakage occuring during the discrete Fourier transform of the data sets. The chosen parameters lead to an increase in the minimally resolvable frequency to 64 Hz, which is still much lower than the relevant frequency scales of the turbulence decay.
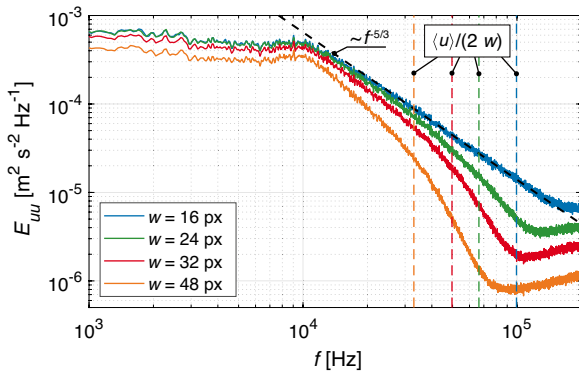
Fig. 9 Temporal power spectral density estimation from 400 kHz TR-PIV at $x = 1.2D$ (centerline)

The power spectral density curves all start to decay around a frequency of 10 kHz, marking the onset of the inertial subrange. This again shows that repetition rates beyond 100 kHz are necessary to capture large amounts of the turbulence decay. However, the maximum resolvable frequency is not only dependent on the sampling rate but also on several other factors:

– The spatial filtering of the finite interrogation window size also translates into a temporal filter through the convection of particles with the mean streamwise velocity $\langle u \rangle$. According to the sampling theorem and Taylor's hypothesis, the highest resolvable frequency through spatial filtering is computed through $\langle u \rangle/(2w)$ and highlighted by dashed lines for each IW size in Fig. 9. Beyond this limit, all curves but the smallest IW size of 16 px show a steeper slope of decay due to the spatial low-pass filtering, which seems to be the main limiting factor of the highest resolvable frequency for the given flow configuration and TR-PIV system. It is however interesting to note that the curves are already slightly separated before reaching the respective resolution limits. This behavior could be the result of the shear flow characteristics (similar to the changes observed in the velocity histograms) or the increased amount of noise for smaller IW sizes that increases the amplitude of the power spectral density.

– The frequency response of tracer particles is another factor that determines the maximum resolvable frequency of turbulent fluctuations. Following the analysis of Melling (1997), the used DEHS particles with a mean diameter of 0.5 μm have a response time τ_p of 0.8 μm, which is calculated as $\rho_p d_p^2/(18\mu)$. This can be used to derive the ratio between the kinetic energies of the particle velocity fluctuations and the fluid velocity fluctuations for high density ratios between particles and fluid as

$$\frac{\overline{u_p^2}}{\overline{u_f^2}} = (1 + 2\pi f \tau_p)^{-1}. \tag{10}$$

This ratio gradually decreases with the sampling frequency f such that a ratio of 0.5 (as suggested by Mei (1996)) is reached at a frequency of 190 kHz. Beresh et al. (2020) argues that this ratio can be further lowered to still resolve smaller velocity fluctuations as these contain a smaller amount of kinetic energy than large scales which is supported by in situ measurements of the particle response time. Hence, the particle response should not be the limiting factor in the presented TR-PIV measurements in this work.

– As was already observed earlier, velocity time series calculated from smaller IW sizes are subject to higher amounts of noise, which adds to the overall spectral density estimation. Although the spatial low-pass filtering effect is less pronounced for smaller interrogation windows, the amplitude of the high-frequency noise floor is increased compared to larger IW lengths. Again, the trade-off between noise (or uncertainty of velocity measurements) and spatial resolution is apparent and has to be considered when performing turbulence analysis using PIV data.

It should be noted that multi-frame correlation algorithms could decrease the high-frequency correlation noise level as was recently assessed (Beresh et al. 2021). However, the particle shift per image pair of the presented measurements at 400 kHz was too large such that a multi-frame correlation algorithm could not improve the noise level of the high-frequency content of the measurements.

The results show that several factors have to be considered when assessing the temporal dynamic range of spectral density estimations. Despite these limitations however, the continuously pulsing fiber laser architecture enables unprecedented amounts of consecutively recorded samples at similar repetition rates to pulse-burst laser systems (Beresh et al. 2018; Miller et al. 2016) enabling a detailed analysis of small-scale turbulent flow structures.

4.6 Space–time correlations and applicability of Taylor's hypothesis

Due to the decreased amount of active pixels of the CMOS camera at high repetition rates, the computation of spatial spectra relies on the transformation of temporal to spatial quantities. This is classically performed using Taylor's hypothesis of frozen turbulence (Taylor 1938), which relies on the assumption that turbulent structures are convected by the mean velocity such that a straightforward

transformation of temporal to spatial frequencies is performed as $\kappa = f/\langle u \rangle$. This hypothesis is, however, only applicable in flows with low turbulence levels and is known to fail in free shear flows (Pope 2012; Del Álamo and Jiménez 2009). One option to experimentally test the applicability of Taylor's hypothesis is an analysis of the space–time correlation $\rho_{uu}(\xi, \tau)$ (Wallace 2014; He et al. 2017). As TR-PIV offers the extraction of space–time correlations from a single measurement (Wernet 2007), it has been recently applied to analyze the deviations from Taylor's hypothesis in the intermediate regions of a turbulent jet at a repetition rate of 100 kHz (Roy et al. 2021). It is therefore interesting to test if a deviation is observable on the centerline of the potential core, which shows a much lower turbulence level ($\mathrm{Tu}_u \approx 5\%$) than the fully developed region of the turbulent jet ($\mathrm{Tu}_u \approx 25\%$) (Xu and Antonia 2002; Mi et al. 2001). Although the spatial extent of the TR-PIV measurements of this work is fairly limited, a calculation of the space–time correlation $\rho_{uu}(\xi, \tau)$ according to equation (3) at moderate spatials lags is possible and was performed for both 200 kHz and 400 kHz as is shown in Fig. 10.

The isocorrelations, which are displayed by filled contours, represent elongated ellipses, as both numerical and experimental investigations of turbulent shear flows have shown before (Wernet 2007; Wallace 2014; Del Álamo and Jiménez 2009). If Taylor's hypothesis would hold true, the isocorrelation contours were straight lines, whose slope represent the convection velocity with which turbulent structures are transported through the flow field (Zhao and He 2009; He et al. 2017). In the limited field of view of the 400 kHz measurements in Fig. 10b, this assumption is met with minor deviations. However, due to the decay of turbulence, the value of the correlation decreases from 1 at zero temporal and spatial lag as turbulent structures are convected downstream. The space–time correlations at 200 kHz in Fig. 10a provide a more complete view of the isocorrelation

shapes, which become more asymmetric as the spatial and temporal lags increase.

A direct measure of this deviation can be given by comparing the convection of fluid elements by the mean axial velocity $\langle u \rangle$ (dashed line) with the location of the correlation peak over several time lags (circles) in Fig. 10. It should be noted that the change in mean velocity over spatial lags was taken into account when calculating the convection of fluid elements. While the convection of turbulent structures is initially matching the mean velocity of the flow field, it deviates significantly at large lags. The decreased axial turbulent convection speed on the centerline is in parts a direct consequence of the local magnitude and direction of turbulent fluctuations, as fluid elements, which are radially transported away from the centerline through fluctuations are subject to lower mean velocities and will hence be convected more slowly in the axial direction. Further detailed investigations are, however, necessary to quantify the contributions of different influences to this phenomenon, especially considering the coupling between Eulerian and Lagrangian space–time correlations (He et al. 2017; Viggiano et al. 2021). While the differences are much smaller than those observed in the intermediate region by Roy et al. (2021), they show that a high-resolution TR-PIV system equipped with a fiber laser is capable of reliably measuring deviations from Taylor's hypothesis in a region of relatively low turbulence intensity.

5 Conclusion

The application of a Yb:YAG fiber laser for ultra-high-speed time-resolved particle image velocimetry was demonstrated in the potential core of a turbulent round jet. The system provides sufficient pulse energy and excellent beam profile characteristics at repetition rates up to 1 MHz for the velocimetry of highly transient turbulent flows. Two different high-speed cameras, a CMOS and an in situ storage CCD camera,
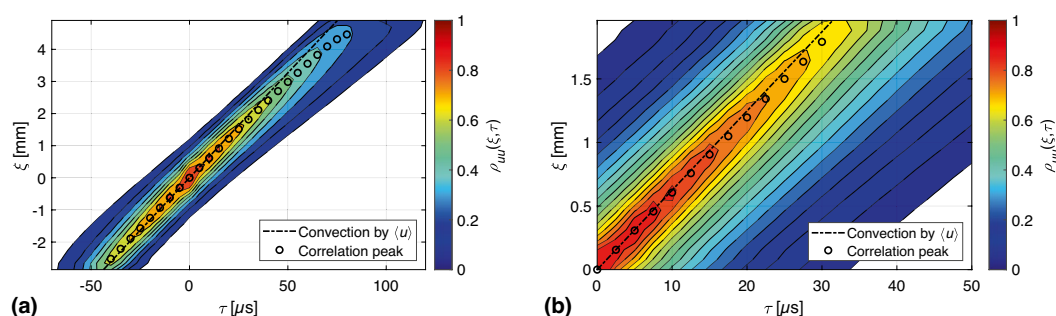
Fig. 10 Space–time correlations of the streamwise velocity fluctuations $\rho_{uu}(\xi, \tau)$ on the centerline: **a** 200 kHz TR-PIV centered around $x = 1.2D$, **b** 400 kHz TR-PIV encompassing $x = 0.9D$ to $x = 1.6D$. Convection of fluid elements through the mean streamwise velocity $\langle u \rangle$ is shown by a dashed line, while the convection of the correlation peak is shown by circles

© Springer

were employed to demonstrate turbulence measurements at repetition rates up to 500 kHz.

The continuously pulsing laser enables the recording of large time series, which can be used to derive statistical quantities of turbulence, space–time correlations, and turbulence spectra. The quality of the PIV recordings was assessed in terms of their spatial resolution and measurement uncertainty, whose dependence on the interrogation window size was quantified. The computation of turbulent scales was demonstrated at a repetition rate of 400 kHz, which was necessary to resolve the autocorrelations reasonably well. The influence of the interrogation window size on the power spectral density was investigated, which showed that the spatial resolution was the limiting factor of the frequency resolution of the presented TR-PIV measurements. Finally, space–time correlations revealed the deviations from Taylor's hypothesis of frozen turbulence through a comparison of the convection velocity of the correlation peak with the mean axial flow velocity.

The demonstrated measurements show that the recent development of pulsed fiber laser technology can provide new insights into turbulent flows at a compact footprint and high flexibility. Future high-speed PIV investigations will strongly benefit from this advancement as unprecedented temporal dynamic ranges are possible, which challenge existing laser solutions for high-speed flow velocimetry.

Declarations

References

Batchelor GK (1953) The theory of homogeneous turbulence. Cambridge science classics. Cambridge University Press, Cambridge

Baum E, Peterson B, Böhm B, Dreizler A (2014) On the validation of LES applied to internal combustion engine flows: Part 1: Comprehensive experimental database. Flow Turbul Combust 92(1–2):269–297. https://doi.org/10.1007/s10494-013-9468-6

Beresh SJ (2021) Time-resolved particle image velocimetry. Meas Sci Technol 32(10):102003. https://doi.org/10.1088/1361-6501/ac08c5

Beresh S, Kearney S, Wagner J, Guildenbecher D, Henfling J, Spillers R, Pruett B, Jiang N, Slipchenko M, Mance J, Roy S (2015) Pulse-burst PIV in a high-speed wind tunnel. Meas Sci Technol 26(9):095305. https://doi.org/10.1088/0957-0233/26/9/095305

Beresh SJ, Henfling JF, Spillers RW, Spitzer SM (2018) 'Postage-stamp PIV': small velocity fields at 400 kHz for turbulence spectra measurements. Meas Sci Technol 29(3):034011. https://doi.org/10.1088/1361-6501/aa9f79

Beresh SJ, Spillers R, Soehnel M, Spitzer S (2020) Extending the frequency limits of postage-stamp PIV to MHz rates. In: AIAA Scitech 2020 Forum, American Institute of Aeronautics and Astronautics, Reston, Virginia. https://doi.org/10.2514/6.2020-1018

Beresh SJ, Neal D, Sciacchitano A (2021) Validation of multi-frame PIV image interrogation algorithms in the spectral domain. In: AIAA Scitech 2021 Forum, American Institute of Aeronautics and Astronautics, Reston, Virginia. https://doi.org/10.2514/6.2021-0019

Bertens G, van der Voort D, Bocanegra-Evans H, van de Water W (2015) Large-eddy estimate of the turbulent dissipation rate using PIV. Exp Fluids. https://doi.org/10.1007/s00348-015-1945-3

Böhm B, Heeger C, Gordon RL, Dreizler A (2011) New perspectives on turbulent combustion: multi-parameter high-speed planar laser diagnostics. Flow Turbul Combust 86(3–4):313–341. https://doi.org/10.1007/s10494-010-9291-2

Brock B, Haynes RH, Thurow BS, Lyons GW, Murray NE (2014) An examination of MHz rate PIV in a heated supersonic jet. In: 52nd Aerospace Sciences Meeting, American Institute of Aeronautics and Astronautics, Reston, Virginia. https://doi.org/10.2514/6.2014-1102

Burattini P, Lavoie P, Antonia RA (2005) On the normalized turbulent energy dissipation rate. Phys Fluids 17(9):098103. https://doi.org/10.1063/1.2055529

Del Álamo JC, Jiménez J (2009) Estimation of turbulent convection velocities and corrections to Taylor's approximation. J Fluid Mech 640:5–26. https://doi.org/10.1017/S0022112009991029

Eitel F, Pareja J, Geyer D, Johchi A, Michel F, Elsäßer W, Dreizler A (2015) A novel plasma heater for auto-ignition studies of turbulent non-premixed flows. Exp Fluids. https://doi.org/10.1007/s00348-015-2059-7

Etoh TG, Poggemann D, Kreider G, Mutoh H, Theuwissen A, Ruckelshausen A, Kondo Y, Maruno H, Takubo K, Soya H, Takehara K, Okinaka T, Takano Y (2003) An image sensor which captures 100 consecutive frames at 1 000 000 frames/s. IEEE Trans Electron Dev 50(1):144–151. https://doi.org/10.1109/TED.2002.806474

Gabzdyl J (2008) Fibre lasers make their mark. Nature Photon 2(1):21–23. https://doi.org/10.1038/nphoton.2007.268

Hayes MH (1996) Statistical digital signal processing and modeling. Wiley, New York, NY

He G, Jin G, Yang Y (2017) Space-time correlations and dynamic coupling in turbulent flows. Ann Rev Fluid Mech 49(1):51–70. https://doi.org/10.1146/annurev-fluid-010816-060309

Kähler CJ, Scharnowski S, Cierpka C (2012) On the resolution limit of digital particle image velocimetry. Exp Fluids 52(6):1629–1639. https://doi.org/10.1007/s00348-012-1280-x

Lempert W, Wu PF, Miles R, Zhang B, Lowrance J, Mastrocola V, Kosonocky W (1996) Pulse-burst laser system for high-speed flow diagnostics. In: 34th Aerospace Sciences Meeting and Exhibit, American Institute of Aeronautics and Astronautics, Reston, Virigina

Mei R (1996) Velocity fidelity of flow tracer particles. Exp Fluids 22(1):1–13. https://doi.org/10.1007/BF01893300

Melling A (1997) Tracer particles and seeding for particle image velocimetry. Meas Sci Technol 8(12):1406–1416. https://doi.org/10.1088/0957-0233/8/12/005

Mi J, Nobes DS, Nathan GJ (2001) Influence of jet exit conditions on the passive scalar field of an axisymmetric free jet. J Fluid Mech 432:91–125. https://doi.org/10.1017/S0022112000003384

Michaelis D, Neal DR, Wieneke B (2016) Peak-locking reduction for particle image velocimetry. Meas Sci Technol 27(10):104005. https://doi.org/10.1088/0957-0233/27/10/104005

Miller JD, Jiang N, Slipchenko MN, Mance JG, Meyer TR, Roy S, Gord JR (2016) Spatiotemporal analysis of turbulent jets enabled by 100-kHz, 100-ms burst-mode particle image velocimetry. Exp Fluids. https://doi.org/10.1007/s00348-016-2279-5

Murphy MJ, Adrian RJ (2010) PIV space-time resolution of flow behind blast waves. Exp Fluids 49(1):193–202. https://doi.org/10.1007/s00348-010-0843-y

Nobach H (2015) A model-free noise removal for the interpolation method of correlation and spectral estimation from laser Doppler data. Exp Fluids. https://doi.org/10.1007/s00348-015-1975-x

Oxlade AR, Valente PC, Ganapathisubramani B, Morrison JF (2012) Denoising of time-resolved PIV for accurate measurement of turbulence spectra and reduced error in derivatives. Exp Fluids 53(5):1561–1575. https://doi.org/10.1007/s00348-012-1375-4

Papadopoulos G, Pitts WM (1998) Scaling the near-Field centerline mixing behavior of axisymmetric turbulent jets. AIAA J 36(9):1635–1642. https://doi.org/10.2514/2.565

Philo JJ, Frederick MD, Slabaugh CD (2021) 100 kHz PIV in a liquid-fueled gas turbine swirl combustor at 1 MPa. Proc Combust Inst 38(1):1571–1578. https://doi.org/10.1016/j.proci.2020.06.066

Pope SB (2012) Turbulent flows. Cambridge University Press, Cambridge. https://doi.org/10.1017/CBO9780511840531

Raffel M, Willert CE, Scarano F, Kähler CJ, Wereley ST, Kompenhans J (2018) Particle image velocimetry. Springer International Publishing, Cham. https://doi.org/10.1007/978-3-319-68852-7

Rossi M, Pierron F, Forquin P (2014) Assessment of the metrological performance of an in situ storage image sensor ultra-high speed camera for full-field deformation measurements. Meas Sci Technol 25(2):025401. https://doi.org/10.1088/0957-0233/25/2/025401

Roy S, Miller JD, Gunaratne GH (2021) Deviations from Taylor's frozen hypothesis and scaling laws in inhomogeneous jet flows. Commun Phys. https://doi.org/10.1038/s42005-021-00528-0

Samson B, Dong L (2013) Fiber lasers. In: Handbook of solid-state lasers, Elsevier, pp 403–462, https://doi.org/10.1533/9780857097507.2.403

Scharnowski S, Bross M, Kähler CJ (2019) Accurate turbulence level estimations using PIV/PTV. Exp Fluids. https://doi.org/10.1007/s00348-018-2646-5

Sciacchitano A, Wieneke B (2016) PIV uncertainty propagation. Meas Sci Technol 27(8):084006. https://doi.org/10.1088/0957-0233/27/8/084006

Sciacchitano A, Neal DR, Smith BL, Warner SO, Vlachos PP, Wieneke B, Scarano F (2015) Collaborative framework for PIV uncertainty quantification: comparative assessment of methods. Meas Sci Technol 26(7):074004. https://doi.org/10.1088/0957-0233/26/7/074004

Slipchenko MN, Miller JD, Roy S, Meyer TR, Mance JG, Gord JR (2014) 100 kHz, 100 ms, 400 J burst-mode laser with dual-wavelength diode-pumped amplifiers. Opt Lett 39(16):4735–4738. https://doi.org/10.1364/OL.39.004735

Slipchenko MN, Meyer TR, Roy S (2020) Advances in burst-mode laser diagnostics for reacting and nonreacting flows. Proc Combust Inst 38(1):1533-1560. https://doi.org/10.1016/j.proci.2020.07.024

Smyser ME, Rahman KA, Slipchenko MN, Roy S, Meyer TR (2018) Compact burst-mode Nd:YAG laser for kHz-MHz bandwidth velocity and species measurements. Opt Lett 43(4):735–738. https://doi.org/10.1364/OL.43.000735

Suzuki M, Sugama Y, Kuroda R, Sugawa S (2020) Over 100 Million Frames per Second 368 Frames Global Shutter Burst CMOS Image Sensor with Pixel-wise Trench Capacitor Memory Array. Sensors. https://doi.org/10.3390/s20041086

Taylor GI (1938) The Spectrum of Turbulence. Proc Royal Soc London Series A - Math Phys Sci 164(919):476–490. https://doi.org/10.1098/rspa.1938.0032

Ter-Mikirtychev VV (2019) Fundamentals of fiber lasers and fiber amplifiers, vol 181. Springer International Publishing, Cham. https://doi.org/10.1007/978-3-030-33890-9

Thurow B, Jiang N, Lempert W (2013) Review of ultra-high repetition rate laser diagnostics for fluid dynamic measurements. Meas Sci Technol 24(1):012002. https://doi.org/10.1088/0957-0233/24/1/012002

Tochigi Y, Hanzawa K, Kato Y, Kuroda R, Mutoh H, Hirose R, Tominaga H, Takubo K, Kondo Y, Sugawa S (2013) A global-shutter CMOS image sensor with readout speed of 1-Tpixel/s burst and 780-Mpixel/s continuous. IEEE J Solid-State Circuits 48(1):329–338. https://doi.org/10.1109/JSSC.2012.2219685

Tsuji K (2018) The micro-world observed by ultra high-speed cameras. Springer International Publishing, Cham. https://doi.org/10.1007/978-3-319-61491-5

Viggiano B, Basset T, Solovitz S, Barois T, Gibert M, Mordant N, Chevillard L, Volk R, Bourgoin M, Cal RB (2021) Lagrangian diffusion properties of a free shear turbulent jet. J Fluid Mech. https://doi.org/10.1017/jfm.2021.325

Wallace JM (2014) Space-time correlations in turbulent flow: a review. Theo Appl Mech Lett 4(2):022003. https://doi.org/10.1063/2.1402203

Welch P (1967) The use of fast Fourier transform for the estimation of power spectra: a method based on time averaging over short, modified periodograms. IEEE Trans Audio Electroacous 15(2):70–73. https://doi.org/10.1109/TAU.1967.1161901

Wernet M, Opalski A (2004) Development and application of a MHZ frame rate digital particle image velocimetry system. In: 24th AIAA Aerodynamic Measurement Technology and Ground Testing Conference, American Institute of Aeronautics and Astronautics, Reston, Virigina. https://doi.org/10.2514/6.2004-2184

Wernet MP (2007) Temporally resolved PIV for space-time correlations in both cold and hot jet flows. Meas Sci Technol 18(5):1387–1403. https://doi.org/10.1088/0957-0233/18/5/027

Westerweel J (2008) On velocity gradients in PIV interrogation. Exp Fluids 44(5):831–842. https://doi.org/10.1007/s00348-007-0439-3

Westerweel J, Scarano F (2005) Universal outlier detection for PIV data. Exp Fluids 39(6):1096–1100. https://doi.org/10.1007/s00348-005-0016-6

Westerweel J, Elsinga GE, Adrian RJ (2013) Particle image velocimetry for complex and turbulent flows. Ann Rev Fluid Mech 45(1):409–436. https://doi.org/10.1146/annurev-fluid-120710-101204

Wieneke B (2015) PIV uncertainty quantification from correlation statistics. Meas Sci Technol 26(7):074002. https://doi.org/10.1088/0957-0233/26/7/074002

Willert CE (2015) High-speed particle image velocimetry for the efficient measurement of turbulence statistics. Exp Fluids. https://doi.org/10.1007/s00348-014-1892-4

Williams E, Brousseau EB, Rees A (2014) Nanosecond Yb fibre laser milling of aluminium: effect of process parameters on the achievable surface finish and machining efficiency. Int J Adv Manuf Technol 74(5–8):769–780. https://doi.org/10.1007/s00170-014-6038-6

Xu D, Chen J (2013) Accurate estimate of turbulent dissipation rate using PIV data. Exp Therm Fluid Sci 44:662–672. https://doi.org/10.1016/j.expthermflusci.2012.09.006

Xu G, Antonia R (2002) Effect of different initial conditions on a turbulent round free jet. Exp Fluids 33(5):677–683. https://doi.org/10.1007/s00348-002-0523-7

Yang L, Huang W, Deng M, Li F (2016) MOPA pulsed fiber laser for silicon scribing. Opt Laser Technol 80:67–71. https://doi.org/10.1016/j.optlastec.2016.01.006

Zhao X, He GW (2009) Space-time correlations of fluctuating velocities in turbulent shear flows. Phys Rev E Stat Nonlinear Soft Matter Phys 79(4 Pt 2):046316. https://doi.org/10.1103/PhysRevE.79.046316

A.2 Paper II – Two-phase velocimetry of biomass-laden jets

Reproduced with permission from Elsevier.

Pulse picking of a fiber laser enables velocimetry of biomass-laden jets at low and ultra-high repetition rates

Christopher Geschwindner*, Katharina Westrup, Andreas Dreizler,
Benjamin Böhm

*Technical University of Darmstadt, Department of Mechanical Engineering, Reactive Flows and Diagnostics,
Otto-Berndt-Str. 3, Darmstadt 64287, Germany*

Abstract

The introduction of fibrous aspherical biomasses for the substitution of coal as a sustainable solid fuel causes complex particle-turbulence interactions, which need to be captured using minimally invasive laser-based diagnostics. High-resolution two-phase particle image velocimetry (PIV) of high-velocity biomass-laden turbulent flows require laser inter-pulse times of only a few microseconds, which is usually achieved with separate laser systems for low-speed statistical and time-resolved measurements. In this work, we introduce a novel approach to achieve low-speed dual-pulse and ultra-high-speed time-resolved two-phase PIV using a single laser system. The flexible repetition rate laser output is realized by coupling a continuously pulsing fiber laser to an acousto-optic deflector (AOD) for pulse picking. The selective deflection of two adjacent laser pulses into the measurement volume is presented at a camera repetition rate of 25 Hz and laser repetition rate of 312.5 kHz resulting in an inter-pulse time of 3.2 µs. Temporal limitations of the AOD pulse picking system are evaluated beyond the access time limit for partially overlapping pulse pairs. To demonstrate the feasibility of the diagnostic system, low-speed measurements and additional ultra-high-speed measurements at 200 kHz are performed at high spatial resolutions to resolve individual biomass particles and their surrounding flow field in a non-reacting turbulent round jet. Simultaneous diffuse back-illumination measurements using a pulsed LED for particle size measurements of a high-aspect-ratio biomass (miscanthus) are conducted. The diagnostic system offers the capability of determining the slip velocity field and projected particle size, enabling a direct measurement of the local particle Reynolds number under high-velocity turbulent conditions at low and ultra-high repetition rates.

1. Introduction

The interaction of particles with surrounding carrier-phase turbulence is of high relevance in many combustion applications. For instance, the

* Corresponding author.
E-mail address: geschwindner@rsm.tu-darmstadt.de
(C. Geschwindner).

utilization of pulverized biomass in boilers in combination with carbon capture and storage is a potential solution to generate negative carbon dioxide emissions [1]. Both the retrofit of existing coal-fired power stations to support bioenergy with carbon capture and storage (BECCS) as well as the design of new plants based on this technology require accurate predictive simulation tools to capture the complex multi-phase phenomena occurring in biomass-fired combustion chambers. State-of-the art computational studies of turbulent particle-laden flows often make use of a Lagrangian point-particle approach, which requires knowledge of empirical correlations of the unresolved fluid-particle interaction [2]. This is especially relevant for aspherical particle shapes [3], which represent a better approximation for elongated fibrous biomasses such as miscanthus giganteus [4]. Fully-resolved simulations of ellipsoids in uniform flows have been conducted to derive such correlations [5–7], but detailed simulations of large-scale furnaces will remain computationally unfeasible for the foreseeable future. Model development demands the ongoing enhancement of high-resolution experimental methods to capture particle-turbulence interactions of complex shapes in technically relevant turbulent flows.

The majority of recent experimental studies employing simultaneous velocimetry of particles and carrier phase have been realized by particle image velocimetry (PIV), which has replaced laser Doppler velocimetry. In dispersed gas flows, this approach is commonly realized by imaging of small tracers and larger particles of the dispersed phase with a single camera, followed by a phase separation using image processing algorithms [8]. Alternatively, phase separation methods based on the emitted wavelength of scattered light by flow tracers and larger particles including fluorescence [9], phosphorescence (often used for the measurement of both the velocity and temperature field in thermographic PIV) [10], incandescence [11], or a combination of them [12] can be employed. However, all of these methods require at least two monochrome cameras for capturing both phases separately using color filters. Fluorescence and phosphorescence methods mostly also require multiple excitation wavelengths and therefore multiple laser systems, further complicating the optical setup. For instance, two-phase PIV has enabled the measurement of the turbulence modulation by spherical particles at high spatial resolutions [13] and particle slip velocity measurements in laboratory-scale coal combustors [14]. However, multi-phase investigations of aspherical particles are sparse [3]. Sabban et al. have used time-resolved high-speed PIV (TR-PIV) at 3 kHz to study the behavior of fibers in forced homogeneous isotropic turbulence in combination with holographic imaging to address the particle orientation [15]. However, TR-PIV systems with similar projected pixel sizes of only a few micrometers require laser and camera repetition rates far beyond 10 kHz to study technically relevant dispersed shear flows at high velocities. This is especially important for capturing transient effects like particle rotation.

Camera systems for PIV can be classified as low-speed (LS) dual-frame and high-speed (HS) cameras, the latter of which can be operated both continuously and in dual-frame mode. LS cameras provide large amounts of small-sized pixels for high spatial resolutions and large fields of view (FOV). Besides, the high dynamic range typically facilitates intensity-based two-phase separation. HS cameras provide high recording speeds but require cropping of the active sensor area for time-resolved measurements of highly turbulent flow phenomena at recording speeds beyond several tenths of kilohertz. Hence, to achieve high resolutions and dynamic ranges in the spatial and temporal domain, measurements with both LS and HS systems are desirable.

Typically, LS and HS diagnostics of turbulent flows also require separate laser sources. Especially for LS systems, dual-cavity (or dual-pulse, DP) lasers are needed as inter-pulse times are in the order of microseconds compared to inter-frame times of several milliseconds. At ultra-high repetition rates beyond 200 kHz, burst-mode lasers have been the only available choice, which also provide high pulse energies but suffer from a limited operation time to prevent overheating [16].

To overcome this problem and essentially introduce a flexible repetition rate single-cavity laser system, a continuously pulsing ultra-high-speed laser is necessary, whose output pulses can be selectively chosen at the camera recording rate. In this study, we demonstrate such a system based on pulse picking of a nanosecond-pulsed fiber laser. In an earlier work, the authors have conducted TR-PIV of a turbulent jet at repetition rates up to 400 kHz using the same laser system [17], which has previously only been possible with pulse-burst lasers [18]. Further, as the fiber laser does not suffer from limited burst rates, the amount of consecutively recorded vector fields exceeded 1.2 million as this value is solely limited by the storage capacity of the HS camera. As will be shown, a fiber laser system extended with a pulse picker can be used for both LS and HS PIV systems in both time-resolved and dual-pulse modes. Next to the advantage that only cameras need to be changed to switch between LS and HS investigations, a single laser source does not demand the spatial adjustment of the pulse overlap in dual-cavity lasers, similar to dual-pulse burst-laser systems [19]. To demonstrate the capabilities of such an approach, two-phase PIV of a biomass-laden jet was conducted with both LS and HS camera systems at low and ultra-high repetition rates,
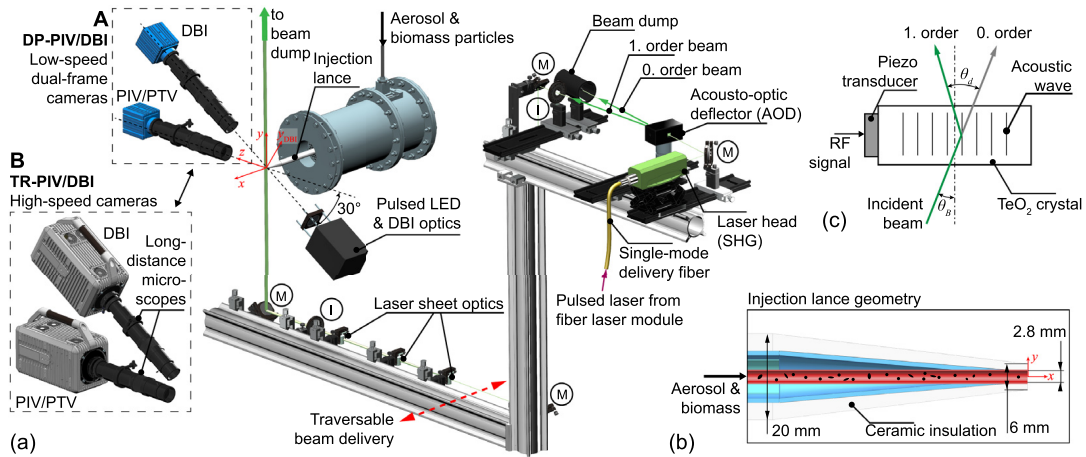
Fig. 1. (a) Experimental setup and optical beam path. Cameras of the low-speed dual-pulse system **A** were changed to high-speed system **B** for TR-PIV measurements at 200 kHz. Mirrors (M) and irises (I) are highlighted by their encircled initial. (b) Geometry of the injection lance generating a particle-laden turbulent jet. (c) Working principle of an acousto-optic deflector.

resolving interactions of turbulent flow structures with aspherical particles.

2. Experimental methodology

2.1. Biomass-laden jet

A biomass-laden turbulent jet emerging from a ceramic-insulated round pipe (also referred to as injection lance) with an inner diameter of $D = 2.8$ mm was investigated. The lance was mounted in the burner head of the microwave plasma heater test stand at TU Darmstadt [20] with only the air supply through the lance running during the experiment at ambient conditions ($T = 297$ K, $p = 1$ bar). Fig. 1(a) displays the experimental setup with a close-up of the injection lance in Fig. 1(b). The air flow rate was set by mass-flow controllers (EL-Flow Prestige, Bronkhorst), which was subsequently split to feed an aerosol generator filled with Di-Ethyl-Hexyl-Sebacate as fluid tracers (UGF 2000, Palas, particle size 0.2 μm) and a custom biomass particle seeder before entering the L-shaped pipe. The length of the final straight pipe section was 185D to ensure a fully developed turbulent pipe flow. A flow rate of 14.18 ln/min resulted in a jet Reynolds number of 7500 at an axial bulk velocity u_b of 41.75 m/s.

Pulverized raw miscanthus sieved in a particle size range of 90–125 μm was investigated. A fibrous biomass like miscanthus can exhibit large aspect ratios beyond 8 at bulk densities of approximately $\rho_p = 0.2$ g/cm³. To mitigate strong inter-particle interaction, low particle concentrations were chosen such that each particle and its closest neighbor were around 5 projected particle

diameters apart from each other. This seeding strategy largely avoids the merging of neighboring particle wakes occurring at higher particle number densities.

The Stokes number St describes the ratio between particle response time τ_p and fluid time scale τ_f. In particle-laden jets, it is convenient to define τ_f as D/u_b [21]. When taking the aspect ratio β and the minor axis radius a into account for the calculation of τ_p of a spheroid [3,22], the Stokes number can be calculated as

$$St = \frac{\tau_p}{\tau_f} = \frac{2a^2\rho_p u_b}{9\mu D} \frac{\beta \ln\left(\beta + (\beta^2 - 1)^{1/2}\right)}{(\beta^2 - 1)^{1/2}}, \qquad (1)$$

where μ is the dynamic viscosity of the fluid. Assuming typical values of $a = 50$ μm and $\beta_{\mathrm{mis}} = 5$, the Stokes number is $St_{\mathrm{mis}} \approx 210$. As $St \gg 1$, particles are expected to drag behind the flow within the pipe but will decelerate slower than the carrier phase as the jet expands axially as was shown by Lau and Nathan [21], creating a slip velocity $\boldsymbol{u}_s = \boldsymbol{u} - \boldsymbol{u}_p$, where $\boldsymbol{u}_p$ and $\boldsymbol{u}$ are the particle and fluid velocity vectors, respectively. Simultaneous knowledge of slip, particle diameter d_p, and kinematic viscosity of the surrounding fluid ν enables the computation of the particle Reynolds number $Re_p = |\boldsymbol{u} - \boldsymbol{u}_p|d_p/\nu$, which determines the local flow structure around a particle. Knowledge of the local highly-resolved slip velocity field is especially relevant for the assessment of turbulence modification mechanisms like local dissipation from particle drag or vortex shedding [2].

2.2. Optical diagnostics

Fig. 1 (a) displays the experimental setup including the interchangeable low-speed camera system

A and high-speed camera system **B**, both equipped with long-distance microscopes (K2 DistaMax, Infinity). System **A** consists of two low-speed dual-frame cameras (Imager sCMOS, LaVision) running at a repetition rate of 25 Hz, capturing a field of view of 12.84×10.83 mm^2 at a pixel resolution of 5 µm each. System **B** makes use of two high-speed cameras (SA-X2, Photron) operated at a repetition rate of 200 kHz, which requires the sensors to be cropped to 384×112 px^2 equal to a FOV of 3.8×1.1 mm^2 at a pixel resolution of 10 µm.

One of each cameras was used for PIV measurements, while the other one was facing a pulsed LED (LPS V3, ILA_5150, central emission wavelength of 523 nm) running in sync with the camera frame rate with a pulse duration of 800 ns for diffuse back-illumination (DBI) imaging. DBI has proven to be a reliable diagnostic to measure solid fuel particle sizes in contrast to Mie scattering, which often leads to overpredicted sizes due to large particle scattering images [23]. Due to the spectral overlap, a temporal separation of LED and laser pulses was chosen to mitigate cross-talk between DBI and PIV systems using a delay of 1 µs between each LED pulse and the previous laser pulse. The FOV of the DBI system is inclined by 30° to the PIV FOV, which still guarantees matching of the axial coordinate x of both techniques in the calibration process. For HS TR-PIV investigations, laser, LED, and cameras were all operated in sync, while for LS dual-pulse PIV measurements, a pulse picking approach was utilized. In the following, the fiber laser system and pulse picking PIV approach will be presented and discussed.

2.2.1. Pulsed fiber laser

A nanosecond-pulsed Yb-doped fiber laser (GLPN-500-1-50-M, IPG Photonics) was used as an illumination source for PIV measurements. Similar to pulse-burst lasers, this system is based on the master oscillator power amplifier (MOPA) architecture in which a seed pulse is amplified by a diode-pumped gain medium. However, the pulse amplification takes place in rare-earth doped optical fibers, which guarantees an efficient heat transfer to the outside as the surface area to volume ratio is large. For this reason, continuous operation of the laser is possible at high repetition rates, which is the prerequisite for usage in a duty-cycle pulse picking approach. A polarization-maintaining single-mode delivery fiber connects the laser module with the head, in which second-harmonic generation (SHG) to the final output wavelength of 515 nm takes place. This flexibility allowed a direct mounting of the head on the traversing system, simplifying the beam path adjustment for measurements at different axial positions of the jet.

The laser can be operated at pulse repetition rates between 10 kHz and 1 MHz with an adjustable pulse width, which was set to 10 ns in this study. The maximum pulse energy of 500 µJ

is emitted between repetition rates of 10 kHz and 100 kHz and further decreases with higher repetition rates at a nominal output power of 50 W. The laser output shows a beam quality factor of $M^2 = 1.4$ displaying the ability to achieve thin laser sheets, which are needed to reach high spatial resolutions. The laser sheet optics consisted of a set of cylindrical lenses ($f_1 = -50$ mm, $f_2 = 300$ mm, $f_3 = 500$ mm). Beam profile measurements (WinCamD-LCM, DataRay) of the laser sheet showed a thickness of 140 µm at full width half maximum, which was adjusted as a compromise between high spatial resolution and the prevention of out-of-plane loss of tracer particles between pulses.

2.2.2. Possible inter-pulse times of pulse picking PIV

To utilize a continuously pulsing high-speed laser for dual-pulse measurements with low-speed dual-frame sensors, one cannot freely choose a suitable inter-pulse delay time t_l as the laser repetition rate f_l requires to be an integer multiple of the camera system frame rate f_c such that

$$f_l = c\, f_c, \tag{2}$$

where c is the duty cycle factor ($c \in \mathbb{N}$). Further, from all possible f_l computed using Eq. (2), only those should be chosen, whose inverse (or inter-pulse time t_l) are also integers in units of the smallest acceptable time accuracy. While the delay generator (9520 Series, Quantum Composers) works at an accuracy of 1 ns, choosing a longer acceptable resolution of t_l in the order of the pulse width of the laser beam of 10 ns should be considered. Still, the amount of suitable f_l passing these criteria is fairly high. In this study we have chosen an inter-pulse time of 3.2 µs for reasonable particle displacements at a camera repetition rate of 25 Hz, which requires a steady operation of the fiber laser at a repetition rate of 312.5 kHz with a pulse picking duty cycle factor of $c = 12{,}500$. Essentially, this means that every 40 ms, 2 pulses are picked for LS PIV, while the 12,498 following ones need to be blocked by a suitable device. This picking approach will be discussed next.

2.2.3. AOD pulse picking at high repetition rates

To separate a defined amount of laser pulses from a continuous pulse train, a controllable light switch or pulse picking device altering some property of the incident light in a timely manner is necessary. Commonly, such devices operate by utilizing either the acousto-optic or electro-optic effect [24]. In this work, we utilize an acousto-optic deflector or AOD (DTSX-400, AA Opto Electronic), whose working principle is schematically shown in Fig. 1(c). An incident beam is deflected at multiple diffraction orders as a radio frequency (RF) signal controls a piezo transducer, which generates a
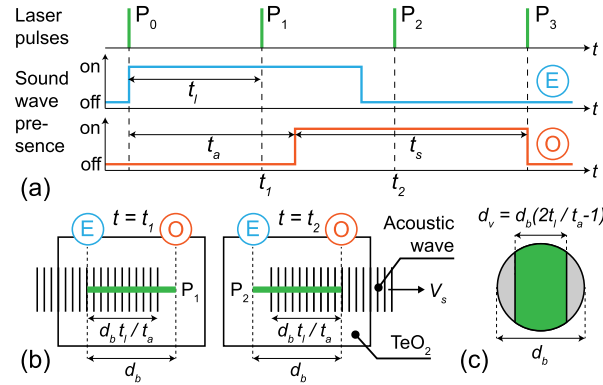
Fig. 2. AOD-based selection of two pulses at $t_a > t_l$ including (a) a timing chart and (b) visualizations of the interaction between the acoustic wave and the laser pulse (green line). (c) Calculation of the beam overlap of picked pulses. (For interpretation of the references to colour in this figure legend, the reader is referred to the web version of this article.)

sound wave propagating through a tellurium dioxide (TeO_2) crystal. A voltage-controlled oscillator generating the RF signal (DRFA10Y, AA Opto Electronic) enables a flexible setting of amplitude and frequency of the sound wave for adjustment of the deflection angle of the first-order beam, which is guided into the measurement volume, while the zeroth-order beam is led into a beam dump. The switching duration of the RF driver t_s is controlled by a function generator (33500B Series, Keysight), which receives a trigger every c laser pulses from the delay generator. A detailed description of the working principles and applications of AODs for laser diagnostics can be found in Li et al. [25] and Bass [26].

To select pulses from a high repetition rate laser source, the access time t_a of the AOD needs to be considered, which is the time period a sound wave requires to travel along the beam diameter d_b. For an acousto-optic deflector working in the Bragg regime with small incident beam angles θ_B, the access time is given by

$$t_a = d_b/V_s, \qquad (3)$$

where V_s is the speed of sound in the crystal [26]. For the given configuration, a beam width of $d_b = 2.68$ mm (at a normalized intensity of $1/e^2$) and the speed of sound in TeO_2 of $V_s = 650$ m/s lead to an access time of $t_a = 4.12$ µs. As long as the time period between two adjacent laser pulses t_l is greater than t_a, an arbitrary amount of pulses can be deflected along their full beam width without interference from neighboring unwanted pulses. However, PIV measurements at high optical magnifications and fluid velocities often require inter-pulse times $t_l < 4$ µs. Hence, the following analysis briefly outlines to which extent an AOD can be operated for multi-pulse picking beyond the access time limit.

Fig. 2 (a) displays a timing chart of two symmetrically picked pulses P_1 and P_2 at a laser repetition rate $f_l = 1/t_l > 1/t_a$. In addition, the presence of the sound wave at the transducer-facing beam edge position E and the opposite edge O is shown. Assuming a negligible laser pulse duration (10 ns in this study) and fast rise time of the RF driver (<50 ns) and hence the sound wave, the optimal arrival time of the sound wave at position E is just after P_0 has passed the AOD. Between this point in time and the time of arrival t_1 of P_1, the sound wave has traveled a distance of $d_b t_l/t_a$ as outlined in Fig. 2(b). Therefore, only a fraction of t_l/t_a of the beam width of P_1 is deflected. Similarly, at $t = t_2$ an interaction length of $d_b t_l/t_a$ at the opposite beam edge is realized for P_2, as the switching window t_s is limited by avoidance of the deflection of P_3 to a value of

$$t_s = 3t_l - t_a. \qquad (4)$$

For the utilization of both pulses in DP-PIV, the spatial overlap d_v/d_b is important to quantify as it determines the necessary beam expansion at a given axial extent of the field of view, where d_v describes the absolute width of the spatial overlap. Fig. 2(c) visualizes the calculation of the overlap as

$$d_v/d_b = 2t_l/t_a - 1. \qquad (5)$$

The limit of this approach for DP-PIV is reached when the overlap of both deflected pulses vanishes, which can be observed at $t_l = t_a/2$. At higher laser repetition rates, both picked pulses are spatially fully separated. For $t_l = t_a/3$, t_s will become zero indicating that a deflection of unwanted neighboring pulses cannot be avoided.

To verify the applicability of the presented analysis, beam profile measurements of the individual picked beams behind the AOD are presented for the selected laser repetition rate of 312.5 kHz in Fig. 3(a-b). A switching window of 5.6 µs was set according to Eq. (4). As can be observed, both pulses have been cut off at opposite sides and are approximately equal in size, indicating that the delay between the laser and AOD has been set to
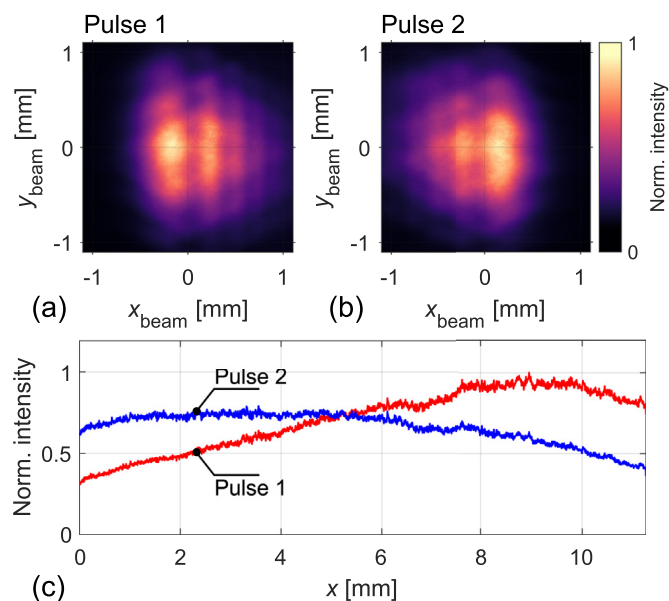
Fig. 3. Beam profiles of the first (a) and second (b) deflected pulse at $t_l = 3.2$ µs. (c) Normalized intensity of individual laser sheets of each pulse along the axial jet coordinate x.

fulfill the symmetric picking strategy presented in Fig. 2. The beam overlap can be calculated by binarizing both beam images at a threshold of $1/e^2$ of the maximum beam intensity and subsequently calculating the width of the conjunction of both binarized beams, which can be compared to the output beam diameter. A measured value of the beam overlap of 0.52 is similar to the theoretical value of 0.55 calculated using Eq. (5). It should be noted that the peak intensity position of the Gaussian beam was altered by the diffraction across the sound wave, which explains deviations from the calculated value.

Fig. 3 (c) shows the axial distribution of the intensity within the laser sheet captured in the PIV measurement volume. As can be observed, both pulses show similar intensity values in the central overlapping region and start to deviate from each other towards the edges. Still, images captured with the dual-frame PIV system show easily trackable particles in the edges of the large FOV of the LS system, which is also evidence of the ideal lateral beam overlap of both pulses usually being an additional source of uncertainty for dual-cavity laser systems when focused to small beam waists. It should be noted that a further optimization of the axial overlap of both laser sheets can be achieved by directly monitoring the intensity distribution of the individual laser sheets in the measurement volume instead of the laser beams behind the AOD as it was done in this investigation.

In conclusion, to realize two perfectly axially overlapping picked laser sheets, the access time of the pulse picking device should not exceed the inter-pulse duration. However, when the desired laser fluence in the sheet is still sufficient at an increased axial expansion, centrally overlapping pulses can be generated at inter-pulse times of down to $t_l = t_a/2$. When examining Eq. (3), one could further decrease the access time of the AOD by focusing down the incident beam, lowering d_b. However, this will risk reaching the AOD crystal's damage threshold and will lower the resolution of single deflected beams N, which is directly proportional to the access time [24]. Hence, decreasing t_a by decreasing d_b comes at the cost of losing diffraction resolution, resulting in larger diffraction patterns than those observed in Fig. 3(a-b). Consequently, alternative pulse picking approaches based on electro-optic modulation need to be considered when even shorter inter-pulse durations t_l are needed.

3. Image processing

Fig. 4 exemplarily shows image recordings of representative miscanthus particles of both LS and HS systems. As can be seen in the detail views (Fig. 4(c-d)), the superior dynamic range and pixel resolution of the LS system results in higher detail of the imaged particle. However, the HS recordings at 200 kHz still offer high-resolution images in a limited FOV compared to the LS system.

The two-phase PIV recordings were divided into separate images for tracer and biomass particles based on their intensity and size difference. Similar to Tanaka and Eaton [13], the high spatial resolu-
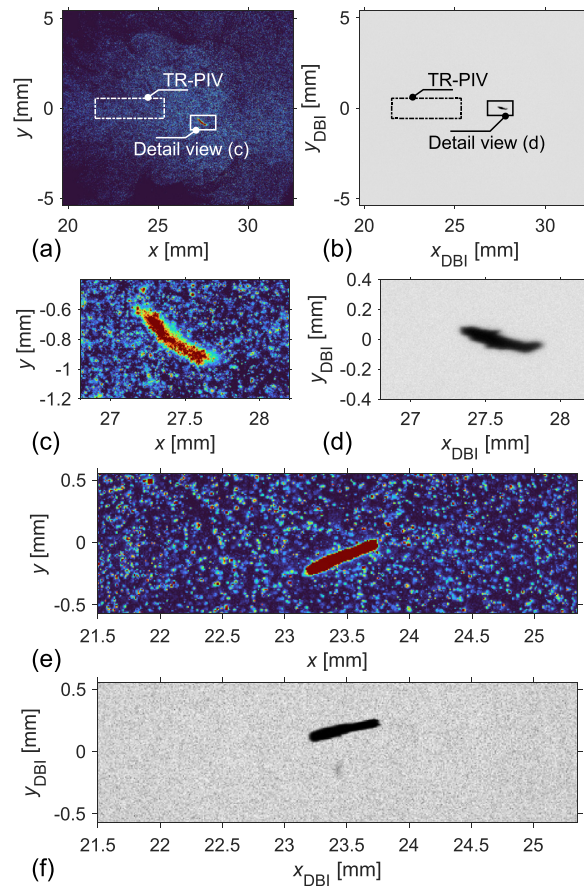
Fig. 4. Selected single images of both LS and HS camera systems. LS PIV (a) and simultaneously recorded LS DBI (b) images including detail views of a miscanthus particle (c-d). (e-f) Single shots of TR-PIV and TR-DBI recordings. The outlines of the HS fields of view are displayed in the LS images by a dash-dotted rectangle (a-b).

tion of both LS and HS investigations enabled a binarization based on a user-defined threshold. Small structures exceeding the intensity threshold were inserted back into the tracer images, while large structures were first dilated isotropically to prevent scattering halos around them and then masked in the tracer images.

The fluid velocity was calculated from the tracer images using a multi-pass correlation-based PIV algorithm (DaVis 10.1, LaVision) with an interrogation window size of 32×32 px^2 for the HS system and 64×64 px^2 for the LS system at an overlap of 75%, resulting in a similar vector spacing of 80 μm. Biomass particle velocities $\boldsymbol{u}_p$ were computed by tracking the individual centroids of the binarized particle images. Due to the large scattering intensity differences between tracers and biomass particles, most of the large particles were imaged close to or in saturation of the imaging sensors (especially using the 12 bit HS camera). Hence, this centroid-based tracking

approach yielded more accurate results than classical particle tracking velocimetry (PTV) methods, which assume a Gaussian scattering intensity distribution across the particle.

Biomass particle images were identified in the DBI recordings if an intensity reduction of at least 85% of the local background intensity was detected. Large particles in the PIV recordings were then matched to particles in the DBI images. Subsequent parameter extraction for the DBI images included the circle-equivalent diameter based on the projected particle area and the orientation and aspect ratio of a fitted ellipse.

4. Results and discussion

As an initial frame of reference, Fig. 5 displays the mean axial velocity $\langle u \rangle$ and standard deviation σ_u of the single-phase turbulent jet, which was measured using more than 1000 individual vector
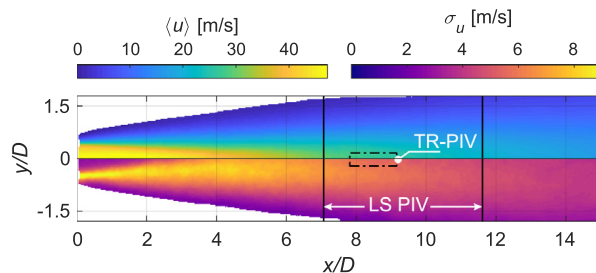
Fig. 5. Mean axial velocity $\langle u \rangle$ (top half) and standard deviation σ_u (bottom half) of the single-phase jet. A single FOV of LS pulse picking PIV (vertical lines) and HS TR-PIV (dash-dotted box) is outlined.

fields acquired with the LS pulse picking PIV system. Additionally, a TR-PIV FOV of the HS system is shown. When comparing LS and HS (TR-PIV) measurements, the advantage of the large LS camera sensor to capture larger portions of the jet for statistical measurements is apparent. However, despite its limited FOV, TR-PIV provides additional information about integral time scales and spectra [18,19]. Therefore, a combination of both approaches is desirable for a comprehensive characterization of the flow field, which is achieved by simply exchanging cameras with the pulse picking laser system as outlined in Section 2.2.

Similarly, multi-phase investigations benefit from a combined HS/LS approach as time-resolved quantities like particle rotation and the temporal evolution of the instantaneous particle-turbulence interaction can be measured in a small FOV at ultra-high repetition rates, while LS pulse picking PIV provides large-field statistical data on quantities such as particle orientation, slip velocity, and particle Reynolds numbers. In the following, the capability of the HS system to investigate time-resolved particle-turbulence dynamics in the outlined TR-PIV FOV in Fig. 5 at $x/D \approx 8$ is demonstrated. In this region, the shear layers surrounding the potential core merge, which results in a rise of the centerline turbulence level. The high Stokes number of particles crossing this area can therefore result in strong temporal changes of the slip velocity, which determines turbulence enhancement through vortex shedding and influences the devolatilization of pulverized biomass in a jet flame.

A time-resolved two-phase measurement of a representative aspherical miscanthus particle moving through the turbulent flow field recorded with a repetition rate of 200 kHz is displayed in Fig. 6. A total of 22 consecutive frames equivalent to a transit time of 105 μs could be captured. The velocity fields in Fig. 6(a) reveal that the particle passes through a region of decreasing fluid velocity, which is depicted at two selected points in time relative to its first appearance in the FOV (referred to as t_I and t_{II}). Further, the interaction between the adjacent flow field and the particle is observed in the reference system of the particle using the corresponding slip velocity fields $\boldsymbol{u} - \boldsymbol{u}_p$ illustrated together with both binarized particle shapes for the respective particle velocity calculation in Fig. 6(b). This visualization replicates the scenario used in highly resolved simulation frameworks of a fixed particle interacting with a surrounding flow to derive empirical correlation functions [7]. As almost all of the slip velocity vectors point left, the axial particle velocity largely exceeds the axial fluid velocity potentially leading to a wake on the lee side of the miscanthus particle, which is in accordance with the high magnitude of the projected Stokes number. As the axial velocity of the particle decreases less drastically than that of the carrier-phase, the magnitude of the slip velocity increases over time, which is recognizable when comparing t_I and t_{II} in Fig. 6(b).

To investigate the temporal evolution of the flow structure around these particles, the particle Reynolds number Re_p is evaluated. In contrast to the uniform flow approaching fixed particles in a simulation, the turbulent flow structures interacting with the particle require an adapted definition of the slip velocity magnitude, which is calculated as the average value along all positions adjacent to the masked area of the biomass particle. The circle-equivalent diameter $d_p = 244$ μm and aspect ratio $\beta = 6.9$ are calculated as mean values observed from the DBI sequence. Additionally, the temporal evolution of the particle centroid and orientation visualized by ellipse fits is shown in Fig. 6(c) for the PIV and Fig. 6(d) for the DBI images.

The dynamics of the particle Reynolds number are shown in Fig. 7(a). Values for Re_p increase from 80 to almost 300 as the magnitude of the slip velocity increases. For comparison, the particle Reynolds number $Re_{p,\langle u \rangle}$ calculated with the pseudo slip $\langle \boldsymbol{u} \rangle - \boldsymbol{u}_p$ based on the mean velocity at the particle position measured with single-phase pulse picking PIV is depicted. As expected, this approach significantly deviates from the instantaneous slip of the two-phase PIV system, confirming the need of simultaneous multi-phase velocimetry to assess the particle-turbulence interaction. For spherical particles, $Re_p \geq 20$ indicates flow separation, which
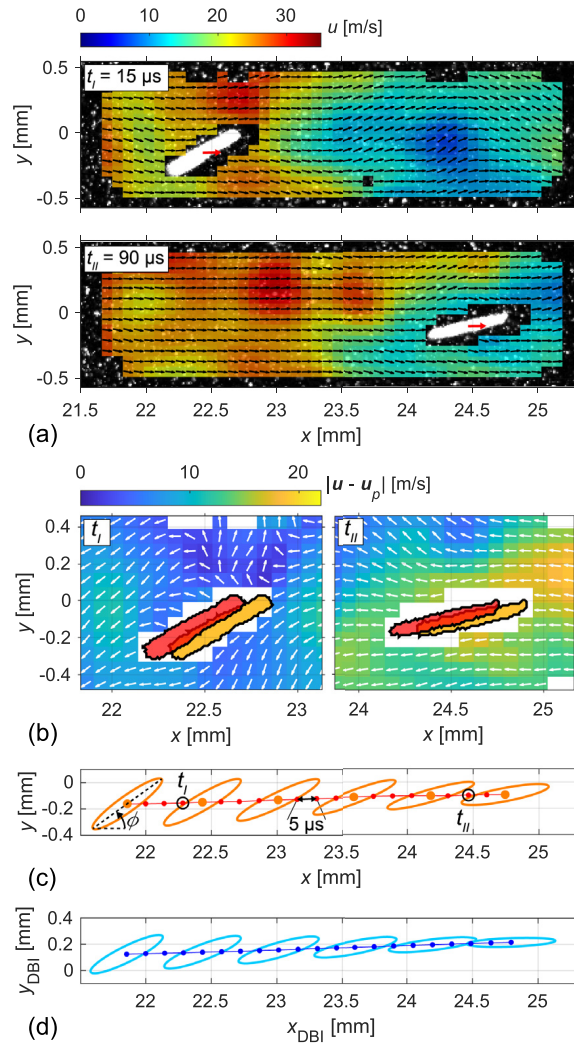
Fig. 6. Miscanthus particle moving through a region of high turbulence. (a) Two-phase velocimetry visualizations at two selected instants. (b) Corresponding slip velocity fields. (c-d) Temporal evolution of particle centroid position of the PIV (c) and DBI measurements (d) including ellipse fits and the definition of the angle of orientation ϕ.

is, however, dependent on the angle of orientation ϕ for aspherical particles. Highly resolved simulations for $Re_p \leq 100$ have shown that no separation occurs for horizontally aligned particles with aspect ratios $\beta > 3$ [7]. As is shown in Figs. 6(c-d) and 7(b), the angle of orientation ϕ steadily decreases over time as the particle rotates clockwise. Hence, even though Re_p increases, the particle rotation results in the flow around an increasingly streamlined body, which induces less drag and might reduce the turbulence enhancement through vortex shedding. Still, the rotation speed $\dot{\phi}$ reduces only minimally as can be observed in Fig. 7(b), indicating that the particle will not stay aligned with the axial jet coordinate after it has left the FOV. It is expected that the

rotation speed of particles with lower aspect ratios further increases as the rotational inertia decreases, emphasizing the necessity of repetition rates beyond 100 kHz. As can be seen from this analysis, time-resolved two-phase diagnostics at ultra-high repetition rates enables an observation of the dynamics of micrometer-sized aspherical particles interacting with a turbulent flow at high flow speeds.

5. Conclusions

An ultra-high repetition rate pulsed fiber laser was equipped with a pulse picker to generate a flexible repetition rate single-cavity laser system
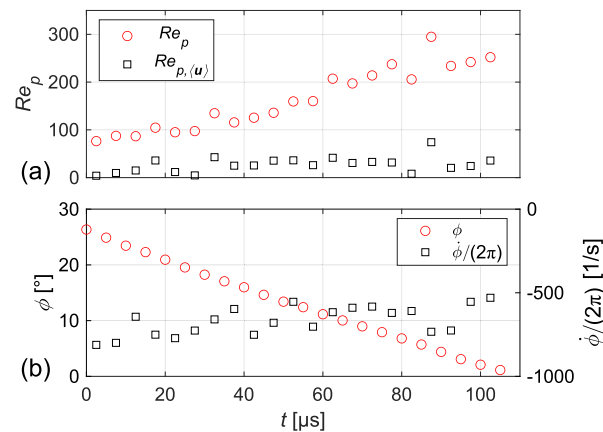
Fig. 7. (a) Temporal dynamics of the Reynolds particle numbers Re_p and $Re_{p,\langle u \rangle}$. (b) Angle of orientation ϕ and rotation speed $\dot{\phi}$ normalized to particle revolutions per second measured with the DBI system.

for dual-pulse and time-resolved PIV measurements. An acousto-optic deflector is used to select a pulse pair from the continuously pulsing laser output. The smallest possible inter-pulse time t_l is dependent on the access time of the AOD t_a and the available pulse energy at a given laser repetition rate $1/t_l$. For $t_a/2 < t_l < t_a$, partially overlapping pulses can be picked if the resulting overlap is sufficient for the desired FOV. This approach was demonstrated at a laser repetition rate of 312.5 kHz resulting in an inter-pulse time of $t_l = 3.2\,\mu s$ for a low-speed PIV measurement at a camera repetition rate of 25 Hz.

Further, time-resolved two-phase PIV/PTV measurements of a micrometer-sized aspherical biomass particle moving through a turbulent jet at a repetition rate of 200 kHz using the same laser system are presented, highlighting the benefit of high repetition rate velocimetry to study the interaction of biomass particles and their surrounding carrier-phase turbulence. The simultaneous measurement of slip velocity, projected particle diameter and orientation using an additional DBI imaging system enables a temporally resolved analysis of the particle Reynolds number. The ultra-high repetition rates of the laser system facilitate the highly resolved study of particle-turbulence interaction at elevated flow speeds relevant to large-scale combustion systems.

Future pulse picking PIV systems can be improved by utilization of the electro-optic effect in Pockels cell pulse pickers as they are currently used for mode-locked lasers emitting ultrashort pulses [24]. Furthermore, higher output powers of future fiber laser systems will enable larger fields of view and improved signal-to-noise ratios for PIV measurements. For a measurement of the local slip velocity field, the method can be easily extended to reactive flows using sub-micron sized aluminum oxide flow tracers, which are commonly used for PIV measurements in flames. However, it should be

noted that a computation of Re_p in reactive flows requires the simultaneous measurement of the local carrier-phase temperature, which is challenging to achieve at ultra-high repetition rates. Still, many PIV applications in the fields of combustion and fluid mechanics might potentially benefit from this flexible methodology.

Declaration of Competing Interest

The authors declare that they have no known competing financial interests or personal relationships that could have appeared to influence the work reported in this paper.

References

[1] J. Kemper, Biomass and carbon dioxide capture and storage: areview, Int. J. Greenh. Gas Control 40 (2015) 401–430, doi:10.1016/j.ijggc.2015.06.012.

[2] S. Balachandar, J.K. Eaton, Turbulent dispersed multiphase flow, Annu. Rev. Fluid Mech. 42 (1) (2010) 111–133, doi:10.1146/annurev.fluid.010908.165243.

[3] G.A. Voth, A. Soldati, Anisotropic particles in turbulence, Annu. Rev. Fluid Mech. 49 (1) (2017) 249–276, doi:10.1146/annurev-fluid-010816-060135.

[4] A. Panahi, N. Vorobiev, M. Schiemann, M. Tarakcioglu, M. Delichatsios, Y.A. Levendis, Combustion details of raw and torrefied biomass fuel particles with individually-observed size, shape and mass,

Combust. Flame 207 (2019) 327–341, doi:10.1016/j.combustflame.2019.06.009.

[5] M. Zastawny, G. Mallouppas, F. Zhao, B. van Wachem, Derivation of drag and lift force and torque coefficients for non-spherical particles in flows, Int. J. Multiph. Flow 39 (2012) 227–239, doi:10.1016/j.ijmultiphaseflow.2011.09.004.

[6] S.K. Sanjeevi, J. Kuipers, J.T. Padding, Drag, lift and torque correlations for non-spherical particles from Stokes limit to high Reynolds numbers, Int. J. Multiph. Flow 106 (2018) 325–337, doi:10.1016/j.ijmultiphaseflow.2018.05.011.

[7] K. Fröhlich, M. Meinke, W. Schröder, Correlations for inclined prolates based on highly resolved simulations, J. Fluid Mech. 901 (2020), doi:10.1017/jfm.2020.482.

[8] B.E. Schmidt, J.A. Sutton, Evaluation of gas- and particle-phase separation methods for velocity measurements in turbulent multiphase flows, Exp. Fluids 61 (12) (2020), doi:10.1007/s00348-020-03082-7.

[9] D.P. Towers, C.E. Towers, C.H. Buckberry, M. Reeves, A colour PIV system employing fluorescent particles for two-phase flow measurements, Meas. Sci. Technol. 10 (9) (1999) 824–830, doi:10.1088/0957-0233/10/9/309.

[10] B. Fond, C. Abram, A.L. Heyes, A.M. Kempf, F. Beyrau, Simultaneous temperature, mixture fraction and velocity imaging in turbulent flows using thermographic phosphor tracer particles, Opt. Express 20 (20) (2012) 22118–22133, doi:10.1364/OE.20.022118.

[11] L. Fan, D. McGrath, C.T. Chong, M.N. Mohd Jaafar, H. Zhong, S. Hochgreb, Laser-induced incandescence particle image velocimetry (LII-PIV) for two-phase flow velocity measurement, Exp. Fluids 59 (10) (2018), doi:10.1007/s00348-018-2610-4.

[12] X. Bi, Z. Sun, T. Lau, Z. Alwahabi, G. Nathan, Simultaneous imaging of two-phase velocities in particle-laden flows by two-color optical phase discrimination, Opt. Lett. 46 (16) (2021) 3861–3864, doi:10.1364/OL.428357.

[13] T. Tanaka, J.K. Eaton, Sub-Kolmogorov resolution partical image velocimetry measurements of particle-laden forced turbulence, J. Fluid Mech. 643 (2010) 177–206, doi:10.1017/S0022112009992023.

[14] L.G. Becker, S. Pielsticker, B. Böhm, R. Kneer, A. Dreizler, Particle dynamics in a gas assisted coal combustion chamber using advanced laser diagnostics, Fuel 269 (2020) 117188, doi:10.1016/j.fuel.2020.117188.

[15] L. Sabban, A. Cohen, R. van Hout, Temporally resolved measurements of heavy, rigid fibre translation and rotation in nearly homogeneous isotropic turbulence, J. Fluid Mech. 814 (2017) 42–68, doi:10.1017/jfm.2017.12.

[16] M.N. Slipchenko, T.R. Meyer, S. Roy, Advances in burst-mode laser diagnostics for reacting and nonreacting flows, Proc. Combust. Inst. 38 (1) (2020) 1533–1560, doi:10.1016/j.proci.2020.07.024.

[17] C. Geschwindner, K. Westrup, A. Dreizler, B. Böhm, Ultra-high-speed time-resolved PIV of turbulent flows using a continuously pulsing fiber laser, Exp. Fluids 63 (4) (2022), doi:10.1007/s00348-022-03424-7.

[18] S.J. Beresh, J.F. Henfling, R.W. Spillers, S.M. Spitzer, 'Postage-stamp PIV': small velocity fields at 400 kHz for turbulence spectra measurements, Meas. Sci. Technol. 29 (3) (2018) 034011, doi:10.1088/1361-6501/aa9f79.

[19] J.D. Miller, N. Jiang, M.N. Slipchenko, J.G. Mance, T.R. Meyer, S. Roy, J.R. Gord, Spatiotemporal analysis of turbulent jets enabled by 100-kHz, 100-ms burst-mode particle image velocimetry, Exp. Fluids 57 (12) (2016), doi:10.1007/s00348-016-2279-5.

[20] F. Eitel, J. Pareja, D. Geyer, A. Johchi, F. Michel, W. Elsäßer, A. Dreizler, A novel plasma heater for auto-ignition studies of turbulent non-premixed flows, Exp. Fluids 56 (10) (2015), doi:10.1007/s00348-015-2059-7.

[21] T.C.W. Lau, G.J. Nathan, The effect of Stokes number on particle velocity and concentration distributions in a well-characterised, turbulent, co-flowing two-phase jet, J. Fluid Mech. 809 (2016) 72–110, doi:10.1017/jfm.2016.666.

[22] M. Shapiro, M. Goldenberg, Deposition of glass fiber particles from turbulent air flow in a pipe, J. Aerosol Sci. 24 (1) (1993) 65–87, doi:10.1016/0021-8502(93)90085-N.

[23] T. Li, M. Schiemann, J. Köser, A. Dreizler, B. Böhm, Experimental investigations of single particle and particle group combustion in a laminar flow reactor using simultaneous volumetric OH-LIF imaging and diffuse backlight-illumination, Renew. Sustain. Energy Rev. 136 (2021) 110377, doi:10.1016/j.rser.2020.110377.

[24] F. Träger, Springer Handbook of Lasers and Optics, Springer, Berlin, Heidelberg, 2012, doi:10.1007/978-3-642-19409-2.

[25] T. Li, J. Pareja, L. Becker, W. Heddrich, A. Dreizler, B. Böhm, Quasi-4D laser diagnostics using an acousto-optic deflector scanning system, Appl. Phys. B 123 (3) (2017), doi:10.1007/s00340-017-6663-5.

[26] M. Bass, Handbook of Optics, second ed., McGraw-Hill, New York, 1995.

A.3 Paper III - Group combustion of solid fuel particles

Reproduced with permission from Elsevier.

ELSEVIER

An experimental study of coal particle group combustion in conventional and oxy-fuel atmospheres using multi-parameter optical diagnostics

Tao Li*, Christopher Geschwindner, Andreas Dreizler, Benjamin Böhm

*Technical University of Darmstadt, Department of Mechanical Engineering, Reactive Flows and Diagnostics,
Otto-Berndt-Straße 3, Darmstadt 64287, Germany*

Abstract

The present work reports an experimental study of particle group combustion of pulverized bituminous coal in laminar flow conditions using advanced multi-parameter optical diagnostics. Simultaneously conducted high-speed scanning OH-LIF, diffuse backlight-illumination (DBI), and Mie scattering measurements enable analyses of three-dimensional volatile flame structures and soot formation in conventional (i.e., N_2/O_2) and oxy-fuel (i.e., CO_2/O_2) atmospheres with increasing O_2 enrichment. Particle-flame interaction is assessed by calculating instantaneous particle number density (PND), whose uncertainties are estimated by generating synthetic particles in DBI image simulations. Time-resolved particle sequences allow the evaluation of the particle velocity, which indicates a PND dependency and interactions between particles and volatile flames. 3D flame structure reconstruction and soot formation detection are first demonstrated in single-shot visualizations and then extended to analyze effects of O_2 concentration, PND, and inert gas composition statistically. The increasing O_2 concentration significantly reduces local flame extinction and suppresses soot formation in N_2 and CO_2 atmospheres. Volatile flames reveal higher intensities and lower lift-off heights as O_2 concentration increases. In contrast to that, an increased PND leads to earlier flame extinction and stronger soot formation due to the local gas temperature reduction and oxygen depletion. The lift-off height reduces with increasing PND, which is explained by the complex interaction between particle dynamics, heat transfer, and volatile reactions. Slightly stronger soot formation and delayed ignition are observed in CO_2 atmospheres, whereas CO_2 replacement reveals insignificant influences on the flame extinction behavior. Finally, non-flammability is quantified for particle group combustion at varying PNDs in different atmospheres.
© 2022 The Combustion Institute. Published by Elsevier Inc. All rights reserved.

Keywords: Bituminous coal; Particle group combustion; Volatile flame topology; Soot formation; Multi-parameter diagnostics

---

* Corresponding author.
E-mail address: tao.li@rsm.tu-darmstadt.de (T. Li).

1. Introduction

Oxy-fuel combustion is reported as one of the most energy-efficient approaches among the carbon capture and storage (CCS) technologies [1]. However, combustion processes are significantly impacted by introducing carbon dioxide (CO_2), instead of nitrogen (N_2), as the primary inert species due to its different chemical and thermal properties. To enable industrial employment of oxy-fuel combustion in pulverized-fuel-fired power plants, fundamental investigations on the laboratory scale are essential to understand the individual sub-processes and their interactions. For this purpose, temporally and spatially resolved non-intrusive laser diagnostics provide novel insights into the combustion fundamentals.

To understand solid fuel combustion at the particle level, drop tube furnaces (DTF) and laminar flow reactors (LFR) are two established configurations to achieve particle heating rates in the order of 10^5 K/s. Most DTFs are electrically heated, capable of providing controlled wall temperatures and gas compositions for fuel particle combustion, whereas LFRs utilize the exhaust gas of a hydrocarbon flame to create desired combustion environments. Due to the better accessibility, LFRs are preferred for optical measurements. Hencken and McKenna-type burners are different technical realizations [2,3]. In the literature, studies on solid fuel combustion can be divided into two groups, namely single particle combustion (SPC) and particle group combustion (PGC). These two combustion modes differ in whether the particle-particle interaction significantly modifies the flame characteristics. The present work focuses on particle group combustion in a LFR using advanced optical diagnostics.

Regarding particle group combustion, a considerable diversity in the experimental apparatus and analysis approaches can be found in the literature. Cost-effective digital single-lens reflex (DSLR) cameras were adapted to record color images of burning particle groups [4] or to perform pyrometric temperature measurements using the RGB channels [5]. Although temperature information was obtainable via pyrometry measurements [4,5], a clear distinction between particle surface temperature and soot particle temperature was not feasible, especially for bituminous coal. CH^* chemiluminescence imaging using spectral filters [2,5], broad-band thermal radiation detection using ICCD [6] or CMOS cameras [3,7,8] were reported to study particle cloud flames. Recent advancements with high-speed volumetric laser-induced fluorescence measurements of OH radicals (OH-LIF) enabled the 3D reconstruction of volatile flames and an in-depth analysis of flame topology [9]. Combined with instantaneous particle number density (PND) measured with diffuse backlight-illumination (DBI), ignition and flame extinction
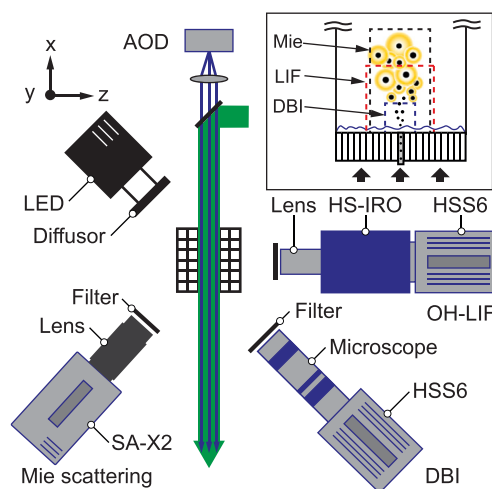

Fig. 1. Experimental setup of simultaneous scanning quasi-4D OH-LIF, DBI, and Mie scattering measurements in the laminar flow reactor.

characteristics were investigated [10] in a conventional atmosphere with 10 vol% oxygen (O_2).

A further understanding of solid fuel combustion requires an in-situ acquisition of multiple essential quantities (i.e., scalars and velocities) with high spatiotemporal resolutions. The present work extends the previous laboratory-scale experiments in [9,10] to different oxygen-rich environments, including both conventional air (i.e., N_2/O_2) and oxy-fuel (i.e., CO_2/O_2) atmospheres. The particle group combustion of solid fuels with gas temperatures at about 1800 K is investigated by using simultaneous DBI, 3D OH-LIF and Mie scattering measurements.

In the following, experimental configurations and methods are introduced with high-speed multi-parameter diagnostics highlighted in Section 2. PND is determined by defining a particle residence volume, and the uncertainties in its calculation are carefully estimated in Section 3.1. Particle velocities are evaluated in Section 3.2 based on time-resolved DBI measurements. In Section 3.3, the influences of O_2 concentration, PND, and inert gas composition (N_2 vs. CO_2) on flame topology and soot formation is discussed based on single-shot visualizations and statistical comparison. Finally, the non-flammability of 3D volatile flame structures is analyzed for different atmospheres and PNDs.

2. Experimental methodology

2.1. Laminar flow reactor

Fig. 1 illustrates a schematic layout of multi-parameter experiments with a generic laminar flow reactor for solid fuel combustion studies. A ce-

ramic honeycomb structure was utilized to stabilize a premixed flat flame, and particles were fed through a central tube by carrier gases. To study particle group combustion, a particle injection tube with an inner diameter of 2.9 mm operated with fully premixed gases was installed, replacing the 0.8 mm N_2-inert jet in the previous study [10]. With other boundary conditions kept identical, the larger jet tube allows for seeding more particles for particle group combustion experiments. N_2/O_2 atmospheres with inlet mixtures of $CH_4/O_2/N_2$ and CO_2/O_2 atmospheres with inlet mixtures of $CH_4/O_2/CO_2$ can be operated in the current LFR. In this study, measurements were performed in four N_2/O_2 atmospheres with increased post-flame O_2 content from 10 to 40 vol%, denoted as AIR10, AIR20, AIR30, and AIR40, and three CO_2/O_2 atmospheres with 20 to 40 vol% O_2, denoted as OXY20, OXY30, and OXY40. The mass diffusivity of O_2 in CO_2 is lower than in N_2, e.g, it reduces by approximately 20% at 1400 K [11]. Details of each atmosphere are described in [12], providing well-characterized boundary conditions, e.g., equivalence ratios, gas temperature profiles, and axial gas velocities. Colombian high-volatile bituminous (hvb) coal particles sieved within a diameter range between 106 - 125 μm were studied with a broad variation of particle number densities. Other parameters such as particle size and type of fuel particles also influence particle group combustion; they will be considered in future work. The proximate and ultimate analyses were reported in [13].

2.2. Scanning OH-LIF

For volatile flame visualization, the scanning-based quasi-4D OH-LIF measurement was performed. A 10 kHz diode-pumped solid-state Nd:YAG laser (Innoslab, Edgewave) was used to pump a dye laser (Credo, Sirah) operated with Rhodamine 6G dissolved in ethanol. The wavelength was tuned to 283.01 nm to excite the $Q_1(6.5)$ line of the A-X(1-0) system with a pulse energy of approximately 0.4 mJ at the laser output. The fundamental wavelength and line width were measured using a wavemeter (WSU-30, HighFinesse), which was calibrated using a temperature-stabilized single-mode HeNe laser. Using an acousto-optic deflector (AOD, D1340, ISOMET), the laser beam was scanned at a frequency of 1 kHz, resulting in 10 individual deflection angles. The deflected laser beam was collected and parallelized by sheet optics and focused at the burner centerline. The laser sheet revealed a height of about 25 mm and a thickness of 130 μm (FHWM) with an average distance of 420 μm between scan planes and an entire scan depth of approximately 3.8 mm. Further details regarding the scanning LIF method with an AOD are described in [9,10]. The OH fluorescence was detected by a CMOS camera (HSS6, LaVision) cou-

pled with a high-speed intensifier (HS-IRO, LaVision). A 100 mm UV lens (Cerco, f/5.6) provided a depth of field (DOF) of > 4 mm. A band-pass filter (T $\geqslant$ 90% between 310 - 320 nm) and a short intensifier gate of 100 ns suppressed the flame luminosity and LIF signals of polycyclic aromatic hydrocarbons (PAH). The field of view (FOV) of OH-LIF slices was approximately 25 × 25 mm^2 with a projected pixel size of 32.4 μ.

2.3. Diffuse backlight-illumination

For the measurement of particle spatial distribution and number densities, a high-speed DBI system was employed, which was inclined by about 64° to the OH-LIF cameras. Particles were backward illuminated by a high-power LED (IPS2, ILA) operated with a pulse duration of 1 μs at 1 kHz. The LED pulses were temporally synchronized to the middle of each OH-LIF scan cycle, providing one shot for every tenth OH-LIF image. A CMOS camera (HSS6, LaVision) equipped with a long-distance microscope (K2, Infinity) collected particle shadow images with a high spatial resolution. A band-pass filter (T $\geqslant$ 50% between 500 - 550 nm) was selected to match the LED emission spectrum (peak at 518 nm) and maximize the signal-to-noise ratio (SNR). The FOV of DBI images was 9.4 × 9.4 mm^2 with a projected pixel size of 9.2 μm.

2.4. Mie scattering

For detection of solid and soot particles in a large FOV, Mie scattering measurements were conducted by using a diode-pumped single-head Nd:YAG laser (Innoslab, Edgewave) with a pulse energy of 2.5 mJ at 10 kHz and 532 nm. Mie scattering was synchronized with OH-LIF measurements with a time offset of 5 μs between 283 nm and 532 nm laser pulses. Both laser beams were combined by a dichroic mirror and aligned to the burner centerline. The 532 nm laser beam was expanded to a volume with a thickness of approximately 8 mm for covering the entire particle jet. A CMOS camera (SA-X2, Photron), equipped with a macro lens (Sigma, f = 180 mm, f/32, DOF > 10 mm) was angled at 32° to the z-axis in the forward scattering direction. The exposure time was reduced to 5 μs. A band-pass filter (T $\geqslant$ 50% between 527 - 537 nm) suppressed the interference signals from luminescent particle flames. The Mie scattering camera provided a FOV of 37.7 (height) × 21.6 (width) mm^2 with a projected pixel size of 36.8 μm. The relative positions of FOVs from the three diagnostics are schematically illustrated in Fig. 1.
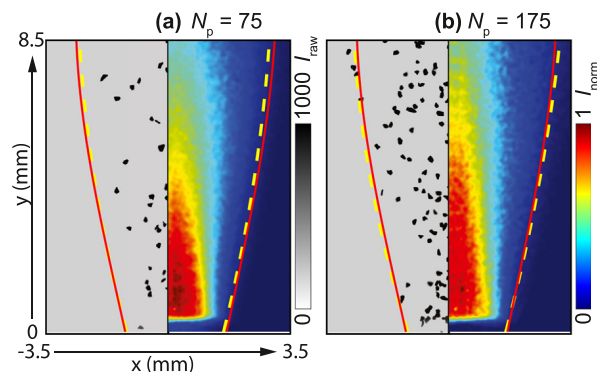
Fig. 2. Particle DBI raw images (left, raw intensities I_{raw}) and normalized mean images (right, normalized intensities I_{norm}) for two different particle numbers N_p.

3. Results and discussion

3.1. PND determination and uncertainties

PND is an important parameter to evaluate the volatile flame topology and flame stabilization in particle group combustion. PND can be evaluated based on the particle number N_p and the 3D particle residence volume V_{jet} obtained from DBI measurements, namely PND = N_p/V_{jet} [10]. Here, N_p, obtained from binarized DBI images using gradient-based particle detection, varies between 1 and 250 particles per frame. The mean 3D volume V_{jet} is computed from a projected particle jet boundary by assuming rotational symmetry. Determination of both parameters is associated with intrinsic uncertainties and limitations by the line-of-sight nature of DBI measurements.

Fig. 2 compares two different particle numbers, $N_p = 75$ and $N_p = 175$, by showing the single-shot and mean DBI images side by side. The mean images are conditioned on N_p between 51 - 100 in Fig. 2(a) and 151 - 200 in Fig. 2(b), and are normalized by their own maximum intensity. Particles within the flat flame (about 1 mm high) are excluded due to strong beam steering. The 2D particle residence boundaries (yellow dashed lines) are determined by using a fixed threshold of 0.95 for each respective N_p, while the red solid line represents the boundary with the same threshold but includes all N_p from 1 to 250 particles, indicating an overall mean boundary. Generally, particle residence area expands along the y-axis mainly due to the volatile release and thermal expansion within the flame. With an increasing N_p, the area of dense particle cloud penetrates further downstream and becomes slightly wider.

Fig. 3(a) compares the PND calculated using an average volume V_{mean} (circles) based on all N_p and V_{bin} (squares), which is computed for each N_p-segment with a bin width of 50 particles. Compared to V_{mean}, PNDs calculated with V_{bin} are slightly

higher for small N_p and lower at large N_p. This is mainly due to the expansion of the particle residence area with increasing particle number. Considering the minor discrepancies, V_{mean} is consistently used in the present work for PND calculation. It also avoids the small drops of PND when changing from one bin size to another by using V_{bin}. Additionally, the number density determined in the previous experiment [10] is shown in Fig 3(a). A higher maximum PND was achieved in [10], but the smaller jet diameter of 0.8 mm limited N_p to about 130. In the present work, a larger tube diameter of 2.9 mm allows for the seeding of more particles, whereas the particle residence volume V_{jet} enlarges by a factor of 2, leading to smaller PND values with the same N_p. It should be noted that a quantitative comparison of PND should be carefully considered as it is highly sensitive to the residence volume.

Due to the line-of-sight nature of DBI measurements, particle overlap is an inevitable problem for dense particle clouds, leading to an underestimation of particle numbers. To assess this uncertainty, synthetic particle image simulations are performed, in which generic ellipsoids are first generated in 3D space and then projected onto the xy-plane. The simulation considers the frame size, pixel pitch, particle size distribution, and particle aspect ratios of the real DBI measurements and randomly distributes a defined number of ellipsoids $N_{p,3D}$ within the 3D volume V_{mean}. The particle number from 2D projection $N_{p,proj}$ is evaluated with the same processing steps as real measurement data. Fig. 3(b) shows the mean and standard deviation (error bars) of $N_{p,proj}$ by increasing $N_{p,3D}$ with an increment of 10 particles and repeating 100 simulations for each increment. Above $N_{p,3D} = 100$, the particle number is gradually underestimated in 2D projections and the discrepancy enlarges with an increasing particle number. Considering that N_p is mostly smaller than 200 in the current experiment, the uncertainty in PND calculation is less than 15% due to the particle
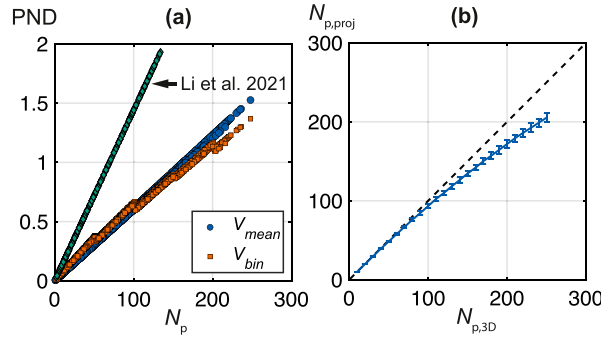
Fig. 3. (a) PNDs (in mm^{-3}) with an increasing particle number N_p detected in DBI measurements. (b) 2D projected particle numbers $N_{p,\text{proj}}$ from synthetic DBI image simulations with particle numbers $N_{p,\text{3D}}$.

overlap. Towards a more accurate PND determination in dense particle clouds, tomographic particle tracking velocimetry (tomo-PTV) is highly desired to resolve the 3D particle location in the future.

3.2. Particle velocity

The particle velocity is evaluated by applying the PIV algorithm (Davis, LaVision) to the time-resolved DBI particle sequences. An interrogation window size of 96×96 pixels is selected, and vectors with correlation values of less than 0.6 are neglected. The statistical velocity evaluation is conditioned on the PND of instantaneous DBI images and performed for AIR and OXY atmospheres, respectively. Fig. 4 exemplarily presents the average velocity $V_{y,p}$ (y-component) and $V_{x,p}$ (x-component) for AIR30 in (a-b) and OXY30 in (c-d) and a side-by-side comparison for PND of 0.15 mm^{-3} (left half) and 0.95 mm^{-3} (right half). Note that velocities outside the reference volume (dashed lines) are associated with higher uncertainties due to smaller particle densities. Generally, $V_{y,p}$ reduces with increasing PNDs, which is consistent with the previous observation of particle jet expansion, indicating a longer particle residence time at higher PNDs. The non-zero $V_{x,p}$ is probably due to the acceleration by the flat flame, which reveals a small Bunsen-like flame structure above the particle exit with a vertical length of about 2 mm. Besides, $V_{y,p}$ is higher in AIR atmospheres due to higher gas velocity than OXY atmospheres [12], whereas $V_{x,p}$ is very similar. At PND = 0.95 mm^{-3}, $V_{y,p}$ first increases along the radial direction and then decreases towards the outside of the particle residence volume (dashed line). Differences in mean particle velocities are also observed by varying O$_2$ concentrations within AIR or OXY atmospheres (not shown), although the gas bulk velocity was kept the same. Both observations are correlated to the lift-off height of volatile flames, which reduces with increasing PNDs and increasing O$_2$ concentrations. The reduced flame lift-

off height leads to a more intense interaction between flame and particles downstream. Further discussion of the flame lift-off height continues in Section 3.3, including O$_2$ and PND effects.

3.3. Volatile flame topology and soot formation

Three-dimensional volatile flame structures are reconstructed by applying linear interpolation between 10 OH-LIF images of each scan sequence. The OH-LIF intensity is corrected with respect to the inhomogeneous laser profile and normalized to the background signal resulting from the water dissociation reaction. Fig. 5 presents four instantaneous flame visualizations represented by isocontours of the OH-LIF intensity for AIR10 - AIR40 atmospheres. These flames have a similar N_p of about 60 particles in frame, corresponding to a PND of approximately 0.35 mm^{-3}. In AIR10, a non-flammable region enclosed by the enveloping flame is observed, which extensively reduces as the O$_2$ concentration increases and entirely disappears in AIR40. With the same O$_2$ concentration, a reduction of gas temperatures before ignition with increasing PNDs was reported in previous experiments [10], due to a higher energy demand for particle heating. Further numerical simulations suggested that the oxygen depletion and low gas temperatures within the flame were mainly responsible for the non-flammable phenomena [14]. On the other hand, with the same PND, a similar amount of heat transferred from gas to solid phase and thus similar gas temperatures before ignition could be assumed. In this case, the local O$_2$ availability extends the flammability and suppresses the flame extinction from AIR10 to AIR40. In addition, volatile flames reveal higher OH-LIF intensities and lower lift-off heights with increasing O$_2$ concentrations, indicating overall enhanced gas-phase reactions.

Fig. 6 illustrates four instantaneous Mie scattering images for the same instants shown in Fig. 5. Both coal particles and soot particles are
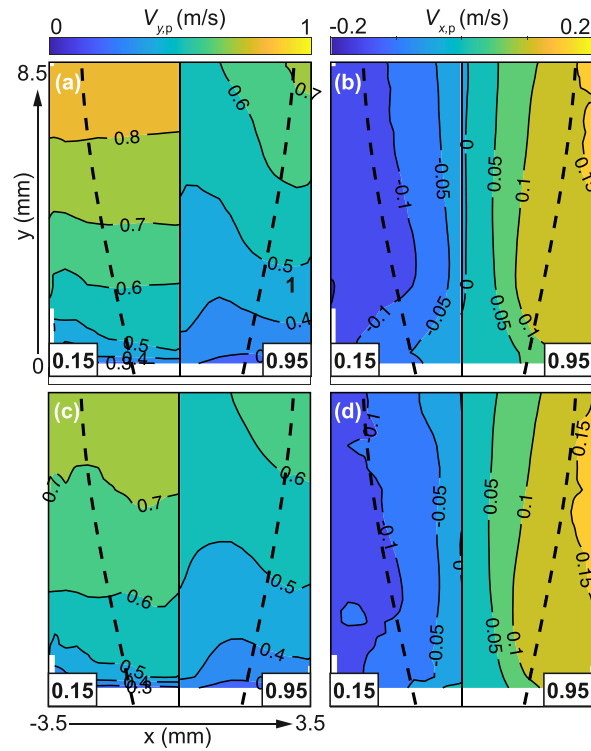
Fig. 4. Velocity components $V_{y,p}$ and $V_{x,p}$ for AIR30 (a-b) and OXY30 conditions (c-d) at two different PNDs of 0.15 and 0.95 mm^{-3}.
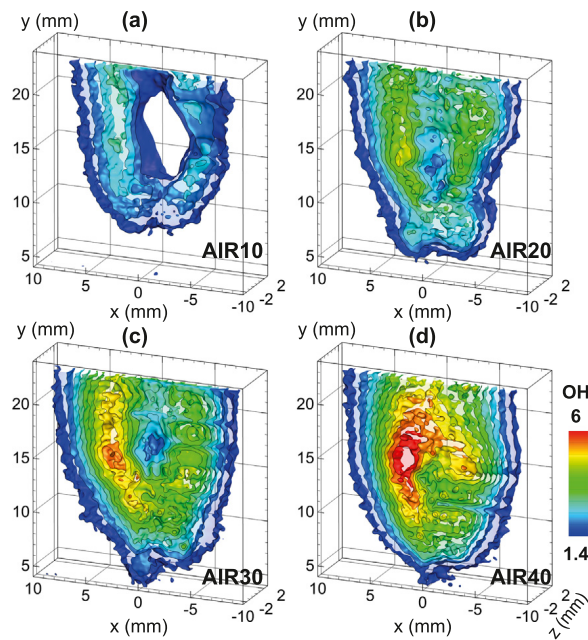

Fig. 5. Individual 3D visualization of volatile flames in AIR conditions with increasing O$_2$ content.
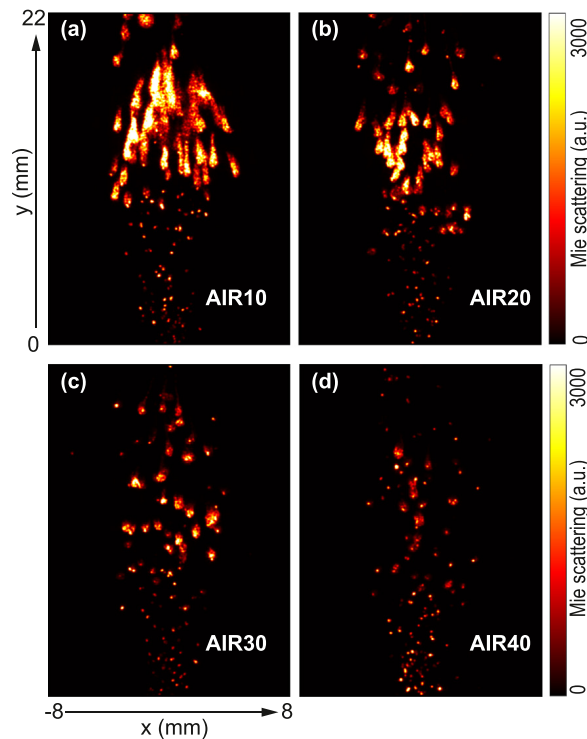
Fig. 6. Simultaneous Mie scattering images corresponding to the sequence in Fig. with increasing O_2 concentrations at PND = 0.35 mm^{-3}.

recorded via Mie scattering. In AIR10, the particle group shows intensive soot formation starting approximately from $y = 10$ mm. Molecular diffusion limits the reaction rate of volatile gas mixtures in laminar flows. The local oxygen depletion promotes the formation pathway of soot through PAH, which could be formed from light hydrocarbon molecules such as CH_4 and C_2H_4 in rich conditions or released directly from the coal during the devolatilization process [15]. Since the volatile release mostly depends on the particle heating rate, which is kept constant in air and oxy-fuel conditions, the directly released PAHs can be expected similar. Hence, soot formation at lower O_2 concentrations mainly results from direct release of tars. The appearance of soot is in accordance with faint shadows in particles' surroundings observed in previous DBI measurements [9]. As O_2 content increases from 10 to 40 mol%, soot formation is significantly suppressed and only appears in the vicinity of individual particles in AIR40. Higher global O_2 concentrations avoid extended fuel-rich conditions near particles and promote fuel and soot oxidation. A better understanding requires simultaneous measurements of PAH and soot particles via laser-induced incandescence (LII) [16] in future investigations.

The influence of the atmospheric O_2 concentration on flame topology and soot formation is further investigated by statistically comparing Mie scattering and OH-LIF signals conditioned on PNDs, which are sliced with a bin width of 0.1 mm^{-3} starting from 0.05 mm^{-3}. Fig. 7 presents a comparison at PND = 0.35 mm^{-3} for AIR conditions with mean Mie (left half) and OH-LIF (right half, center scan plane only) images shown side by side. OH-LIF intensity isocontours begin with 1.4, a threshold applied to define the lift-off height h_{ign}, approximating the location of the maximum OH-LIF intensity gradient. In consistence with the discussion on Fig. 6, OH-LIF intensities increase with O_2 concentrations, whereas Mie scattering intensities reveal an opposite trend. Considering that coal particles exist outside and within the volatile flame region, the change of Mie scattering intensities within the flame is mostly attributed to soot particle clouds. The area of the soot particle cloud is mostly enclosed by the volatile flame and shrinks axially and radially as more O_2 molecules become available. Moreover, the size of the enveloping volatile flames enlarges due to the expansion of the flammability limit with higher O_2 fractions. A clear correlation between soot formation and flame extinction or non-flammability can be noticed. A significant decrease of h_{ign} is observed, indicating a shortened ignition delay time and a stronger interaction between flame and particles (residence area indicated by dashed lines).
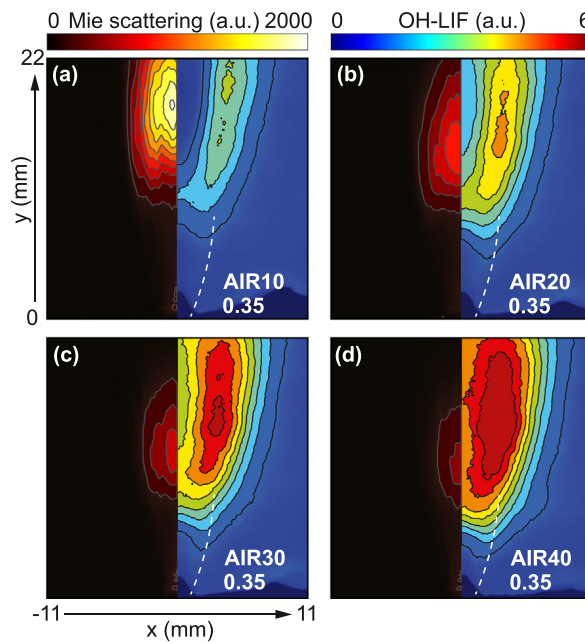
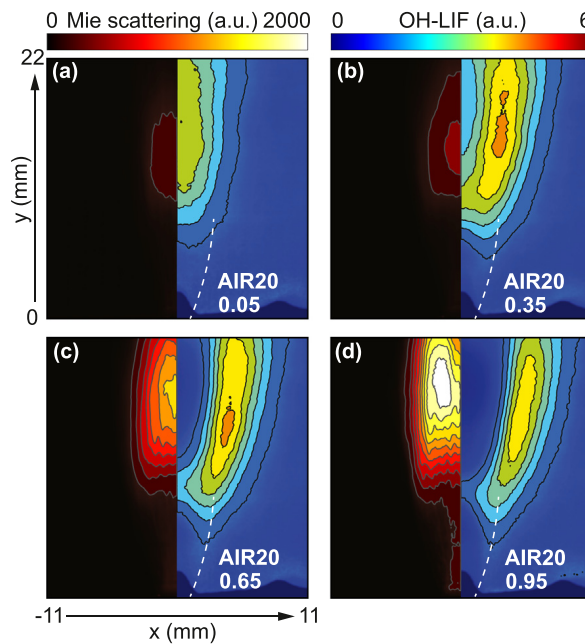Fig. 7. Mean Mie scattering images (left) and mean OH-LIF images (right) with increasing O_2 concentration at PND = 0.35 mm^{-3}.

Fig. 8. Mean Mie scattering images (left) and mean OH-LIF images (right) with increasing PNDs (mm^{-3}) for AIR20.

An evident transition of flame structures with increasing PNDs has been discussed in previous experiments [10] and simulations [14,17]. The present work extends the data set and evaluation to different AIR and OXY atmospheres. Fig. 8 exemplifies conditional mean Mie and LIF images at PND = 0.05, 0.35, 0.65, and 0.95 mm^{-3} for AIR20. A non-flammable region enclosed by the enveloping flame grows extensively with increasing PNDs. The high temperature region becomes thinner and is pushed away from the centerline by the substantial release of volatile matter and enlarg-
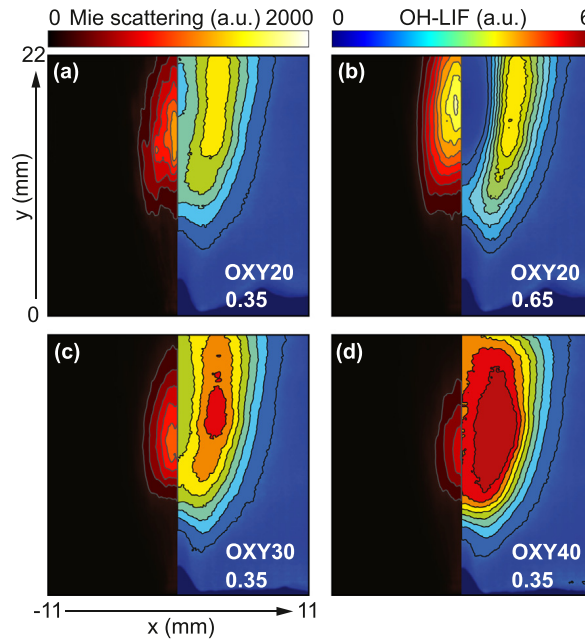
Fig. 9. Mean Mie scattering images (left) and mean OH-LIF images (right) with different O_2 concentration and PNDs (mm^{-3}) in OXY atmospheres.

ing non-flammable regions. A reduction of background OH signals before ignition indicates lower gas temperature as more heat is required for particle heating. Correspondingly, soot particles start forming inside the flame and soot regions significantly increase in size (indicated by isocontours) and intensity with PNDs.

Different from the previous observation in [10], volatile flames in the present study show a decreasing h_{ign} with PNDs, which is similar to the observations reported in [2]. The strong soot formation at higher PNDs might enhance the heat transfer between gas and unignited particles upstream via thermal radiation, accelerating the volatile release and chemical reactions. Besides, lower particle velocities at higher PNDs could lead to decreasing lift-off heights. For a better understanding of the ignition and devolatilization process, particle surface temperature measurements are highly desired in future work. In addition, the structure near the flame base appears similar to a non-premixed lifted gas flame. The "*leading edge*" of this lifted volatile flame is spatially aligned with the particle volume boundary (dashed line in Fig. 7 and Fig. 8). Stronger interaction between flame and particles near this boundary has been noticed in the vertical velocity (Fig. 4), as they are accelerated by the surrounding gas when approaching the high-temperature volatile flame. These particles are substantially heated and are expected to release volatiles faster, forming a flammable mixture near the jet boundary.

Regarding the influence of CO_2 replacement, Fig. 9 exemplarily illustrates the flame structure and soot formation in (a) OXY20, (c) OXY30, and (d) OXY40 at PND = 0.35 mm^{-3}. Compared to AIR conditions, the same effects of additional O_2 on soot reduction and enhancement of gas-phase reactions can be observed. With the same O_2 concentration, volatile flames reveal structural similarity in flame size, intensity, and lift-off height between AIR and OXY conditions. However, slightly higher Mie scattering intensities are noticed in OXY atmospheres indicating stronger soot formation probably due to lower O_2 diffusivity in CO_2 atmospheres. Comparing PNDs of 0.35 and 0.65 mm^{-3} in OXY20, a heavier soot load and the growth of the non-flammable region are observed in Fig. 9 (a) and (b). Additionally, the flame base is similar in AIR and OXY conditions. Since the particle velocity is lower, as shown in Fig. 4, a delayed ignition time can be expected in CO_2 atmospheres.

The combined effects of O_2 concentration, PND, and inert gas composition (N_2 or CO_2) on the flame topology are quantified by evaluating the non-flammability ratio R_{nf} of the 3D volatile flame. R_{nf} is calculated by dividing a 3D flame structure into a flammable region and a non-flammable region with respective volume of V_f and V_{nf}, and defined as $R_{nf} = V_{nf}/(V_f + V_{nf})$. The spatial separation is based on a fixed intensity threshold of 1.4 to deal with the intensity fluctuations in the post-flame region of the premixed flat flame. This parameter has been applied to quantify
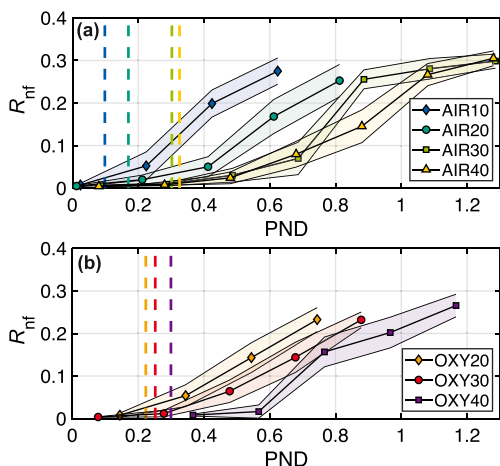
Fig. 10. Comparison of non-flammability ratio R_{nf} over increasing PND and O_2 concentrations in (a) AIR and (b) OXY atmospheres.

the transition from single to particle group combustion [10].

Fig. 10 shows the conditional mean (symbols) and standard deviation (colored polygons) of R_{nf} in different AIR and OXY atmospheres over increasing PNDs. Only the flame structures with $R_{nf} \geqslant 0.3\%$ are included in the statistical analysis to deal with erroneous R_{nf} values due to a partially blocked laser sheet by solid particles. The remaining flames with $R_{nf} < 0.3\%$ are considered to reveal full flammability, and the mean PND of them are indicated by dashed lines. This mean PND represents a transition limit from weak to strong particle-flame interaction leading to local flame extinction. Since the particle number is roughly modulated by the seeder during the experiments, data collected in different atmospheres do not have the same PND range. Nevertheless, the significant influence of PND and O_2 on local flame extinction can be qualitatively analyzed. Generally, volatile flames show higher resistance against local flame extinction for accommodating higher particle densities if more O_2 is available in the atmosphere. Besides, in AIR and OXY conditions, R_{nf} consistently increases with PND due to the local gas temperature reduction and oxygen depletion, as discussed in section 3.3. However, in the limits of experimental uncertainty, it remains unclear whether CO_2 replacement plays a significant role in promoting the flammability, as no obvious differences are noticed between AIR and OXY conditions with the same O_2 concentration.

4. Conclusions

Particle cloud flames of pulverized hvb coal is experimentally studied in a laminar flow reac-

tor with well-defined boundary conditions using multi-parameter optical diagnostics. Compared to our previous studies on particle group combustion [9,10], this work is extended to different combustion environments with a larger diameter of the particle injection tube. Simultaneously applied quasi-4D OH-LIF, high-speed DBI and Mie scattering measurements allow for detection of volatile flame structures, particle velocity, number density, and soot formation in various AIR and OXY atmospheres. For PND determination, generic particle simulations suggest an underestimation of the particle number up to 15% due to particle overlap in the line-of-sight DBI measurements. Particle velocity decreases with increasing PNDs and shows an evident acceleration by the enveloping volatile flame. Based on experimental observations, effects of O_2 concentration, PND and inert gas composition can be conclusively summarized as follows.

(1) Local flame extinction is gradually suppressed by increasing O_2 concentrations, indicating that local oxygen availability extends the gas flammability and counteracts the negative effect of gas temperature reduction during particle heating. Additional O_2 enhances the reactivity of volatile gas mixtures, leading to reduced soot formation and a lower flame lift-off height. (2) An increased PND induces stronger flame extinction and soot formation likely due to local oxygen depletion and gas temperature reduction. Importantly, the lift-off height decreases at higher PNDs, and the flame structure near the stabilization point is similar to the edge flame in non-premixed combustion. This structure is spatially aligned with the boundary of particle residence volume, indicating a complex interaction between particle dynamics, heat transfer and volatile reactions. (3) A similar lift-off height is observed in OXY and AIR atmospheres with the identical O_2 concentration and PND, but a larger ignition delay time can be expected in OXY conditions as a result of lower particle velocities. No obvious difference is observed in the flame extinction behavior with CO_2 replacement, however, soot formation slightly increases, probably due to the lower O_2 diffusivity in CO_2.

Declaration of Competing Interest

The authors declare that they have no known competing financial interests or personal relationships that could have appeared to influence the work reported in this paper.

Acknowledgments

References

[1] M.B. Toftegaard, J. Brix, P.A. Jensen, P. Glarborg, A.D. Jensen, Oxy-fuel combustion of solid fuels, Prog. Energy Combust. Sci. 36 (5) (2010) 581–625, doi:10.1016/j.pecs.2010.02.001.

[2] Y. Liu, M. Geier, A. Molina, C.R. Shaddix, Pulverized coal stream ignition delay under conventional and oxy-fuel combustion conditions, Int. J. Greenhouse Gas Control 5 (2011) S36–S46, doi:10.1016/j.ijggc.2011.05.028.

[3] W. Prationo, L. Zhang, Influence of steam on ignition of victorian brown coal particle stream in oxyfuel combustion: in - situ diagnosis and transient ignition modelling, Fuel 181 (2016) 1203–1213, doi:10.1016/j.fuel.2016.03.003.

[4] Z. Zeng, T. Zhang, S. Zheng, W. Wu, Y. Zhou, Ignition and combustion characteristics of coal particles under high-temperature and low-oxygen environments mimicking MILD oxy-coal combustion conditions, Fuel 253 (2019) 1104–1113, doi:10.1016/j.fuel.2019.05.101.

[5] Y. Yuan, S. Li, F. Zhao, Q. Yao, M.B. Long, Characterization on hetero-homogeneous ignition of pulverized coal particle streams using CH* chemiluminescence and 3 color pyrometry, Fuel 184 (2016) 1000–1006, doi:10.1016/j.fuel.2015.11.032.

[6] Y. Yuan, S. Li, G. Li, N. Wu, Q. Yao, The transition of heterogeneous–homogeneous ignitions of dispersed coal particle streams, Combust. Flame 161 (9) (2014) 2458–2468, doi:10.1016/j.combustflame.2014.03.008.

[7] A. Adeosun, Z. Xiao, Z. Yang, Q. Yao, R.L. Axelbaum, The effects of particle size and reducing-to-oxidizing environment on coal stream ignition, Combust. Flame (2018), doi:10.1016/j.combustflame.2018.05.003.

[8] A.C. Sarroza, T.D. Bennet, C. Eastwick, H. Liu, Characterising pulverised fuel ignition in a visual drop tube furnace by use of a high-speed imaging technique, Fuel Process. Technol. 157 (2017) 1–11, doi:10.1016/j.fuproc.2016.11.002.

[9] T. Li, M. Schiemann, J. Köser, A. Dreizler, B. Böhm, Experimental investigations of single particle and particle group combustion in a laminar flow reactor using simultaneous volumetric OH-LIF imaging and diffuse backlight-illumination, Renewable Sustainable Energy Rev. 136 (2021) 110377, doi:10.1016/j.rser.2020.110377.

[10] T. Li, C. Geschwindner, J. Köser, M. Schiemann, A. Dreizler, B. Böhm, Investigation of the transition from single to group coal particle combustion using high-speed scanning OH-LIF and diffuse backlight-illumination, Proc. Combust. Inst. 38 (3) (2021) 4101–4109, doi:10.1016/j.proci.2020.06.314.

[11] A. Suriyawong, M. Gamble, M.-H. Lee, R. Axelbaum, P. Biswas, Submicrometer particle formation and mercury speciation under o 2 - CO 2 coal combustion, Energy Fuels 20 (6) (2006) 2357–2363, doi:10.1021/ef060178s.

[12] T. Li, P. Farmand, C. Geschwindner, M. Greifenstein, J. Köser, C. Schumann, A. Attili, H. Pitsch, A. Dreizler, B. Böhm, Homogeneous ignition and volatile combustion of single solid fuel particles in air and oxy-fuel conditions, Fuel 291 (1) (2021) 120101, doi:10.1016/j.fuel.2020.120101.

[13] S. Pielsticker, S. Heuer, O. Senneca, F. Cerciello, P. Salatino, L. Cortese, B. Gövert, O. Hatzfeld, M. Schiemann, V. Scherer, R. Kneer, Comparison of pyrolysis test rigs for oxy-fuel conditions, Fuel Process. Technol. 156 (2017) 461–472, doi:10.1016/j.fuproc.2016.10.010.

[14] H. Nicolai, T. Li, C. Geschwindner, F. Di Mare, C. Hasse, B. Böhm, J. Janicka, Numerical investigation of pulverized coal particle group combustion using tabulated chemistry, Proc. Combust. Inst. 38 (3) (2021) 4033–4041, doi:10.1016/j.proci.2020.06.081.

[15] P.R. Solomon, M.A. Serio, E.M. Suuberg, Coal pyrolysis: experiments, kinetic rates and mechanisms, Prog Energy Combust Sci 18 (2) (1992) 133–220, doi:10.1016/0360-1285(92)90021-R.

[16] J. Hayashi, N. Hashimoto, N. Nakatsuka, K. Tainaka, H. Tsuji, K. Tanno, H. Watanabe, H. Makino, F. Akamatsu, Simultaneous imaging of Mie scattering, PAHs laser induced fluorescence and soot laser induced incandescence to a lab-scale turbulent jet pulverized coal flame, Proc. Combust. Inst. 37 (3) (2019) 3045–3052, doi:10.1016/j.proci.2018.09.028.

[17] P. Farmand, H. Nicolai, C. Schumann, A. Attili, L. Berger, T. Li, C. Geschwindner, F. Di Mare, C. Hasse, B. Böhm, J. Janicka, H. Pitsch, Numerical investigation and assessment of flameletbased models for the prediction of pulverized solid fuel homogeneous ignition and combustion, Combust. Flame 235 (2022) 111693, doi:10.1016/j.combustflame.2021.111693.

A.4 Paper IV - OH-PLIF of flame retarded polymer particles

Reproduced with permission from Springer Nature.

RESEARCH ARTICLE

Investigation of flame retarded polypropylene by high-speed planar laser-induced fluorescence of OH radicals combined with a thermal decomposition analysis

Christopher Geschwindner[1] · Daniela Goedderz[2,3] · Tao Li[1] · Jan Köser[1] · Claudia Fasel[4] · Ralf Riedel[4] · Volker Altstädt[5] · Christian Bethke[5] · Florian Puchtler[6] · Josef Breu[6] · Manfred Döring[3] · Andreas Dreizler[1] · Benjamin Böhm[1]

Abstract
The combustion of micrometer-sized polypropylene (PP) particles is analyzed in situ using a combination of high-speed planar laser-induced fluorescence of the OH radical (OH-PLIF) and a thermal decomposition analysis. The gas phase is investigated by multiple analytical techniques to gain comprehensive knowledge on the decomposition products of flame retardants and their effect on the combustion process. Neat PP is compared with a formulation consisting of 10 wt% of a phosphorus-containing flame retardant (pentaerythritol spirobis(methylphosphonate), PSMP) which is known to provide gas phase activity. The decomposition of the neat flame retardant, PP and the flame retardant formulation is investigated using a simultaneous analysis (STA) consisting of a thermal gravimetric analysis and a differential thermal analysis device which is coupled to Fourier-transform infrared spectroscopy and mass spectrometry devices. By this, the release of decomposition products of the flame retardant additive can be determined. The excitation of OH radicals is used to temporally track the diffusion flame surrounding the particles during combustion in a laminar flow reactor. The radial distance to the peak reactivity zone of flame retardant containing particles increased by about 70 µm compared with neat PP particles. Tracking the peak OH signal in the diffusion flame, during ignition and the early phase of combustion, a decrease in the peak intensity is observed for flame retardant polymer particles. Additionally, cone calorimeter tests are used to evaluate the combustion behavior as a standard test in flame retardancy.

✉ Christopher Geschwindner
  geschwindner@rsm.tu-darmstadt.de

1 Reaktive Strömungen und Messtechnik, Technische Universität Darmstadt, Otto-Berndt-Straße 3, 64287 Darmstadt, Germany

2 Ernst-Berl Institute for Chemical Engineering and Macromolecular Science, Technische Universität Darmstadt, Alarich-Weiss-Straße 4, 64287 Darmstadt, Germany

3 Fraunhofer Institute for Structural Durability and System Reliability LBF, Schlossgartenstraße 6, 64289 Darmstadt, Germany

4 Institut für Materialwissenschaft, Technische Universität Darmstadt, Otto-Berndt-Straße 3, 64287 Darmstadt, Germany
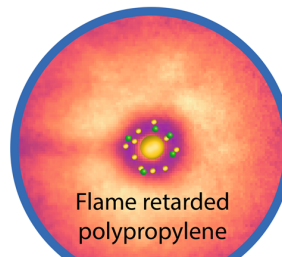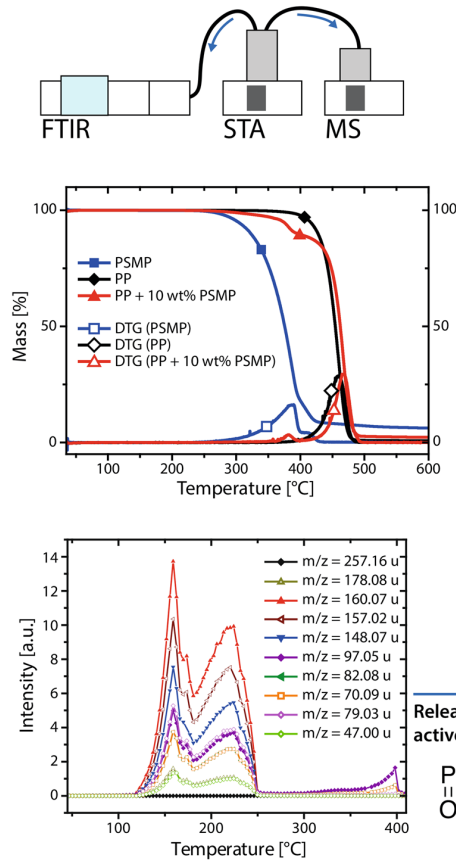
5 Department of Polymer Engineering, University of Bayreuth, Universitätsstraße 30, 95447 Bayreuth, Germany

6 Department of Chemistry, Bavarian Polymer Institute, University of Bayreuth, Universitätstraße 30, 95447 Bayreuth, Germany

⌀ Springer

109

Graphic abstract
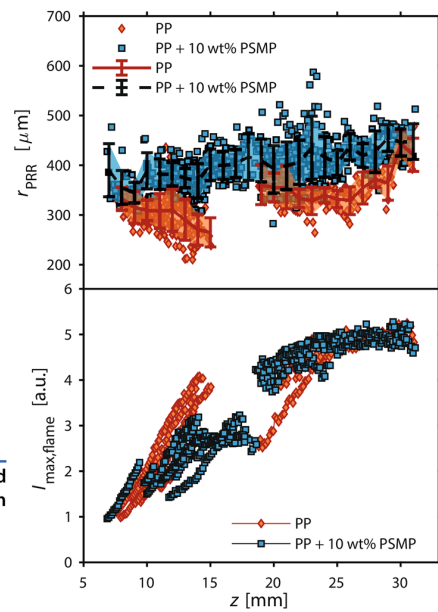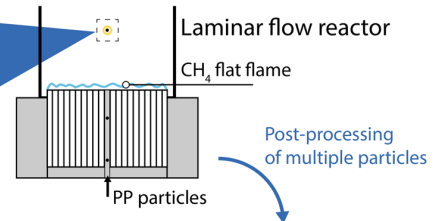
1 Introduction

Combustible organic polymeric materials require tailor-made flame retardant solutions to lower the fire hazard by supplying suitable flame retardancy. The price, the influence on properties of the polymer, and the release of toxic decomposition products are selection criteria which have to be considered. Flame retardants can be classified in terms of their mode of action into gas phase active agents, condensed phase active agents, and a combination of both mechanisms. The condensed phase activity of flame retardants is mainly based on the formation of a protective char layer (Lewin and Weil 2001; Schartel 2010), while gas phase active flame retardants are able to scavenge OH and H radicals in the flame by decomposing into highly reactive radicals themselves (Eqs. 1–4) (Green 1996; Hastie 1973; Klinkowski et al. 2015; Schartel 2010).

The volatile decomposition products of methylphosphonate containing flame retardants are phosphorus-based radicals like PO, PO_2, and their corresponding acids HPO and HPO_2 which poison the flame by chemical inhibition (Hastie 1973; Klinkowski et al. 2015; Lewin and Weil 2001; Schartel 2010).

$$PO^. + H^. \rightarrow HPO, \tag{1}$$

$$PO^. + OH^. \rightarrow HPO_2, \tag{2}$$

$$HPO + H^. \rightarrow H_2 + PO^., \tag{3}$$

$$HPO_2^. + OH^. \rightarrow H_2O + PO_2. \tag{4}$$
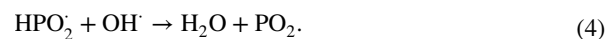
The evolved decomposition products of the polymer during the combustion process can be analyzed using various methods such as thermal desorption mass spectrometry

(TDMS), thermogravimetry coupled with mass spectrometry (TG–MS), thermogravimetry coupled with Fourier-transform infrared spectroscopy (TG–FTIR) or pyrolysis–gas chromatography (Py–GC) which are most commonly used.

If a sample is exposed to a defined temperature program, volatile products are released in the gas phase. The evolved products can be analyzed by mass spectrometry, FTIR or other suitable devices. The gaseous products can be transferred by a direct inlet (TDMS) or with a heated column (TG–MS, TG–FTIR) into the ion source (Bart 2006; Salmeia et al. 2015).

Based on this approach, the decomposition mechanism of the flame retardant can be assessed, but these techniques are not comparable to a real combustion scenario due to an oxygen-free environment, the absence of an ignition source and a relatively low heating rate of 10 K/min (Salmeia et al. 2015).

Apart from the experimental methods used to observe the thermal decomposition products with respect to the polymer chemistry, an analysis of highly active radicals in combustion systems is of great interest to evaluate the effectiveness of flame retardants and to replicate similar conditions as they appear in a fire. The detection of active radicals in flames doped with flame retarding substances has been achieved using molecular beam mass spectrometry (MBMS) (Beach et al. 2009; Korobeinichev et al. 2013; Shmakov et al. 2007), chemiluminescence imaging (Beach et al. 2009), vacuum ultraviolet (VUV) photoionization (Liang et al. 2015) coupled with time-of-flight MS, and laser-induced fluorescence (LIF) (MacDonald et al. 2001; Siow and Laurendeau 2004; Vora and Laurendeau 2001; Vora et al. 2001). In the context of in situ measurements, optical techniques such as LIF are non-intrusive and therefore have negligible instrumental effects on the results in contrast to MBMS, which requires a probe perturbing the observed flame (Hartlieb et al. 2000; Kohse-Höinghaus et al. 2005; Liang et al. 2015; Salmeia et al. 2015).

So far, the influence of flame retardants on the combustion process using laser-induced fluorescence of the hydroxyl radical (OH-LIF) was mainly analyzed in counter-flow burner gas flames by adding vaporized agents to the fuel or oxidizer streams. The objects of interest of these studies were organophosphorus substances and halons including phosphorus-containing substances such as dimethyl methylphosphonate (DMMP) (MacDonald et al. 2001; Siow and Laurendeau 2004), trimethyl phosphate (TMP) (Siow and Laurendeau 2004), and bromotrifluoromethane (Vora and Laurendeau 2001; Vora et al. 2001). The quantitatively measured OH number density along the centerline of the burner decreased as the amount of flame retardants increased, indicating a reduction of the reactivity. Apart from hydroxyl concentration measurements, the decrease of

the global extinction strain rate was used to determine the effectiveness of flame retardancy for the investigated additives in counter-flow burners (MacDonald et al. 1999). As non-combustible gas phase active flame retardants generally lower the reactivity within the flame by both dilution and radical scavenging, the decrease of the OH signal and the extinction strain rates, respectively, were compared with nitrogen which provided a measure for flame retardant efficacy solely induced by dilution. Subsequently, halons and organophosphorus substances showed a higher efficacy than nitrogen pointing towards the importance of flame poisoning in the inhibition process (MacDonald et al. 1999; Vora et al. 2001).

As the pyrolysis and ignition are key aspects of the combustion of solids, the influence of flame retardants on polymers has to be investigated in situ at high spatial and temporal resolutions to approach realistic conditions in experiments when compared with burning polymer materials in fire scenarios. The advancement of laser and camera systems in recent years has enabled the application of high-speed OH-PLIF to investigate the devolatilization and ignition of coal particles (Köser et al. 2017). The ignition and combustion of flame retarded polymer particles can be investigated using a similar methodology.

To the best of the author's knowledge, this work describes the detection of OH radicals within the diffusion flame of flame retarded polymers for the first time by the application of OH-PLIF. For this purpose, the combustion of polypropylene (PP) particles of a defined size distribution was initiated within a laminar flow reactor. The influence of the flame retardant pentaerythritol spirobis(methylphosphonate) (PSMP) on the relative OH intensity as well as the flame shape was observed using a well-defined post-processing methodology by extracting parameters of the flame topology from the radial OH signal profiles. A combination of chemical decomposition analyses using differential thermal analysis (DTA) coupled to Fourier-transform infrared spectroscopy and mass spectrometry devices (TGA–DTA–FTIR–MS) and TDMS provides knowledge on the chemical aspect of flame retardancy regarding the mode of action and the identification of evanescent fragments of the flame retardant participating at the flame inhibition. Additionally, cone calorimetry results as a standard test procedure for the determination of heat release of polymer compounds are included to evaluate the flame retardant efficacy. Thus, the combination of the used methods OH-PLIF, TDMS, TGA–DTA–FTIR–MS and cone calorimetry supplies information about the gas phase during the combustion process in the flame zone as well as the pyrolysis process and offers a more detailed insight about the combustion process than the individual methods.

2 Experimental setups and procedure

2.1 Materials and preparation

PP (Moplen HP 500N) was provided by LyondellBasell, the Netherlands. Pentaerythritol spirobis(methylphosphonate) (PSMP) was supplied by Thor, Germany. The compounding was carried out using a co-rotating twin-screw extruder (Thermo Fisher Scientific Process 11; screw diameter: 11 mm) with a screw rotation speed of 150 rpm. The first temperature zone (1) was set to 210 °C, while all other temperature zones (2–7) were stabilized at 220 °C. The die temperature was set to 220 °C. The melt strand was cooled with a water bath and pelletized in a pelletizing system (VariCut Granulator). The extrusion process is pictured in Fig. 1.

The pelletized polymer was ground several times with a centrifugal mill (Retsch ZM 200). The grinded polymer was separated by size using a vibratory sieve shaker operated for 15 min. Particles in the range of 100–150 μm were collected using different sieves (DIN ISO 3310, $\varnothing = 200$ mm, openings 100 μm and 150 μm). Optical

microscope images of the particles and the particle distribution are displayed in Figs. 2 and 3.

2.2 Characterization of thermal decomposition products and cone calorimetry

The thermogravimetric analysis (TA Instruments TGA Q500) was carried out with a heating rate of 10 K/min under constant nitrogen atmosphere. The simultaneous thermal analysis was carried out using a TGA/STA (Netzsch Gerätebau GmbH STA 449C Jupiter) coupled to FTIR (Bruker Tensor 27) and MS (Netzsch Gerätebau GmbH QMS 403C Aëolos) at a constant heating rate of 10 K/min in a temperature range of 35–600 °C under a flowing

Fig. 3 Particle size distribution of 15 obtained particles per compound. The average of the mean particle size is 213 μm for PP and 237 μm for PP + 10 wt% PSMP
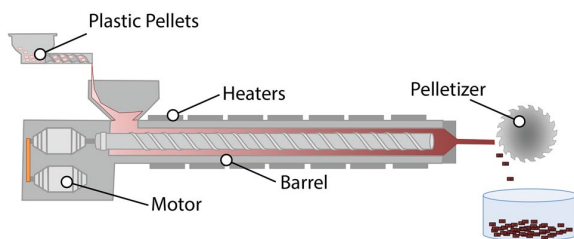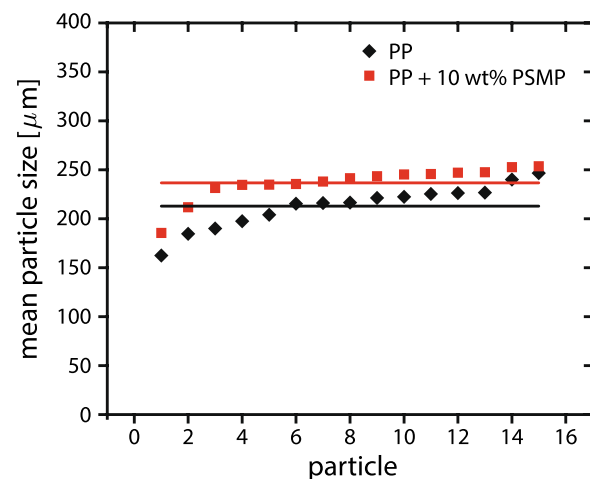
Fig. 1 Scheme of the extrusion process
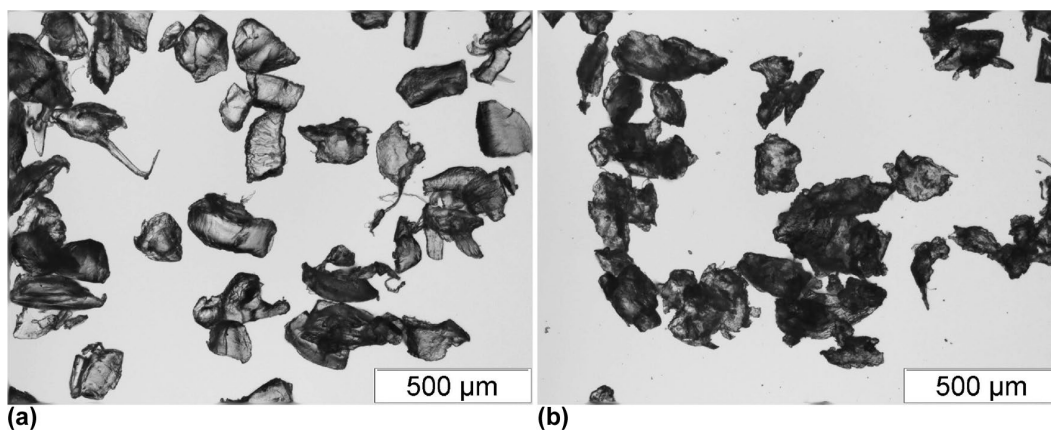
Fig. 2 Optical microscope images of neat PP particles (**a**) and PP particles with 10 wt% PSMP (**b**)

nitrogen atmosphere (30 ml/min). Thermodesorption MS (Finnigan MAT 95) experiments were conducted using a constant heating rate of 25 K/min in a temperature range of 40–400 °C. Previous experiments showed that the pathway of the decomposition products is heating rate independent which is in accordance to studies presented in the literature (Wang et al. 2019).

PSMP is a well-known phosphorus-containing flame retardant for polypropylene applications. The gas phase activity of this flame retardant has been the subject of some earlier studies (Goedderz et al. 2020; Pfaendner et al. 2014; Salmeia et al. 2018). The decomposition products of the flame retardant can be detected by simultaneous thermal analysis including TG–MS and TG–FTIR due to the volatility of the decomposition products. Neat PSMP as a phosphonate has a phosphorus content of 24.2%. Compounds containing neat PP and PP + 10 wt% PSMP with a calculated phosphorus content of 2.4% were prepared (Table 1).

The cone calorimeter samples were obtained by hot pressing (300E, Collin) of the compounds at 220 °C and 5 bar for 5 min. The cone calorimeter tests were carried out according to ISO 5660 on a device (Fire Testing Technology, according to ASTM E 1354) with 35 kW/m^2 heat flux burning

Table 1 Phosphorus content of neat PSMP, neat polypropylene and polypropylene containing 10 wt% PSMP

Composition	Calculated phosphorus content (%)
PSMP	24.2
PP	–
PP + 10 wt% PSMP	2.4

specimen with a size of $100 \times 100 \times 2$ mm^3. All samples were tested in triplicate.

2.3 High-speed planar laser-induced fluorescence of the OH radical (OH-PLIF)

For the present study, the polymer chosen for the analysis of flame retardancy is PP. When excited with UV radiation, PP as a non-aromatic polymer shows a less intense fluorescence emission than aromatic polymers such as PET and is therefore better suited for monitoring the adjacent gas phase combustion using OH-PLIF. To visualize the reaction zones surrounding igniting PP particles in the gas phase, planar laser-induced florescence of the OH radical was applied within a laminar flow reactor test rig depicted in Fig. 4a. The experimental setup has been previously used to study the ignition and volatile combustion of solid fuel particles and is well described in Köser et al. (2017, 2019). A fully premixed flat flame was stabilized upon a ceramic honeycomb using a gas mixture of CH_4, O_2 and N_2 such that the exhaust gases contain an oxygen volume fraction of 10 vol%. Single polymer particles were injected through a centrally mounted tube (inner diameter 0.8 mm) using a carrier gas flow of N_2. As the particles passed through the region of strong heat-up ($\approx 10^5$ K/s) within the premixed flat flame, pyrolysis of combustible products was induced which further lead to ignition and combustion. Assuming convective heat transfer with a constant surrounding gas temperature, the maximum heat flux from the surrounding flat flame to a particle of diameter 220 μm is 1600 kW/m^2. The coordinates x and z were defined with respect to the exit of the particle injection tube on the top surface of the ceramic honeycomb which is hereafter referred to as the burner head.

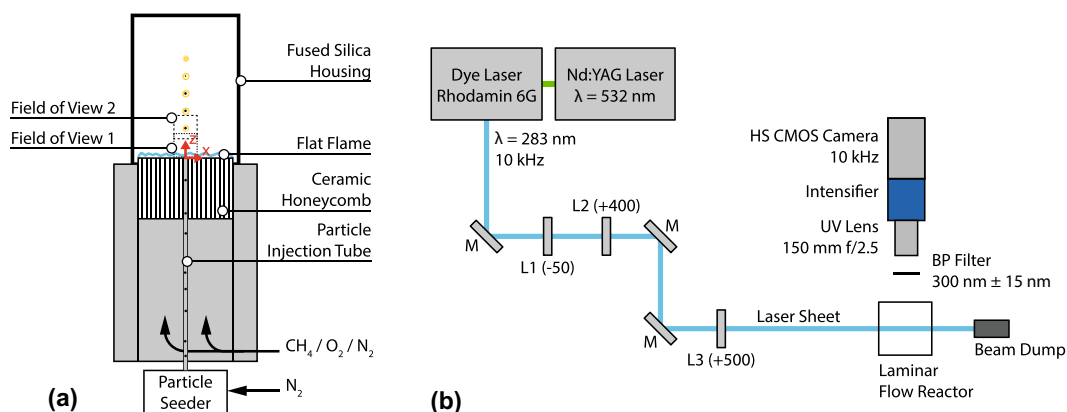**Fig. 4** **a** Schematic drawing of the laminar flow reactor test rig. The outlines of the fields of view imaged within this work are represented by two dashed rectangles. **b** Experimental setup including the beam path of the laser excitation as well as the fluorescence detection unit consisting of a high-speed CMOS camera coupled with an image intensifier, a UV lens as well as a bandpass filter

As shown in Fig. 4b, a frequency-doubled dye laser (Sirah Credo; Rhodamine 6G) was pumped by a solid-state Nd:YAG laser (EdgeWave IS8II-E) at 532 nm. The dye laser was tuned to an output wavelength of 283.01 nm to excite the $Q_1(6)$ line of the A-X(1-0) transition of the OH radical. The repetition rate of the laser source was set to 10 kHz with a mean pulse energy of ~0.4 mJ obtained directly after exiting the enclosure of the laser. Subsequently, the laser beam was shaped into a 90 µm thick sheet using a set of cylindrical lenses ($f_{L1} = -50$ mm, $f_{L2} = +400$ mm, $f_{L3} = +500$ mm) as well as UV-reflective mirrors guiding the beam into the test rig. The detection unit consisted of a high-speed CMOS camera (LaVision HSS6) operating at 10 kHz in sync with the laser pulses as well as an image intensifier (LaVision HS-IRO) and a UV lens (Halle 150 mm f/2.5) which was equipped with a bandpass filter (300 nm ± 15 nm) to restrict the detection of fluorescence in a defined spectral range. By traversing the burner in the z-direction, two fields of view with a size of 19.10×19.25 mm each and an overlap of about 5 mm were recorded to investigate both the ignition (field of view 1: $z = 0.94$–20.18 mm) as well as the fully developed flame (field of view 2: $z = 15.94$–35.18 mm) surrounding the polymer particles. The pixel resolution of the obtained images, measured with a calibration plate, was 24.6 µm/px, while the optical resolution of the imaging system, measured with a Siemens star, was ≈ 100 µm.

3 Data processing of OH-PLIF images

The obtained OH-PLIF raw images were analyzed using a custom post-processing strategy. At first, a normalization of the OH signal was conducted for every image individually. Assuming a constant OH background from the flue gas of the flat flame, a 100 px wide background in a region without interference with particle combustion was sampled over the entire height of the field of view similar to previous OH-PLIF studies of coal particles by Köser et al. (2015). This image section was averaged over the x-coordinate to generate a mean OH background for every image obtained. As both the spatial distribution of the laser intensity beam profile as well as the shot-to-shot intensity fluctuations affect the detected OH signal, a row-wise normalization of the image based on the intensity value of the mean OH background signal was applied to compensate for both effects. This qualitative approach enables the comparison of normalized OH signal intensities I_{norm} with respect to the background assuming minor influence of changing temperature environments.

Figure 5a illustrates further processing of preprocessed OH-PLIF images of burning polymer particles. The combustion of a PP particle in the upper field of view is depicted. As the laser approaches the particle flame

from the positive x-direction (from the right in Fig. 5a), a shadow is cast on the left side of the particle indicating its central position in the light sheet. To ensure that the particles are centrally positioned within the laser sheet, only particles with this recognizable feature are included within this study. Otherwise, an underestimation of the distance of the particle to its reaction zone would be possible. Next, the normalized intensity signal of the right half of the particle signal is averaged along a semicircle generating the normalized radial intensity profile indicated in Fig. 5b. Both the peak intensity value in the flame $I_{max,flame}$ and the radius of peak reactivity rate r_{PRR} are extracted from the intensity profile. The latter parameter represents the radial distance of the particle center to the onset of the reaction zone of the diffusion flame and is calculated using the radial derivative of the intensity profile according to Eq. (5). The methodology uses the mean radius of the radii corresponding to the peak 95% of the radial derivative of the normalized intensity and therefore assures a robust calculation of r_{PRR}, as the gradient curve does not always show one single pronounced peak. Prior to calculating the derivative, the radial profile is smoothed using a spline interpolation which prevents any oscillations between values for r_{PRR} caused by the pixel discretization.

$$r_{PRR} = \text{mean}\left[r\left(0.95 \times \max\left(\frac{\partial I_{norm}}{\partial r}\right)\right)\right]. \tag{5}$$

One of the challenges of LIF measurements of PP particles is the photoluminescence of neat PP (Osawa et al. 1984) and its decomposition products when excited with UV radiation. This is obvious from inspecting the center of the particle shown in Fig. 5a. Therefore, the luminescence images were recorded tuning the dye laser off-resonance by 10 cm^{-1} to analyze the spatial influence of the fluorescence of PP and its decomposition products (Fig. 5c). Figure 5d shows that the detected signal quickly decays to 10% of the peak intensity in the center of the particle within a radius of 200 µm with respect to the particle center. This confirms that the circular signal detected for resonant excitation can be solely attributed to the OH signal within a diffusion flame surrounding the particle.

4 Results and discussion

4.1 Simultaneous thermal analysis of flame retardant formulations

The neat flame retardant PSMP, PP and 10 wt% of PSMP in PP were analyzed using an STA in a nitrogen atmosphere (Fig. 6, Table 2). The sample is heated at 10 K/min,
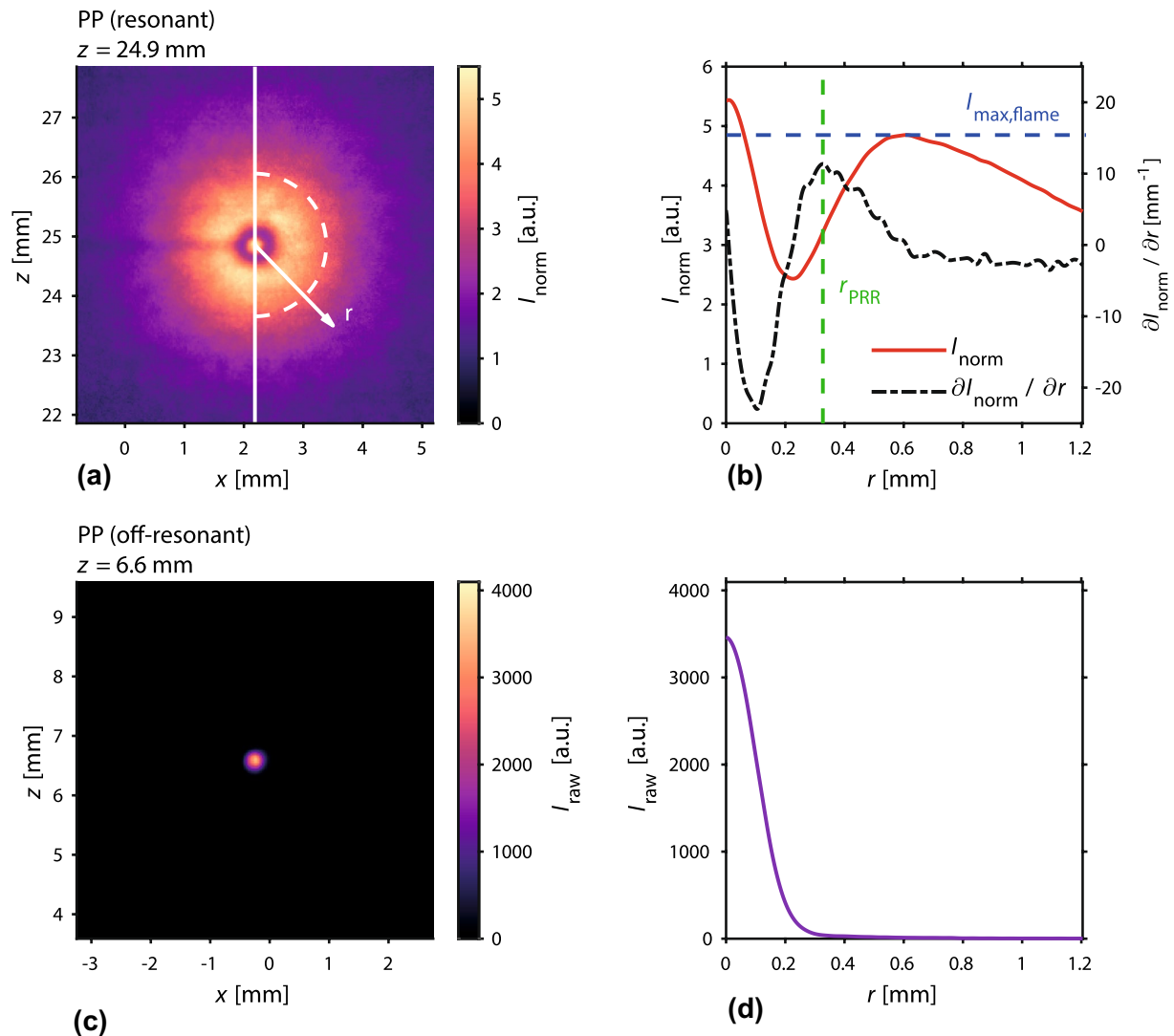
Fig. 5 **a** Preprocessed OH-PLIF signal of a PP particle in the upper field of view. The right section of the signal without the cast shadow is averaged for every radius indicated by a dashed semicircle. **b** Associated normalized radial intensity profile of the OH signal (solid line) and corresponding gradient curve (dashed line). The peak flame intensity $I_{max,flame}$ and the radius of peak reactivity rate r_{PRR} for the resonant case are marked with dashed lines. **c** Raw off-resonant OH-PLIF image of a PP particle. **d** Radial intensity profile of a particle imaged off-resonant

while transformations of the sample mass are monitored to investigate the pyrolysis behavior regarding the mass loss with respect to temperature. The sample mass and its derivative (Fig. 6a) as well as the differential temperature (Fig. 6b) are plotted against the temperature. The flame retardant PSMP and PP both decompose in one step. However, the formulation 10 wt% of PSMP in PP decomposes in a two-step process with a weight loss of 10% in the first step. The addition of the flame retardant leads to a decomposition of the mixture at lower temperatures compared with the neat polymer. A weight loss

of 1% occurs at 383 °C for PP and at 299 °C for the flame retardant formulation. The decomposition temperature of 10 wt% PSMP + PP is significantly lowered by 84 °C when compared with neat PP. The residues of both polymer samples at 600 °C are 1–2%, so the addition of 10 wt% flame retardant leads to no significant increase of the residue at 600 °C. In the DTA curve of PP + 10 wt% PSMP, the melting point of PSMP at 250 °C is apparent.

TDMS is a method used to detect desorbed molecules or fragments while the sample is being heated up. The TDMS diagrams of neat PSMP, neat PP and PP + 10 wt%
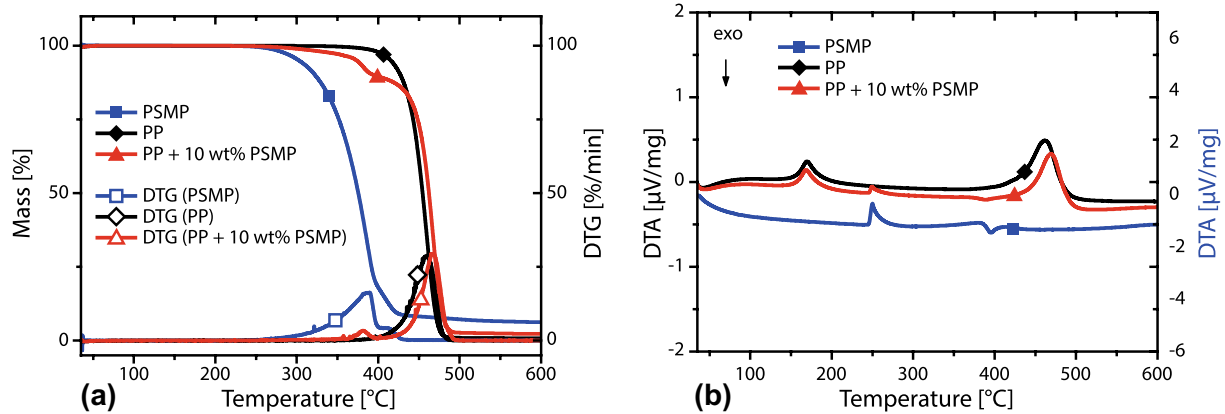
Fig. 6 Thermogravimetric analysis with its first derivative plot (DTG, **a**) and DTA curve (**b**) of neat flame retardant PSMP, PP and PP + 10 wt% PSMP at 10 K/min under nitrogen

Table 2 Thermal properties of the flame retardant formulations in PP by simultaneous thermal analysis (TGA–DTA)

Composition	$T_{1\%}$ (°C)	T_m (°C)	$T_{\text{max dec rate}}$ (°C)	Residue at 600 °C (%)
PSMP	267	250	386	6
PP	383	170	455	1
PP + 10 wt% PSMP	300	169	467	2

PSMP were measured in vacuum in a temperature range of 40–400 °C with a heating rate of 25 K/min. The intensity of the desorbed molecules or fragments with respect to the temperature as well as the corresponding mass spectrum for neat PP, the flame retardant and the flame retarded compound are shown in Fig. 7.

The decomposition temperatures of all investigated samples are lower in TDMS measurements than in TG–MS/TG–FTIR because the decomposition in TDMS measurements is taking place in vacuum, whereas TG–MS/TG–FTIR measurements are conducted under a nitrogen atmosphere. The thermodesorption MS diagram of neat PP (Fig. 7b) depicting the total ion current (TIC) shows a maximum at 396 °C, whereas the release of decomposition products of neat PSMP reaches a maximum at 156 °C (Fig. 7d). The decomposition of 10 wt% PSMP in PP shows maxima at 159 °C, 224 °C and 398 °C (Fig. 7f). The first decomposition step at 159 °C results from the starting decomposition of PSMP and is similar to neat PSMP (Fig. 6b). The third decomposition step at 398 °C is similar to the decomposition of neat PP (Fig. 6a). The second decomposition step at 224 °C shows a delayed release of flame retardant fragments from the polymer matrix which is caused by an interaction between the flame retardant and the polymer. The decomposition products of the polymer matrix retain the

decomposition fragments of the flame retardant. The fragments of the flame retardant PSMP are easily identifiable in all three decomposition steps of the TDMS diagrams. The TIC curves for neat PSMP and PP + 10 wt% PSMP are shown in the supplementary material.

The retreat effect is already described in literature for polystyrene formulations containing sulfur- and phosphorus-based flame retardants (Wagner et al. 2016; Wagner 2012). The release of PO radicals from flame retardant formulations affects a gas phase activity of the flame retardant and is already described in literature for PSMP in polyester flame retardant formulations (Goedderz et al. 2020; Salmeia et al. 2018). The release of PO radicals ($m/z = 47$ u) is obvious in the second and third decomposition step in the TDMS diagrams. The intensity of the released decomposition products of PSMP in the flame retarded formulation decreases with proceeding pyrolysis process. The decomposition mechanism of PSMP in terms of MS studies has been the subject of investigation in the literature and is in accordance to the results obtained from TDMS analysis (Fig. 8).

TG–FTIR allows to monitor the absorbance of the sample based on its dependence on time and temperature and is depicted in Fig. 9 for neat PP, neat PSMP and PP + 10 wt% PSMP. The measurements were conducted in a nitrogen atmosphere with a heating rate of 10 K/min from 35–600 °C. The neat substances PP and PSMP decompose in one step, whereas the formulation consisting of PP + 10 wt% PSMP shows two decomposition steps.

The course of the absorbance of a specific band with respect to the temperature is depicted in Fig. 9. For the decomposition of PP, different absorption bands confirming the release of alkene species were detected: 1672–1628 cm^{-1}, 2944–2904 cm^{-1}, 2986–2950 cm^{-1}, 3099–3062 cm^{-1}, 915–873 cm^{-1}, 1394–1366 cm^{-1} and 1481–1435 cm^{-1}. The maxima of the evolution of alkenes
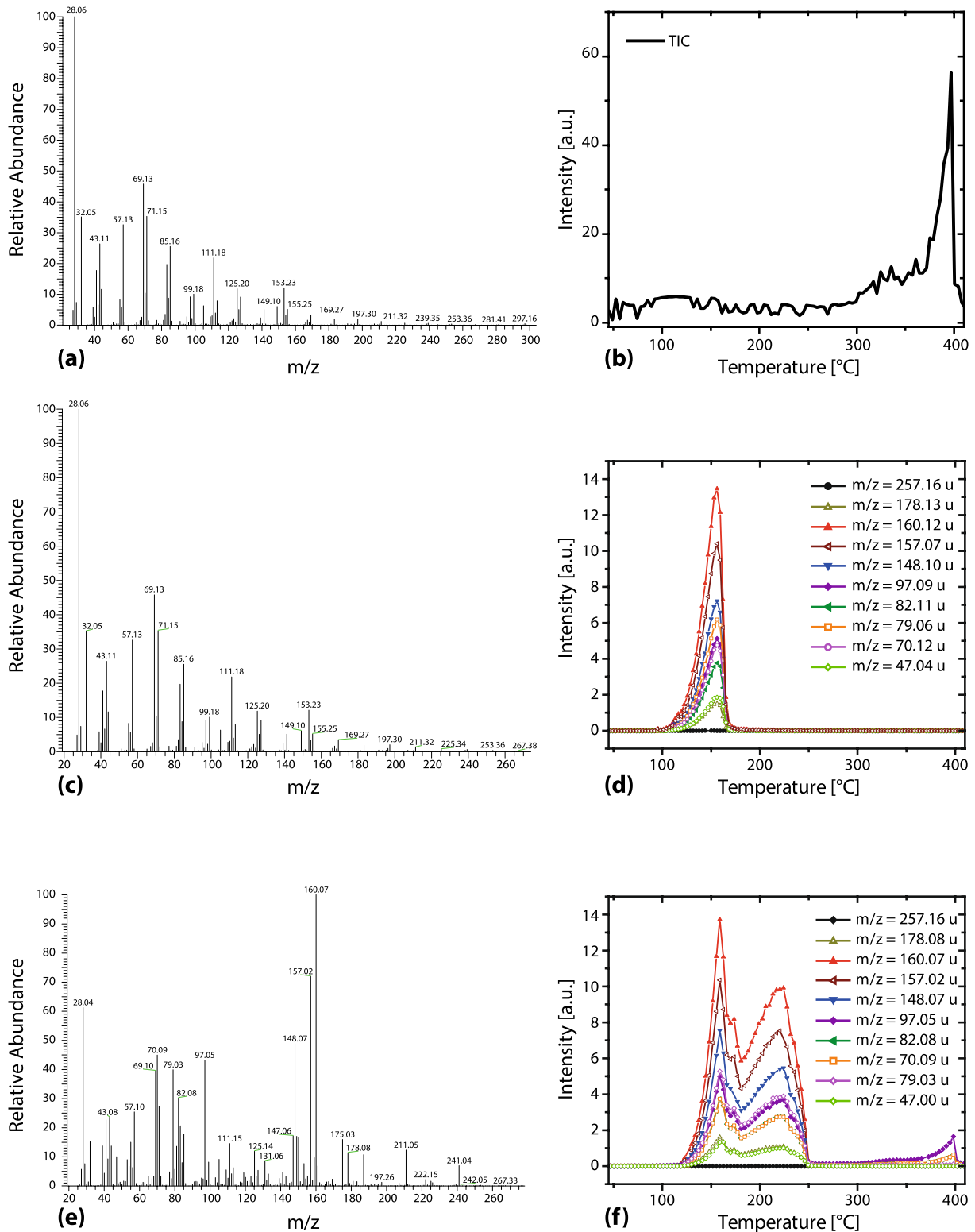
Fig. 7 Mass spectrum of PP (**a**), PSMP (**c**) and 10 wt% PSMP in PP (**e**) in a mass range of 0–270 u with the corresponding thermodesorption MS diagrams (**b**, **d**, **f**) showing the total ion current (TIC). The samples are measured in vacuum with a heating rate of 25 K/min from 40–400 °C

117

Fig. 8 Fragmentation mechanism of PSMP based on Saeidian et al. (2014) and Salmeia et al. (2018)
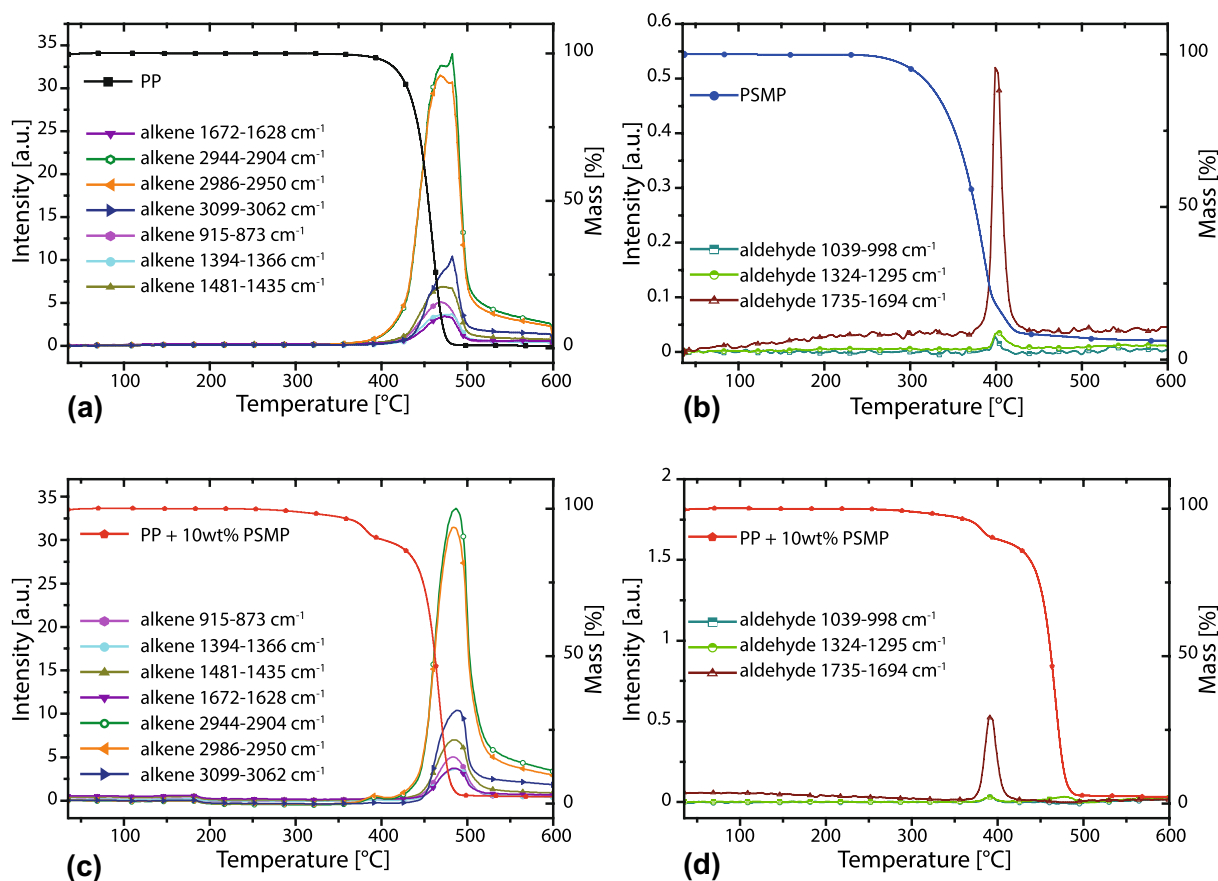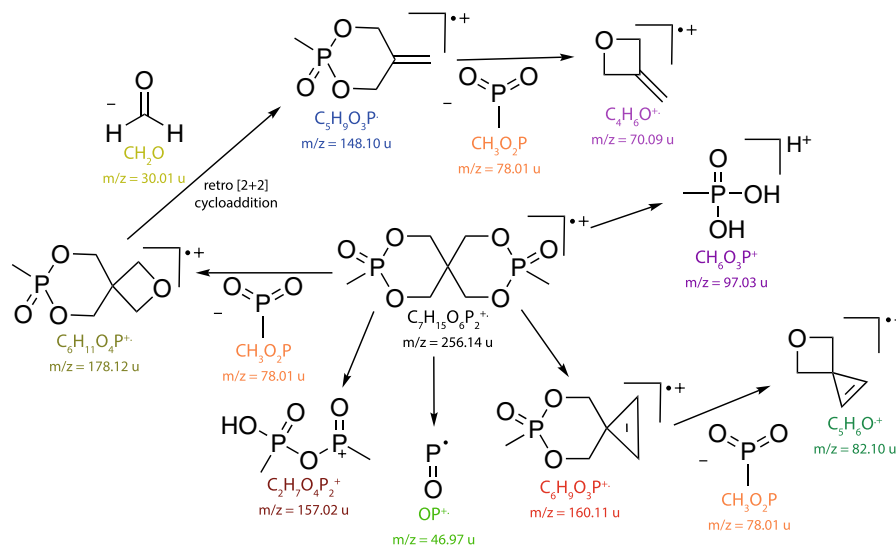
Fig. 9 TG–FTIR results of neat PP (**a**), neat PSMP (**b**) and PP + 10 wt% PSMP (**c**, **d**) in a temperature range of 35–600 °C with a heating rate of 10 K/min in nitrogen atmosphere

from PP range from 468 to 482 °C. For the samples containing PSMP, the evolution of aldehydes is obvious. The maxima of the released aldehyde absorption bands of neat PSMP range from 398 to 408 °C. In the first decomposition step regarding TGA results of the formulation PP + 10 wt% PSMP, the release of aldehydes and alkenes was detected, which is in accordance to the formerly described retreat effect. The second decomposition step confirms mainly the evolution of alkenes. The maxima of released aldehyde and alkene absorption bands of the formulation PP + 10 wt% PSMP range from 389 to 477 °C. Due to the ratio of the released alkenes in the first and second decomposition step, the polymer matrix decomposes mainly in the second decomposition step which is in accordance with the TDMS results in which the intensity of the decomposition products of PSMP in the flame retarded formulation is increased in the beginning.

4.2 OH-PLIF combustion analysis of neat and flame retarded PP particles

In the following, the parameters introduced in Sect. 3, the peak normalized intensity $I_{\text{max,flame}}$ and the radius of peak reactivity rate r_{PRR}, are evaluated in terms of ignition and combustion behavior of neat and flame retarded polypropylene particles using high-speed OH-PLIF. For this purpose, the temporal evolution of selected single particles is compared and an analysis of multiple particle trajectories is presented.

Figure 10 illustrates preprocessed OH-PLIF images displaying the normalized spatial intensity distribution with respect to the OH background for three different regions downstream of the burner head. In the first column, the early combustion phase after ignition is shown for both compounds. At a height of $z = 10.9$ mm, the displayed PP particle shows a circular diffusion flame structure with a peak normalized OH intensity value of 2.7, whereas the flame retarded compound has just undergone ignition with a peak normalized intensity value of 1.8 indicating a retardation of the ignition process. Simultaneously, the radius of peak reactivity rate is 310 μm for neat PP, while the PP with addition of PSMP shows a larger r_{PRR} of 400 μm. As the ignition process continues, $I_{\text{max,flame}}$ at a height of $z = 13$ mm in the second column reveals an increase for the PP particle up to a value of 3.6, while the peak normalized intensity of the flame retarded polymer at $z = 13.2$ mm only increased to 2.9. Values for r_{PRR} decreased for neat PP to a radius of 260 μm, while for the flame retarded compound, the flame front distance decreased to 370 μm. For the particles containing PSMP in the lower field of view, the ignition and flame development process were delayed and at larger distances from the particle center.

In the rightmost column, the normalized OH signal of two particles in the upper field of view is compared at a height of $z = 24.9$ mm. A circular diffusion flame has developed at this stage with a pronounced gap to the particle in its center. The values for $I_{\text{max,flame}}$ are 4.8 for neat PP and 4.7 for the flame retarded PP indicating that the peak reactivity is similar for both particles. At this stage of the combustion process, the diffusion flame is fully developed and only marginally inhibited in its reactivity. Nevertheless, at this height above the burner, the radial distance to the zone of the highest reactivity rate is still larger with a value of 400 μm for flame retarded PP compared to an r_{PRR} value of 330 μm for neat PP. The fuel-rich gap between the pyrolyzing particle and the diffusion flame is maintained in its size over the course of the combustion process. This indicates that similar diffusion speeds of fuel and oxygen into the reaction zone stabilize the position of the flame. As the ignition and evolution of the diffusion flame are observed for larger radii in case of flame retardant particles, r_{PRR} remains larger even though flame inhibition is not evident anymore, as values for $I_{\text{max,flame}}$ are similar for both compounds. Nevertheless, flame inhibition might still be present for the flame retarded compound within the gap between reaction zone and particle which is not possible to detect solely from the OH signal.

The previously presented results from TGA–DTA (Fig. 6) and TG–FTIR (Fig. 9) measurements show that the radical scavenging agent thermally decomposes at lower temperatures than PP and hence imply that it might not be present in the peak reactivity zone anymore. As the heating rate of the thermal decomposition analyses is significantly smaller than in the laminar flow reactor, comparisons drawn between both methods are yet limited. Lau et al. (2019) have shown that increased heating rates delay the thermal decomposition of polymers to higher temperatures. Furthermore, due to the high thermal stress, they have shown that the decomposition temperatures of the flame retardant and the polymer merge. Therefore, the release of flame retardant fragments is likely to be delayed, too.

As comparisons of single particles are not necessarily representative of the processes investigated, multiple particle trajectories are analyzed. A total of 10 neat PP and 18 PP particles flame retarded with PSMP are included in the subsequent investigation. The values of r_{PRR} are shown for a variety of heights above the burner head z in Fig. 11a including the mean curves for a bin size of 1 mm, whereas the evolution of $I_{\text{max,flame}}$ is depicted for various individual particles in Fig. 11b. Each data point represents a value extracted from the radial intensity profile of a single OH-PLIF image. For reasons of clarity, individual points of a single particle are not connected by lines in Fig. 11a.

As obvious from Fig. 11a, values of r_{PRR} of the flame retarded polymer are on average larger than those of neat PP. The mean value curves of the depicted data points reveal

(a) PP, $z = 10.9$ mm
(b) PP, $z = 13$ mm
(c) PP, $z = 24.9$ mm
(d) $r_{PRR} = 310\,\mu m$, $I_{max,flame} = 2.7$
(e) $r_{PRR} = 260\,\mu m$, $I_{max,flame} = 3.6$
(f) $r_{PRR} = 330\,\mu m$, $I_{max,flame} = 4.8$

Field of View 1 | Field of View 2

(g) PP + 10 wt% PSMP, $z = 10.9$ mm
(h) PP + 10 wt% PSMP, $z = 13.2$ mm
(i) PP + 10 wt% PSMP, $z = 24.9$ mm
(j) $r_{PRR} = 400\,\mu m$, $I_{max,flame} = 1.8$
(k) $r_{PRR} = 370\,\mu m$, $I_{max,flame} = 2.9$
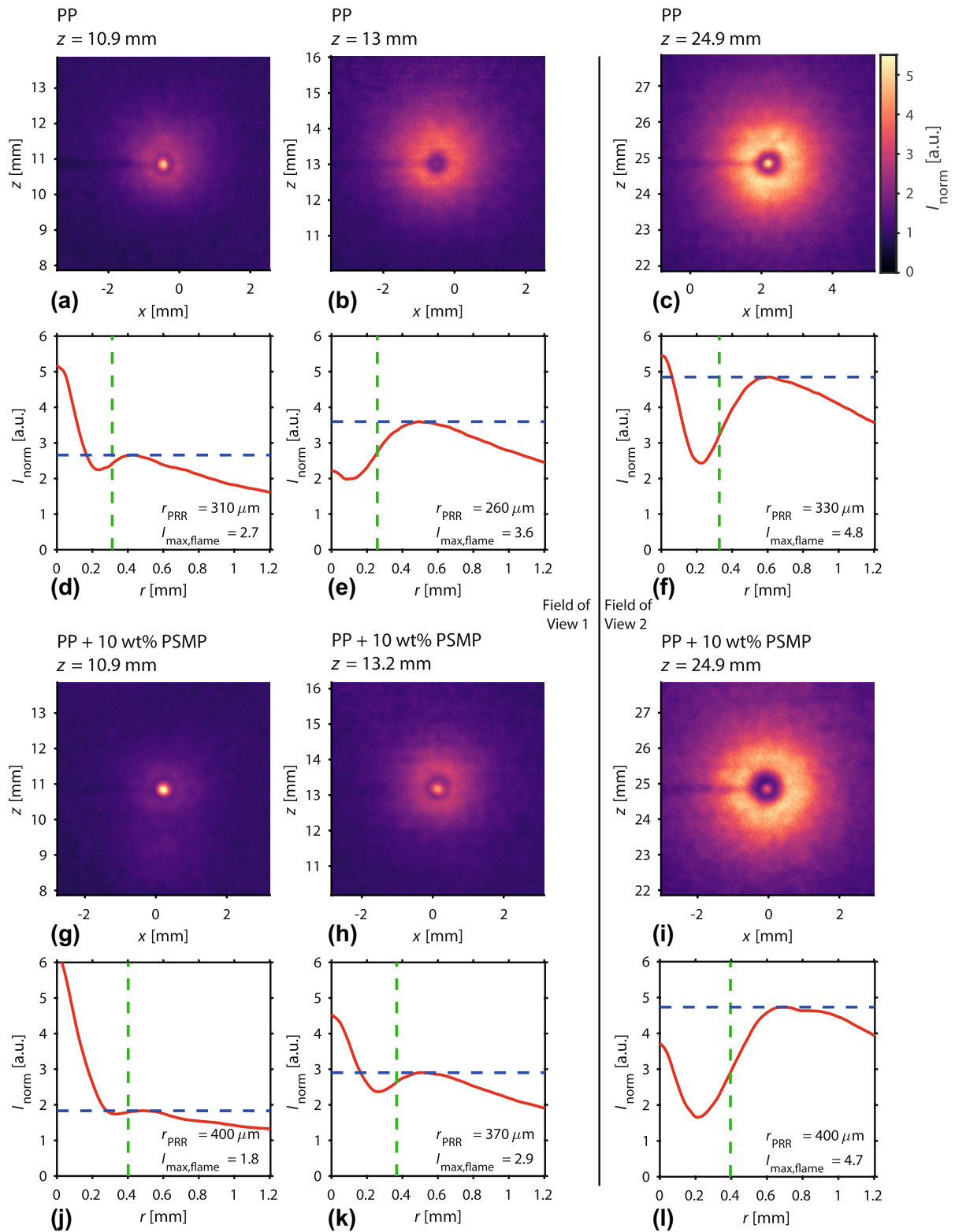(l) $r_{PRR} = 400\,\mu m$, $I_{max,flame} = 4.7$

120

◄**Fig. 10** Normalized OH-PLIF signal of neat PP (**a**–**c**) and the flame retardant formulation PP + 10 wt% PSMP (**g**–**i**) for three different heights above the burner head with their corresponding radial intensity curves (**d**–**f, j**–**l**). The first two columns show the OH signal of one particle for each material formulation during the early phase of combustion, while the third column shows the fully developed diffusion flame of another particle recorded in the upper field of view

that r_{PRR} of neat PP particles is 309 ± 21 μm at $z = 10$ mm and increases to 373 ± 17 μm at 28 mm, whereas the flame retarded polypropylene exhibits respective r_{PRR} values of 389 ± 37 μm and 427 ± 42 μm at 10 mm and 28 mm. Therefore, independent of the axial position, the difference between values of r_{PRR} for PP and PP + 10 wt% PSMP can be distinguished clearly. This indicates that the outgassing flame retardant shifts the radial position already at the onset of ignition. Over the course of the combustion process, the outgassing decomposition products slightly push the diffusion flame outwards until both curves coincide at z = 30 mm when the flame retardant's activity is not detectable anymore. This is in accordance to the findings for the individual particles shown in Fig. 10. The TDMS experiments show that all decomposition fragments of the flame retardant are released over a broad temperature range, but the major part is released before the decomposition of PP (Fig. 7b, f). This cannot be observed for TG–FTIR experiments due to higher sensitivity of TDMS than TG–FTIR.

The retardation of the ignition process becomes obvious from the evolution of $I_{max,flame}$ shown in Fig. 11b. Particles ignite at approx. $z = 7$ mm, indicated by values of $I_{max,flame}$ exceeding the background intensity. Ignition and the phase of subsequent flame development where $I_{max,flame}$ rises dramatically are observed between $z = 6$ mm and 16 mm. While almost all neat PP particles have already reached a value of $I_{max,flame} = 4$ at $z = 14$ mm, the flame retarded PP particles show a significantly lower value of $I_{max,flame} = 3$ at the same height indicating a gas phase activity of the PSMP fragments. Single deviations from this trend might be caused by either particles which are on average smaller and therefore ignite at lower heights or particles which are larger on average and therefore show a retarded ignition which might as well be caused by agglomeration of several particles to one large sample. For $z > 20$ mm, both compounds show a similar evolution of $I_{max,flame}$ which approaches a value of 5 identified as a fully developed diffusion flame in which the effect of flame inhibition is not noticeable anymore. Nevertheless, flame retardant fragments might still be present in the fuel-rich gap between reaction zone and particle. TDMS experiments have shown that fragments of the flame retardant are still evolving in a sophisticated pyrolysis process (Fig. 7b, f).

4.3 Cone calorimetry of flame retardant formulations

As a standard test for the estimation of the flame retardant efficacy, cone calorimetry was conducted to evaluate the flame retardant performance of the flame retardant formulation of PP + 10 wt% PSMP in contrast to neat PP. The sample is being heated up with a heat flux of 35 kW/m^2 and the heat release rate (HRR) is monitored over time. The heat release rate curves (heat flux of 35 kW/m^2), time to ignition (TTI), total heat release (THR), maximum average rate of heat emission (MARHE), and peak heat release rate (PHRR) of both samples are shown in Fig. 12 and Table 3. The flame inhibition efficacy of 10 wt% PSMP in PP is evident through a reduction of PHRR by 29%. The ignition of the samples starts at 51–62 s with no significant difference in TTI between both specimen, but the PHRR is reached at 115 s (t_{max}) for neat PP and at 180 s (t_{max}) for PP + 10 wt% PSMP resulting in a significant delay reaching the PHRR value. The reduced PHRR and delayed t_{max} are the main effects of the flame retardant. The THR value of the flame retardant formulation is 4% lower than in neat PP. The total smoke release (TSR) takes the irradiated area into account and contains no information about the smoke toxicity which can be tested according to ISO 5659-2. If a flame retardant with a condensed phase activity is compared to a flame retardant which is active in the gas phase, the TSR is expected to be higher for the flame retardant formulation containing the gas phase active flame retardant, because a condensed phase active flame retardant can promote the formation of a dense char layer which acts as a barrier. The use of gas phase active flame retardants leads to incomplete combustion in the gas phase. A combination of both—gas and condensed phase activity—can result in a reduced TSR in combination with flame retardant efficacy for certain applications. The TSR is increased by 84% for the flame retarded compound, which indicates that a flame inhibition effect takes place in the gas phase when compared to neat polypropylene.

5 Conclusions

The efficacy of the flame retardant pentaerythritol spirobis(methylphosphonate) (PSMP) in polypropylene was investigated using a combination of TDMS, TG–MS, and TG–FTIR simultaneously, cone calorimeter tests, and high-speed OH-PLIF imaging in a laminar flow reactor. The flame retardant efficacy of 10 wt% PSMP in polypropylene (PP) showed a reduction of PHRR by 34%. The analysis of the evolved products showed mainly decomposition products of PSMP in the first pyrolysis step. Using TDMS, the decomposition products of PSMP were identified and correlated with the flame retardant effect of PSMP in PP.
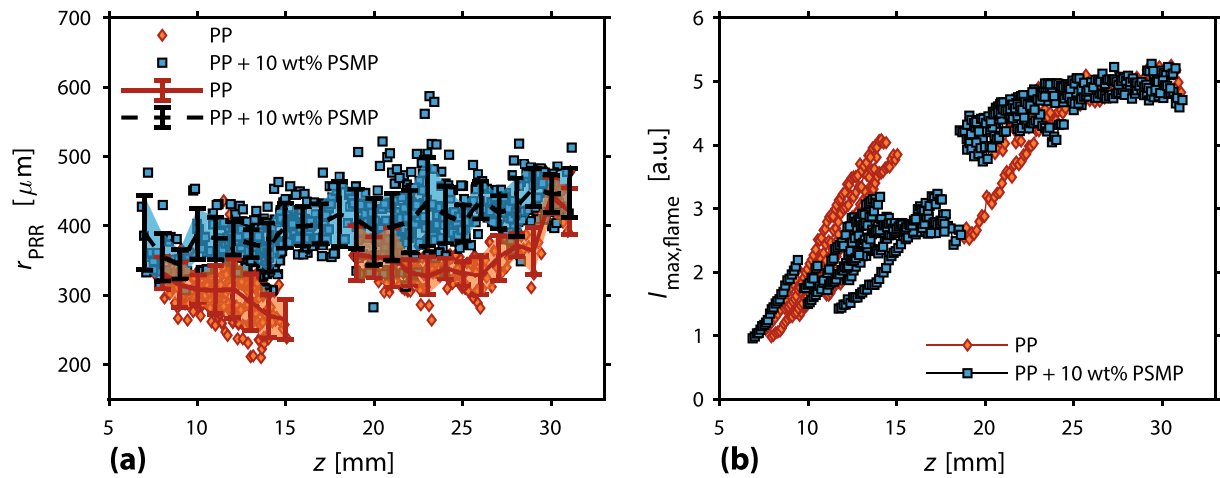
Fig. 11 a Radius of peak reactivity rate for all analyzed particles over the height above the burner head z. Error bars depict one standard deviation for a mean within a bin of 1 mm in size. **b** Normalized peak OH signal within the diffusion flame for neat PP and the flame retarded formulation with respect to the height above the burner head z
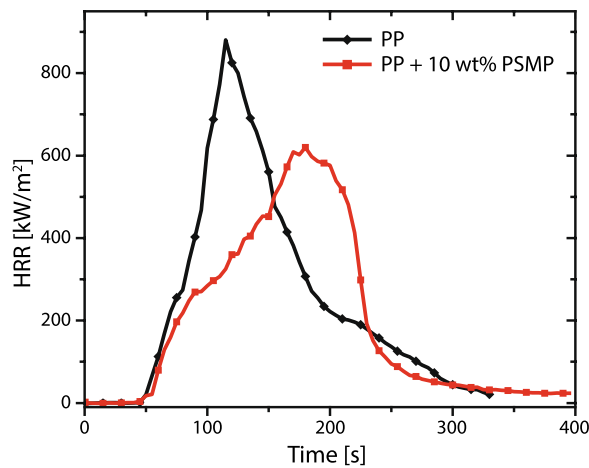

Fig. 12 Heat release rate curves (heat flux of 35 kW/m^2) for PP and PP + 10 wt% PSMP with a sample thickness of 2 mm (sample size: 100 × 100 mm)

High-speed OH-PLIF imaging was applied to track the ignition and early combustion phase of neat PP and flame retarded particles. The radial distance towards the

region of the peak reactivity rate of the flame retardant sample is increased throughout the entire observed region above the burner head compared with neat polypropylene which implies that the ignition and flame development happen further away from the particle when compounded with PSMP. Furthermore, the normalized peak OH signal intensity in the diffusion flame increases slower during the ignition process showing the retardation effect of the investigated additive. In later stages of combustion when the diffusion flame is fully developed, the radial distance between the particle and the diffusion flame is still increased for the flame retarded compound although no inhibition of the OH peak signal is detectable anymore. As the ignition and flame development of the flame retarded particles happen at larger radii, the outgassing polymer decomposition products, which diffuse into the reaction zone, maintain a larger radial distance of the reaction zone. At this stage of combustion, the primary inhibition effect of the flame retardant on the OH intensity has vanished, but the repercussion of the effect of PSMP on the location of ignition at increased distances is still detectable through the radial intensity profile.

Table 3 Cone calorimetry (irradiation 35 kW/m^2) results of flame retardant formulations in PP with a sample thickness of 2 mm

Composition	TTI (s)	PHRR (kW/m^2)	t_{max} (s)	PHRR reduction (%)	THR (MJ/m^2)	MARHE (kW/m^2)	Total smoke release (m^2/m^2)
PP	51	880 ± 97.1	115	–	82	345	1115
PP + 10 wt% PSMP	62	620 ± 51	180	30	79	302	1786

The TDMS, TG–MS and TG–FTIR results are consistent with the results obtained by OH-PLIF, as the decomposition products of the flame retardant in PP + 10 wt% PSMP are released in the gas phase before the main part of pyrolysis products of polypropylene are evolved in the gas phase. Therefore, the early inhibition effect at ignition is accompanied by a decreased relative peak OH intensity induced by phosphorous-containing scavenging radicals, while this effect is not detectable in the fully developed flame where most of the flame retardants have already thermally decomposed. In summary, the combination of both experimental approaches led to a more thorough understanding of the mode of action of flame retardants in polymers as they are investigated in situ. Although phosphorous-containing radicals are known to provide a gas phase activity with a combination of radical scavenging and dilution within the reaction zone, the presented method is not suitable to distinguish between the two mechanisms individually, as no inert flame retardant is compared with the investigated compounds. To visualize radical scavenging of these radicals, future investigations should focus on the visualization of the chemical inhibitors themselves.

Author contributions DTA–MS–FTIR analysis: DG, CF and RR; TGA analysis: DG; OH-PLIF analysis: CG, TL, JK, AD, BB; cone calorimeter tests: FP, JB and CB.

References

Bart JCJ (2006) Plastics additives: advanced industrial analysis. IOS Press, Amsterdam

Beach MW, Vozar SE, Filipi SZ, Shmakov AG, Shvartsberg VM, Korobeinichev OP, Morgan TA, Hu TI, Sick V (2009) Screening approaches for gas-phase activity of flame retardants. Proc Combust Inst 32:2625–2632

Goedderz D, Weber L, Markert D, Schießer A, Fasel C, Riedel R, Altstädt V, Bethke C, Fuhr O, Puchtler F (2020) Flame retardant polyester by combination of organophosphorus compounds and an NOR radical forming agent. J Appl Polym Sci 137:47876

Green J (1996) Mechanisms for flame retardancy and smoke suppression—a review. J Fire Flammabil 14:426–442

Hartlieb AT, Atakan B, Kohse-Höinghaus K (2000) Effects of a sampling quartz nozzle on the flame structure of a fuel-rich low-pressure propene flame. Combust Flame 121:610–624

Hastie J (1973) Molecular basis of flame inhibition. J Res 77:733–754

Klinkowski C, Burk B, Bärmann F, Döring M (2015) Moderne Flammschutzmittel für Kunststoffe. Chem unserer Zeit 49:96–105

Kohse-Höinghaus K, Schocker A, Kasper T, Kamphus M, Brockhinke A (2005) Combination of laser-and mass-spectroscopic techniques for the investigation of fuel-rich flames. Zeitschrift für Physikalische Chemie 219:583–599

Korobeinichev O, Paletsky A, Kuibida L, Gonchikzhapov M, Shundrina I (2013) Reduction of flammability of ultrahigh-molecular-weight polyethylene by using triphenyl phosphate additives. Proc Combust Inst 34:2699–2706

Köser J, Becker LG, Vorobiev N, Schiemann M, Scherer V, Böhm B, Dreizler A (2015) Characterization of single coal particle combustion within oxygen-enriched environments using high-speed OH-PLIF. Appl Phys B 121:459–464

Köser J, Becker LG, Goßmann A-K, Böhm B, Dreizler A (2017) Investigation of ignition and volatile combustion of single coal particles within oxygen-enriched atmospheres using high-speed OH-PLIF. Proc Combust Inst 36:2103–2111

Köser J, Li T, Vorobiev N, Dreizler A, Schiemann M, Böhm B (2019) Multi-parameter diagnostics for high-resolution in-situ measurements of single coal particle combustion. Proc Combust Inst 37:2893–2900

Lau S, Gonchikzhapov M, Paletsky A, Shmakov A, Korobeinichev O, Kasper T, Atakan B (2019) Wirkungsweise von Aluminiumdiethylphosphinat als Flammenhemmer für ultrahochmolekulares Polyethylen, vol 29. Deutscher Flammentag, Bochum

Lewin M, Weil E (2001) Mechanisms and modes of action in flame retardancy of polymers. In: Horrocks A, Price D (eds) Fire retardant materials, 1st edn. Woodhead Publishing, Cambridge, pp 31–68

Liang S, Hemberger P, Neisius NM, Bodi A, Grützmacher H, Levalois-Grützmacher J, Gaan S (2015) Elucidating the thermal decomposition of dimethyl methylphosphonate by vacuum ultraviolet (VUV) photoionization: pathways to the PO radical, a key species in flame-retardant mechanisms. Chem Eur J 21:1073–1080

MacDonald MA, Jayaweera T, Fisher EM, Gouldin F (1999) Inhibition of nonpremixed flames by phosphorus-containing compounds. Combust Flame 116:166–176

MacDonald MA, Gouldin FC, Fisher EM (2001) Temperature dependence of phosphorus-based flame inhibition. Combust Flame 124:668–683

Osawa Z, Kuroda H, Kobayashi Y (1984) Luminescence emission of isotactic polypropylene. J Appl Polym Sci 29:2843–2849

Pfaendner R, Metzsch-Zilligen E, Stec M (2014) Verwendung von organischen Oxyimiden als Flammschutzmittel für Kunststoffe sowie flammgeschützte Kunststoffzusammensetzung und hieraus hergestellte Formteile. WO 2014154636 A1

Saeidian H, Babri M, Mirjafary Z, Naseri MT, Sarabadani M, Ashrafi D, Faraz SSM (2014) Fragmentation mechanisms in mass spectrometry of Chemical Weapons Convention related spiro alkylphosphonates and alkyldioxaphosphinane oxides. Int J Mass Spectrom 369:59–70

Salmeia KA, Fage J, Liang S, Gaan S (2015) An overview of mode of action and analytical methods for evaluation of gas phase activities of flame retardants. Polymers 7:504–526

Salmeia KA, Gooneie A, Simonetti P, Nazir R, Kaiser J-P, Rippl A, Hirsch C, Lehner S, Rupper P, Hufenus R, Gaan S (2018) Comprehensive study on flame retardant polyesters from phosphorus additives. Polym Degrad Stab 155:22–34

Schartel B (2010) Phosphorus-based flame retardancy mechanisms—old hat or a starting point for future development? Materials 3:4710–4745

Shmakov A, Shvartsberg V, Korobeinichev O, Beach M, Hu T, Morgan T (2007) Structure of a freely propagating rich CH4/air flame containing triphenylphosphine oxide and hexabromocyclododecane. Combust Flame 149:384–391

                      ⚛ Springer

Siow JE, Laurendeau NM (2004) Flame inhibition activity of phosphorus-containing compounds using laser-induced fluorescence measurements of hydroxyl. Combust Flame 136:16–24

Vora N, Laurendeau NM (2001) Analysis of CF3Br flame suppression activity using quantitative laser-induced fluorescence measurements of the hydroxyl radical. Combust Sci Technol 166:15–39

Vora N, Siow JE, Laurendeau NM (2001) Chemical scavenging activity of gaseous suppressants by using laser-induced fluorescence measurements of hydroxyl. Combust Flame 126:1393–1401

Wagner S (2012) Novel phosphorus based flame retardants for engineering plastics and epoxies. Dissertation, Ruprecht-Karls-Universität Heidelberg

Wagner J, Deglmann P, Fuchs S, Ciesielski M, Fleckenstein CA, Döring M (2016) A flame retardant synergism of organic disulfides and phosphorous compounds. Polym Degrad Stab 129:63–76

Wang B, Xu F, Zong P, Zhang J, Tian Y, Qiao Y (2019) Effects of heating rate on fast pyrolysis behavior and product distribution of Jerusalem artichoke stalk by using TG-FTIR and Py-GC/MS. Renew Energy 132:486–496

Supplementary Material

Experiments in Fluids

Investigation of flame retarded polypropylene by high-speed planar laser-induced fluorescence of OH radicals combined with a thermal decomposition analysis

Christopher Geschwindner[1*], Daniela Goedderz[2,3], Tao Li[1], Jan Köser[1], Claudia Fasel[4], Ralf Riedel[4], Volker Altstädt[5], Christian Bethke[5], Florian Puchtler[6], Josef Breu[6], Manfred Döring[3], Andreas Dreizler[1], Benjamin Böhm[1]

[1] Reaktive Strömungen und Messtechnik, Technische Universität Darmstadt, Otto-Berndt-Straße 3, Darmstadt, D-64287, Germany

[2] Ernst-Berl Institute for Chemical Engineering and Macromolecular Science, Technische Universität Darmstadt, Alarich-Weiss-Straße 4, Darmstadt, D-64287, Germany

[3] Fraunhofer Institute for Structural Durability and System Reliability LBF, Schlossgartenstraße 6, Darmstadt, D-64289, Germany

[4] Institut für Materialwissenschaft, Technische Universität Darmstadt, Otto-Berndt-Straße 3, Darmstadt, D-64287, Germany

[5] Department of Polymer Engineering, University of Bayreuth, Universitätsstraße 30, Bayreuth, D-95447, Germany

[6] Bavarian Polymer Institute and Department of Chemistry, University of Bayreuth, Universitätsstraße 30, D-95447 Bayreuth, Germany

*Correspondence to: Christopher Geschwindner (E-mail: *geschwindner@rsm.tu-darmstadt.de*)
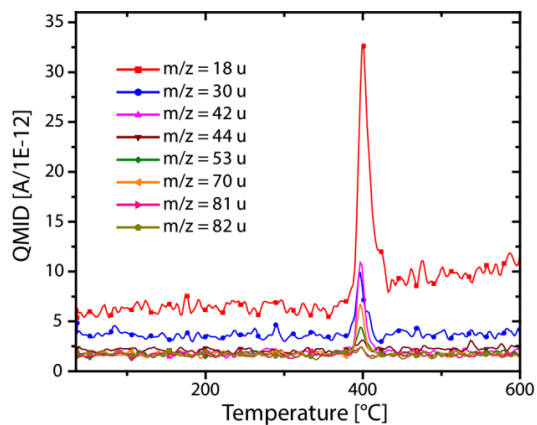
Figure S1 TG-MS analysis of neat PSMP with 10 K/min from 35-600 °C under nitrogen atmosphere.
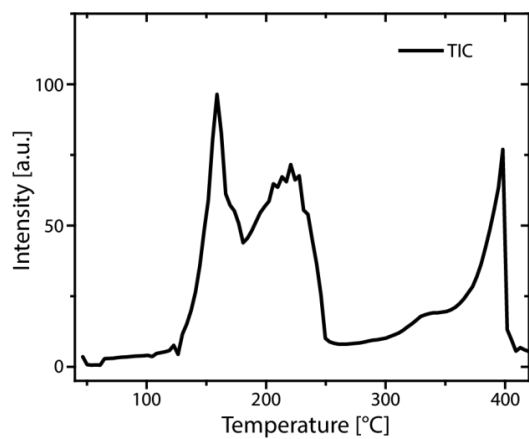
Figure S2 TDMS of 10 wt% PSMP in PP showing the total ion current (TIC) in a temperature range of 40-400 °C with a heating rate of 25 K/min.
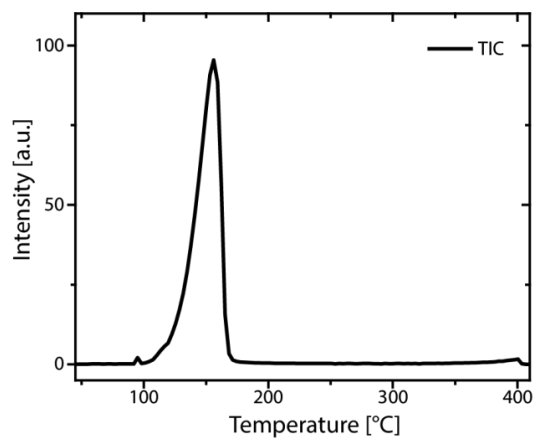
Figure S3 TDMS of neat PSMP showing the total ion current (TIC) in a temperature range of 40-400 °C with a heating rate of 25 K/min.
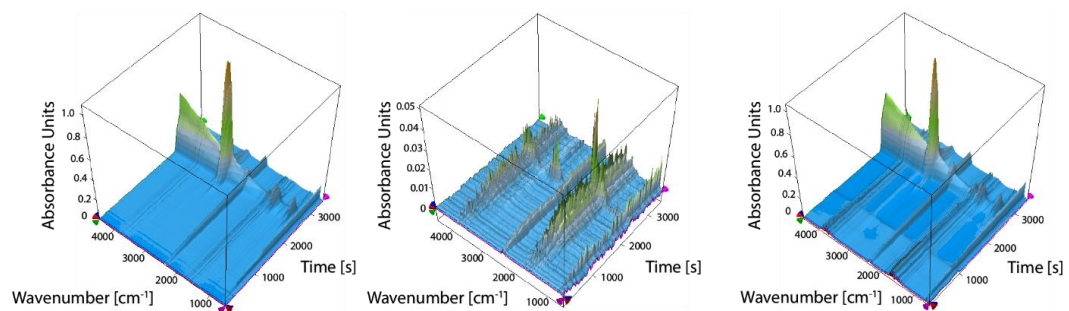
Figure S4 3D TG-FTIR diagrams of neat PP (left), neat PSMP (center) and PP + 10 wt% PSMP (right) in a temperature range of 35-600 °C with a heating rate of 10 K/min in nitrogen atmosphere.

A.5 Paper V - Optical diagnostics of flame retarded polymers

Reproduced with permission from Elsevier.

The effects of various flame retardants on the combustion of polypropylene: Combining optical diagnostics and pyrolysis fragment analysis

Christopher Geschwindner [a],[*], Daniela Goedderz [b], Tao Li [a], Johannes Bender [c], Benjamin Böhm [a], Andreas Dreizler [a]

[a] Department of Mechanical Engineering, Reactive Flows and Diagnostics, Technical University of Darmstadt, Otto-Berndt-Str. 3, Darmstadt 64287, Germany
[b] Fraunhofer Institute for Structural Durability and System Reliability LBF, Schlossgartenstr. 6, Darmstadt 64289, Germany
[c] Institute of Chemical Process Engineering (ICVT), University of Stuttgart, Boeblinger Str. 78, Stuttgart 70199, Germany

ARTICLE INFO

ABSTRACT

The assessment of the efficacy and mode of action of flame retardants in polymers requires a thorough knowledge of the coupling of the presence of chemical inhibitors with the underlying heat and mass transport processes. In this experimental work, we combine a thermal decomposition analysis with optical combustion diagnostics in different test environments to gain a comprehensive understanding of the relevant sub-processes and demonstrate how this approach provides future opportunities for the research regarding the mode of action of flame retardants. Four different composites of polypropylene (PP) and 10 wt% of selected flame retardants as well as neat PP are prepared. Flame retardants include pentaerythritol spirobis(methylphosphonate) (PSMP), zinc diethylphosphinate (DEPZn), aluminum hydroxide (i.e. aluminum trihydrate, ATH) and ammonium polyphosphate (APP). The released substances in the gas phase are investigated by using thermogravimetric analysis coupled to Fourier-transform infrared spectroscopy (TGA-FTIR), and the burning behavior regarding carbon monoxide concentration and heat release rate (HRR) is studied in cone calorimeter experiments. The ignition and combustion of flame retarded micrometer-sized particles of PP are experimentally investigated in a laminar flat flame burner by means of simultaneous scanning planar laser-induced fluorescence of OH radicals (OH-PLIF) and diffuse back-illumination (DBI) at a repetition rate of 10 kHz. Particles with gas-phase activity show a decreased normalized OH signal intensity during combustion. A dependency of the dimensionless flame radius on the particle size is found which can be linked to the faster heating and pyrolysis of smaller particles compared to large particles and agglomerations. Eventually, the interaction with an external premixed flame and the subsequent extinction of self-sustaining flames of polymer sticks is investigated using OH-PLIF in an adapted horizontal burning test suited for the application of optical diagnostics. This approach allows to link the findings of investigations encompassing multiple scales, resulting in a thorough understanding of both polymer chemistry and combustion dynamics in flame retarded polymers.

1. Introduction

Polymer components have replaced metals in many industrial sectors and can be found in almost all areas of daily life. A crucial disadvantage of polymers, however, is their high flammability, which can be reduced by effective and tailor-made flame retardant additives. Particularly with regard to the use of polymers in safety-critical applications, research on innovative flame retardant concepts is necessary [1].

Flame retardants are classified based on their modes of action. These include, for example, condensed-phase active flame retardants, which inhibit pyrolysis by promotion of charring, intumescence, formation of a protective barrier, and gas-phase active flame retardants, which thermally decompose into radicals in order to prevent radical chain reactions in the reaction zone of the flame [2–5]. In addition, endothermically decomposing flame retardants such as aluminum trihydrate (ATH) remove heat from the reaction zone and thus indirectly influence flame stabilization [6–8]. The mode of action of flame retardants is also a result of the complex interaction of the flame retardant and the polymer matrix and thus dependent on the polymer matrix used [9–11].

129

Studies of the inhibition effect of gas-phase active flame retardants are usually performed in laminar canonical hydrocarbon flames without pyrolyzing polymers. Experimental investigations of flame retardants added to flames in generic configurations include spherically expanding flames [12], premixed flames (flat flames [13–15] and flames in a side-wall quenching arrangement [16]), co-flow diffusion flames [17, 18] and opposed-jet (i.e. counterflow) flames [19–23]. Beyond, studies in a shock tube have been performed to investigate ignition delay times of dimethyl methylphosphonate (DMMP) added to mixtures of different simple hydrocarbons and oxygen [24]. Additionally, complementing numerical studies are reported in the literature to investigate the effects of flame retardants on the inhibition of various flame configurations [14, 16,25–28] and on the thermal decomposition properties. For instance, Coimbra et al. developed a reaction mechanism for the pyrolysis of polyethylene blended with ammonium polyphosphate including a model of the pyrolysis process and compared their results to experimental data [29]. When comparing different burner setups, it could be observed that the effectiveness of gas-phase active flame retardant additives is highly dependent on the flame type used, further emphasizing the need for a wide range of studies in both various canonical and more complex burner configurations [18]. Apart from canonical investigations of hydrocarbon flames, *in situ* studies of the combustion of flame retarded polymers are necessary [30] as the pyrolysis and combustion is strongly influenced by the polymer itself including studies of burning flame retarded particles [31], slabs [32] and cylindrical specimens [33] (also in microgravity [34]).

An investigation of the efficacy of a flame retardant is possible with a variety of diagnostic methods, which, however, differ greatly from each other, especially in the aspects of closeness to a realistic fire case and the quantity and precision of the measured parameters. In the following, we will briefly introduce the experimental methods used in the literature, limiting ourselves to the diagnostics of the gas phase of the burning polymer.

In the chemical analysis of flame retardants, an investigation of the components of the flame retardant decomposed by pyrolysis is common. The most commonly used method is the thermogravimetric analysis coupled with Fourier transform infrared spectrometry (TG-FTIR). Further complementary methods used for decomposition analysis encompass thermodesorption mass spectrometry (TDMS), thermogravimetric analysis coupled with mass spectrometry (TG-MS) and pyrolysis gas chromatography with mass spectrometry coupling (Py-GCMS). These involve subjecting a sample to a defined temperature increase, typically in the range of 10 K/min. While these methods provide a detailed knowledge of the chemical species formed with respect to the decomposition temperature, the heating rate is much lower than in realistic fire tests [35–37].

In addition to chemical analyses of the decomposition products of the flame retardant, an investigation of the physicochemical phenomena occurring in the reaction zone during the actual combustion of the polymer is helpful. Here, the measurement of chemically active radicals is primarily used to assess the inhibition efficacy of the flame retardant. Such diagnostic methods include molecular beam mass spectrometry (MBMS), vacuum ultraviolet photoionization (VUV), chemiluminescence, and laser-induced fluorescence (LIF) of selected radicals [19–22,31,33,38–40]. Optical methods such as LIF have the advantage of not distorting the processes occurring in the reaction zone due to their minimally invasive nature. In this regard, quantitative laser-induced fluorescence of the OH radical (OH-LIF) has been used in the past for the study of gaseous inhibitors in gas flames, where the addition of phosphorus-containing flame retardants and halons has demonstrated a reduced OH radical concentration in the flame as an indication of flame poisoning [19–22]. In recent studies, Lau et al. investigated the pyrolysis process of diethylphosphinate (AlPi) in ultra-high molecular weight polyethylene (UHMWPE). The pyrolysis behavior of the flame retardant and the released phosphorus-containing decomposition products were monitored by MBMS considering the released decomposition products in

the gas phase decoupled to the fire behavior. In a more recent study, the combustion behavior regarding thermal and chemical structures of diffusion flames was investigated for AlPi in UHMWPE by using differential mass-spectrometric thermal analysis (DMSTA) [40,41].

Furthermore, the application of planar OH-LIF of a flame retarded polymer was presented in an earlier work of the authors, where particulate PP samples were introduced into a laminar flat flame burner and ignited under known ambient conditions [31]. Using high-speed OH-PLIF at a repetition rate of 10 kHz, individual particles could be tracked during ignition and combustion, and the OH fluorescence intensity normalized to the background of the flat flame flue gasses was compared between neat PP and PP with the gas-phase active flame retardant pentaerythritol spirobis(methylphosphonate) (PSMP). The flame retarded particles showed an intensity reduction of the fluorescence signal as well as an increase in the flame radius compared to neat PP. This study revealed the high research potential regarding more detailed clarification of flame retardant modes of action and the ongoing processes in the gas phase.

The present work supplements our previous study including OH-PLIF measurements of PP samples with three additional flame retardants of different modes of action and uses an adapted diagnostic setup for this purpose, which functions as a multi-parameter measurement system. A laser scanner is used to increase the number of particles centrally hit by the UV laser sheet in order to increase the statistical significance. In addition, the particle size is measured simultaneously by diffuse back-illumination (DBI) to generate size-selective statistics, improving the comparability of different samples. In total, four different flame retardants are mixed in PP with a fixed concentration of 10 wt% to maintain the identical amount of combustible polymer. The flame retardants were selected for their different fire behavior and thus their mode of action. PSMP and DEPZn are described in the literature as predominantly gas-phase active flame retardants in different polymers releasing phosphorus-containing radicals in the gas phase [31,42]. In comparison, ATH and APP are predominant condensed-phase active flame retardants promoting char formation by the reaction to aluminum oxide or polyphosphoric acid while releasing water vapor or ammonia in the gas phase. All selected flame retardants are suitable for the usage in PP but are commonly used in flame retardant formulations together with other flame retardants, partially in higher amounts than 10 wt%. Although one-component flame retardant formulations are not very effective in flame inhibition, they are suitable for investigating the influence of the single flame retardant on the combustion process of the polymer matrix [6,7,43–48].

2. Materials

PP (Moplen HP 500 N) was provided by LyondellBasell, the Netherlands. PSMP was provided by Thor, Germany. APP was provided by Budenheim, Germany. ATH was provided by Nabaltec, Germany. DEPZn was provided by Clariant, Germany.

In the present study, PP particles are investigated which have been additivated with a total of 4 different flame retardants at a level of 10 wt %. Structures of the flame retardants are shown in Fig. 1.
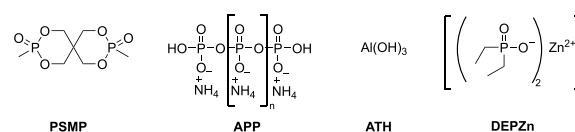

Fig. 1. Structures of used flame retardants in this study.

2

3. Methods

3.1. Sample preparation and chemical decomposition analysis

The flame retarded PP composites contain 10 wt% of the respective flame retardant and were compounded on a co-rotating twin-screw extruder (Thermo Fisher Scientific Process 11; screw diameter: 11 mm) with a screw rotation speed of 150 rpm. The first temperature zone was set to 210 °C, while the temperature zones 2–7 and the die temperature were stabilized at 220 °C. The polymer melt was cooled with a water bath and pelletized in a pelletizing system (VariCut Granulator). To prepare polymer particles, the pelletized polymer was ground several times with a centrifugal mill (Retzsch ZM 200) and separated by size (openings: 100 and 150 μm) using a vibratory sieve shaker.

The thermogravimetric analysis coupled to FTIR was performed on STA449 F3 (Netzsch Instruments, Selb, Germany) and ALPHA FTIR (Bruker Optics, Ettlingen, Germany) in nitrogen atmosphere (gas flow: 80 ml/min) with a constant heating rate of 10 K/min in a temperature range of 25–700 °C. The temperature at which 1 wt% of the sample is released in the gas phase was determined ($T_{1\%}$). 30 mg of powdered samples were used. Cone calorimeter tests were performed according to ISO 5660 with a heat flux of 35 kW/m^2 (Cone Calorimeter Pro, Wazau). The samples were obtained by hot pressing (300E Collin) at 200 °C and 5 bar for 5 min with a sample size of $100 \times 100 \times 3$ mm^3. All samples were tested in triplicate. The interaction with a premixed Bunsen flame was conducted with specimens of size $70 \times 10 \times 4$ mm^3.

3.2. Laser-optical multi-parameter combustion diagnostics

The laser-optical combustion experiments were carried out within two experimental setups at TU Darmstadt, which are both displayed in Fig. 2. The combustion of polymer particles at high heating rates is studied in a laminar flat flame burner shown in Fig. 2(a,c), while the interaction of a premixed methane flame with a horizontally aligned stick-shaped polymer specimen is investigated in a custom-built flame interaction test stand as shown in Fig. 2(b,d). Both facilities were designed to allow the use of optical diagnostics including laser-based measurements.

3.2.1. Particle combustion studies in a laminar flow reactor

The laminar flat flame burner allows the injection of particles through a fully premixed methane flame such that particle ignition in a hot exhaust atmosphere of about 1800 K enriched with a defined amount of oxygen is achieved. The premixed flame is stabilized approx. 2 mm above a ceramic honeycomb. The test rig environment has been previously used to study the particle combustion of coal [49–53] and PP particles additivated with PSMP [31] and has been extensively documented in the literature. In the present work, equivalent to [31], an exhaust gas atmosphere enriched with 10 vol% of oxygen was set, into which PP particles were injected.

Fig. 2(a) displays the experimental setup of the laser optical multi-parameter measurement. Here, two measurement techniques, planar laser-induced fluorescence of the OH radical (OH-PLIF) and diffuse back-illumination (DBI) were combined.

To visualize the reaction zones around burning polymer particles, a dye laser operated with rhodamine 6G and pumped by a Nd:YAG laser was tuned to a wavelength of 283.01 nm such that the $Q_1(6)$ line of the $A^2\Sigma^+ \leftarrow X^2\Pi$ system ($\nu' = 1 \leftarrow \nu'' = 0$) of the OH radical was excited. The laser was operated at a repetition rate of 10 kHz with an average pulse energy of 0.4 mJ. For an accurate measurement of the radial evolution of the spherical flame around a polymer particle, the laser sheet must hit the particle centrally, as shown in Fig. 3(a) by the shadow cast by the laser light on the particle's left side. To increase the probability of such a hit and thus increase the number of available individual measurements for statistical evaluation, an acousto-optic deflector was inserted into the beam path of the dye laser in analogy to [52,53], with the aid of which 10 scans were performed in the depth direction. The laser light section thickness was approximately 130 μm (full width half maximum). The OH-LIF signal was detected as in [31] by means of a high-speed camera equipped with an image intensifier. Here, a pixel resolution of 30.3

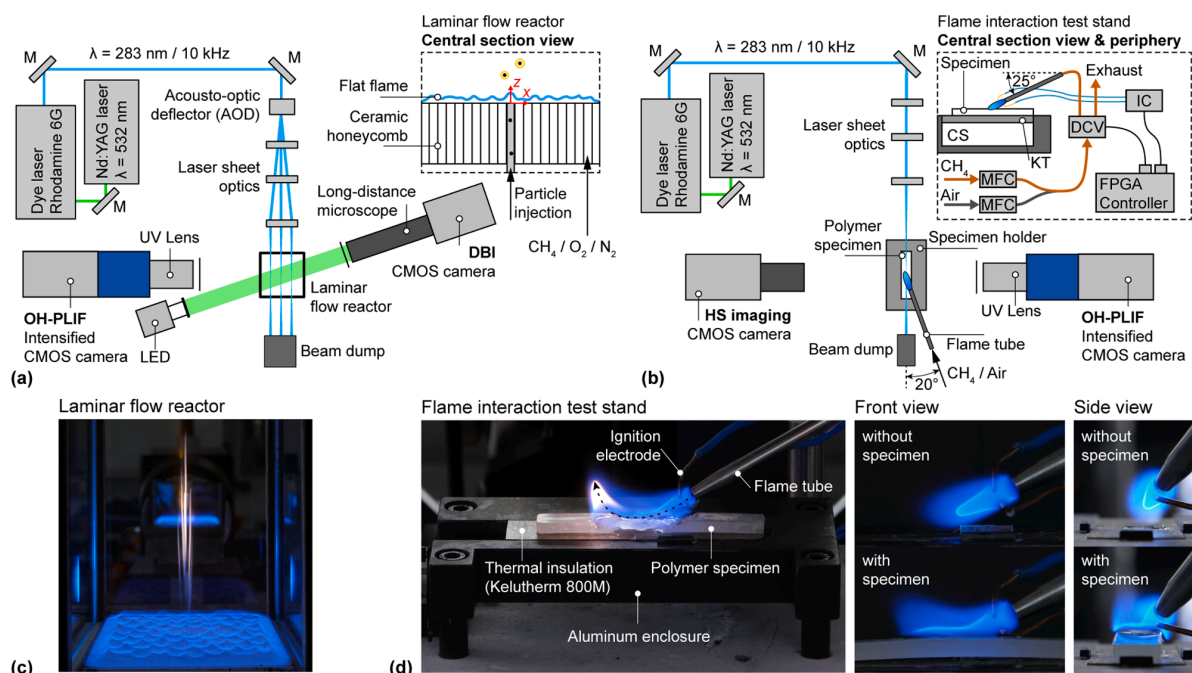**Fig. 2.** Experimental setup of the laser-optical combustion diagnostics. (a) Particle combustion experiments in a laminar flow reactor. (b) Flame interaction test stand. (c) Color photograph of particle streaks of combusting flame retarded PP particles. (d) Color photographs of the flame interaction test stand including images of the premixed methane flame with and without an interacting polymer specimen.
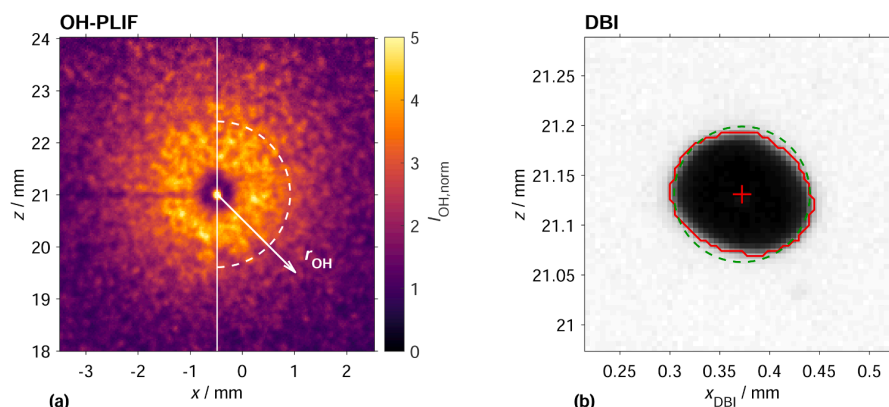
3

Fig. 3. Multi-parameter measurement of an exemplary PP particle in the laminar flow reactor. (a) OH-PLIF signal of a burning PP particle normalized to the background. The radial evolution of the signal was calculated along the right semicircle to exclude shadowing. (b) Corresponding DBI image with algorithmically detected edge of the particle (in red). A circle with the equivalent projection area to derive the circle-equivalent radius r_p is highlighted by a dashed green line.

μm/px was achieved with a field of view of 23.2×23.2 mm^2.

Simultaneously with the OH-PLIF system, a DBI system detected high-resolution images of the particles as exemplified in Fig. 3(b). Here, an LED pulsed at 10 kHz repetition rate was arranged 17° offset from the OH-PLIF detection axis with an opposite high-speed camera capturing the DBI images. The pixel resolution of the system was 5.2 μm/px with a field of view of 9.9×7.0 mm^2, which was centrally positioned at the upper edge of the OH-LIF field of view.

To ensure that a large field of view could be covered by both camera systems, the burner was traversed in height in steps of 8 mm to a total of 4 different fields of view, so that the range from the particles leaving the injection tube at $z = 0$ mm to the fully developed spherical flame at approximately $z = 35$ mm could be covered with sufficient overlap of the individual measurements.

From both measurements, several simultaneously recorded parameters can be extracted, facilitating the calculation of conditioned statistics as is shown in Fig. 3. From the OH-PLIF measurements, the maximum normalized OH signal in the flame $I_{max,OH}$ and the radius at which this maximum signal occurs $r_{max,OH}$ were determined. For each frame, the fluorescence signal was normalized to the background intensity of the hot flat flame exhaust gasses on the side of the image facing the laser in analogy to [31] in order to enable comparisons between individual images. Since both the temperature and OH concentration of the flat flame exhaust are minimally affected by particle combustion, this assumption is justified [49].

From the DBI images, the circle-equivalent radius of the projected image r_p (or diameter d_p) were measured simultaneously, which is schematically shown in Fig. 3(b). The combination of both measurement techniques thus allows the selective observation of certain parameter effects, which is only possible by simultaneous measurements of all relevant parameters and their subsequent statistical evaluation. This methodology will be demonstrated by selectively linking properties of the volatile flame to the particle size.

3.2.2. External flame interaction test stand

To replicate a fire scenario in which a flame retarded polymer component of representative size is exposed to an external source of heat, we further extend our investigation to a second test environment in which we analyze the combustion of polymer sticks using optical combustion diagnostics. Flame retarded specimens usually undergo a standardized testing procedure such as the horizontal or vertical burning test specified in the UL94 plastics flammability standard, whereas the vertical test setup of the UL94 burning test is of greater importance [54]. However, these tests are not designed for the use of laser-based optical diagnostics and have to be adapted. Consequently, we have designed a novel flame interaction test stand inspired by the horizontal burning test (HB) in which a premixed Bunsen flame heats up a polymer specimen of defined dimensions.

Even though realistic fire scenarios of burning polymers are characterized by diffusion flames, the stabilization of a laminar premixed flame at a fixed equivalence ratio represents a highly repeatable setup with a temporally and spatially stable flame front which simplifies a comparison between different polymer specimens. As explained in the introduction, the study of flame retardants and their inhibition effectiveness is highly dependent on the used burner and flame setup [18]. This reasoning is especially important for combustion studies of flame retarded polymer specimens in contrast to doped canonical hydrocarbon flames, as the level of complexity is further increased. In this case, premixed flames show higher flue gas temperatures, influencing the thermal decomposition of the flame retarded polymer and hence the inhibition processes both in the gas phase as well as the formation of char layers in the condensed phase.

Fig. 2(b) schematically displays the setup of both the flame interaction test stand and the optical diagnostics systems. The polymer specimen is placed on top of a thermal insulation plate (made from Kelutherm 800 M, thermal conductivity of 0.26 W/mK) which is put on top of a fireproof calcium silicate (CS) plate. The first insulation plate also serves as an easily cleanable base from which molten plastic can be removed without residue after the combustion tests. All insulation plates are fit into a custom-built aluminum enclosure and can be exchanged for mounted calibration plates for the determination of the pixel to real-world coordinate conversion of the camera systems.

The external flame is stabilized on the chamfered tip of a stainless-steel pipe with an inner diameter of 4 mm fed by separate mass flow controllers (MFC, Bronkhorst EL-Flow) for methane (CH$_4$) and air at an equivalence ratio of 1.6. The flame provides a thermal output power of 79.4 W calculated using the lower heating value of CH$_4$, where the volume flow of methane is 0.145 l/min and the volume flow of air is 0.858 l/min. After exiting the MFCs, the premixed gasses are led through a directional control valve (DCV), which guides the mass flow either to the flame tube (solenoid active) or the exhaust (solenoid inactive). The flame can be ignited remotely using an automotive-grade ignition coil (IC, Mercedes-Benz) connected to copper wires serving as electrodes. Both the DCV and the IC are controlled by a FPGA controller (National Instruments CompactRIO) running a custom software compilation controlled through LabVIEW. This configuration allows the experimentalist to ignite and extinguish the flame at pre-defined points in time with a high temporal accuracy (down to 25 ns given by the clock speed of the FPGA chip) and simultaneously provides the trigger signals for the diagnostics systems. While the ignition spark is initiated only a few

microseconds after receiving the trigger signal (checked with an oscilloscope and a photodiode monitoring the spark), the shutdown of the flame using the DCV happens at a lag of approx. 50 ms. This value is given by both the time the solenoid requires to shut off after operation and the subsequent downstream propagation of the change of the ignitable fluid mixture until the external flame is no longer stabilized.

Similar to the particle combustion experiment, high-speed OH-PLIF measurements at a repetition rate of 10 kHz were performed during the combustion of the polymer sticks using the same diagnostics setup apart from the acousto-optic deflector resulting in a single centrally aligned laser sheet across the length axis of the polymer specimen. For the OH-PLIF camera, a pixel resolution of 32.3 µm/px was achieved with a field of view of 24.8 × 24.8 mm². The flame tube was fixed in position at an angle to the polymer specimens (as shown in Fig. 2(b)) to avoid reflections of the UV laser sheet. Simultaneously, a high-speed camera positioned at the opposite side of the OH-PLIF detection unit recorded luminosity images of the burning polymer at a repetition rate of 500 Hz with a pixel resolution of 23.8 µm/px resulting in a field of view of 24.4 × 24.4 mm² similar in size to the OH-PLIF images. Both cameras were centrally pointed at the horizontal midpoint of the polymer specimens.

The ignition and extinction signals for the external flame and the trigger signals of the diagnostics systems were automatically created in a pre-defined test procedure, which was controlled by the custom LabVIEW program. All specimens were exposed to the external premixed flame for 60 s, equal to the time interval between the point of ignition t_i and the point of extinction t_e. The test procedure can be summarized as follows:

- $t = t_i$ - 5 s: The DCV is switched on to guide the methane-air mixture through the flame tube.
- $t = t_i$: The IC is triggered, resulting in the spark ignition of the premixed flame.

- $t = t_i + 55$ s $= t_e$ - 5 s: The HS imaging system is triggered and starts recording.
- $t = t_i + 59.8$ s $= t_e$ – 0.2 s: The OH-PLIF imaging system is triggered and starts recording.
- $t = t_e = t_i + 60$ s: The DCV is switched off and the external flame is extinguished.

4. Results and discussion

4.1. Thermal decomposition of flame-retardant polypropylene

The neat flame retardants APP, ATH, DEPZn, PSMP and their composites in PP (10 wt% flame retardant) were analyzed by using TGA coupled to FTIR (Fig. 4 and Table 1). The first derivative of the TGA curve (DTG) is plotted in Fig. 4(c) and (d). The flame retarded samples and the neat PP were extruded by using a co-rotating twin-screw extruder. The amount of all flame retardants was kept at 10 wt% to maintain the amount of combustible polymer. Some flame retardants require higher amounts to cause a self-extinguishing behavior to PP.

Table 1
Thermal properties of APP, ATH, DEPZn, PSMP and their composites (10 wt% flame retardant) in PP using a heating rate of 10 K/min in nitrogen atmosphere.

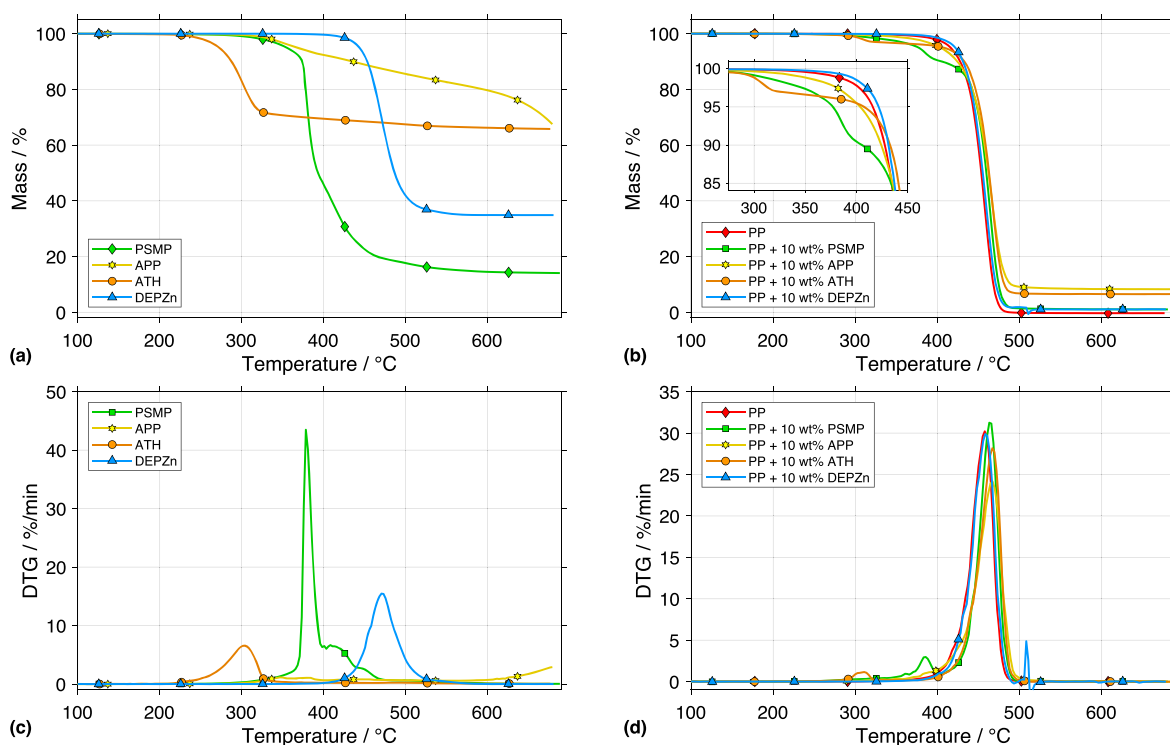| Composition	$T_{1\%}$ / °C	Residue at 600 °C / %
PSMP	301	15
APP	319	80
ATH	237	66
DEPZn	418	35
PP	378	0
PP + 10 wt% PSMP	303	1
PP + 10 wt% APP	342	8
PP + 10 wt% ATH	297	7
PP + 10 wt% DEPZn	391	1

Fig. 4. Thermogravimetric analysis of neat flame retardants ((a), PSMP, APP, ATH, DEPZn) and their composites in PP ((b), PP, PP + 10 wt% PSMP, PP + 10 wt% APP, PP + 10 wt% ATH, PP + 10 wt% DEPZn) with a heating rate of 10 K/min in a nitrogen atmosphere. (c,d) Corresponding DTG curves.

5

Different amounts of flame retardants result in different amounts of combustible polymer. A decreased fuel concentration in the gas phase can be induced by a flame retardant effect and the amount of used flame retardant. To overcome this problem, a total level of 10 wt% flame retardant was used [31]. Initially, the TGA curves are analyzed and subsequently the FTIR results from the decomposition products are discussed. The neat flame retardants show an increasing residue at 600 °C in the following order:

PSMP < DEPZn < ATH < APP.
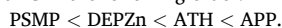
Although the flame retardants are decomposing in a temperature range of 237–418 °C, they are used in PP [44,55–57]. The flame retardants have been selected for their reported different mode of action to analyze their impact on hydroxy radical concentration. The relatively high residue at 600 °C for APP (80%) and ATH (66%) indicates a low volatility of the flame retardants. In comparison, PSMP results in a relatively low residue at 600 °C with 15% indicating a high volatility, which is related to predominantely gas-phase activity [31]. The residue of DEPZn is about 35%. The 10 wt% polymer composites of the flame retardants in PP result in a similar trend: 10 wt% APP and ATH in PP effect a residue of 8 and 7% at 600 °C, whereas DEPZn and PSMP effect 1% residue in PP at 600 °C. The $T_{1\%}$ of PP is reduced by all flame retardants but DEPZn which is caused by the high thermostability of neat DEPZn. ATH affects the $T_{1\%}$ of PP the most with 297 °C which is due to the relatively low thermostability of the neat flame retardant in comparison to PSMP, APP and DEPZn. The decomposition of PP + 10 wt% ATH and PP + 10 wt% PSMP takes place in a two-step process, which is also visible in the corresponding DTG curves (Fig. 4(d)). In the case of PP + 10 wt% ATH, the weight loss in the first decomposition step comprises about 4 wt% rising to 7 wt% at 600 °C corresponding to the calculated residue without an interaction between the flame retardant and the polymer matrix. The first decomposition step of PP + 10 wt% PSMP comprises of approximately 10 wt% corresponding to the amount of flame retardant used. This indicates no interaction between the flame retardant PSMP and the polymer matrix during the decomposition

process due to almost complete evaporation of the flame retardant out of the PP matrix.

All neat flame retardants, the neat PP and the melt extruded flame retarded PP compounds were analyzed by TGA-FTIR. A thermal analysis coupled to FTIR allows the monitoring of released substances depending on temperature by integrating the characteristic absorption bands. The Gram-Schmidt plot as well as the TGA curve are included in every graph of Figs. 5 and 6. The Gram-Schmidt curve represents the total FTIR absorbance intensity of volatile substances during a TGA-FTIR measurement. In contrast to that, the DTG curve quantifies the mass loss rate of a sample. The TGA-FTIR analysis of the neat flame retardants in a nitrogen atmosphere and a heating rate of 10 K/min are shown in Fig. 5. The pyrolysis behavior of PSMP was investigated in detail in Geschwindner et al. [31] using a different device for analysis. Aldehydes and water are characteristic decomposition products released in a one-step degradation at 390 and 385 °C peak temperatures.

Regarding APP, the main decomposition product is ammonia (NH_3), which is released in two steps at about 380 and 450 °C. Bands at 933–927 cm^{-1}, 968–959 cm^{-1}, 1634–1616 cm^{-1} as well as 3338–3330 cm^{-1} correspond to N-H stretching and deformation vibrations. A full list of peak temperatures of all detected decomposition substances is listed in the Supporting Information in Table S1. The two decomposition steps are clearly visible by looking at the release curve of NH_3, but this is not the case for TGA or Gram-Schmidt curves of APP. According to literature, APP releases water in a third step during its decomposition [46] with a peak temperature of about 660 °C, where crosslinking to P-O-P structures (ultraphosphate) [45,47] takes place.

ATH releases water during an endothermic dehydration process, whereas aluminum oxide remains in the condensed phase acting as a barrier for mass and heat transfer. The water release reaches its maximum at 305 °C [47].

The pyrolysis of DEPZn results in the release of ethane and phosphinic acid with a maximum at 475 °C. Phosphinic acid (H_3PO_2) reacts to phosphine and phosphoric acid when heated up. Using MBMS, Lau
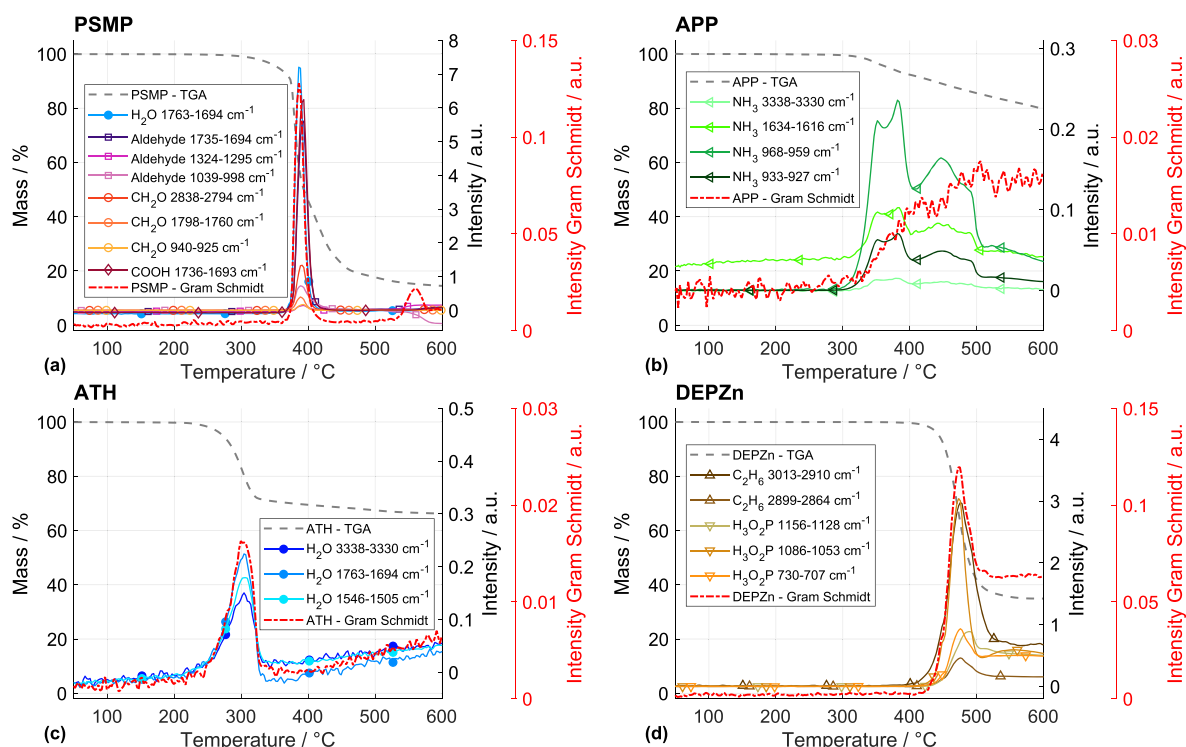

Fig. 5. TGA-FTIR of neat flame retardants in a temperature range of 25–600 °C and a heating rate of 10 K/min in a nitrogen atmosphere.
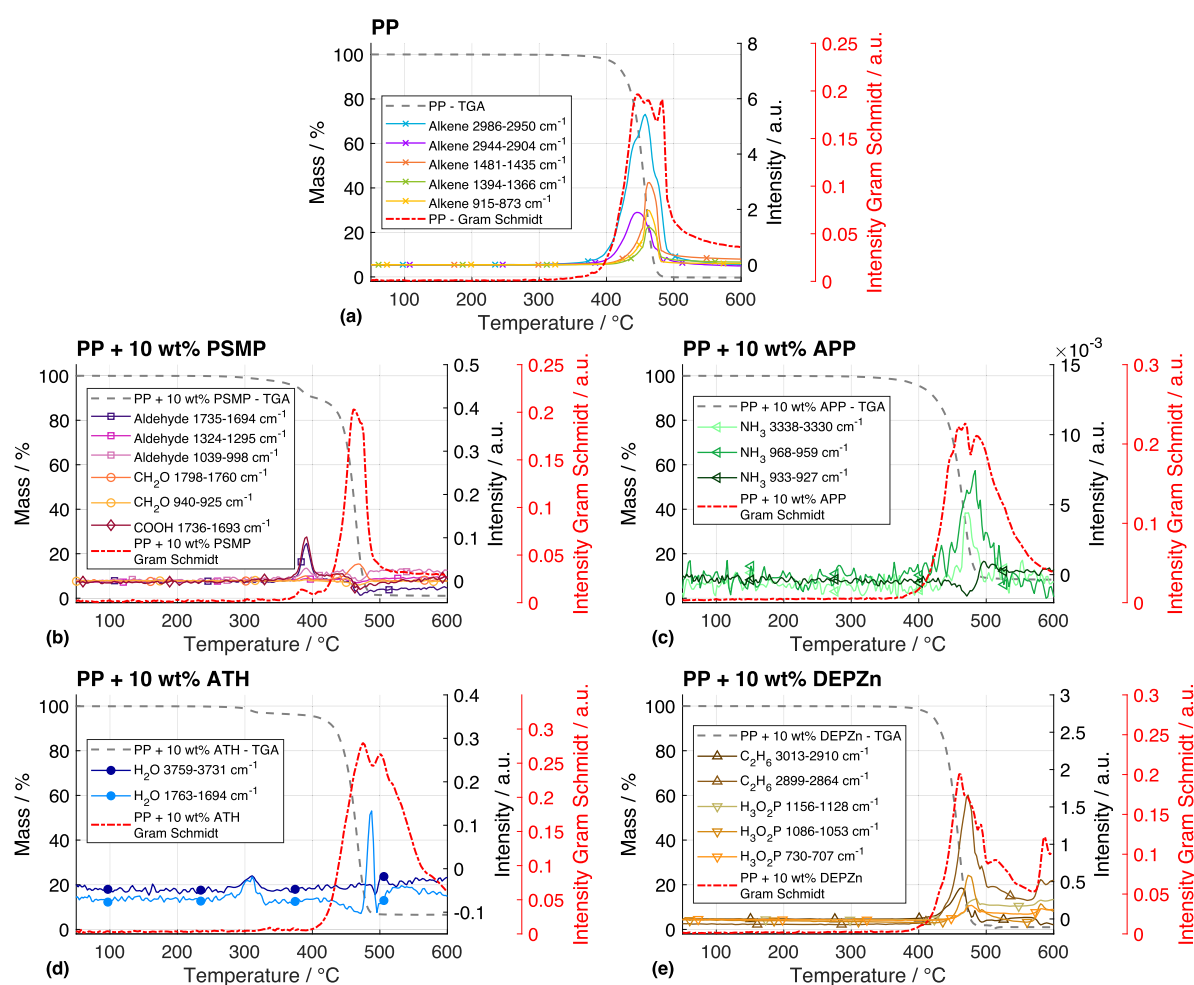
Fig. 6. TGA-FTIR of flame retardants in PP in a temperature range of 25–600 °C and a heating rate of 10 K/min in a nitrogen atmosphere.

et al. proved the formation of phosphinic acid and phosphine (PH$_3$) as decomposition products of AlPi, the alumina derivate of DEPZn [40,41]. Phosphine and ethane (C$_2$H$_6$) are flammable gasses which may not compensate the flame retardant performance of DEPZn, otherwise it would not show a flame retardant effect for engineering plastics. Compared to the other used flame retardants, the pyrolysis products of DEPZn and PSMP contain a high amount of volatile substances resulting in low residues of 35 and 15% at 600 °C indicating a gas-phase activity.

The TGA-FTIR results of neat PP and the flame retardant polymer composites are depicted in Fig. 6. PP (Fig. 6(a)) decomposes in a one-step process in nitrogen atmosphere characterized by typical alkene absorption bands: 2986–2950 cm^{-1}, 2944–2904 cm^{-1}, 1672–1628 cm^{-1}, 1481–1435 cm^{-1}, 1394–1366 cm^{-1} and 915–873 cm^{-1}. The integrated alkene absorption bands are not shown for the flame retarded polymer composites for clarity.

The pyrolysis of 10 wt% PSMP in PP is discussed in detail in Geschwindner et al. [31]. A characteristic aldehyde structure is released during the pyrolysis of PSMP, which cannot be identified by TGA-FTIR results. APP in PP (Fig. 6(c)) results in a slightly delayed release of the decomposition products of PP and APP. NH$_3$ as the main decomposition product in the gas phase of APP pyrolysis is released in neat APP at a peak temperature of 381 °C, whereas the release in PP takes place at a peak temperature of 473–496 °C. The release of alkene-containing structures is affected by the decomposition of APP resulting in 10 °C higher peak temperatures. The remaining residue of 8 wt% at 600 °C

corresponds to approximately 80 wt% of the initial APP mass and is equivalent to the expected residue at 600 °C for neat APP pyrolysis.

The polymer composite of PP and 10 wt% of ATH (Fig. 6(d)) decomposes in two steps at 311 and 488 °C. The first decomposition step at 311 °C mainly corresponds to water release by ATH going along with a mass loss of 3.5 wt%. This temperature maximum is in accordance to the pyrolysis behavior of neat ATH with a temperature maximum of 305 °C regarding water release. The release of alkene structures also shows a flat rise in this temperature range which can be observed in the absorption band 2986–2950 cm^{-1}. The temperature maxima of the alkene species in PP + 10 wt% ATH are in a temperature range of 487–494 °C and significantly higher compared to neat PP with 445–464 °C. The decomposition of ATH to aluminum oxide (Al$_2$O$_3$) acting as a barrier [48] for fuel, oxygen and heat might inhibit the release of gaseous substances from the condensed phase in the gas phase resulting in a delayed release of alkene substances. The residue of 7 wt% at 600 °C for 10 wt% ATH in PP corresponds to 80 wt% residue of neat ATH after pyrolysis indicating a low volatility of ATH in PP.

A significant delay in the pyrolysis process regarding the temperature maxima (461 and 588 °C) can be observed for PP + 10 wt% DEPZn (Fig. 6(e)). A pronounced two-step decomposition process is indicated in the Gram-Schmidt-curve and the corresponding DTG curve, whereas the second decomposition step is not finished at 600 °C, although the residue at 600 °C is 1 wt%. The two-step degradation process in the Gram-Schmidt curve and the corresponding DTG curve results from the

decomposition of the polymer composite in the first step and the decomposition of the residue to CO_2, CO and water in the second step. The residue at 600 °C also indicates a high volatility and thus a gas-phase activity for DEPZn in PP. As observed for the pyrolysis process of neat DEPZn, C_2H_6 and H_3PO_2 are the main decomposition products detected. Additionally, alkene species show a release in two steps.

To sum up this section, all flame retardants are releasing characteristic decomposition products in the gas phase during the pyrolysis process, which can be monitored by TGA-FTIR experiments. The volatility of the decomposed flame retardants and flame retarded composites allows a rough estimation of an evaporation of the flame retardant or its decomposition products in the gas phase acting as a potential flame inhibition or dilution agent, although this pyrolysis behavior is investigated decoupled of a realistic fire scenario. To evaluate a possible flame retardant effect, the combustion process has to be considered. The peak temperatures of the release of characteristic decomposition products of the flame retardants are shifted to higher temperatures regarding their corresponding flame retarded PP composite, which is induced by the interaction of the polymer matrix and the flame retardants during the pyrolysis process.

4.2. Particle combustion in a laminar flat flame burner

Similar to our previous study [31], the investigation of polymer particles in a high heating rate condition provides knowledge about the ignition and combustion of flame retarded PP at the microscale. Using an improved experimental setup in the current study, a comprehensive analysis of the flame retardant effect in such a generic configuration is performed.

Despite previous sieving of the particles with a mesh size of 100–150 μm, a broadly scattered size distribution between 80 μm and in some cases over 300 μm can be seen in the histograms of the DBI particle size

measurements of all particles centrally hit by the OH laser light sheet in Fig. S1. Deviations towards larger particles are particularly noticeable, which cannot be caused by the sieving alone. An observation of individual DBI images reveals that agglomerates of several particles are sometimes noticeable. These particles melt when heated in the flat flame, adhere to each other and finally fuse to form a "superparticle". Due to the high heating rate, this process occurs relatively fast and is completed after a few millimeters of axial movement through the laminar flow reactor.

A statistical comparison of all five sample formulations is influenced by their particle size distributions. Therefore, a determination of the comparable particles based on the circle-equivalent diameter is reasonable if the particles considered in the statistics all have similar particle sizes. Intuitively, this can be realized by setting narrow size intervals for each formulation, but this is opposed by the desire to have as many individual particles per interval as possible to reach statistical convergence. Here, this trade-off is solved by defining three size intervals with cutoff points $d_{p,\min}$ and $d_{p,\max}$ such that the total number of all particles present in each interval is similar. The detailed optimization procedure is explained in Section 2 of the Supporting Information. The penalty function shows a global minimum at $d_{p,\min} = 154$ μm and $d_{p,\max} = 188$ μm. Consequently, based on this histogram classification, the quantities extracted from the OH-PLIF images are compared for small, medium, and large particles or agglomerates.

Fig. 7 shows the maximum normalized OH fluorescence signal $I_{\max,OH}$ detected in the particle flame as a function of the particle height position z, where Fig. 7(a–c) shows the scatter plots of all individual particles and Fig. 7(d–f) shows the corresponding mean values and standard deviations at intervals of 4 mm. For all size intervals considered, the overall shape of the curves is similar to each other, with the ignition of the particles starting at about $z = 5$ mm, which is recognizable by a strong increase of the normalized OH fluorescence signal

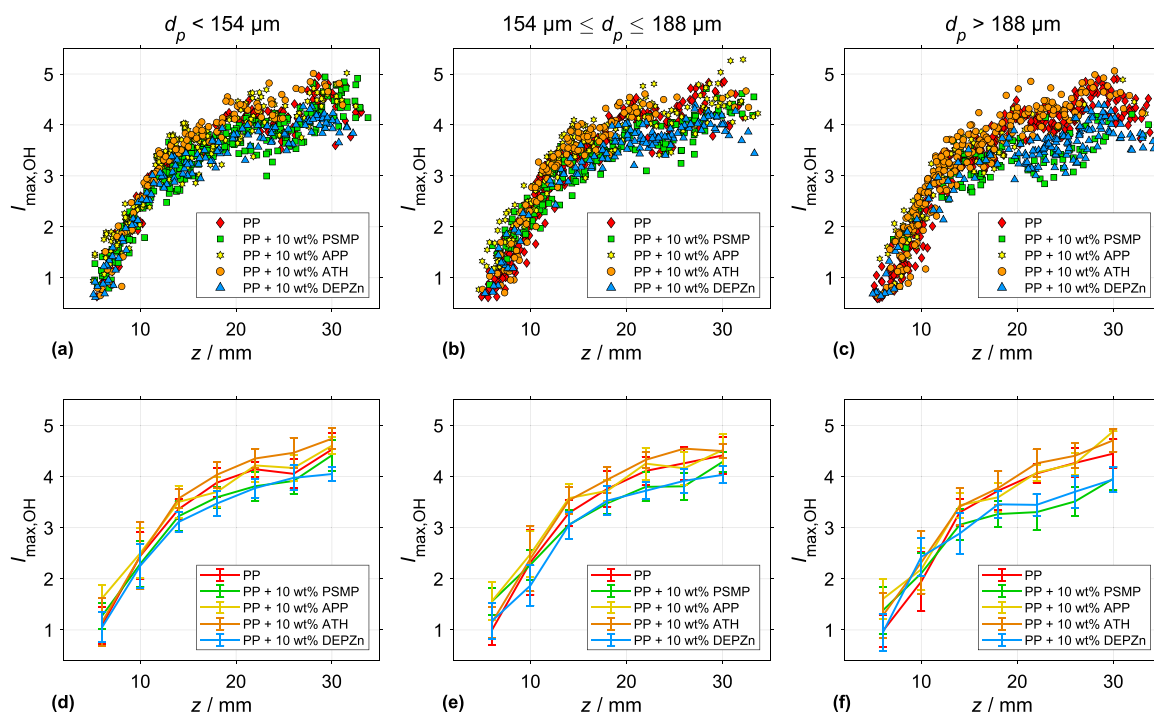**Fig. 7.** Normalized maximum OH-LIF signal intensity $I_{\max,OH}$ as a function of the particle position above the burner head z for all investigated compounds. (a-c) Scatter plots of all selected single frames of particles hit centrally by the UV laser sheet. (d-f) Display of mean and standard deviation of $I_{\max,OH}$ of particles binned into height intervals of 4 mm.

compared to the background. Up to a height of $z = 14$ mm, the different particle compositions deviate only marginally from each other for all size distributions. During the ignition phase, no effect of the flame retardants can yet be detected due to the high heating rate of the individual particles, since the dominant effect at this point is the decomposition of the polymer matrix and the ignition of the released fragments.

Upon reaching a spherical flame from a height of $z = 14$ mm, all curves flatten slightly until the last measured height at $z = 30$ mm. However, for all particle sizes, the two gas-phase active flame retardant additives PSMP and DEPZn branch downward so that a reduction in the OH-LIF signal occurring in the flame can be detected. This reduction in the fluorescence signal is slightly more pronounced for large particles than for smaller particles, which could be due to the larger absolute heat capacity of larger particles. Smaller particles reach higher particle temperatures more quickly and thus higher pyrolysis rates of the polymer matrix, which impedes inhibition of the emerging flame.

The flame retardant APP, which is usually used as a part of an intumescence system with a charring agent providing different modes of action like the formation of glassy polyphosphates, flame inhibition and enhancing charring, shows no change to neat PP for all size intervals and particle height positions, confirming the non-existent gas-phase activity of the flame retardant. The curves of ATH as a water-generating flame retardant reveal a different behavior. From a height of $z = 14$ mm onward, it can be clearly noticed that the normalized OH-LIF signal is higher than that of neat PP. This observation can be interpreted based on two considerations: the released water vapor dissociates to some extent in the hot exhaust atmosphere of the flat flame to OH radicals, which locally increase the fluorescence signal around the particle. On the other hand, the endothermic cooling of this release should lead to a reduction of the OH signal compared to conventional PP, provided that the temperature reduction is sufficiently high. However, the curves of ATH in

Fig. 7 show that the first effect dominates. This could be partly due to the fact that only 10 wt% ATH are present in the polymer samples, which results in a low flame retardant effect compared to commercial amounts of over 50 wt% of ATH [57–59]. However, a higher concentration of ATH would also mean that the concentration of flammable polymer is lowered compared to the other flame retarded samples and thus comparability would not be given. While, as expected, no gas-phase activity is detectable for APP and ATH in the current test setup with OH-PLIF, a clear reduction of the fluorescence signal is detectable for the two gas-phase active flame retardants PSMP and DEPZn.

In addition to the intensity of the OH-LIF signal, the spatial extent of the spherical envelope flame for different particle size intervals is investigated by means of the dimensionless flame radius $r_{max,OH}/r_p$, which is calculated from the radius of the maximum OH-LIF signal $r_{max, OH}$ measured by OH-PLIF and the circle-equivalent radius r_p detected by DBI. Fig. 8 displays this metric as a function of the height above the burner z, with scatter plots of all individual particles shown in Fig. 8 (a–c) and the associated mean values and standard deviations within intervals of 4 mm shown in Fig. 8(d–f). As can be observed, the curves of different compositions only differ slightly for each individual size distribution interval. Even for the gas-phase active flame retardants PSMP and DEPZn, no significant increase in flame radius can be seen compared to neat PP. The flame retardant additive thus only affects the local OH intensity for all size intervals considered, but not the dimensionless flame distance. All dimensionless flame distances increase with the height above the burner, whereas during ignition at a height of about $z = 5$–7 mm values of up to 20 are measurable, which, however, are due to the fact that at the beginning of ignition only a slight increase of the OH fluorescence signal above the background is detectable. For this reason, the position of the local maximum of the OH-LIF signal in the envelope flame varies strongly. Accordingly, the average values in Fig. 8(d–f) are shown starting from a height of 10 mm.

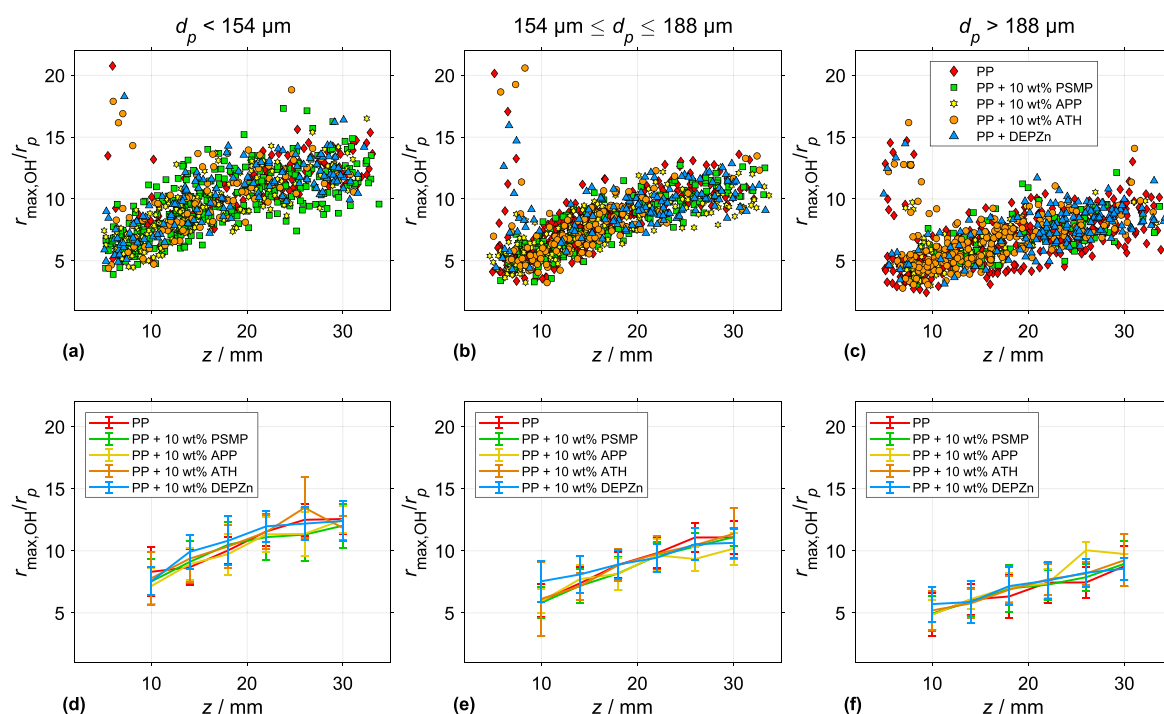**Fig. 8.** Dimensionless stand-off distance $r_{max,OH}/r_p$ of all compounds and size intervals with respect to the particle position above the burner head z. (a-c) Scatter plots of all selected single frames of particles hit centrally by the UV laser sheet. (d-f) Display of mean and standard deviation of $r_{max,OH}/r_p$ of particles binned into height intervals of 4 mm.

The influence of the particle size can be seen when comparing the three size intervals. It is noticeable that the dimensionless flame distance for small particles ($d_p < 154$ μm) at each height is 2–3 higher than for large particles ($d_p > 188$ μm). Accordingly, smaller particles exhibit a larger flame radius relative to the particle radius. This effect has already been observed in a similar way for coal particles with a high volatile content and discussed in [53]. Here, the dimensionless flame radius was also measured by simultaneous OH-PLIF and DBI and a decreasing dimensionless stand-off distance for large particles was found. It was argued that larger particles experience a slower heating and devotialization rate at the same ambient gas temperature and, accordingly, a flame burning closer to the particle is established. This argumentation is conclusive with regard to the evolution of the maximum normalized OH signal intensity in Fig. 7 since greater differences in the inhibition efficiency of the flame retardant can also be observed here for large particles, which can be justified by the reduced devolatilization rate of the polymer matrix.

4.3. Cone calorimetry

Cone calorimetry was performed on samples with 3 mm thickness. The total flame retardant amount was set to 10 wt% for ATH, APP, DEPZn and PSMP to correlate the results with OH-LIF measurements, although a significant flame retardant effect is not expected for the selected flame retardants in this concentration in PP besides the fact that only one-component flame retardant systems are investigated in this study. The amount of ATH in PP to generate a sufficient peak heat release rate (PHRR) reduction is about 60% going along with a significant decrease of combustible polymer [57–59].

The HRR curves and the time-dependent carbon monoxide (CO) concentration of the PP samples are shown in Fig. S2 and the corresponding results of the cone calorimeter measurements are listed in Table S2. The measurements were performed according to ISO 5660 with a retainer frame, but this prevented a complete combustion of the samples due to an overflow of the polymer melt. Problems regarding the use of the retainer frame are reported in the literature [60,61]. For flame retarded samples containing ATH, PSMP and APP, the time to ignition (TTI) is reduced in comparison to neat PP. This phenomenon is a result of the lowered decomposition temperature of the samples, which can also be observed in the TGA curves in Fig. 4. 10 wt% of ATH, APP and DEPZn in PP are not resulting in a sufficient flame retardant effect due to the low concentration of the flame retardants and the incomplete combustion. This results in higher PHRR for those samples than for neat PP. However, PP + 10 wt% ATH shows a sharp increase of the HRR curve, which is significantly pronounced in comparison to the other flame retarded samples. The initial increase of the HRR is a result of the increased OH radical concentration due to water vapor release which can also be observed for coal particle combustion with steam under oxy-fuel conditions. A relatively low steam content enhances the oxidation process of gaseous hydrocarbons accelerating the ignition. With increasing steam content, an inhibition effect of water vapor can be observed [62]. The same accelerated combustion behavior can be observed for a low ATH concentration in PP visible by a sharp HRR increase and an increase in OH radical concentration in OH-LIF experiments. The addition of 10 wt% of PSMP to PP leads to a reduction of the PHRR by 8,5%. All flame retardants lead to a delay of the PHRR.

The corresponding CO concentration curves depicted in Fig. S2(b) show a significantly increased CO concentration for the samples containing DEPZn and PSMP. The increase in CO as an incomplete combustion product as well as the increase of the total smoke release (TSR) is a result of a mode of action in the gas phase. The highest increase of CO and TSR can be observed for the flame retardants DEPZn and PSMP, indicating a gas-phase activity of the flame retardants. The volatility of DEPZn and PSMP in PP is also indicated by TGA measurements resulting in a low residue at 600 °C in comparison to other tested samples. The OH-LIF measurements also pointed out a mode of action in the gas phase

for the samples containing DEPZn and PSMP by the radical scavenging mechanism.

4.4. Interaction of stick-shaped samples with a premixed methane flame

While the thermal decomposition analysis discussed in Section 4.1 was conducted at low heating rates without combustion, particle combustion experiments presented in Section 4.2 were performed in an environment with very high heating rates [31]. The latter setup especially impedes the assessment of flame retardants with different condensed-phase modes of action, as micrometer-sized polymer particles instantly melt, pyrolyze and burn without any available residue. In realistic fire scenarios, a heating rate somewhere in between both discussed environments could be present [63], which motivates the validation of our previous experimental findings in an environment similar to a standard flammability test.

As outlined in Section 3.2.2, a custom test stand inspired by the standardized horizontal burning test was designed in which the interaction of stick-shaped polymer specimens with a premixed methane flame can be investigated using optical diagnostics such as OH-PLIF and high-speed luminosity imaging. A horizontal test setup prevents the polymer from melting away from the reaction zone. Methane was chosen as the fuel of the external flame as it is the simplest alkane and hence should only introduce chemically simple decomposition products similar to the molecular structure of PP. As the external flame interacts with the central portion of the surface of the polymer specimen instead of the edge of the sample, an investigation using OH-PLIF is facilitated due to decreased thermo-structural problems of the sample during the combustion. Additionally, the repeatability of the investigation is improved as the flame interaction region is not dependent on the geometry of the edges but the flat surface of the specimen which is easier to control when preparing samples for testing.

Fig. 9 shows color photographs of the adapted burning test as described in Section 3.2.2 at selected times relative to the ignition of the external flame. After extinguishment of the external flame, PSMP and APP in PP show a relatively fast self-extinguishing behavior (less than one second) in comparison to the other used flame retardants. In contrast, a self-sustaining flame can be observed for neat PP and DEPZn in PP. The combustion of the samples containing ATH in PP showed a self-extinguishing behavior before $t_e + 55$ s at which instant neat PP and DEPZn in PP were externally extinguished.

DEPZn in PP takes up a special role in this test setup since multiple smaller flames emerging from the polymer specimen within the main flame volume can be observed (right column in Fig. 9), which might be a result of the released combustible gasses found in the TGA-FTIR analysis. Due to the high luminosity of the combustion of samples containing DEPZn, a second set of images were taken at an adapted exposure time to prevent overexposure of the image sensor. The flames of the phosphorus-containing samples (PP + 10 wt% PSMP, PP + 10 wt% APP, PP + 10 wt% DEPZn) show a purple to orange hue right after the ignition of the external flame. The reason for this change in color of the flame is likely caused by the formation of luminous decomposition products of the flame retardants. It is unlikely that the orange hue is caused by the formation of soot, which is however visible in a bright zone of luminosity downstream of the attached external flame for neat PP and ATH in PP after approx. 45 s of interaction with the external methane flame. As the samples melt and the devolatilization rate of the polymer specimens increases, the formation of polycyclic aromatic hydrocarbons (PAH) is favored, which are precursors of soot [64–66]. The spatial separation between the blue-colored portion of the flame and the soot luminosity further supports this hypothesis in contrast to the purple or orange luminosity of the phosphorus-containing samples present in the whole region of the flame possibly emerging from decomposition products of the flame retardants. It should be noted that recent investigations have shown that phosphorus-containing flame retardants promote soot formation, which can cause a reduction of the combustion
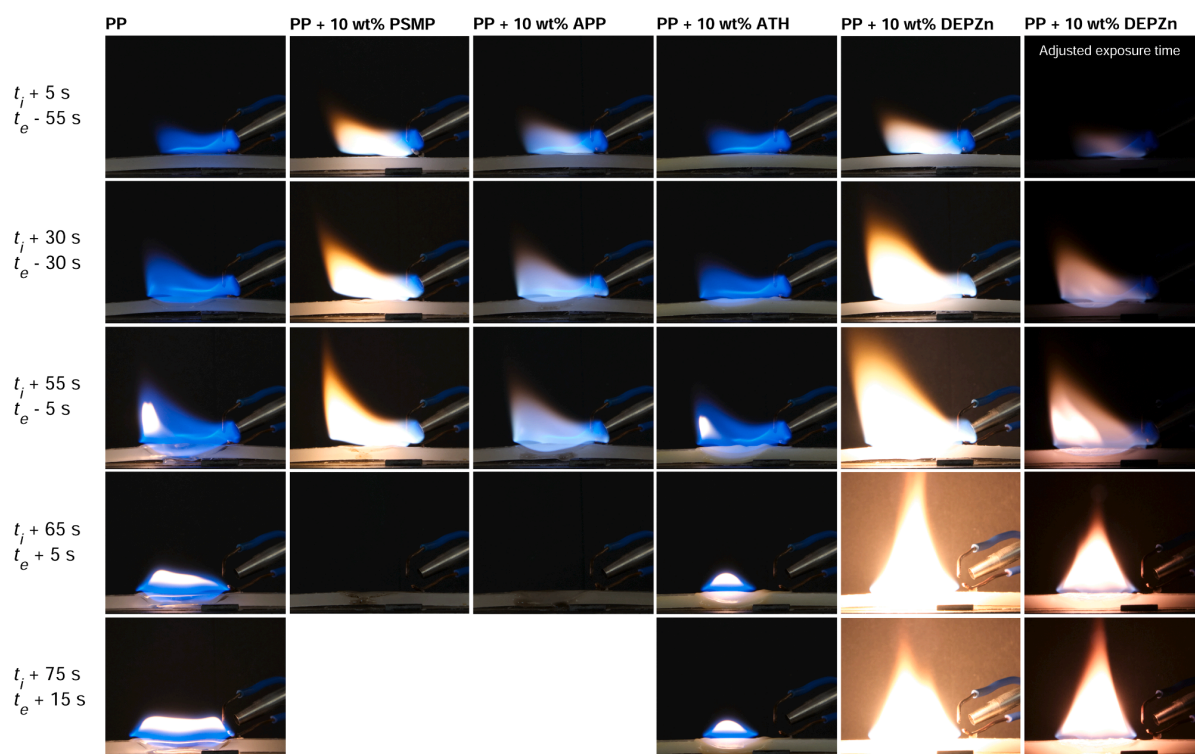
Fig. 9. Color photographs of the adapted horizontal burning test at various times relative to the point of ignition t_i and extinction t_e of the external premixed methane flame.

efficiency of polymers burned in a diffusion flame [67]. Due to the flow arrangement and the high temperatures of the premixed flame used in this study, further investigations of polymers burning in diffusion flames at lower temperatures are necessary to generalize this finding.

Photographs of the samples before and after the flame interaction test procedure are shown in Fig. 10. No significant carbonaceous residue can be observed for all tested samples. The addition of flame retardants has limited the melt-away process of the polymer sample since the region impacted by the external flame causing melting is significantly reduced compared to neat PP.

In the following, we explore the behavior of the fully developed flames of all samples just before and after the extinction of the external flame using OH-PLIF. Fig. 11(a-e) displays OH-PLIF images averaged over the 200 ms time period just before the extinction of the external flame, highlighting the interaction of the CH$_4$ flame with the combusting polymer specimen after almost 60 s of interaction. This post-processing

strategy guarantees a comparability between compounds and experiments as shot-to-shot intensity fluctuations of the UV laser are suppressed. For reference, Fig. 11(f) shows a mean OH-PLIF image computed from the first 200 ms after ignition of the external flame which serves as a comparison for all samples at the later stages of flame interaction as almost no pyrolysis of the polymer specimen has occurred at this stage. Right before the extinction of the external flame, the samples containing PP, PP + 10 wt% ATH and PP + 10 wt% APP show a relatively large region of increased OH fluorescence signal, whereas the addition of phosphorous-containing flame retardants is able to reduce the flame volume in this experiment. The extent of the reaction zone is significantly reduced for PP + 10 wt% PSMP due to its radical scavenging effect in the gas phase. In this case, the propagation of the reaction in the downstream direction of the external flame is least developed from all samples. In the special case of PP + 10 wt% DEPZn, the size of the reaction zone is reduced in comparison to PP, but the
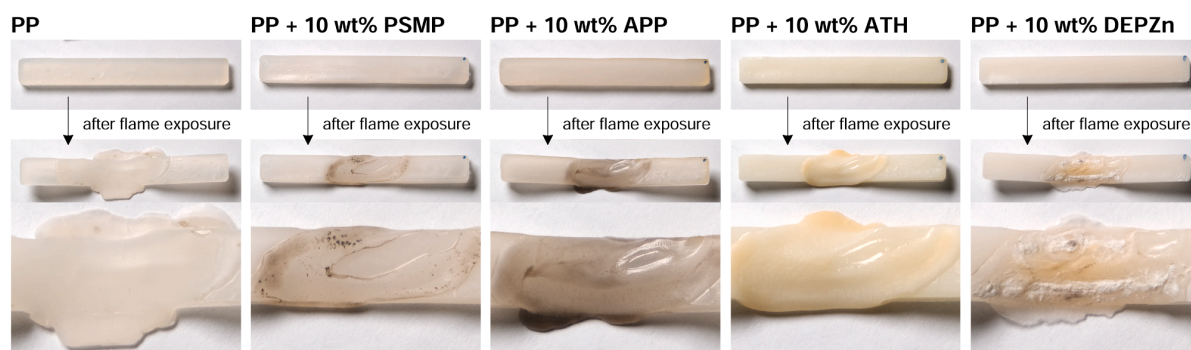

Fig. 10. Polymer specimens before and after a 60 s exposure to a premixed CH$_4$ flame. The self-sustaining flames of PP and PP + 10 wt% DEPZn were externally extinguished at t_i + 115 s.
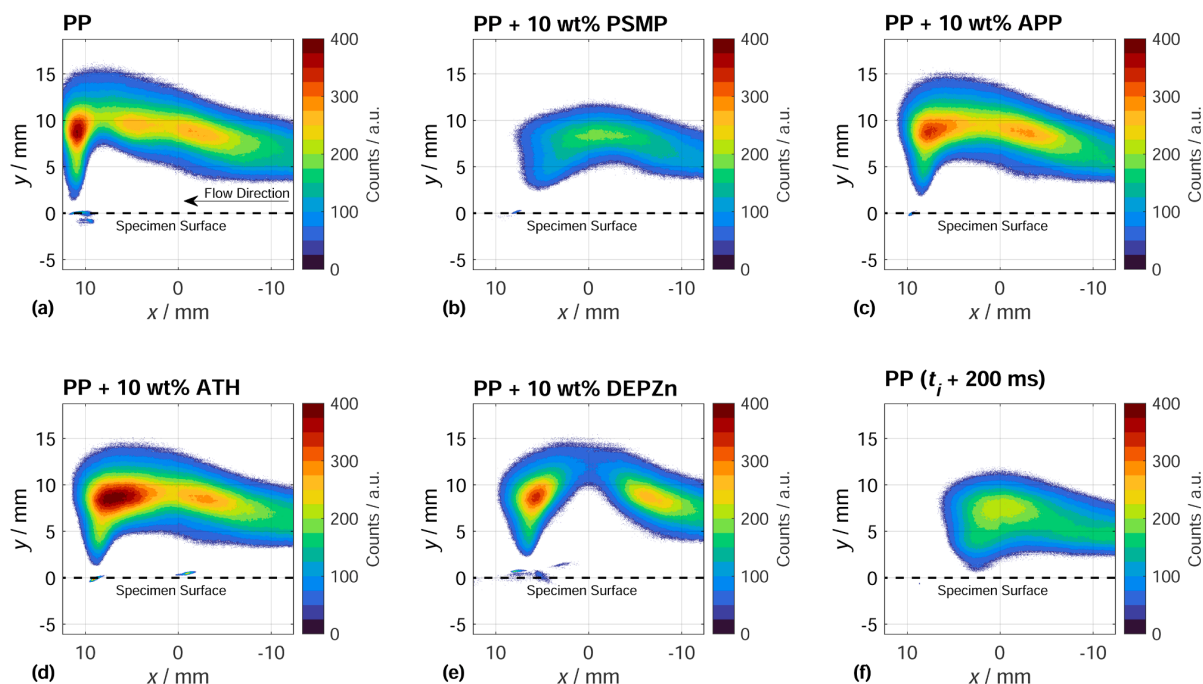
Fig. 11. OH-PLIF images of all investigated compounds interacting with a premixed methane flame. (a-e) Mean of the last 200 ms before extinction of the external flame after 60 s of flame interaction. (f) Reference image taken 200 ms after ignition (mean image of the subsequent 200 ms) of the external flame. All images are intentionally depicted mirrored with regard to the *x* axis to replicate the same viewing direction as the photographs in Fig. 9.

combustion is affected by the additional flames directly emerging from the surface of the specimen caused by the released combustible substances resulting in an additional flame source. According to TGA-FTIR results, combustible substances like ethane and PH_3 might be involved in this process. It can be assumed, that the additional flame source is significantly affecting the local concentration of the substances also due to the additional inertia of the released gasses pushing the flame upward as can be observed by the modified flame shape in Fig. 11(e). In line with the particle experiments, the highest OH signal intensity was observed for PP + 10 wt% ATH. In the gas phase, water as the main product of ATH decomposition is not diluting the fuel in the gas phase as expected for relatively high amounts of ATH in the polymer matrix (up to 60 wt %), but it is decomposing to OH radicals and thus causes an increase of the OH signal intensity in the gas phase. This is a result of the relatively low concentration of ATH used in this sample showing not a less effective flame retardant but a combustion enhancer. As observed for coal particles, a low water steam concentration accelerates the combustion until an increased steam content is reached in the gas phase, which can be achieved by increasing the ATH amount in the polymer [66].

The temporal development of the OH-LIF signal intensity relative to the point of extinction of the external flame is illustrated in Fig. 12, depicting the transient behavior of extinction or self-sustaining polymer flames when no additional source of heat is present anymore. Here, each image represents a moving average encompassing a total of 11 frames (equal to a time period of 1 ms) such that a qualitative comparison between the compounds at a fairly high temporal resolution is valid. After the external flame is switched off, first changes in the flame shape are visible at around t_e + 45 ms, which represents the time period between the initiation of the trigger of the directional control valve (t_e) and the point in time at which the reduction of the gas flow through the flame tube is visible in the chosen field of view of the OH-PLIF detection system. As the external flow pushing the flame to the left ceases, the flames of most compounds restabilize by moving right and displaying a symmetrical conical shape.

For neat PP, this self-sustaining flame above the polymer surface

gradually expands as the heat released by the combustion is sufficient to melt and pyrolyze the stick specimen providing the reaction zone with fuel from the polymer decomposition. In contrast, the depicted sample of PP + 10 wt% PSMP shows a rapid self-extinguishing behavior with an almost entirely vanished reaction zone just 10 ms after the first changes in the flame shape are noticeable. Following this, smoke release can be observed, which causes a scattering of the UV laser onto the surface of the polymer specimen resulting in a luminosity of the polymer surface, similar to the bright appearance of particles in the OH-PLIF study in Section 4.2. This observation is in accordance with the cone calorimetry results presented in Section 4.3, where a significantly increased smoke production was noticeable for PP + 10 wt% PSMP as a result of incomplete combustion in the gas phase, which is a characteristic feature of predominantly gas-phase active flame retardants. For PP + 10 wt% APP and PP + 10 wt% ATH, conical flames form which however start flickering in an oscillatory movement at around t_e + 100 ms indicating that a local fuel deficiency is present in the reaction zones. As the heat release locally decreases due to the flickering behavior, a stabilization of the flame is increasingly difficult up to the point that the flame vanishes entirely. For PP + 10 wt% APP, extinction occurs at around t_e + 550 ms, while the flickering behavior of the reaction zones of samples containing PP + 10 wt% ATH continues for several seconds until combustion eventually stops, too. Due to the tendency of both ATH and APP to act predominantly in the condensed phase with different modes of action like the formation of a protective layer or polyphosphates, a significantly reduced pyrolysis rate is likely to be the reason for this behavior since – similar to the particle combustion experiments – the mode of action in the gas phase is not detectable using OH-PLIF.

Flames of samples containing PP + 10 wt% DEPZn do not extinguish after the interaction with the external flame and form a self-sustaining conical reaction zone, which is accompanied by a luminous signal right above the surface of the specimen. To test our hypothesis that this behavior is caused by gaseous decomposition products released from the surface of the polymer sample, we make use of the high luminescence of the combustion of these samples and record the combustion with a high-

12
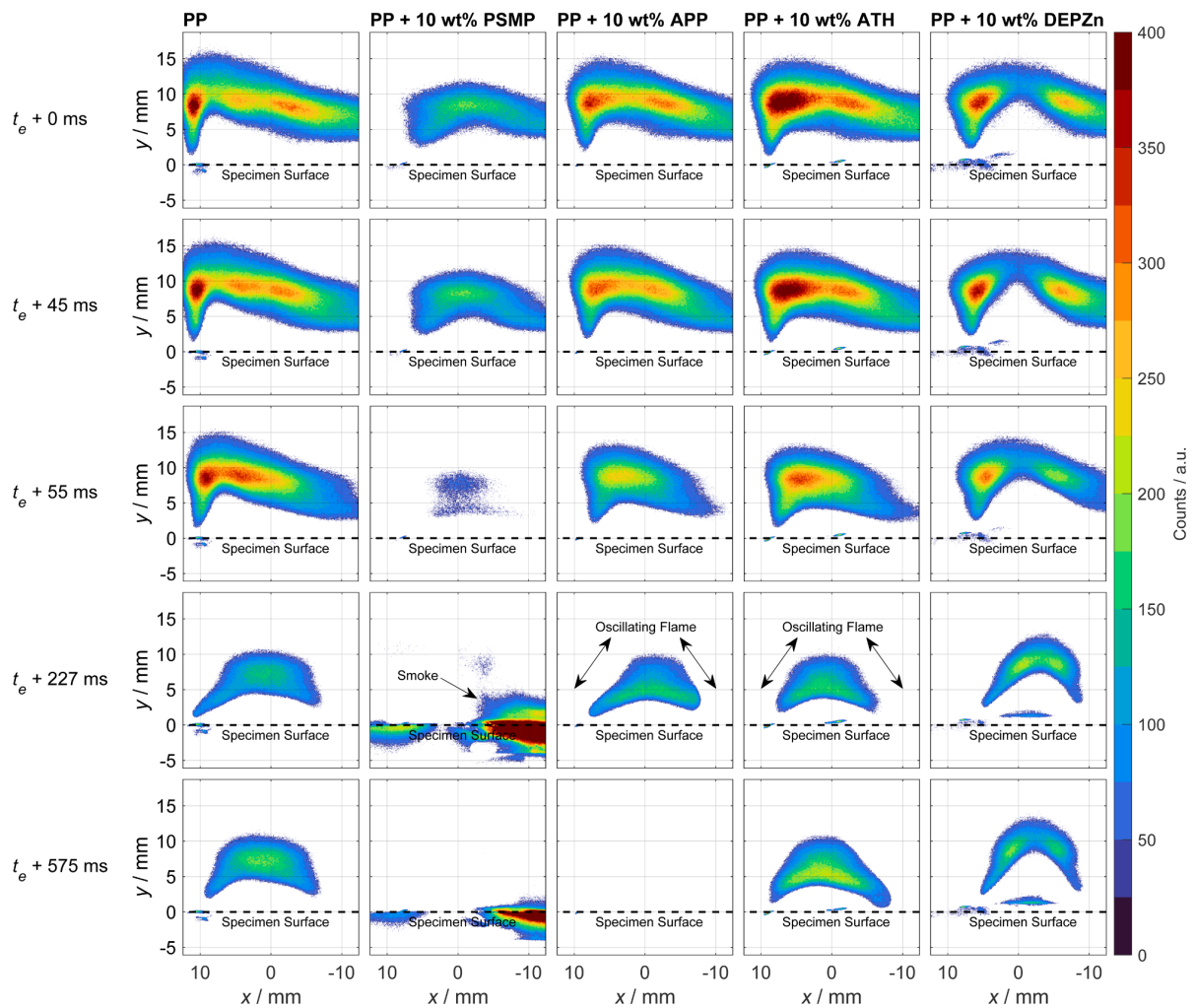
Fig. 12. OH-PLIF time series after extinction of the external methane flame interacting with polymer sticks. A corresponding video file (*Vid1_Sticks_Ext-Flame_Extinction*) is found in the Supplementary material.

speed camera capturing both the polymer sample and the self-sustaining combustion in a similar field of view to the OH-PLIF images.

Fig. 13(a,b) displays the formation of bubbles within the molten polymer sample at a selected instant after extinction of the external flame. As these bubbles rise and burst at the surface of the specimen, a bright jet of gasses shoots upwards, indicating the formation of combustible gasses. However, as the polymer surface is partially charred, the flammable gasses only escape irregularly from the pulsating char surface and possibly after coalescence of several bubbles causing a strong momentum upwards as the gaseous products are released. This
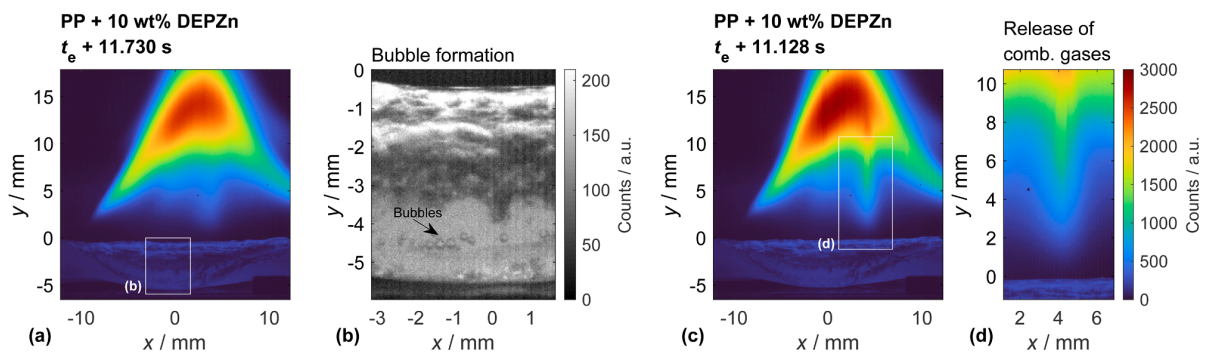
Fig. 13. Selected frames from high-speed luminosity imaging of a polymer stick containing PP and 10 wt% of DEPZn. (a,b) Formation of bubbles inside the molten polymer. (c,d) Release of combustible gasses resulting in a jet-like flame emerging from the surface of the polymer sticks. A corresponding video file (*Vid2_-DEPZn_HS_Imaging*) is found in the Supplementary material.

13

process is selectively displayed in Fig. 13(c,d) but is occurring throughout combustion of the self-sustaining polymer flame. The TGA-FTIR results presented in Section 4.1 have shown a release of ethane and phosphinic acid, which decomposes to combustible phosphine under influence of heat. The jet-like flames caused by this decomposition maintain the combustion of the polymer and compete with the flame inhibition effect. It is apparent that the use of optical diagnostics and imaging provides a straightforward approach to assess the peculiarities of the combustion of PP + 10 wt% DEPZn and the other investigated flame retardants and extends the available methods for testing flame retarded polymers in a meaningful way.

## 5. Discussion of the mode of action of flame retardants and opportunities thereof

Even though the combustion of particles with diameters below 200 μm is not relevant for typical polymer applications, the processes of flame inhibition by flame retardants are of high interest regarding the processes on the microscale, where OH radicals are involved. The particle combustion experiments provide information about the ignition process as well as the early stage of combustion and the combustion with a fully developed diffusion flame. The ignition process is not influenced significantly by any tested flame retardant, whereas the combustion process with a fully developed diffusion flame around the particle is affected by the different flame retardants regarding the OH fluorescence signal and hence, given that the gas temperature differences are negligible, also the OH radical concentration.

The flame retardants, which are described in the literature as gas-phase active like PSMP and DEPZn are capable of scavenging OH radicals and thus lower their concentration in the gas phase. PSMP decomposes thermally into, among other components, the gas-phase active PO radical, which promotes flame poisoning. Regarding the cone calorimetry results, PSMP is a very effective flame retardant in PP, which can be attributed to the high phosphorus-content of the flame retardant. TGA-FTIR results show that most of the flame retardant decomposition products of PSMP are released before the decomposition of the PP matrix and are therefore already capable of inhibition in the early phase of flame formation [31]. The flame retardant effect of DEPZn is described in the literature as a mixture of gas- and condensed-phase activity. The release of phosphinic acid (H_3PO_2) in the gas phase and the formation of zinc phosphates takes place. Phosphinic acid decomposes under heat exposure into flammable phosphine and phosphorous acid. TGA-FTIR detected flammable ethane during the pyrolysis of neat DEPZn. The flame retardant effect of phosphorus-containing decomposition products are predominating the formation of flammable decomposition products, which are visible in the flame color and flame brightness [42]. The visible release of gaseous products in PP + 10 wt% DEPZn leads to a competition of the flame inhibition effect and the combustion of flammable decomposition products in the gas phase.

ATH and APP which are described as predominantly condensed-phase active flame retardants due to the formation of a protective layer or polyphosphates are not able to lower the concentration of the OH radicals. Due to the low concentration of the flame retardants and their use as one-component systems, it is not possible to evaluate the flame retardant effect in the condensed phase. This study focuses on the processes taking place in the gas phase with special regard to the OH radical concentration. APP as sole flame retardant in PP might only generate polyphosphate. An intumescent effect was not observed in this study, because no charring agent was added. Both flame retardants are releasing water or ammonia during the combustion process, which are not able to dilute the OH radicals in the gas phase or to affect the combustion process in the gas phase due to a flame retardant effect. Of course, both flame retardants are used in lower concentrations than requested in PP, but even at this concentration no effect in the gas phase regarding the reduction of the OH radical concentration is visible. However, the addition of ATH leads to an increase in OH radical

concentration. During the decomposition of ATH water is released in the gas phase, which is not diluting the gas phase but the water itself is decomposing into hydrogen and OH radicals in the flame zone and thus increasing the OH radical concentration. The amount of ATH was too low to generate the dilution effect of the water vapor showing an antagonistic effect of ATH in PP in low concentration. This experiment also shows that released water vapor has no flame retardant effect in the gas phase at low ATH loadings [57]. The addition of APP has no effect on the OH radical concentration like neat PP, which shows that APP as a one-component flame retardant system releases no gas-phase active decomposition products. The release of ammonia has also no effect on the OH radical concentration which indicates that under the tested conditions, the condensed-phase activity forming polyphosphoric acid promoting a dense char layer is the predominant process in fire retardancy. At higher loadings of APP, the released ammonia is expected to show a dilution effect similar to water vapor at higher concentrations.

The results regarding the burning behavior of polymer particles and sticks are comparable with respect to the main aspects like the ability to affect the OH-radical concentration. Thus, the mode of action of the investigated flame retardants remains similar for microscale and macroscale samples.

6. Conclusions

The combustion of flame retarded PP containing 10 wt% of flame retardants (PSMP, APP, ATH, DEPZn) with different modes of action was investigated in detail regarding the gas phase. The characteristic decomposition products of the flame retardants were identified by TGA-FTIR. The mode of action of the flame retardants in the gas phase was analyzed using cone calorimetry and OH-PLIF enabling a categorization of the effectivity in the gas phase regarding CO production and flame inhibition by monitoring the OH fluorescence signal. The OH-PLIF experiments were performed with micrometer-sized particles and bulk polymer sticks. Although different effects can be observed during the combustion of both samples, the main effect on the flame inhibition monitored using the local OH-PLIF signal intensity is similar for both sample geometries: the flame retardant PSMP showed the most significant decrease of the OH-LIF signal in the gas phase of all investigated flame retardants. A peculiar combustion behavior was observed for the flame retardants ATH and DEPZn in PP: a 10 wt% concentration of ATH resulted in an increase of the detected OH signal intensity in the gas phase due to the released water decomposing into OH radicals and maintaining the combustion due to a low water steam concentration which is not sufficient to provide a cooling effect in the gas phase. Even though DEPZn decomposition products contain combustible gasses resulting in clearly observable jet-like flames, the flame inhibition effect in the gas phase is detectable during the combustion of PP particles including DEPZn. The use of OH-PLIF in the external flame test stand enabled a detailed investigation of combustion processes including the change in flame topology revealing and enabling access to processes and interactions of the flame retardants during ignition and combustion. Hence, the unique combination of measurement techniques utilized in this work demonstrates how a comprehensive understanding of the combustion of flame retarded polymers can be achieved.

CRediT authorship contribution statement

Christopher Geschwindner: Conceptualization, Methodology, Software, Formal analysis, Investigation, Data curation, Writing – original draft, Writing – review & editing, Visualization. **Daniela Goedderz:** Conceptualization, Formal analysis, Investigation, Data curation, Writing – original draft, Writing – review & editing. **Tao Li:** Investigation. **Johannes Bender:** Investigation. **Benjamin Böhm:** Writing – review & editing, Supervision, Project administration, Funding acquisition. **Andreas Dreizler:** Writing – review & editing, Supervision, Project administration, Funding acquisition.

Declaration of Competing Interest

The authors declare that they have no known competing financial interests or personal relationships that could have appeared to influence the work reported in this paper.

Data availability

Data will be made available on request.

Supplementary materials

Supplementary material associated with this article can be found, in the online version, at doi:10.1016/j.polymdegradstab.2023.110321.

References

[1] M.M. Velencoso, A. Battig, J.C. Markwart, B. Schartel, F.R. Wurm, Molecular firefighting-how modern phosphorus chemistry can help solve the challenge of flame retardancy, Angew. Chem. Int. Ed. Engl. 57 (33) (2018) 10450–10467.

[2] B. Schartel, Phosphorus-based flame retardancy mechanisms-old hat or a starting point for future development? Materials 3 (10) (2010) 4710–4745 (Basel Switzerland).

[3] J. Green, Mechanisms for flame retardancy and smoke suppression -a review, J. Fire Sci. 14 (6) (1996) 426–442.

[4] B. Schartel, B. Perret, B. Dittrich, M. Ciesielski, J. Krämer, P. Müller, et al., Flame retardancy of polymers: the role of specific reactions in the condensed phase, Macromol. Mater. Eng. 301 (1) (2016) 9–35.

[5] M.M. Velencoso, A. Battig, J.C. Markwart, B. Schartel, F.R. Wurm, Molecular firefighting—how modern phosphorus chemistry can help solve the challenge of flame retardancy, Angew. Chem. Int. Ed. 57 (33) (2018) 10450–10467.

[6] A. El-Sabbagh, L. Steuernagel, D. Meiners, G. Ziegmann, O. Toepfer, Optimization of flame retardant content with respect to mechanical properties of natural fiber polymer composites: case study of polypropylene/flax/aluminum trihydroxide, Polym. Compos. 37 (11) (2016) 3310–3325.

[7] N. Ristolainen, U. Hippi, J. Seppälä, A. Nykänen, J. Ruokolainen, Properties of polypropylene/aluminum trihydroxide composites containing nanosized organoclay, Polym. Eng. Sci. 45 (12) (2005) 1568–1575.

[8] S. Bourbigot, M. Le Bras, R. Leeuwendal, K.K. Shen, D Schubert, Recent advances in the use of zinc borates in flame retardancy of EVA, Polym. Degrad. Stab. 64 (3) (1999) 419–425.

[9] P. Gijsman, R. Steenbakkers, C. Fürst, J. Kersjes, Differences in the flame retardant mechanism of melamine cyanurate in polyamide 6 and polyamide 66, Polym. Degrad. Stab. 78 (2) (2002) 219–224.

[10] K.H. Pawlowski, B. Schartel, Flame retardancy mechanisms of triphenyl phosphate, resorcinol bis(diphenyl phosphate) and bisphenol A bis(diphenyl phosphate) in polycarbonate/acrylonitrile–butadiene–styrene blends, Polym. Int. 56 (11) (2007) 1404–1414.

[11] B. Schartel, Phosphorus-based flame retardancy mechanisms—old hat or a starting point for future development? Materials 3 (10) (2010) 4710–4745 (Basel Switzerland).

[12] T. Sikes, O. Mathieu, W.D. Kulatilaka, M.S. Mannan, E.L. Petersen, Laminar flame speeds of DEMP, DMMP, and TEP added to H2- and CH4-air mixtures, Proc. Combust. Inst. 37 (3) (2019) 3775–3781.

[13] I.V. Rybitskaya, A.G. Shmakov, V.M. Shvartsberg, O.P. Korobeinichev, Effect of the equivalence ratio on the effectiveness of inhibition of laminar premixed hydrogen-air and hydrocarbon-air flames by trimethylphosphate, Combust. Explos. Shock Waves 44 (2) (2008) 133–140.

[14] O.P. Korobeinichev, V.M. Shvartsberg, A.G. Shmakov, T.A. Bolshova, T.M. Jayaweera, C.F. Melius, et al., Flame inhibition by phosphorus-containing compounds in lean and rich propane flames, Proc. Combust. Inst. 30 (2) (2005) 2353–2360.

[15] O.P. Korobeinichev, V.M. Shvartsberg, T.A. Bol'shova, A.G. Shmakov, D.A Knyaz'kov, Inhibition of methane-oxygen flames by organophosphorus compounds, Combust. Explos. Shock Waves 38 (2) (2002) 127–133.

[16] M. Steinhausen, F. Ferraro, M. Schneider, F. Zentgraf, M. Greifenstein, A. Dreizler, et al., Effect of flame retardants on side-wall quenching of partially premixed laminar flames, Proc. Combust. Inst. (2022).

[17] N. Bouvet, G.T. Linteris, V.I. Babushok, F. Takahashi, V.R. Katta, R. Krämer, A comparison of the gas-phase fire retardant action of DMMP and Br2 in co-flow diffusion flame extinguishment, Combust. Flame 169 (2016) 340–348.

[18] N. Bouvet, G. Linteris, V. Babushok, F. Takahashi, V. Katta, R Krämer, Experimental and numerical investigation of the gas-phase effectiveness of phosphorus compounds, Fire Mater. 40 (5) (2016) 683–696.

[19] N. Vora, N.M. Laurandeau, Analysis of CF 3 Br flame suppression activity using quantitative laser-induced fluorescence measurements of the hydroxyl radical, Combust. Sci. Technol. 166 (1) (2001) 15–39.

[20] N. Vora, J.E. Siow, N.M. Laurandeau, Chemical scavenging activity of gaseous suppressants by using laser-induced fluorescence measurements of hydroxyl, Combust. Flame 126 (1–2) (2001) 1393–1401.

[21] J.E. Siow, N.M. Laurandeau, Flame inhibition activity of phosphorus-containing compounds using laser-induced fluorescence measurements of hydroxyl, Combust. Flame 136 (1–2) (2004) 16–24.

[22] M. MacDonald, F. Gouldin, E. Fisher, Temperature dependence of phosphorus-based flame inhibition, Combust. Flame 124 (4) (2001) 668–683.

[23] M.A. MacDonald, T.M. Jayaweera, E.M. Fisher, F.C. Gouldin, Inhibition of nonpremixed flames by phosphorus-containing compounds, Combust. Flame 116 (1–2) (1999) 166–176.

[24] O. Mathieu, W.D. Kulatilaka, E.L. Petersen, Experimental and modeling study on the effects of dimethyl methylphosphonate (DMMP) addition on H2, CH4, and C2H4 ignition, Combust. Flame 191 (2018) 320–334.

[25] V.I. Babushok, G.T. Linteris, V.R. Katta, F. Takahashi, Influence of hydrocarbon moiety of DMMP on flame propagation in lean mixtures, Combust. Flame 171 (2016).

[26] T.M. Jayaweera, C.F. Melius, W.J. Pitz, C.K. Westbrook, O.P. Korobeinichev, V.M. Shvartsberg, et al., Flame inhibition by phosphorus-containing compounds over a range of equivalence ratios, Combust. Flame 140 (1–2) (2005) 103–115.

[27] F. Takahashi, V. Katta, G. Linteris, V Babushok, K Harada, K Himoto, K Matsuyama, Y Nakamura, K Wakatsuki, Numerical simulations of gas-phase interactions of phosphorus-containing compounds with cup-burner flames. Fire Science and Technology 2015: The Proceedings of 10th Asia-Oceania Symposium on Fire Science and Technology, 1st ed., Springer Singapore; Imprint: Springer, Singapore, 2017, pp. 751–758.

[28] F. Takahashi, V.R. Katta, G.T. Linteris, V.I. Babushok, Numerical study of gas-phase interactions of phosphorus compounds with co-flow diffusion flames, in: Proceedings of the Combustion Institute. International Symposium on Combustion 37, 2019.

[29] A. Coimbra, J. Sarazin, S. Bourbigot, G. Legros, J.-.L. Consalvi, A semi-global reaction mechanism for the thermal decomposition of low-density polyethylene blended with ammonium polyphosphate and pentaerythritol, Fire Saf. J. 133 (2022), 103649.

[30] O. Korobeinichev, A. Shmakov, A. Paletsky, S. Trubachev, A. Shaklein, A. Karpov, et al., Mechanisms of the action of fire-retardants on reducing the flammability of certain classes of polymers and glass-reinforced plastics based on the study of their combustion, Polymers 14 (21) (2022) (Basel).

[31] C. Geschwindner, D. Goedderz, T. Li, J. Köser, C. Fasel, R. Riedel, et al., Investigation of flame retarded polypropylene by high-speed planar laser-induced fluorescence of OH radicals combined with a thermal decomposition analysis, Exp. Fluids 61 (2) (2020) 2625.

[32] O. Korobeinichev, M. Gonchikzhapov, A. Tereshchenko, I. Gerasimov, A. Shmakov, A. Paletsky, et al., An experimental study of horizontal flame spread over PMMA surface in still air, Combust. Flame 188 (2018) 388–398.

[33] O.P. Korobeinichev, A.A. Paletsky, L.V. Kuibida, M.B. Gonchikzhapov, I.K. Shundrina, Reduction of flammability of ultrahigh-molecular-weight polyethylene by using triphenyl phosphate additives, Proc. Combust. Inst. 34 (2) (2013) 2699–2706.

[34] Y. Li, A. Guibaud, J.M. Citerne, J.L. Consalvi, A. Coimbra, J. Sarazin, et al., Effects of flame retardants on extinction limits, spread rate, and smoke release in opposed-flow flame spread over thin cylindrical polyethylene samples in microgravity, Proc. Combust. Inst. (2022).

[35] K. Salmeia, J. Fage, S. Liang, S. Gaan, An overview of mode of action and analytical methods for evaluation of gas phase activities of flame retardants, Polymers 7 (3) (2015) 504–526 (Basel).

[36] A. Battig, P. Müller, A. Bertin, B. Schartel, Hyperbranched rigid aromatic phosphorus-containing flame retardants for epoxy resins, Macromol. Mater. Eng. 306 (4) (2021), 2000731.

[37] M. Ciesielski, J. Diederichs, M. Döring, A. Schäfer, Advanced flame-retardant epoxy resins for composite materials. Fire and Polymers V, American Chemical Society, 2009, pp. 174–190.

[38] S. Liang, P. Hemberger, N.M. Neisius, A. Bodi, H. Grützmacher, J. Levalois-Grützmacher, et al., Elucidating the thermal decomposition of dimethyl methylphosphonate by vacuum ultraviolet (VUV) photoionization: pathways to the PO radical, a key species in flame-retardant mechanisms, Chemistry 21 (3) (2015) 1073–1080.

[39] M.W. Beach, S.E. Vozar, S.Z. Filipi, A.G. Shmakov, V.M. Shvartsberg, O.P. Korobeinichev, et al., Screening approaches for gas-phase activity of flame retardants, Proc. Combust. Inst. 32 (2) (2009) 2625–2632.

[40] S. Lau, B. Atakan, Isothermal pyrolysis investigation of aluminum diethylphosphinate mixed as a flame retardant additive into ultra-high molecular weight polyethylene, Combust. Flame 222 (2020) 272–284.

[41] S. Lau, M. Gonchikzhapov, A. Paletsky, A. Shmakov, O. Korobeinichev, T. Kasper, et al., Aluminum diethylphosphinate as a flame retardant for polyethylene: investigation of the pyrolysis and combustion behavior of PE/AlPi-Mixtures, Combust. Flame 240 (2022), 112006.

[42] U. Braun, H. Bahr, H. Sturm, B. Schartel, Flame retardancy mechanisms of metal phosphinates and metal phosphinates in combination with melamine cyanurate in glass-fiber reinforced poly(1,4-butylene terephthalate): the influence of metal cation, Polym. Adv. Technol. 19 (6) (2008) 680–692.

[43] M. Le-Bras, M. Bugajny, J.M. Lefebvre, S Bourbigot, Use of polyurethanes as char-forming agents in polypropylene intumescent formulations, Polym. Int. 49 (10) (2000) 1115–1124.

[44] B. Dittrich, K.A. Wartig, R. Mülhaupt, B. Schartel, Flame-retardancy properties of intumescent ammonium poly(Phosphate) and mineral filler magnesium hydroxide in combination with graphene, Polymers 6 (11) (2014) 2875–2895 (Basel).

[45] C. Savides, A. Granzow, J.F. Cannelongo, Phosphine-based flame retardants for polypropylene, J. Appl. Polym. Sci. 23 (9) (1979) 2639–2652.

[46] P.J. Davies, A.R. Horrocks, A. Alderson, The sensitisation of thermal decomposition of ammonium polyphosphate by selected metal ions and their potential for improved cotton fabric flame retardancy, Polym. Degrad. Stab. 88 (1) (2005) 114–122.

[47] A. Castrovinci, G. Camino, C. Drevelle, S. Duquesne, C. Magniez, M. Vouters, Ammonium polyphosphate–aluminum trihydroxide antagonism in fire retarded butadiene–styrene block copolymer, Eur. Polym. J. 41 (9) (2005) 2023–2033.

[48] Z. Qin, D. Li, Q. Li, R. Yang, Effect of nano-aluminum hydroxide on mechanical properties, flame retardancy and combustion behavior of intumescent flame retarded polypropylene, Mater. Des. 89 (2016) 988–995.

[49] J. Köser, L.G. Becker, A.K. Goßmann, B. Böhm, A. Dreizler, Investigation of ignition and volatile combustion of single coal particles within oxygen-enriched atmospheres using high-speed OH-PLIF, Proc. Combust. Inst. 36 (2) (2017) 2103–2111.

[50] J. Köser, T. Li, N. Vorobiev, A. Dreizler, M. Schiemann, B. Böhm, Multi-parameter diagnostics for high-resolution *in-situ* measurements of single coal particle combustion, Proc. Combust. Inst. 37 (3) (2019) 2893–2900.

[51] T. Li, P. Farmand, C. Geschwindner, M. Greifenstein, J. Köser, C. Schumann, et al., Homogeneous ignition and volatile combustion of single solid fuel particles in air and oxy-fuel conditions, Fuel 291 (1) (2021), 120101.

[52] T. Li, C. Geschwindner, J. Köser, M. Schiemann, A. Dreizler, B. Böhm, Investigation of the transition from single to group coal particle combustion using high-speed scanning OH-LIF and diffuse backlight-illumination, Proc. Combust. Inst. (3) (2021) 4101–4109.

[53] T. Li, M. Schiemann, J. Köser, A. Dreizler, B. Böhm, Experimental investigations of single particle and particle group combustion in a laminar flow reactor using simultaneous volumetric OH-LIF imaging and diffuse backlight-illumination, Renew. Sustain. Energy Rev.s 136 (2021), 110377.

[54] DIN Deutsches Institut fuer Normung e.V, Pruefungen Zur Beurteilung der Brandgefahr – Teil 11-10: Pruefflammen – Pruefverfahren Mit Einer 50-W-Pruef-flamme Horizontal Und Vertikal, Beuth Verlag, Berlin, 2014, 2013(DIN EN 60695-11-10 (VDE 0471-11-10)).

[55] Pfaendner R., Metzsch-Zilligen E., Stec M. Use of organic oxy imides as flame retardants for plastics and flame-retardant plastics composition and mouldings produced therefrom; 2014; Available from: https://patents.google.com/patent/WO2014154636A1/en.

[56] P.R. Hornsby, Fire retardant fillers for polymers, Int. Mater. Rev. 46 (4) (2001) 199–210.

[57] N. Perez, X.L. Qi, S. Nie, P. Acuna, M.J. Chen, D.Y. Wang, Flame retardant polypropylene composites with low densities, Materials 12 (1) (2019). Basel, Switzerland.

[58] J. Troitzsch, E. Antonatus, Plastics Flammability Handbook: Principles, Regulations, Testing, and Approval, Carl Hanser Verlag GmbH & Company KG, 2021.

[59] T.R. Hull, A. Witkowski, L. Hollingbery, Fire retardant action of mineral fillers, Polym. Degrad. Stab. 96 (8) (2011) 1462–1469.

[60] A. Sandinge, P. Blomqvist, M. Rahm, A modified specimen holder for cone calorimeter testing of composite materials to reduce influence from specimen edges, Fire Mater. 46 (1) (2022) 80–94.

[61] D. Price, K.J. Bullett, L.K. Cunliffe, T.R. Hull, G.J. Milnes, J.R. Ebdon, et al., Cone calorimetry studies of polymer systems flame retarded by chemically bonded phosphorus, Polym. Degrad. Stab. 88 (1) (2005) 74–79.

[62] Y. Xu, S. Li, Q. Yao, Y. Yuan, Investigation of steam effect on ignition of dispersed coal particles in O2/N2 and O2/CO2 ambiences, Fuel 233 (2018) 388–395.

[63] B. Schartel, Plastics Flammability Handbook: The Burning of Plastics, 4th ed., Carl Hanser Verlag GmbH & Company KG, 2021.

[64] B.D. Crittenden, R. Long, Formation of polycyclic aromatics in rich premixed acetylene and ethylene flames, Combust. Flame 20 (3) (1973) 359–368.

[65] M. Elomaa, E. Saharinen, Polycyclic aromatic hydrocarbons (PAHs) in soot produced by combustion of polystyrene, polypropylene, and wood, J. Appl. Polym. Sci. 42 (10) (1991) 2819–2824.

[66] H. Richter, J. Howard, Formation of polycyclic aromatic hydrocarbons and their growth to soot—a review of chemical reaction pathways, Prog. Energy Combust. Sci. 26 (4) (2000) 565–608.

[67] H. Guo, R.N. Walters, R.E. Lyon, S. Crowley, Effect of phosphorus on soot formation and flame retardancy in fires, Fire Saf. J. 120 (2021), 103068.

Supporting Information

The effects of various flame retardants on the combustion of polypropylene: Combining optical diagnostics and pyrolysis fragment analysis

Christopher Geschwindner[1*], Daniela Goedderz[2], Tao Li[1], Johannes Bender[3], Benjamin Böhm[1], Andreas Dreizler[1]

[1] Technical University of Darmstadt, Department of Mechanical Engineering, Reactive Flows and Diagnostics, Otto-Berndt-Str. 3, 64287 Darmstadt, Germany
[2] Fraunhofer Institute for Structural Durability and System Reliability LBF, Schlossgartenstr. 6, 64289 Darmstadt, Germany
[3] University of Stuttgart, Institute of Chemical Process Engineering (ICVT), Boeblinger Str. 78, 70199 Stuttgart, Germany
[*] Correspondence to: geschwindner@rsm.tu-darmstadt.de

1 Chemical decomposition analysis

Table S1 provides detailed information on the TGA-FTIR traces in addition to Figure 4 in the original manuscript.

Table S1. Peak temperatures of the traces detected by TGA-FTIR (nitrogen atmosphere, heating rate of 10 K/min).

Trace	$T_{peak,1}$ / °C	$T_{peak,2}$ / °C
PSMP		
H_2O 1763-1694 cm^{-1}	385,89	
Aldehyde 2836-2699 cm^{-1}	390,89	
Aldehyde 1735-1694 cm^{-1}	393,39	
Aldehyde 958-882 cm^{-1}	390,89	598,39
CH_2O 2838-2794 cm^{-1}	390,89	
CH_2O 1798-1760 cm^{-1}	388,39	
CH_2O 940-925 cm^{-1}	393,39	
-COOH 1736-1693 cm^{-1}	393,39	
Gram Schmidt	385,89	560,89
APP		
NH_3 3338-3330 cm^{-1}	379,22	446,72
NH_3 1634-1616 cm^{-1}	384,35	441,70
NH_3 968-959 cm^{-1}	381,72	451,72
NH_3 933-927 cm^{-1}	381,72	451,72
Gram Schmidt	506,70	
ATH		
H_2O 3759-3731 cm^{-1}	304,16	
H_2O 1763-1694 cm^{-1}	304,16	
H_2O 1564-1505 cm^{-1}	306,66	
Gram Schmidt	299,16	
DEPZn		
H_2O 3759-3731 cm^{-1}	663,16	
H_2O 1564-1505 cm^{-1}	680,66	
C_2H_6 3013-2910 cm^{-1}	475,67	
C_2H_6 2899-2864 cm^{-1}	475,67	
H_3O_2P 1156-1128 cm^{-1}	488,17	
H_3O_2P 1086-1053 cm^{-1}	473,17	558,17
H_3O_2P 730-707 cm^{-1}	475,67	
Gram Schmidt	475,66	
PP		
Alkene 3099-3062 cm^{-1}	460,08	
Alkene 2986-2950 cm^{-1}	457,59	
Alkene 2944-2904 cm^{-1}	444,80	
Alkene 1672-1628 cm^{-1}	462,58	
Alkene 1481-1435 cm^{-1}	463,80	
Alkene 1394-1366 cm^{-1}	461,30	
Alkene 915-873 cm^{-1}	461,30	
C_2H_4 952-948 cm^{-1}	641,30	
CH_4 3019-3011 cm^{-1}	461,30	
CH_4 1307-1301 cm^{-1}	463,80	
CO_2 2378-2302 cm^{-1}	466,30	
Gram Schmidt	444,80	482,49

1

PP + 10 wt% APP		
CO_2 2378-2302 cm^{-1}	440,90	534,17
Alkene 2986-2950 cm^{-1}	473,72	
Alkene 2944-2904 cm^{-1}	471,22	
Alkene 1481-1435 cm^{-1}	476,22	
Alkene 1394-1366 cm^{-1}	476,22	
Alkene 915-873 cm^{-1}	476,22	
NH_3 3338-3330 cm^{-1}	473,72	
NH_3 968-959 cm^{-1}	483,72	
NH_3 933-927 cm^{-1}	496,22	
Gram Schmidt	469,65	499,94
PP + 10 wt% ATH		
CO_2 2378-2302 cm^{-1}	310,75	
Alkene 2986-2950 cm^{-1}	486,91	
Alkene 2944-2904 cm^{-1}	486,91	
Alkene 1481-1435 cm^{-1}	492,50	
Alkene 1394-1366 cm^{-1}	494,41	
Alkene 915-873 cm^{-1}	489,41	
H_2O 3759-3731 cm^{-1}	688,51	
H_2O 1763-1694 cm^{-1}	310,75	487,80
Gram Schmidt	474,60	531,87
PP + 10 wt% DEPZn		
CO_2 2378-2302 cm^{-1}	395,66	
Alkene 2986-2950 cm^{-1}	468,17	
Alkene 2944-2904 cm^{-1}	465,67	
Alkene 1481-1435 cm^{-1}	473,17	580,67
Alkene 1394-1366 cm^{-1}	473,17	
Alkene 915-873 cm^{-1}	470,67	
H_2O 3759-3731 cm^{-1}	485,66	
H_2O 1564-1505 cm^{-1}	670,66	
C_2H_6 3013-2910 cm^{-1}	463,17	
C_2H_6 2899-2864 cm^{-1}	473,17	
H_3O_2P 1156-1128 cm^{-1}	485,67	
H_3O_2P 1086-1053 cm^{-1}	473,17	
H_3O_2P 730-707 cm^{-1}	478,17	
Gram Schmidt	460,66	588,16
PP + 10 wt% PSMP		
CO_2 2378-2302 cm^{-1}	418,14	
Alkene 2986-2950 cm^{-1}	388,14	463,14
Alkene 2944-2904 cm^{-1}	388,14	460,64
Alkene 1394-1366 cm^{-1}	470,00	
Alkene 915-873 cm^{-1}	465,64	
H_2O 1763-1694 cm^{-1}	468,14	
Aldehyde 2836-2699 cm^{-1}	369,80	470,67
Aldehyde 1735-1694 cm^{-1}	369,80	391,61
Aldehyde 958-882 cm^{-1}	320,63	470,67
CH_2O 2838-2794 cm^{-1}	369,80	470,67
CH_2O 1798-1760 cm^{-1}	595,55	
CH_2O 940-925 cm^{-1}	388,86	
-COOH 1736-1693 cm^{-1}	369,80	391,61
Gram Schmidt	383,14	460,64

2

2   Size classification of polymer particles

The statistical comparison of the combustion behavior of a finite amount of differently sized particles represents a trade-off between a large sample size and a high amount of compared size classifications. Figure S1(a-e) illustrates the histograms of the measured circle-equivalent diameters d_p of the polymer particles based on diffuse back-illumination (DBI) measurements. In this work, we define three size intervals with cutoff points $d_{p,\mathrm{min}}$ and $d_{p,\mathrm{max}}$ (further expressed as $\vec{d}_{p,cut} = \left(d_{p,\mathrm{min}}, d_{p,\mathrm{max}}\right)^T$) such that the total number of all particles present in each interval is similar. The selection of optimal size intervals can therefore be written as

$$\vec{d}_{p,cut} = \operatorname*{arg\,min}_{d_{p,min},\, d_{p,max}} \sqrt{\frac{1}{2}\sum_{i=1}^{3}(N_i - \bar{N})} = \operatorname*{arg\,min}_{d_{p,min},\, d_{p,max}} \;\sigma(N_i)$$

where i denotes the size interval and N_i is the amount particles in a particular interval. Essentially, this expresses a minimization of the standard deviation of the amount of particles between size intervals. The function was computed for all possible combinations of $d_{p,\mathrm{min}}$ and $d_{p,\mathrm{max}}$ and is displayed in Figure S1(f). The penalty function shoes a global minimum at $d_{p,\mathrm{min}} = 154\,\mu\mathrm{m}$ and $d_{p,\mathrm{max}} = 188\,\mu\mathrm{m}$. Consequently, based on this histogram classification, the quantities extracted from the OH-PLIF images can be compared for small, medium, and large particles or agglomerates.
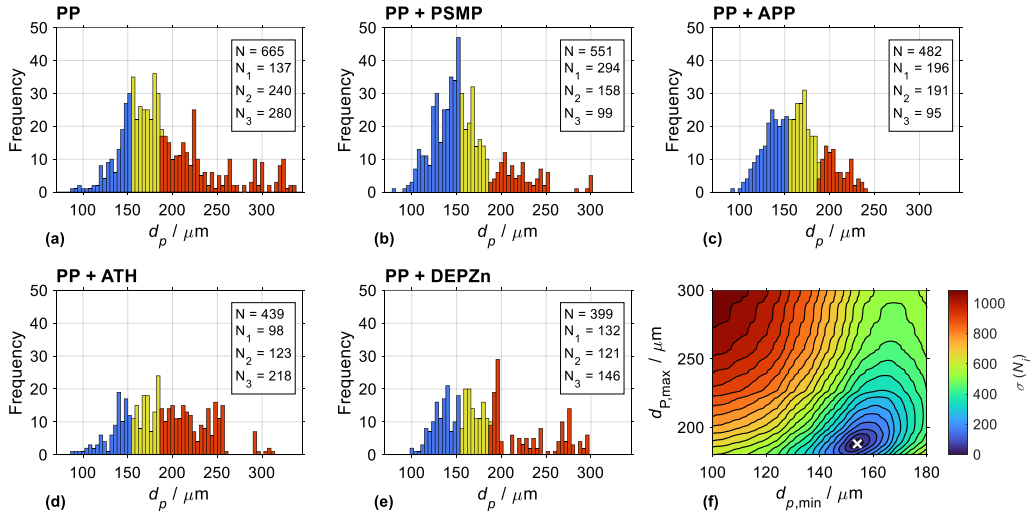

Figure S1. (a-e) Particle size distributions and size classification based on the size distribution optimization. (f) Selection of optimal limits of histogram interval division with global minimum marked with a white cross.

3

3 Cone calorimetry

Figure S3 provides the heat release rate curves and CO concentration measurements taken from cone calorimetry measurements. Figure S3 displays the entire time interval of the cone calorimetry measurements is an extension of the results shown in Figure S2.
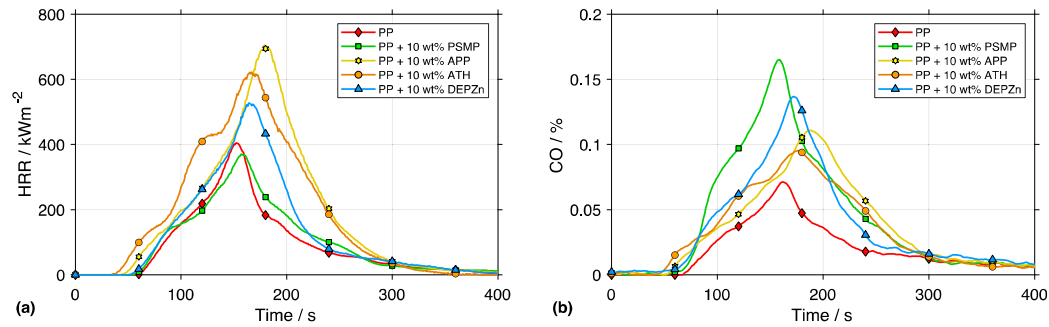

Figure S2. Heat release rate curves (heat flux of 35 kW/m2, left) and CO (%) concentration for different flame retarded PP formulations with a sample thickness of 3 mm (sample size: 100 × 100 mm).
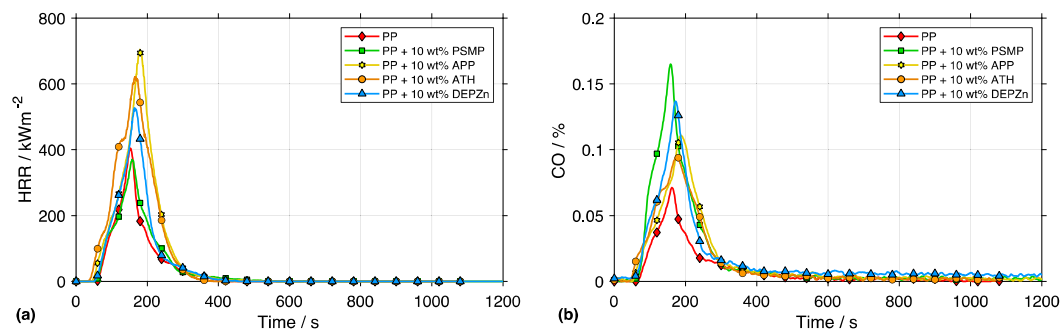

Figure S3. Heat release rate curves (heat flux of 35 kW/m2, left) and CO (%) concentration for different flame retarded PP formulations with a sample thickness of 3 mm (sample size: 100 × 100 mm).

Table S2. Cone calorimetry results of flame retardant formulations in PP with a sample thickness of 3 mm (irradiation: 35 kW/m^2; sample size: 100 x 100 mm).

Sample	PP	PP + 10 wt% PSMP	PP + 10 wt% APP	PP + 10 wt% ATH	PP + 10 wt% DEPZn
TTI / s	58 ± 6	45 ± 3	44 ± 4	38 ± 2	53 ± 4
PHRR / kWm^{-2}	404.9 ± 7.9	370.4 ± 23.6	705.0 ± 80.7	622.2 ± 66.6	526.7 ± 15.8
PHRR$_\Delta$ / %	100.0 ± 0.0	91.5 ± 5.8	174.1 ± 19.9	153.7 ± 16.4	130.1 ± 3.9
t_{max} (PHRR) / s	152 ± 11	157 ± 4	179 ± 10	167 ± 2	164 ± 13
THR / MJm^{-2}	36.6 ± 7.4	40.2 ± 12.8	71.6 ± 2.9	73.2 ± 10.1	51.2 ± 12.2
TSR / m^{2}m^{-2}	208.5 ± 25.6	743.2 ± 123.7	695.2 ± 17.7	463.2 ± 94.8	745.9 ± 111.0
CO$_{max}$ / %	0.1 ± 0.0	0.2 ± 0.0	0.1 ± 0.0	0.1 ± 0.0	0.1 ± 0.0
t_{max} (CO) / s	162 ± 11	158 ± 3	187 ± 9	176 ± 2	172 ± 10

4

B Declarations on the contribution to the scientific publications

DECLARATION ON THE CONTRIBUTION TO THE SCIENTIFIC PUBLICATION
Erklärung zum Eigenanteil der wissenschaftlichen Veröffentlichung

Christopher Geschwindner, M.Sc.

PAPER

C. Geschwindner, K. Westrup, A. Dreizler, B. Böhm: Ultra-high-speed time-resolved PIV of turbulent flows using a continuously pulsing fiber laser. *Experiments in Fluids* 63, 75 (2022). https://doi.org/10.1007/s00348-022-03424-7

CO-AUTHORS

Katharina Westrup, B.Sc.
Andreas Dreizler, Prof. Dr. habil.
Benjamin Böhm, Dr.-Ing

INDIVIDUAL CONTRIBUTIONS

- **Christopher Geschwindner**
  - Developed and conceptualized an experimental method based on particle-image velocimetry (PIV) to measure velocities in turbulent flow fields using a novel fiber laser system
  - Operated and adapted the experimental configuration (burner head of the microwave plasma heater) and performed experiments.
  - Post-processing, analysis and interpretation of the recorded data sets.
  - Main and corresponding author of the paper, performed literature research and managed the review process.
- **Katharina Westrup**
  - Conducted experiments together with C. Geschwindner.
  - Helped with the creation of figures of the experimental setup.
  - Proofreading of the manuscript.
- **Andreas Dreizler and Benjamin Böhm**
  Support for interpretation and discussion of the results, proofreading of the manuscript.

OVERALL CONTRIBUTION OF CHRISTOPHER GESCHWINDNER

A leading role in the conceptualization and conduction of the experiments, data analysis and main author of the manuscript.

USE OF PAPER CONTENTS IN OTHER DISSERTATIONS

This publication is not the subject of any ongoing or completed dissertation.
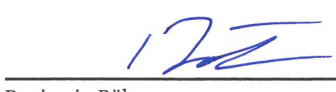
SIGNATURES OF ALL AUTHORS

_____
Christopher Geschwindner

_____
Andreas Dreizler

_____
Katharina Westrup

_____
Benjamin Böhm

1

150

DECLARATION ON THE CONTRIBUTION TO THE SCIENTIFIC PUBLICATION
Erklärung zum Eigenanteil der wissenschaftlichen Veröffentlichung

Christopher Geschwindner, M.Sc.

PAPER

C. Geschwindner, K. Westrup, A. Dreizler, B. Böhm: Pulse picking of a fiber laser enables velocimetry of biomass-laden jets at low and ultra-high repetition rates. *Proceedings of the Combustion Institute* (2022). https://doi.org/10.1016/j.proci.2022.07.138

CO-AUTHORS

Katharina Westrup, B.Sc.
Andreas Dreizler, Prof. Dr. habil.
Benjamin Böhm, Dr.-Ing

INDIVIDUAL CONTRIBUTIONS

- **Christopher Geschwindner**
  - Developed and conceptualized an experimental method to simultaneously measure the velocity of biomass particles and their surrounding carrier phase at low and ultra-high repetition rates based on the acousto-optic deflection of selected laser pulses exiting a novel fiber laser system
  - Operated and adapted the experimental configuration (burner head of the microwave plasma heater) and performed experiments.
  - Post-processing, analysis and interpretation of the recorded data sets.
  - Main and corresponding author of the paper, performed literature research and managed the review process.
- **Katharina Westrup**
  - Conducted experiments together with C. Geschwindner.
  - Helped with the creation of figures of the experimental setup.
- **Andreas Dreizler and Benjamin Böhm**
  Support for interpretation and discussion of the results, proofreading of the manuscript.

OVERALL CONTRIBUTION OF CHRISTOPHER GESCHWINDNER

A leading role in the conceptualization and conduction of the experiments, data analysis and main author of the manuscript.

USE OF PAPER CONTENTS IN OTHER DISSERTATIONS

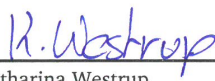This publication is not the subject of any ongoing or completed dissertation.

SIGNATURES OF ALL AUTHORS

_____
Christopher Geschwindner

_____
Andreas Dreizler

_____
Katharina Westrup

_____
Benjamin Böhm

1

151

DECLARATION ON THE CONTRIBUTION TO THE SCIENTIFIC PUBLICATION
Erklärung zum Eigenanteil der wissenschaftlichen Veröffentlichung

Christopher Geschwindner, M.Sc.

PAPER

T. Li, **C. Geschwindner**, A. Dreizler, B. Böhm: An experimental study of coal particle group combustion in conventional and oxy-fuel atmospheres using multi-parameter optical diagnostics. *Proceedings of the Combustion Institute* (2022). https://doi.org/10.1016/j.proci.2022.07.081

CO-AUTHORS

Tao Li, Dr.-Ing.
Andreas Dreizler, Prof. Dr. habil.
Benjamin Böhm, Dr.-Ing.

INDIVIDUAL CONTRIBUTIONS

- **Christopher Geschwindner**
  - Planned and conducted experiments together with T. Li.
  - Developed an algorithm to determine the measurement uncertainty of particle number density (PND) measurements based on the simulation of diffuse back-illumination (DBI). Applied the algorithm to the experimental data, which is reported in Section 3.1 of the paper.
  - Supported T. Li in the post-processing, analysis and interpretation of the recorded data sets and answered questions in the review process.
- **Tao Li**
  - Planned and conducted experiments together with C. Geschwindner.
  - Post-processing, analysis and interpretation of the data sets with special focus on the laser-induced fluorescence and Mie scattering measurements.
  - Corresponding author of the paper, performed literature research and managed the review process.
- **Andreas Dreizler and Benjamin Böhm**
  Support for interpretation and discussion of the results, proofreading of the manuscript.

OVERALL CONTRIBUTION OF CHRISTOPHER GESCHWINDNER

A leading role in the development of the PND measurement uncertainty code and its application to experimental data as well as its documentation in the paper. Planned and conducted experiments together with T.Li and strongly supported further data analysis and manuscript writing.

USE OF PAPER CONTENTS IN OTHER DISSERTATIONS

This publication is not the subject of any ongoing or completed dissertation.

SIGNATURES OF ALL AUTHORS

_____
Christopher Geschwindner

_____
Tao Li

_____
Andreas Dreizler

_____
Benjamin Böhm

1

DECLARATION ON THE CONTRIBUTION TO THE SCIENTIFIC PUBLICATION
Erklärung zum Eigenanteil der wissenschaftlichen Veröffentlichung

Christopher Geschwindner, M.Sc.

PAPER

C. Geschwindner, D. Goedderz, T. Li, J. Köser, C. Fasel, R. Riedel, V. Altstädt, C. Bethke, F. Puchtler, J. Breu, M. Döring, A. Dreizler, B. Böhm: Investigation of flame retarded polypropylene by high-speed planar laser-induced fluorescence of OH radicals combined with a thermal decomposition analysis. *Experiments in Fluids* 61, 30 (2020). https://doi.org/10.1007/s00348-019-2864-5

CO-AUTHORS

Daniela Goedderz, Dr. rer. nat.
Tao Li, Dr.-Ing.
Jan Köser, Dr.-Ing.
Claudia Fasel, Dipl.-Ing.
Ralf Riedel, Prof. Dr.
Volker Altstädt, Prof. Dr.-Ing.

Christian Bethke, M.Sc.
Florian Puchtler
Josef Breu, Prof. Dr.
Manfred Döring, Prof. Dr.
Andreas Dreizler, Prof. Dr. habil.
Benjamin Böhm, Dr.-Ing.

INDIVIDUAL CONTRIBUTIONS

- **Christopher Geschwindner**
  - Developed and conceptualized an experimental method to detect and track the combustion of micrometer-sized polymer particles based on the laser-induced fluorescence (LIF) of the OH radical.
  - Operated and adapted the experimental configuration (laminar flow reactor) and performed experiments.
  - Post-processing and analysis of the recorded data sets. Joint interpretation with co-authors from the fields of combustion science, optical diagnostics and polymer chemistry.
  - Main and corresponding author of the paper, performed literature research, wrote and managed the review process.
- **Daniela Goedderz**
  - Sample preparation of the flame retarded polymer specimens.
  - Coordinated the thermal decomposition analysis with external groups (including TGA/STA coupled to FTIR and MS and cone calorimetry) and interpreted the data.
  - Joint analysis of the results with C. Geschwindner.
  - Used this publication in her dissertation (see details under the section *Use of paper contents in other dissertations* below).
- **Tao Li**
  Conducted LIF experiments together with C. Geschwindner, consulting during manuscript preparation, proofreading.
- **Jan Köser**
  Preparation and consulting of the optical diagnostics measurements.
- **Claudia Fasel and Ralf Riedel**
  Provided technical infrastructure and conducted chemical analysis (TGA/STA coupled to FTIR and MS).
- **Volker Altstädt and Christian Bethke**
  Provided technical infrastructure and conducted cone calorimetry.
- **Florian Puchtler and Josef Breu**
  Provided technical infrastructure and conducted cone calorimetry.
- **Manfred Döring, Andreas Dreizler and Benjamin Böhm**
  Support for interpretation and discussion of the results, proofreading of the manuscript.

1

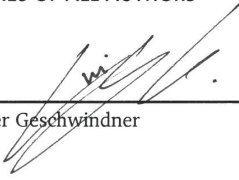## Overall Contribution of Christopher Geschwindner

A leading role in the conceptualization and conduction of the experiments, data analysis and main author of the manuscript.
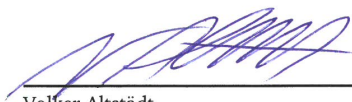
Use of paper contents in other dissertations

This paper was part of the dissertation of Daniela Goedderz, who was leading the chemical decomposition analysis and sample preparation. She specifically states the contribution and leading role of Christopher Geschwindner to the journal publication in her dissertation. Other than the work of Dr. Goedderz, this publication is not the subject of any further ongoing or completed dissertation.

Goedderz, Daniela (2021): Neue Flammschutzmittel für PET und Aufklärung der Wirkmechanismen. Dissertation. https://doi.org/10.26083/tuprints-00018599

Signatures of all authors

_____
Christopher Geschwindner

_____
Daniela Goedderz

_____
Tao Li

_____
Jan Köser

_____
Claudia Fasel

_____
Ralf Riedel

_____
Volker Altstädt

_____
Christian Bethke

_____
Florian Puchtler

_____
Josef Breu

_____
Manfred Döring

_____
Andreas Dreizler

_____
Benjamin Böhm

2

A leading role in the conceptualization and conduction of the experiments, data analysis and main author of the manuscript.

Use of paper contents in other dissertations

This paper was part of the dissertation of Daniela Goedderz, who was leading the chemical decomposition analysis and sample preparation. She specifically states the contribution and leading role of Christopher Geschwindner to the journal publication in her dissertation. Other than the work of Dr. Goedderz, this publication is not the subject of any further ongoing or completed dissertation.

Goedderz, Daniela (2021): Neue Flammschutzmittel für PET und Aufklärung der Wirkmechanismen. Dissertation. https://doi.org/10.26083/tuprints-00018599

Signatures of all authors

_____
Christopher Geschwindner

_____
Daniela Goedderz

_____
Tao Li

_____
Jan Köser

_____
Claudia Fasel

_____
Ralf Riedel

_____
Volker Altstädt

_____
Christian Bethke

_____
Florian Puchtler

_____
Josef Breu

_____
Manfred Döring

_____
Andreas Dreizler

_____
Benjamin Böhm

2

155

DECLARATION ON THE CONTRIBUTION TO THE SCIENTIFIC PUBLICATION
Erklärung zum Eigenanteil der wissenschaftlichen Veröffentlichung

Christopher Geschwindner, M.Sc.

PAPER

C. Geschwindner, D. Goedderz, T. Li, J. Bender, A. Dreizler, B. Böhm: The effects of various flame retardants on the combustion of polypropylene: Combining optical diagnostics and pyrolysis fragment analysis
Polymer Degradation and Stability 211, 110321 (2023).
https://doi.org/10.1016/j.polymdegradstab.2023.110321

CO-AUTHORS

Daniela Goedderz, Dr. rer. nat.
Tao Li, Dr.-Ing.
Johannes Bender, Dr. rer. nat.

Benjamin Böhm, Dr.-Ing.
Andreas Dreizler, Prof. Dr. habil.

INDIVIDUAL CONTRIBUTIONS

- **Christopher Geschwindner**
  - Developed and adapted experimental methods to detect and track the combustion of micrometer-sized polymer particles and stick-shaped specimen based on the laser-induced fluorescence (LIF) of the OH radical and other optical combustion diagnostics.
  - Operated and adapted the experimental configurations (laminar flow reactor and external flame interaction test stand) and performed experiments.
  - Post-processing and analysis of the recorded data sets. Joint interpretation with co-authors from the fields of combustion science, optical diagnostics and polymer chemistry.
  - Main and corresponding author of the paper, performed literature research, wrote and managed the review process.
- **Daniela Goedderz**
  - Sample preparation of the flame retarded polymer specimens.
  - Coordinated the thermal decomposition analysis with external groups, post-processed and interpreted the data. Conducted cone calorimetry measurements.
  - Joint analysis of the results with C. Geschwindner.
- **Tao Li**
  Conducted LIF experiments together with C. Geschwindner, consulting during manuscript preparation, proofreading.
- **Johannes Bender**
  Conducted TGA-FTIR (thermogravimetric analysis with decomposition gas analysis) measurements and consultation.
- **Andreas Dreizler and Benjamin Böhm**
  Support for interpretation and discussion of the results, proofreading of the manuscript.

OVERALL CONTRIBUTION OF CHRISTOPHER GESCHWINDNER

A leading role in the conceptualization and conduction of the experiments, data analysis and main author of the manuscript.

USE OF PAPER CONTENTS IN OTHER DISSERTATIONS

This publication is not the subject of any ongoing or completed dissertation.

1

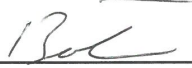SIGNATURES OF ALL AUTHORS

_____
Christopher Geschwindner

_____
Daniela Goedderz

_____
Tao Li

_____
Johannes Bender

_____
Andreas Dreizler

_____
Benjamin Böhm

2

157